E-SPARC

Make Aerobatic Racing Innovative and Eco-friendly for the Future

Joey Hoogendoorn	4231155	Christel Prins	4197534
Paul Hulsman	4208412	Bastiaan Röell	4226224
Daan Peschier	4232739	Luc de Ruiter	4223500
Ole Pfeifle	4206150	Eva Smeets	4222016
Wouter Plaetinck	4219724	Noel Weber	4211251

Final Report

Design Synthesis Excercise

June 30, 2015

ESPARC

Electrically, Sustainably Propelled Aerobatic Racing Aircraft

Make Aerobatic Racing Innovative and Eco-friendly for the Future

Supervisor:	Dr. Ir. S. Shroff ,	TU Delft
Coaches:	Dr. Ir. A. in 't Veld ,	TU Delft
	Ir. M. Hoogreef,	TU Delft
External Expert:	H.J. van Overvest,	Aerobatic Pilot

Supported by: TU Delft Delft University of Technology

June 30, 2015

PREFACE

Hereby we proudly present you the final report, which has been prepared by the E-SPARC team (Group 14) for the 2015 Spring Design and Synthesis Exercise (DSE) of the Aerospace Engineering department at the Delft University of Technology. This Final report describes the conceptual design phase and the preliminary design phase in which various design trade-offs have been made to come to one final design.

The goal is to design an experimental category aircraft for use as an aerobatic racer competing in Red Bull Air Races in 2025 at the latest. The design should be innovative, must be in partial fulfilment of the regulations and rules set by the stakeholders and by Red Bull.

We would like to express our gratitude to everyone who supported us in the design of E-SPARC. We would especially like to thank Sonell Shroff, Maurice Hoogreef, Alexander in 't Veld and Hendrik Jan van Overvest, our tutor and coaches throughout the project who have helped us choose the right concept and who have coached us during the project.

Delft, 30/6/2015

SUMMARY

Following in the footsteps of the automotive industry with the successful implementation of Formula E, the E-SPARC design is the world's first all-electric racing aircraft. E-SPARC's mission is to proof the feasibility of a sustainable and high performance alternative for the current state-of-the-art in aerobatic racing. Thereby, the aim is to present a design worthy of competing in the popular Red Bull Air Races. Given the combination of being the world's fastest growing international motorsport with the commitment towards reducing the carbon footprint [1], Red Bull Air Races provide the optimal platform for the E-SPARC design. The leading design question is therefore whether an all-electric racing aircraft can be designed with performance characteristics equal to or exceeding the performance characteristics of the current competition. This report describes the design decisions and outcomes taken during the preliminary design phase, continuing upon the pusher canard configuration that was selected during the conceptual design phase.

Aerodynamically, the canard configuration chosen for E-SPARC, combined with the aimed for performance characteristics for optimal results in the Red Bull Air Races provided an additional challenge. The configuration required the simultaneous optimization of the main wing and canard designs in terms of aerodynamic efficiency, maintaining lift at high angles of attack during high G turns, as well as strict stall characteristics to ensure stall of the canard prior to stall of the main wing. Using a genetic algorithm the optimal airfoils combination was found for both lifting surfaces. The main wing features a NACA 9216-42, modified NACA four series airfoil and the canard has a NACA 12311-62 airfoil. Using XFLR-5, various 3D effects on both wing surfaces were estimated, including the effect of downwash from the canard on the wing as well as tip vortices, which allowed the determination of 3D aerodynamic wing and canard characteristics. Finally, a separate drag estimation was also performed using statistical analysis tools, which resulted in a zero-lift drag coefficient estimate of 0.034. The resulting preliminary wing design has a maximum lift coefficient of 1.78 and an efficiency factor of 0.78. With an aspect ratio of 6 and a wing area of 5.2 square meters, the wing span is only 5.6 meters. The canard design features a maximum lift coefficient of 2.0 with an aspect ratio of 8 and area of 1.1 square meters.

Preliminary designs for the wing and fuselage structural lay-out were performed, as well as for the landing gear. With the aim for a lightweight yet robust wing design, a sandwich panel wing design was chosen for both the wing and canard produced using CFRP skin material. Similar to the wing, CFRP was selected as material for the fuselage. The fuselage has a semi-monocoque structure, providing the best combination of strength, usable space and weight for the E-SPARC. Using simplified structural layouts for both the wing and fuselage structures, the required thicknesses were determined based on analytical tools. This resulted in a preliminary structural aircraft weight of 140 kilograms.

The decision was made to use vertical stabilizer fins positioned on the wing tips, rather than a conventional vertical tail. This decision was based on the potentially negative effects of rudder deflections on the flow entering the pusher propeller. Using the scissor plot method, the required center of gravity location was determined to achieve longitudinal stability and control. Similarly, the scissor plot was used for lateral stability and control, with which the size of the vertical fins could be obtained. Furthermore, preliminary sizing of the control surfaces was performed using reference aircraft. The Datcom method was used to size the ailerons. Performance analysis predicts a roll rate of 460 degrees per second. Rudder sizing was performed using cross-wind requirements on approach. Elevator performance was achieved by satisfying the requirements for stick position stability and stick displacement per G. The requirement for stick force stability is yet to be satisfied. This requires a detailed analysis of the control system design as well as better estimated for the hinge moment coefficients by means of CFD analysis or wind tunnel tests.

The powertrain analysis consists of a propeller- and shaft design, electric motor sizing, battery pack and module design as well as a thermal analysis of the designed modules which elaborates on the feasibility of air cooling. The sizing of the propeller was based on McCormick (1979) and XRotor. The latter uses an extension of the classical blade-element/vortex formulation for the blade and propeller design. The sizing of the electric motor was based on an off-the-shelf YASA 750 motor with proposed alterations. The battery pack and module were designed using an optimization script for minimized weight and volume. An analytical solution method was used for the thermal analysis of separate battery modules. Weight iterations showed a required power of 115.5 kW, resulting in a preliminary electric motor and total battery pack weight of 26.2 and 100.7 kilograms respectively. Smart design of the battery pack allowed for a modular battery design consisting of 12 exchangeable Lithium-Sulfur battery modules in parallel with 273 cells in series each, allowing for both easy maintainability as well as manipulation of the center of gravity location during the design phase, such that the desired center of gravity location for stability and control objectives could be obtained. Furthermore, an inverter/controller had to be

added to complete the preliminary power train design. Thermal analysis of the battery modules showed the feasibility of air cooling for E-SPARC, allowing for a major reduction in complexity and cost of the aircraft. The resulting preliminary design has a total aircraft weight of 415 kilograms.

By means of a track analysis, the performance of the E-SPARC design was compared to the performance of its current competitors. An estimation of the 2008 San Diego Red Bull Air Race track was implemented into a Python program together with the aerodynamic characteristics of both the E-SPARC aircraft and Extra-300S. The track analysis revealed that the current E-SPARC design flies the simulated track in 95.3 seconds, whereas the Extra-300S finishes in 87.2 seconds. Thus, the current E-SPARC design is about 8 seconds slower than the current state-of-the-art. This was attributed to the relatively low power to weight ratio and higher zero-lift drag coefficient of the E-SPARC design. Based on this result from the track analysis it is recommended to perform several additional design iterations in order to increase the power to weight ratio. Although this will also add weight, the current lightweight design provides sufficient margin to do so.

Based on the preliminary design, E-SPARC may be considered a success. It exhibits performance characteristics similar to those of current competitors, proving the feasibility of a sustainable and high performance race aircraft. However, further iterations are recommended to increase the power to weight ratio. As this will also impact the design of other subsystems, this will require more iterations of the complete design. A more accurate determination of various aircraft parameters including the size of the control surfaces, structural characteristics e.g. skin and spar thicknesses and aerodynamic characteristics like the form drag require more advanced analysis tools such as CFD and FEA. These tools are beyond the scope of the current Design and Synthesis Exercise.

List of Symbols

α	Angle of attack	$[deg]$
β	Sideslip angle	$[rad]$
$\beta_{0.75R}$	Blade pitch angle at 0.75R	$[°]$
δ	Deflection of a control surface	$[rad]$
$\dot{\alpha}$	Angular acceleration	$[rad \cdot s^{-2}]$
$\dot{Q}_{l,c}$	Heat loss single cell	$[W]$
η	Efficiency	$[-]$
κ_{CR}	Correction factor C-Rate	$[-]$
Λ	Sweep angle	$[rad]$
λ	Taper ratio	$[-]$
μ	Dynamic viscosity	$[kg/m \cdot s]$
ν	Poisson's ratio	$[-]$
ω	Angular velocity	$[rad/s]$
ρ	Air density	$[kg/m^3]$
σ	Normal stress	$[Pa]$
τ	Shear stress	$[Pa]$
A	Aspect ratio	$[-]$
b	Wingspan	$[m]$
b_f	Fuselage maximum width	$[m]$
c	Chord	$[m]$
$C(x)$	Chord as a function of x	$[m]$
C_d	Drag coefficient	$[-]$
C_L	Lift coefficient	$[-]$
C_l	Moment coefficient about X-axis	$[-]$
C_m	Moment coefficient about Y-axis	$[-]$
C_n	Moment coefficient about Z-axis	$[-]$
C_P	Propeller power coefficient	$[-]$
C_S	Propeller speed power coefficient	$[-]$
C_T	Propeller thrust coefficient	$[-]$
c_V	Volume coefficient	$[-]$
C_Y	Force coefficient in Y-direction	$[-]$
$C_{Ah,c}$	Single cell capacity	$[Ah]$
C_{tot}	Battery pack total capacity	$[kWh]$
CR	C-Rate	$[C]$
D	Drag	$[N]$
d	Propeller diameter	$[m]$
d_{gw}	Wheel diameter	$[m]$
E	Young's modulus	$[Pa]$
e	Oswald factor	$[-]$
e	Specific energy	$[J/kg]$
$E_r eq$	Required energy for mission	$[J]$
e_v	Span efficiency factor	$[-]$
G	Shear modulus	$[Pa]$
g	Gravitational constant	$[m/s^2]$
h	Height	$[m]$
I	Area moment of inertia	$[m^4]$
I	Current/amperage	$[A]$
J	Advance ratio	$[-]$
J	Shaft polar moment of inertia	$[m^4]$
J	Torsional constant	$[m^4]$

k	Plate buckling coefficient	$[-]$
k_L	Sweep correction factor	$[-]$
L	Lift	$[N]$
l	Distance in longitudinal direction from centre of gravity	$[m]$
l	Length	$[m]$
$L(x)$	Lift distribution	$[N/m]$
M_Z	Bending moment around Z-axis	$[Nm]$
N	Load factor	$[-]$
n	Rotational speed	$[RPM]$
N_p	Number of cells in parallel	$[-]$
N_s	Number of cells in series	$[-]$
P	Power	$[W]$
p	Specific power	$[W/kg]$
Q	Torque	$[Nm]$
q	Dynamic pressure	$[N/m^2]$
R	Radius of curvature	$[m]$
r_f	Fuselage shape factor	$[-]$
r_t	Tail drag as percentage of wing and fuselage drag	[%]
r_w	Type of wing support	$[-]$
Re	Reynolds number	$[-]$
S	Surface area	$[m^2]$
S_Y	Shear force in Y-direction	$[N]$
$s_{takeoff}$	Takeoff distance	$[m]$
T	Thrust	$[N]$
t	Thickness	$[m]$
t	Time	$[s]$
t/c_{root}	Thickness over chord ratio at the root	$[-]$
V	Velocity	$[m/s]$
V	Voltage	$[V]$
v	Energy density	$[J/L]$
v	Kinematic viscosity	$[m^2/s]$
V_{nom}	Cell nominal voltage	$[V]$
W	Weight	$[N]$
w_{gw}	Wheel width	$[m]$
x	Distance in longitudinal direction from the front	$[m]$

Subscripts

0	At initial conditions
$0.25c$	At the quarter-chord line
α	Derivative with respect to α
a	Aileron
ac	Aerodynamic centre
b,in	Battery input
b,out	Battery output
bat	Battery
c	Canard
cg	Centre of gravity
ch	Battery module channel
E	Empty
e	Elevator
f	Fan(s)
f	Fuselage
h	Horizontal component
$land$	Landing

m	Main gear
m,in	Motor input
m,out	Motor output
min	Minimum
n	Nose gear
p	Propeller
r	Root
r	Rudder
req	Required
SC	Supercharger
$struct$	Structural
t	Tip
TO	Takeoff
ult	Ultimate
v	Vertical component
vt	Vertical tail
w	Wing

LIST OF ACRONYMS

AHRS	Altitude and Heading Reference System
BMS	Battery Management System
AC	Aerodynamic Centre
AWG	Aural Warning Generator
BMS	Battery Management System
CFD	Computational Fluid Dynamics
CFRP	Carbon Fiber Reinforced Polymer
CG	Centre of Gravity
EFIS	Electronic Flight Information System
EOM	Equation Of Motion
FEA	Finite Element Analysis
FEM	Finite Element Method
HLD	High Lift Device
LEMAC	Leading Edge Mean Aerodynamic Chord
MFD	Multi-Function Display
MOI	Moment of Inertia
MTOW	Maximum Take-Off Weight
OEW	Operational Empty Weight
PDD	Project Design and Development
PFD	Primary Flight Display
PVI	Peripheral Vision Indicator
RBAR	Red Bull Air Race
RC	Rate of Climb
RoI	Return on Investment
SM	Stability Margin
SoC	State of Charge
TOP	Takeoff Parameter

CONTENTS

1 INTRODUCTION

Electric flight propulsion is a highly anticipated but challenging field. Electric propulsion could be a sustainable solution to reduce the impact of aviation on the environment. However, long flight durations and the current limiting energy storage capacities are often an obstacle for the application of these technologies to power aircraft. Only certain target areas are possible nowadays. An example of such a target area might be air racing, since these flights are of short duration. Growing in popularity and technical complexity, air racing is an exciting sport, both today and in the future.

The design of an aerobatic racing aircraft has to be altered and adapted for the challenges of an all electric aircraft, to achieve a competitive and sustainable product. In this project, the conceptual and preliminary design of such an aircraft is performed. The project objective statement is stated as follows:

> *Make aerobatic racing innovative and eco-friendly for the future.*

Following from this, the mission need statement is defined as follows:

> *To design an electric propelled aerobatic racing aircraft with a group of 10 Aerospace Engineering students of the TU Delft and have its first flight in 2025 costing no more than 300,000 Euro, in order to test and show the feasibility of electrically propelled, high performance, sustainable aircraft.*

This report explains the methods and design steps to come to the final design of E-SPARC. A deviation of around 10% from the weights calculated here is to be expected as the design was carried out up to and including the preliminary design phase. It is based on choices made in the Baseline and Mid Term Report where the stakeholders were identified and the different concepts were treated. This was a crucial step for the project since it determined which concepts were feasible and further investigated in more detail to find the final concept. A canard configuration was chosen based on criteria of L/D, maneuverability, complexity, propulsive efficiency, visibility, safety, take-off and landing and the uncertainty of the design. The focus in this report is to give a more detailed design of the components of the canard configuration for the fuselage, wing, canard, power unit and the landing gear. The design is optimized for the different departments from structures, aerodynamics, stability & control and power & propulsion to find the best combination and one final design. The design of E-SPARC aircraft is based on top-level requirements with the most important requirement that it shall have the fastest race at RBAR. It should be electrically propelled to open an new target area and manufacturing and certification cost shall be less than 300,000 Euro. A limiting factor in the design is the design load factor of 12g at turns. It shall be fabricated at Delft Aerospace Structures and Materials Lab at the Aerospace faculty and have its first flight before 2025.

The report is divided in three parts, a Project & Development Strategy, Preliminary Aircraft Design and Aircraft Analysis. The first part describes the logical order of functions that the product must perform in a functional diagram given in Chapter 2. Then in Chapter 3 the market analysis is discussed to investigate the market for this racing aircraft. The mission profile is given in Chapter 4 describing what the aircraft is actually supposed to do during its mission. Finally a logical order of activities after the DSE project is given in Chapter 5 for future developments. Thereafter the actual design of E-SPARC on weight and dimensions is given with a Class I method and with a more refined Class II method in Chapter 6. The detailed design of each different department is given for the powertrain in Chapter 7, the wing and canard in Chapter 8, the empennage in Chapter 9, the landing gear in Chapter 10 and finally the fuselage is discussed in Chapter 11, . In the last part the performance analysis is carried out in Chapter 12 to look how the aircraft will perform in the race. Chapter 13 discusses the aerodynamic characteristics of the aircraft, where Chapter 14 treats the stability and control characteristics. Chapter 15 provides an overview of the main data handling and a RAMS analysis is performed in Chapter 16. Finally a compliance & sensitivity analysis is performed in Chapter 17.

I

Project & Development Strategy

2 PROJECT ANALYSIS

This chapter describes the logical order of functions that the product must perform in a functional diagram given in Section 2.1, and hierarchically represented in a funtional breakdown structure in Section 2.2. The technical risk assessment in Section 2.3 will focus on the phases that come after the DSE and identifies the technical risks thay may occur in the development of the system, with the consequence that technical performance, schedule or cost requirements are not met.

2.1 FUNCTIONAL FLOW DIAGRAM

The functional flow diagram shows the consecutive order of tasks the aircraft has to perform during its lifetime as a racing aircraft as well as when it is used in later stages of its life. As an example, a typical functional flow for a race with possible multiple races is shown. Furthermore, it depicts which functions the aircraft has to fulfill when it is being disposed of. The functional flow diagram is shown in Figure 2.1.

2.2 FUNCTIONAL BREAKDOWN STRUCTURE

The functional breakdown diagram shows the most important functions the aircraft has to fulfill. It is shown in Figure 2.2.

2.3 TECHNICAL RISK ASSESSMENT

The risk assessment will focus on the phases that will come after the DSE. This means that these risks are the main risks that apply to either the further design of the E-SPARC or to the production and testing of the prototype. The following risks were identified.

1. **Delay in the design process.** This can occur when there are less people working on the design than initially anticipated. There is also the possibility that the CFD and/or the FEM analysis show that there are important problems in the design which means that a part of the design process will need to be performed again.
2. **Certain design changes that are made affect the performance badly.** In a design process there are always compromises that have to be made (for example the designs of a structural engineer and an aerodynamics engineer will have to be merged, even if contradicting). This could result in some decisions that affect the performance of E-SPARC badly, leading to a non-ideal design.
3. **Certain production methods are not possible.** As E-SPARC should be produceable at TU Delft, there is the possibility that machines at TU Delft will be discarded due to defects. If that machine was supposed to be used for the production of E-SPARC, an alternative will have to be found.
4. **Miscommunications with the suppliers or within the team.** Misunderstandings during human interaction can lead to mistakes and delays. This will affect the production process negatively.
5. **Delay in the production.** There could be unexpected problems during the production which would delay it.
6. **Error in the production or assembly.** Mistakes being made during the production and assembly lead to increasing time and cost. Human errors thus have to be accounted for. Depending on the severity of the error, this could be a big or a small problem.
7. **A certain supplier has a shortage of a material or component that is needed for production.** Suppliers usually have a limited stock, which means that certain products could not be available when they are needed for the production of E-SPARC.
8. **Material shortage in the local material stock for E-SPARC.** It is possible that the amount of material was underestimated and that there is not enough material in our own stock. This would require ordering and waiting for new material.
9. **The battery is not ready at the expected time.** The battery is expected to be ready in 2019. This is based on forecasts by experts. There is still a possibility that the battery is not ready when it is needed.
10. **The aircraft is not fast enough to compete.** There is a chance that the flight tests show that E-SPARC is not as fast as expected.
11. **The aircraft is unstable.** Wind tunnel tests could show that E-SPARC is either statically or dynamically unstable, contrary to the preliminary analysis.
12. **The aerodynamic characteristics are not as expected.** There is also a possibility that the wind tunnel test show that the aerodynamic characteristics do not meet the expectations. This would lower the performance of E-SPARC and could thus be detrimental to the success of the product.

13. **Failed structural test.** Structural tests will be performed to ensure the integrity of the structure. It is possible that these test show that the structure can not withstand the load factors that it should.
14. **Failed motor and/or battery test.** The electric motor and the battery will be tested to make sure that the perform adequately. If this is not the case, alternatives have to be found and implemented, or it has to be accepted that the performance is lower.
15. **Battery leakage.** If the battery is not manufactured correctly, leakage could happen, leading to losses and safety problems, as well as environmental threats.

In order to assess whether a risk needs mitigation or not, a risk map is constructed. All the risks are given a score for likelihood and magnitude of the consequences, on a scale from very low to very high and insignificant to catastrophic respectively. The risk map can be seen in Table 2.1.

Table 2.1: Risk map of all risk identified

	LIKELIHOOD				
MAGNITUDE	1. Very low	2. Low	3. Moderate	4. High	5. Very high
5. Catastrophic		10	7	9	
4. Major		2, 13, 15	6		
3. Moderate		11, 14	3, 8	4, 5	
2. Minor		1, 12			
1. Insignificant					

green	yellow	red

From the risk map it is concluded that risks 9 and 7 need a mitigation plan. Both of those risks are related to the manufacturing process.

Risk 9 could be mitigated by making sure that the battery is ready before starting production. The reason why the magnitude of the consequences is so big is because the production process can not be stopped in the middle to wait for the battery because of deterioration of the materials and growing costs due to increasing overlay times. If the start of the production is postponed until there is certainty that the battery will be ready, the consequences will be smaller. The likelihood of occurrence of this risk can not be changed because it is completely dependent on the company that produces the battery, which is the only party that has an influence on this.

Risk 7 is dependent on the different suppliers. The likelihood of occurrence can be decreased by choosing established suppliers because they usually have a bigger stock and a more consistent delivery due to a larger network and client experience. The magnitude of the consequences can be diminished by making sure that all the suppliers have the materials and components available more than a week before the production starts and maybe build up a stock of products that are in high demand.

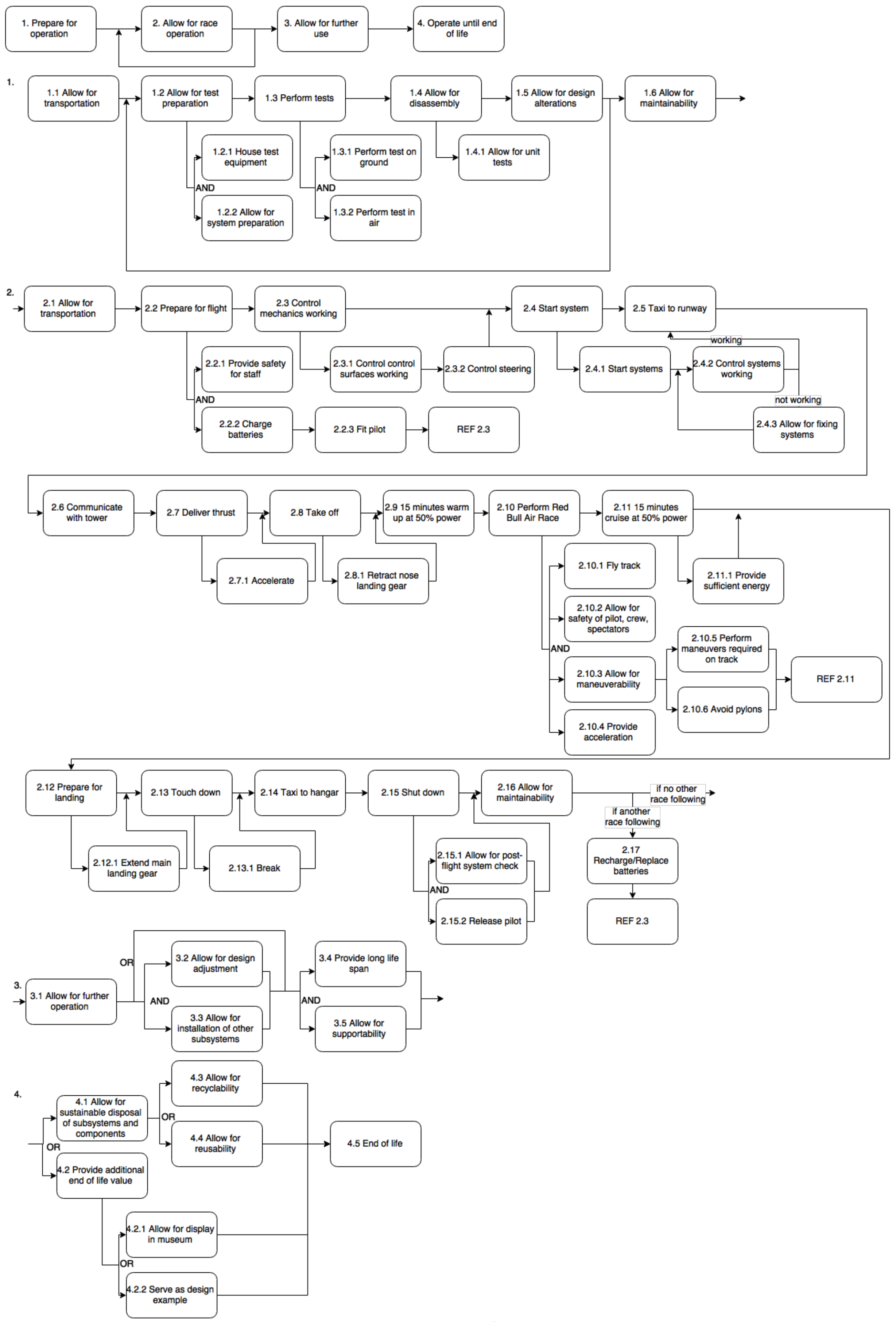

Figure 2.1: Functional flow diagram

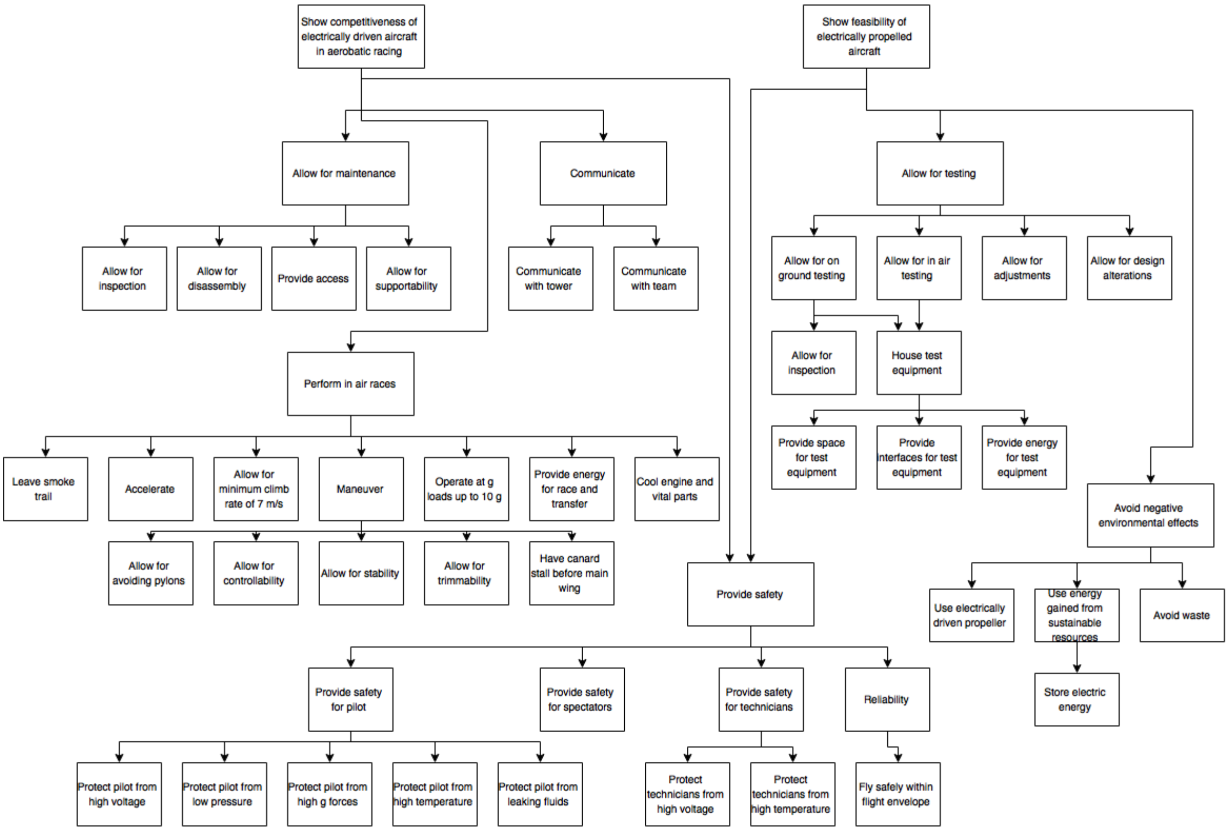

Figure 2.2: Functional breakdown diagram

3 Market Analysis

Since E-SPARC brings forth a new aerobatic racing aircraft concept it is important to investigate whether there is a market for the new technology that is implemented. This chapter first focuses on setting a design strategy (Section 3.1) in which it is be discussed how the technology will be launched and how it will have the highest potential for success. In Section 3.2, the focus shifts to the business plan of E-SPARC for a first production version. The latter section will also briefly discuss the benefits that customers of an E-SPARC aircraft will have over a conventional aircraft.

3.1 Design Strategy

Before major design decisions can be made and a proper market analysis can be performed, a project strategy has to be decided upon. The project strategy contains the focus of the project, adding direction and targets to come to a successful final product. It follows from the overall design objective and mission need statement outlines as stated in the introduction. These indicate the possibilities of the technology as well as its target group and the consequent requirements to meet the needs of the future clientele of the technology.

Possible Strategies

There are various possible usages for an electric aerobatic racing aircraft. Each of these possible usages requires a different design strategy. These strategies determine which market to target and will influence, amongst other design decisions, the need to certify the aircraft or the possibility to convert it to a two-seater aircraft.

- **Design for race**: specifically targeting the air race market. When designing for air racing, no certification is required and a one seat version would be sufficient.
- **Design for aerobatics**: targeting the aerobatic competition market. The aircraft will have to perform a wide variety of maneuvers, depending on the aerobatic category it participates in. As with the air races, certification is not necessary for aerobatic aircraft. However, the aircraft could be designed either as a one or two-seater. The latter would increase the market volume but possibly decrease the performance.
- **Design for aerobatic training/ aerobatic inaugural flights**: targeting the flight school market. The aircraft should be a two-seater and should be competitive in endurance and operational costs. In most countries certification is a requirement for performing these tasks commercially [2–4].
- **Design for private flights**: target the private market. The aircraft could be either a one or two-seater. Certification is not a necessity but could increase the market volume.

The strategy is also influenced by how the aircraft is to be produced and sold. Depending on the feasibility either solely the first aircraft, or prototype, is produced at the Delft Faculty of Aerospace Engineering, outsourcing subsequent productions, or all aircraft are produced at the faculty. Furthermore, it has to be decided whether to design the aircraft solely as a prototype showing a proof of concept, or to design for series production.

Chosen Strategy

It has been decided to design E-SPARC specifically for the air racing market, focusing on the Red Bull Air Races, therefore optimizing the design to be able to achieve similar or better lap times than currently competing aircraft. The chosen design focus resulted in a different design than conventional racers, which are designed for aerobatics and optimised for racing afterwards. E-SPARCs competitiveness on the aerobatic market is thus compromised. Since E-SPARC is purely designed for the races, it will be designed primarily as a experimental category one-seater aircraft.

In addition it has been decided to design E-SPARC as a prototype to showcase the feasibility and potential of electric propulsion technology and to manufacture E-SPARC at the Aerospace Faculty of Delft University of Technology. Therefore the complexity of production for E-SPARC is limited to the available facilities. On the other hand, less attention will be paid to optimising the (structural) design of E-SPARC for series production and production cost. As an example, the wing sandwich panel will have a continuous varying facesheet thickness, which increases E-SPARCs performance, but consequently also increases the required man-hours for production.

This strategy was chosen as it is believed that successfully demonstrating the feasibility and potential of the technology is the most important aspect of this design. A focus on racing will show the potential of electric propulsion in general aviation to a large audience. After the feasibility is shown with a competitive design the focus can be shifted to a production version, which should result in a profitable product. The remainder of this market analysis focuses mainly on the marketability of this first production version, which is assumed to have similar performance and design characteristics as the prototype design explained in this report.

3.2 E-SPARC BUSINESS PLAN

Since the E-SPARCs chosen design strategy is to design a prototype, the first E-SPARC is not aimed at profitability. After a successful demonstration of the E-SPARC prototype a production version can be introduced, which is expected to have similar performance characteristics and with which a cost revenue can be achieved. In order to acquire sufficient funding for the E-SPARC project, investors should first be convinced of the market potential of such a production version of E-SPARC. First of all, all markets that can be addressed by E-SPARC, based on its performance and design characteristics, are to be listed. In the following, the market price and potential volume per market are studied.

Since E-SPARCs design is optimized to minimize the track time during (aerobatic) air racing, the first market to address is the racing market. Additionally, since some amateur pilots also have an interest in a high performance racing aircraft, the private market and market for amateur pilots can be addressed at the same time. Although the E-SPARC design is optimized for racing, there are several other aircraft categories that could benefit from E-SPARCs technology in the future, such as all aircraft types within general aviation. However, for these markets the E-SPARC should be redesigned as it is mainly optimized for racing.

3.2.1 POTENTIAL MARKET VOLUME & ACHIEVABLE MARKET SHARE

The E-SPARC prototype will not be sold, as it is designed specifically to promote the new technology and only one will be produced. The E-SPARC production version will have a relatively small market consisting of race teams, that want to compete in a new racing category, and private recreational pilots that want a high performance electrical aircraft. For the race teams E-SPARC can be an appealing option because it will be able to offer similar performance as current racing aircraft, while not emitting any greenhouse gases. Therefore, E-SPARC provides the teams (and their sponsors) the unique opportunity to contribute to environmental concerns as well as being publicly associated with sustainability, which will be a hot topic during the coming decades. In addition, the first customers will be able to draw special attention due E-SPARCs unique design with a canard, distinguishing it from its competitors. For private recreational pilots E-SPARC appeals due to its ability to provide a new and unique flying experience, as it is a completely new concept and might add a new dimension to flying (as Tesla did for driving with the Model S in the automotive industry). Another major selling point for the E-SPARC is its reduced operational costs with respect to conventional combustion-engine-powered aircraft. This reduces the overall cost of flying for the private owner.

The air race that is focussed on is the Red Bull Air Race (RBAR), with a total of 14teams participating [5]. The amount of private pilots is much larger but they are less likely to have an interest in electric propulsion at this stage of development. E-SPARC aims at creating a whole new, all electric racing category it is expected that once the E-SPARC prototype has competed in the RBAR one time, 10 out of the 14 teams will show interest in buying an electric aerobatic racer. Taking into account possible competitors this results in an achievable market share of at least 8 aircraft in the first two years for the race teams alone. Taking into account the fact that also some private owners will be interested, the total achievable market share is estimated to be 20 aircraft in the first two years of production.

Once the E-SPARC aircraft have shown their capabilities a new aircraft can be developed for bigger markets in general aviation. A conventional aerobatic aircraft that would be optimized for aerobatic competitions could be developed, there are over 70 aerobatic teams that regularly perform at airshows and hundreds of private pilots that perform aerobatics as a sport in competitions.

3.2.2 COMPETITIVE PRODUCT COST

E-SPARC will be the first high performance electric racing aircraft, therefore creating a new market. Since it should also compete with the current aerobatic racing aircraft market, the decision on a competitive market price for the E-SPARC is based on prices of currently used racing aircraft. These prices indicate what teams and private owners are able and willing to pay for a factory new racing aircraft. Currently used air racing aircraft and their unit cost are shown in Table 3.1.

Based on the pricing of current aircraft and the fact that E-SPARC, with its electric propulsion and mostly composite structure, is very innovative, the market price can be at the higher end and even exceed the prices of current aircraft. As can also be seen in other markets, e.g. the automotive market with the Tesla Model S, it is generally accepted that innovation comes at a price.

Table 3.1: Current air race aircraft and their factory prices

Aircraft	**Unit cost, ready to fly [€]** (23-04-2015)
Extra 330SC	338,000 [6]
MX Aircraft MXS	345,800 [7]
MX Aircraft MX-2	350,000 [8]
Zivko Edge 540	265,000 [9]

In order to determine a value for the selling price and based on the number of 20 expected sales, a break-even point after a total of ten sold aircraft was set as a target. With an initial investment of

$$\text{Development cost} + \text{Series Production Start Up cost} = 86,512 + 250,000 = 336,512$$

the price of the E-SPARC for a break-even point at ten aircraft was calculated using Equation 3.1.

$$\text{price} = \text{Manufacturing cost} + \frac{\text{Initial investment}}{\#\text{sold}} = 296,518 + \frac{336,512}{10} = 330,169.2 \tag{3.1}$$

In order to allow for a small margin for cost increase the price was rounded up to € 335,000. This price is based on the current aircraft design and should be updated once the final design is finished and is expected to go up slightly. However, when the E-SPARC gains popularity as a racing aircraft, further innovation as well as a further decrease of production cost (based on increasing production volumes) are expected. Therefore, E-SPARCs competitiveness in additional general aviation markets is increased.

3.2.3 RETURN ON INVESTMENT

Now that the market price is set it can be estimated how much money can be made per aircraft. Equation 3.2 shows the return of investment (RoI) per aircraft if the expected 20 aircraft are sold. The manufacturing cost for each aircraft is derived in Section 6.4.3. The maximum development cost of E-SPARC comes from requirement ESP-MIS-003. The expected RoI is € 36,656 per aircraft sold for the first 20 aircraft. When more aircraft are sold the RoI per aircraft will increase as the development cost can be split over more aircraft.

$$\begin{aligned} \text{RoI} &= \frac{(\text{Selling price - Manufacturing cost}) \cdot \#\text{sold - Development cost - Series Production Start Up cost}}{\#\text{sold}} \\ &= \frac{(350,000 - 296,518) \cdot 20 - 86,512 - 250,000}{20} = €36,656/\text{aircraft} \end{aligned} \tag{3.2}$$

For the costumers the operational costs of E-SPARC are also relevant. The operational costs can be split into fixed costs and variable costs that depend on usage of the aircraft. The fixed costs are €15,600 per year (see Section 6.4.3). The current estimate for the variable costs per flight cycle is €31 for E-SPARC based on the Dutch energy price, battery capacity from Section 7.5 and the battery replacement costs from Section 6.4.3. To put this value in perspective, the variable costs per flight cycle for a conventional Extra 300LL (for the same flight cycle) would be almost €100, which is 5 times higher compared to E-SPARC. Although the difference does decrease for countries that charge less tax on fossil fuels, there is still a clear advantage in favour of E-SPARC with respect to operational costs. The derivation of the operational costs is shown in Section 6.4.3.

To conclude, after the introduction of the E-SPARC prototype the E-SPARC can be profitable with a production version. It is expected that there will be a a considerable number of customers for E-SPARC as it has added benefits for the customer, such as a lower operating cost and a sustainable label which can be used for promotion.

4 Mission Analysis

This chapter gives an overview of the mission profile in Section 4.1. The mission profile is derived from the performance requirements and the rules that are set by Red Bull. Afterwards Section 4.2 elaborates on the actions that should be taken before the race can start. It focuses on the transportation of the aircraft to its race destination, maintenance and on the preparation of team before the race.

4.1 Mission Profile

From requirements ESP-PW-EST-007 and ESP-PW-EST-008 it is known that the aircraft shall be able to fly the race at full throttle for 3 minutes and at 50% throttle for 30 minutes for taxi, take off, landing and flying to the race location. The complete mission profile is shown in Figure 4.1. The race profile is different for every race, one of the old races is analysed in Chapter 12.

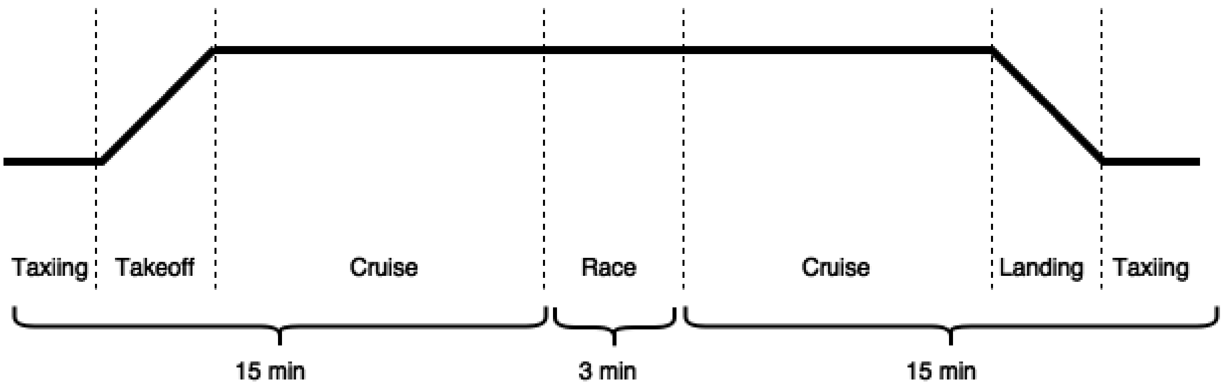

Figure 4.1: The mission profile of E-SPARC aircraft

4.2 Operations and Logistics Concept Description

The operations and logistics concept for an air race such as the RBAR investigates the actions that have to be taken to ensure a smooth race process. This includes the preparation of the team at the race location, maintenance tasks, as well as transport to the next race location. The Operations and Logistics Flow Block Diagram in Figure 4.2 shows the actions taken, as well as their consecutive order.

These actions have to be performed within short time. Usually, the team has to be ready for transport only 2 days after a race. Taking the aircraft apart, meaning stripping of its wings and taking out systems and electronics for easier transport and safety takes 6 hours for a conventional racing aircraft, while the assembly takes up to 18 hours [10]. For the electric aircraft, it is aimed at meeting these times as well. For safety and easier transport, the power storage units should be taken out as well.

For logistics, there are several means of transport. For intercontinental travel, the race aircraft can be transported by airliner or shipped when time allows. Continental travel could be done by train or truck. From this chapter it can be concluded that there is one major criterion for the design due to the logistics; the aircraft should be able to be easily and quickly disassembled and assembled, while ensuring safety during the process.

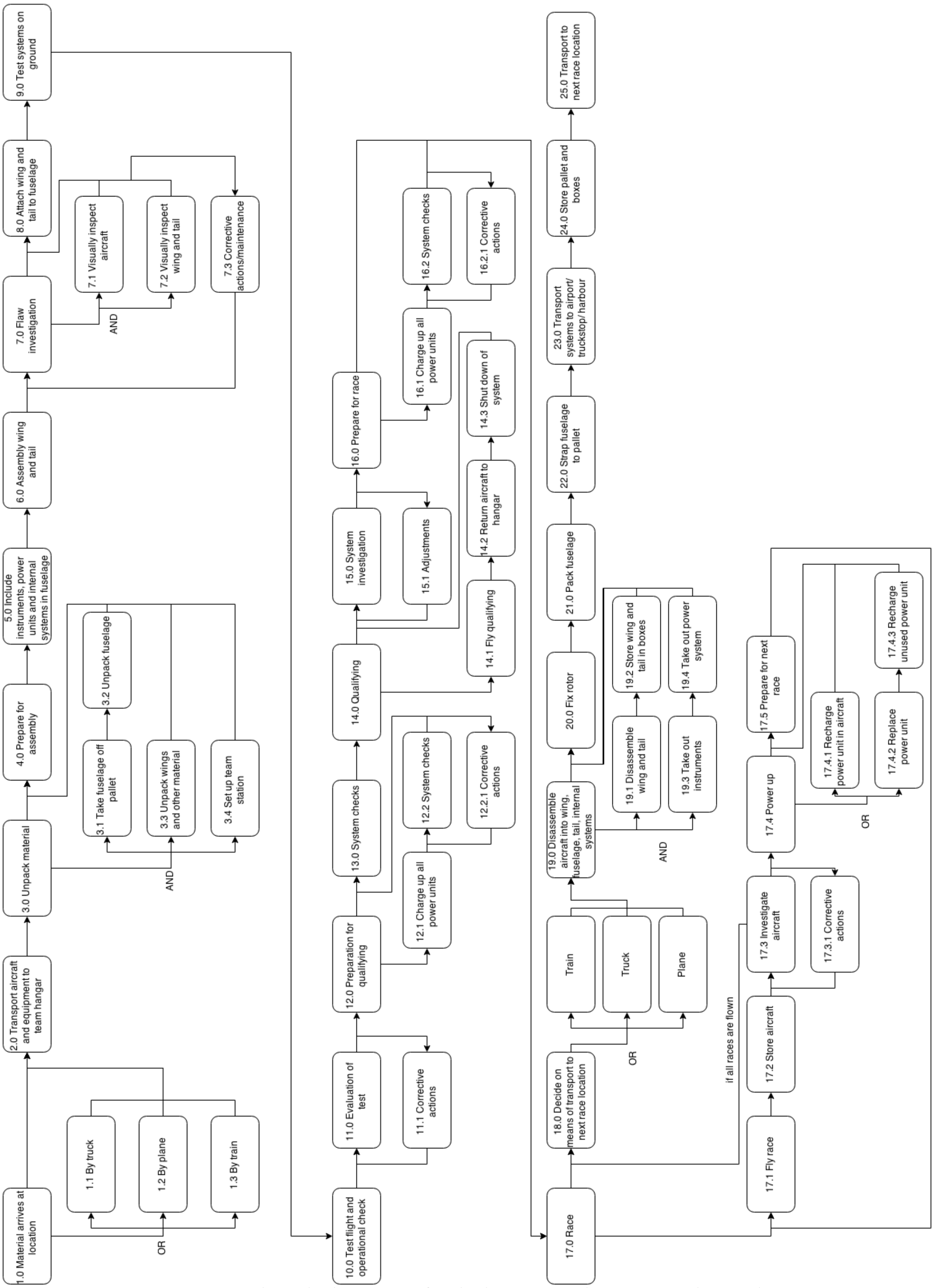

Figure 4.2: Operations Flow Block Diagram for the logistics and operations during the race season.

5 Future Developments

In this chapter the future developments in the design process will be discussed. First in Section 5.1 the logical order of activities to be executed in the post-DSE phases of the project are discussed. This is supported with a Gantt Chart in Section 5.2 which adds a start and end date to each block in the PDD-diagram to have a better overview of the time order of the project. Finally Section 5.3 shows a plan for the manufacturing, assembly and integration of the aircraft.

5.1 Project Design and Development Logic

This section will present an outline of the activities following the DSE project required for further development of the E-SPARC design, production and operational life. Various milestones have been identified, starting with the end of the preliminary phase, which corresponds to the end of the DSE project, followed by production, first flight, operational life and disposal. A distinction has been made between technical milestones (Section 5.1.1) and commercial ones (Section 5.1.2). This overview of the required further development activities, also referred to as the Project Design & Development (PDD) Logic is depicted in Figure 5.1. Furthermore, a planning of these activities is given in Section 5.2 by means of a Gantt chart.

5.1.1 Technical Milestones

By the end of the DSE, the E-SPARC design has reached an overall level of detail based on the preliminary design phase. This design phase provided a general subsystem design, with overall subsystem characteristics. Using this framework a refined, more detailed design can be performed on component level. This phase is known as the pre-production stage, or also as the detailed design phase (Block A1 in the flow diagram). In order to accomplish this level of refinement, CFD tools will be required to model aircraft performance, providing better insight in the aircraft aerodynamic characteristics, as well as for stability & control characteristics (Block A2). As the detailed design progresses towards a more finalized aircraft design, CFD results ought to be validated by performing wind tunnel tests on wind tunnel models of the aircraft (Block A6).

In the detailed design phase, regarding the structures and materials department, the exact geometry of each component and the characteristics of the material are determined (Block A3). Everything, until the last rivet hole, has to be designed and analysed such that by the end of the detailed design phase all structural components including the wing, fuselage, canard, vertical fins etc. are ready for production. Finite element analysis will be required to accurately estimate the load paths and stress distributions for the highly complex structural components, incorporating material and structural characteristics such as thicknesses, Young's moduli, densities etc (Block A4). Similar to other departments, a detailed analysis ought to be performed for the battery, power train and electrical system (including the wiring, electrical control unit etc.) to finalize the power and propulsion aspect of the E-SPARC design. For the power unit of the aircraft, a model has to be defined with which system characteristics can be analysed, including results on battery discharge rate, temperature distribution, efficiencies, battery life cycle and refined results on the degradation of capacity over its life time (Block A5).

The following milestone is the manufacturing of tooling, (Block A7 & A8). The appropriate tools for production should be chosen or manufactured before the actual manufacturing of parts can be initiated. Although for the most part the detailed design has been completed at this phase, minor or major design iterations may be discovered during initial part and sub-assembly production and construction (Block A9). These sub-assemblies are to be tested individually, performing both nondestructive as well as destructive tests. For example, the landing gear should be tested on damping characteristics and and the wing on static or dynamic load tests (fatigue). These tests are necessary to confirm whether or not components meet the predefined design specifications. Having completed the sub-assembly production and testing phase, the very first complete aircraft, or prototype can be manufactured (Block A10).

Prior to the series production of E-SPARC, at which stage aircraft will actually be delivered to customers (Block A16), the aircraft prototype has to be tested both on the ground and in-flight (Block A12 & Block A13). The aircraft requirements that were set by at the beginning of the design should be verified and validated at this point. Certification is not a necessity for the E-SPARC design, as it is intended to be an experimental aircraft. Nevertheless, certification is included in the development activities as this may still become desirous based on further market analysis (Block A14) proving that the type of aircraft meets the safety requirements set by the European Union (EASA) or the Federal Aviation Administration (FAA).

Having obtained certification and with the series production initiated, the E-SPARC aircraft will start their op-

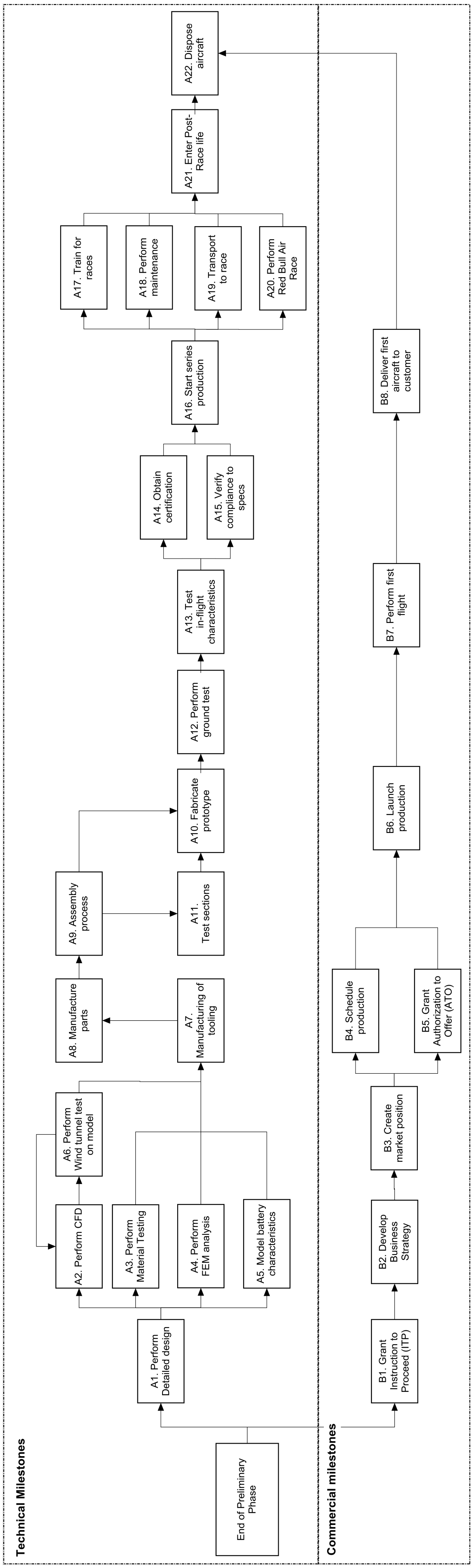

Figure 5.1: PD&D activities for the post-DSE phases of the project

erational life time. The operational life of the aircraft consists of various activities. First and foremost E-SPARC will participate in the Red Bull Air Races, and possibly various other race competitions (Block A20). The pilots will use the aircraft intensely to train and prepare prior to each race (Block A17), increasing their confidence in both the track and aircraft. Throughout its operational life, the aircraft will require various types of maintenance, including repairs, overhauls and preventive maintenance (Block A18). Finally, the aircraft should be transported to the various destinations where it will compete in races (Block A19). Currently the race aspect of the E-SPARC's operational life is estimated to be about 5 years, see the Gantt chart in Section 5.2. Following its race life the aircraft enters its post-race life, where the aircraft may be used for other purposes than racing (Block A21), like aerobatics and recreational flight. At some stage the aircraft will reach its end of life, at which stage the aircraft will be disposed (Block A22).

5.1.2 COMMERCIAL MILESTONES

In figure 5.1 an indicative timeline is plotted with a number of commercial milestones in the development of E-SPARC. The first milestone is the ITP (Block B1), which stands for Instruction To Proceed. At this point the company is ready to develop and start the detailed design phase, building on the baseline aircraft configuration coming from the preliminary studies after the DSE. The design and manufacturing of E-SPARC aircraft involves a huge investment for the E-SPARC company and other investors. Multiple risk sharing partners are therefore involved in the project, who might share in the risk by providing funds. These stakeholders will influence the design and development of the aircraft (Block B2).

Based on this business strategy the market position could be increased to make the aircraft more renowned within the worldwide aircraft industry and race community (Block B3). A schedule of the production plan is the next milestone which involves the selection of the tools to be used for manufacturing (Block B4). This should be done in such a way to successfully launch the production on time and also on budget. ATO means that the aircraft design has a sufficient level of maturity. The specification of all systems as well as all the details in structural layout are completed and can be presented to the customers (Block B5) [11]. Thereafter the launch of production (Block B6) can start with the first flight performed a few months later (Block B7). The last commercial milestone is to deliver the aircraft to the customer after which the aircraft enters into service.

5.2 GANTT CHART

A time estimate has been added to the post DSE activities mentioned in Section 5.1. An overview of the estimated planning of these activities is given by the Gantt chart in Figure 5.2.
It should be noted that the Gantt chart has not been depicted in full, because of the extensive operational life time of the aircraft both while performing races, as well as its post race life.

5.3 MANUFACTURING, ASSEMBLY AND INTEGRATION PLAN

The manufacturing, assembly and integration process consist of many different activities. These activities are summarized in a flowchart in Figure 5.3 and in a Gantt chart in Figure 5.4. The first task to be completed is to order all the materials and components that are needed for the production of E-SPARC. The only raw materials that are CFRP and Airex foam. Besides from these raw materials there will be a need for various items that are not included in the flowchart. This includes components such as nuts and bolts, fasteners, etc. After all the materials and components are ordered and have arrived, the actual production can start. The Gantt chart shows that the expected duration of the whole process is 111 days. Taking into account that no work is done during the weekend this is about 5 months. Note that this Gantt chart is constructed based on the assumption that the production team can only perform one task at a time. If the team would be much bigger this is not true and the process would take less than 111 days. There are a few things that are more important than others in this process.

- The attachment of the propeller is the very last task in the assembly process. This is to ensure that the propeller is not damaged during the assembly.
- The propeller will be produced by an external company to ensure a high enough quality. The design drawings and specifications have to be send to the manufacturer as soon as possible to give the manufacturer enough time to produce it and to make sure that the propeller is ready when it is needed.
- The fuselage is manufactured in two parts. They are both made with the same mould and put together after curing.

ID	Task Name	Duration	Start	Finish	Predecessors
1	Instruction to Proceed	0 days	Fri 3-7-15	Fri 3-7-15	
2	**Detailed Design Phase**	**870 days**	**Fri 3-7-15**	**Thu 1-11-18**	**1**
3	Perform CFD Analyses	180 days	Fri 3-7-15	Thu 10-3-16	1
4	Perform Wind Tunnel Tests with Models	180 days	Fri 11-3-16	Thu 17-11-16	3
5	Perform FEM Analyses	180 days	Fri 3-7-15	Thu 10-3-16	1
6	**Perform Battery Analyses (Models)**	**300 days**	**Fri 18-11-16**	**Thu 11-1-18**	**4**
7	Detailed Power Train Design	300 days	Fri 18-11-16	Thu 11-1-18	
8	Detailed Electrical System Design	300 days	Fri 18-11-16	Thu 11-1-18	7SS
9	Integration of Subsystems	180 days	Fri 12-1-18	Thu 20-9-18	8
10	Schedule Production	30 days	Fri 21-9-18	Thu 1-11-18	9
11	**Business and Marketing**	**1682 days**	**Fri 3-7-15**	**Mon 13-12-21**	**1**
12	Develop Business Strategy	30 days	Fri 3-7-15	Thu 13-8-15	1
13	Develop Market Position	927 days	Fri 25-5-18	Mon 13-12-21	29FF
14	Authorization to Offer	0 days	Thu 1-11-18	Thu 1-11-18	2
15	**Subsystem Testing**	**510 days**	**Fri 2-11-18**	**Thu 15-10-20**	**2**
16	Manufacturing of Tools	90 days	Fri 2-11-18	Thu 7-3-19	2
17	Manufacturing of Parts	120 days	Fri 8-3-19	Thu 22-8-19	16
18	Subsystem Assembly Process	60 days	Fri 23-8-19	Thu 14-11-19	17
19	Testing of Sections	240 days	Fri 15-11-19	Thu 15-10-20	18
20	Launch of Production	0 days	Thu 15-10-20	Thu 15-10-20	19
21	**Full Prototype Testing**	**256 days**	**Fri 16-10-20**	**Fri 8-10-21**	**20SS**
22	Production of Prototype	111 days	Fri 16-10-20	Fri 19-3-21	20SS
23	On-ground Testing	35 days	Mon 22-3-21	Fri 7-5-21	22
24	First Flight	1 day	Mon 10-5-21	Mon 10-5-21	23
25	In-flight Testing	89 days	Mon 10-5-21	Thu 9-9-21	24SS
26	Verify Compliance with Specifications	145 days	Mon 22-3-21	Fri 8-10-21	23SS
27	**Production**	**46 days**	**Mon 11-10-21**	**Mon 13-12-21**	**26**
28	Series Production	45 days	Mon 11-10-21	Fri 10-12-21	26
29	Delivery of First Aircraft to Customer	1 day	Mon 13-12-21	Mon 13-12-21	28
30	**Operational Life**	**1800 days**	**Tue 14-12-21**	**Mon 6-11-28**	**29**
31	Training for Races	1800 days	Tue 14-12-21	Mon 6-11-28	29SS
32	Maintenance	1800 days	Tue 14-12-21	Mon 6-11-28	29SS
33	Transportation to Races	1800 days	Tue 14-12-21	Mon 6-11-28	29SS
34	Compete in Red Bull Air Races	1800 days	Tue 14-12-21	Mon 6-11-28	29SS
35	**Post Race Life**	**5475 days**	**Tue 7-11-28**	**Mon 1-11-49**	**34;32;33;31**
36	Post Race Life	5475 days	Tue 7-11-28	Mon 1-11-49	
37	**Disposal**	**1 day**	**Tue 2-11-49**	**Tue 2-11-49**	**36**
38	Disposal	1 day	Tue 2-11-49	Tue 2-11-49	36

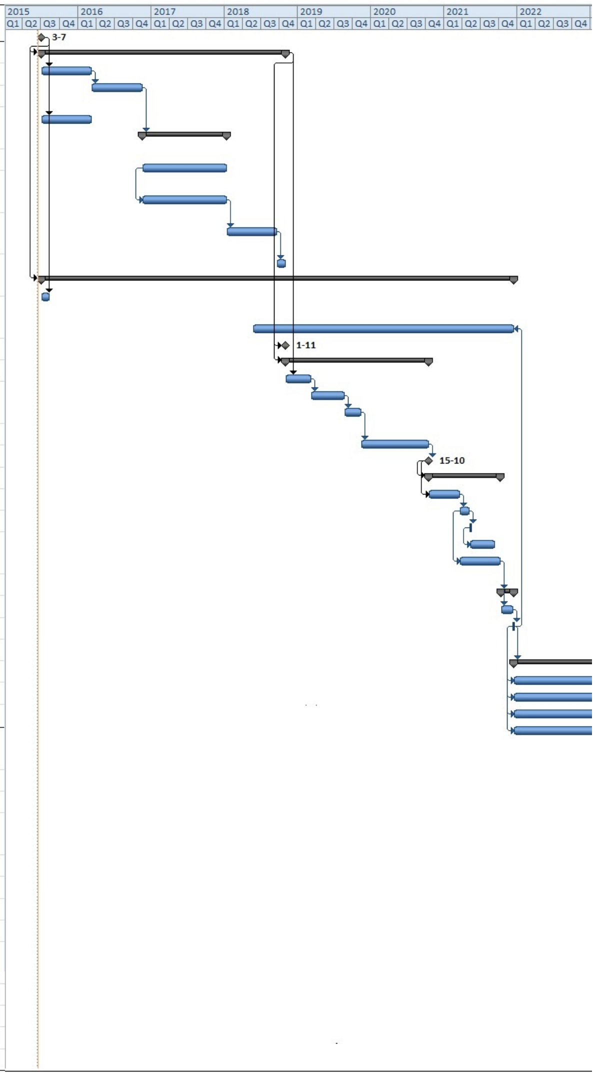

Figure 5.2: Gantt chart depicting an estimated planning of the post development activities until end of life

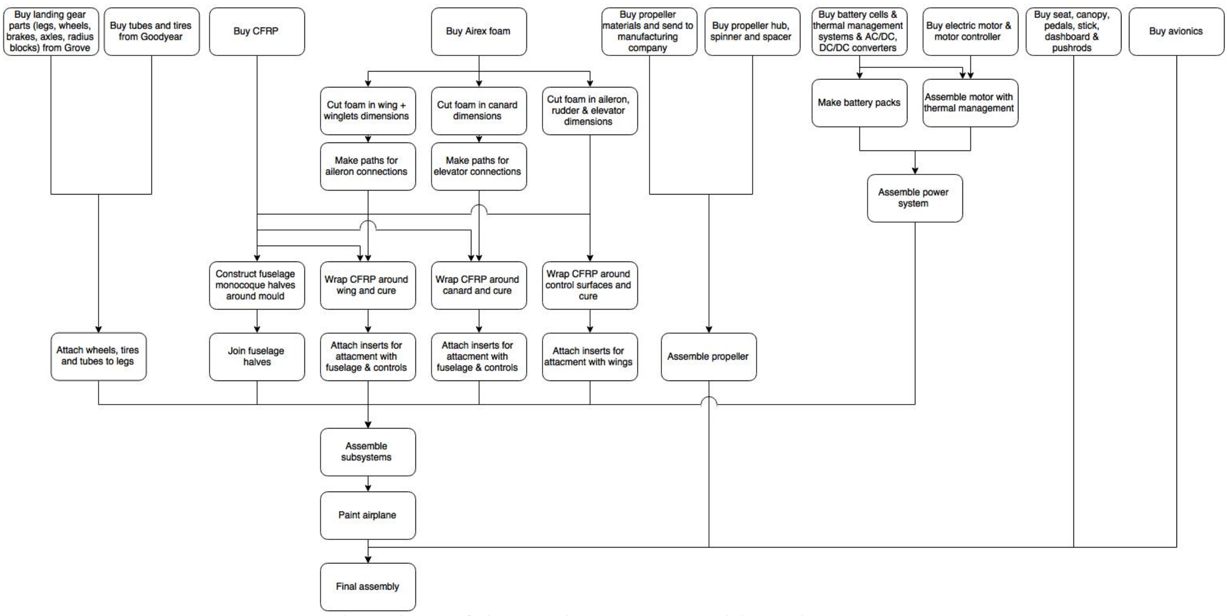

Figure 5.3: Flow chart of the production, assembly and integration process

Task Name	Duration	Start	Finish
Production, assembly & integration	**111 day**	**Mon 19-10-2**	**Mon 22-3-21**
Order & receive all materials & Compone	7 days	Mon 19-10-20	Tue 27-10-20
Send propeller design	91 days	Mon 19-10-20	Mon 22-2-21
Manufacturing	**48 days**	**Wed 28-10-20**	**Fri 1-1-21**
Wing Manufacturing	**17 days**	**Wed 28-10-20**	**Thu 19-11-20**
Canard Manufacturing	**11 days**	**Mon 16-11-20**	**Mon 30-11-20**
Control surface manufacturing	**13 days**	**Wed 25-11-20**	**Fri 11-12-20**
Cut core	3 days	Wed 25-11-20	Fri 27-11-20
Wrap foam in CFRP	3 days	Tue 1-12-20	Thu 3-12-20
Curing and post-processing	4 days	Fri 4-12-20	Wed 9-12-20
Unwrap	2 days	Thu 10-12-20	Fri 11-12-20
Fuselage	**21 days**	**Fri 4-12-20**	**Fri 1-1-21**
Landing gear assembly	**3 days**	**Mon 28-12-20**	**Wed 30-12-20**
Protective layer on subsystems	**6 days**	**Tue 5-1-21**	**Tue 12-1-21**
Subsystem assembly	**6 days**	**Thu 14-1-21**	**Thu 21-1-21**
Paint E-SPARC	**7 days**	**Mon 25-1-21**	**Tue 2-2-21**
Apply desired paint scheme	4 days	Mon 25-1-21	Thu 28-1-21
Let paint dry	2 days	Fri 29-1-21	Mon 1-2-21
Second paint layer	3 days	Fri 29-1-21	Tue 2-2-21
Battery pack assembly	**10 days**	**Fri 29-1-21**	**Thu 11-2-21**
Electric motor assembly	**2 days**	**Fri 12-2-21**	**Mon 15-2-21**
E-SPARC assembly	**11 days**	**Wed 17-2-21**	**Wed 3-3-21**
Check E-SPARC assembly	**7 days**	**Thu 4-3-21**	**Fri 12-3-21**
Test data flow	**3 days**	**Mon 15-3-21**	**Wed 17-3-21**
Test propulsion and power	**3 days**	**Thu 18-3-21**	**Mon 22-3-21**

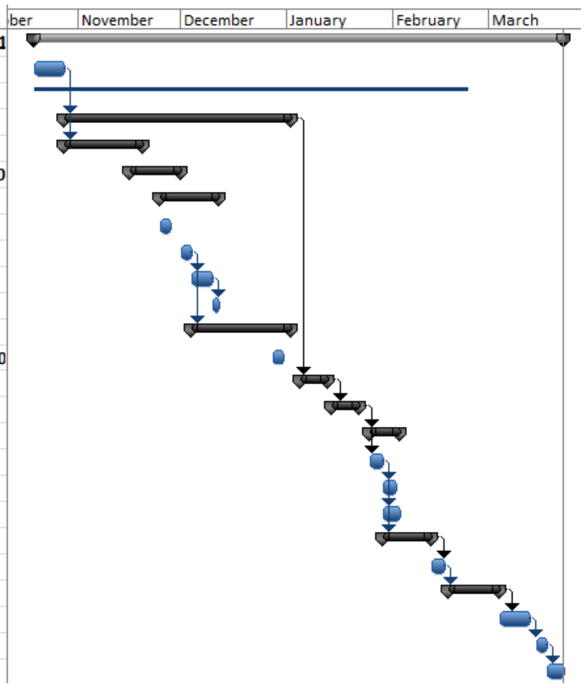

Figure 5.4: Gantt chart of the production, assembly and integration process

5.4 Strategy for Sustainability

"Sustainable Development is development that meets the needs of the present without compromising the ability of future generations to meet their own needs" [12].
The sustainability of the design is a requirement of this project and included in the mission need statement. Preserving the environment is a topic of increasing importance today as well as in the future.

5.4.1 Sustainability in the Design

Sustainability was an important factor during the design. However, it was not considered to be the most design driving requirement since the race performance was deemed more important and the fact that the aircraft is propelled electrically is believed to already make the aircraft a good product to showcase sustainability in the race application. The sustainability of all major components of the aircraft is presented in the following.

Fuselage

The fuselage is made up of carbon fibre reinforced polymer (CFRP). While these are efficient to produce in the sense that little waste is created and the shapes and properties can be precisely controlled, they can be expensive and require a lot of energy during a complex production process. As for the material selection, it was decided to use CFRPs that do not contain halogenated polymers such as vinyl and to generally use the materials that are as environmental friendly as the state of the industry allows by the year 2020. This should yield enough time to implement the technology in the aircraft. A more detailed design decision on what kind of material components are used is thus saved for later stages of the design process.

Batteries

Lithium-sulfur batteries were chosen to power the E-SPARC. Compared to lithium-ion batteries, the second best battery candidate, lithium-sulfur batteries do not use toxic heavy metals [13]. Although the amount of lithium used in this series of aircraft is foreseen to be limited compared to other lithium resource users, lithium compound mining is considered to be environmentally unfriendly. Furthermore chemical processing to extract the lithium is necessary [14]. This has a negative environmental impact, however no alternative battery with the same power density exists yet. Sulfur is a waste product during petroleum processing, which by using this type of battery would transform in a useful resource [15].

5.4.2 Sustainability in Operation and Production

E-SPARC is expected to be the first all-electrical racing aircraft that competes in races such as the Red Bull Air Race. Thus, it can not only contribute to sustainability through the components used in its production, but also the way it is operated and the afterlife and disposal. Several aspects are discussed in the following.

Reduce emissions

The Red Bull Air Races have a substantial carbon footprint because of the organisational effort, but also because of the aircraft flying in the races. From the flight manual of one of the most common planes, the Zivko Edge 540, an hourly fuel consumption of 28 gallons at full throttle was found and 18 gallons at half throttle [16]. Assuming that a comparable plane performs the same mission as the E-SPARC, this would result in a fuel consumption of 5.3 litres at full throttle for 3 minutes, and of 34 litres at half throttle for 30 min. The fuel used is AVGAS. Over the course of one year only, and only accounting for the 8 races that are performed in a season, E-SPARC could save 1129.4 litres over all races and trainings, with an average of 4 flights per event. This does not even include additional test flights. If the electric racing was promoted enough and a new category of racing was founded with 14 pilots flying in it, this would account for 15815 litres of fuel saved per year. This shows the sustainability of the E-SPARC concept, and the possibility to promote it as sustainable. However, the batteries have to be recharged and it is apparent that the sustainability of the design and the operation strongly depends on where the energy comes from. Therefore, E-SPARC should be charged with energy from renewable sources, such as solar panels or wind farms. The trend towards these sources of energy should not make it difficult to acquire them. A broad implementation of the use of renewable energy for charging the aircraft can also serve as advertisement and push towards the use of more sustainable energy sources. Finally, as one of the main arguments for electric propulsion, the efficiency of the electric engine is considered. Electric engines achieve an efficiency of 90% or even higher [17], and are thus considerably more efficient than combustion engines.

Set an example to promote sustainable technology

Through the participation in air races and the expected increase in popularity, E-SPARC proves the working of electrical propulsion and a sustainable design approach in high performance competition. As such, E-SPARC is expected to contribute to the overall trend for a more sustainable future by setting an example for the industry as well as the sport of air racing. An own race category, comparable to the Formula E in motorsports, is a possibility for the future. The promotional aspect is also enforced by the design itself. It is expected that the unconventional canard configuration with its electrical propulsion can attract and catch the interest of more and more people, increasing the target area and promoting the sport, as well as sustainable technologies. The aircraft design is therefore planned to serve a greater value besides racing.

5.4.3 END OF LIFE AND DISPOSAL

After the aircraft does not serve a purpose in flying any more, there is an option to store the airframe in a museum for displaying purposes. Also, flight enthusiasts or hobbyists could be interested in acquiring the aircraft. This could be attractive due to the uniqueness of the design. Otherwise, the aircraft components have to be reused or disposed properly to fulfill the goal of sustainability. Two examples are provided here.

Fuselage disposal

Currently a lot of research is being performed on applications and economical disposal of CFRP material. Research suggests, that small pieces created by breaking CFRP panels can be implemented as reinforcements in concrete to be used in the construction industry [18]. When breaking up the panels, the created dust has to be captured and can even be used as micro-particles to be incorporated in other applications. Furthermore, E-SPARC can be made more sustainable by reusing fibres and fillers that can be separated from their matrices in new CFRP parts. It is suggested by Hedlund-Astrom that an incorporation of about 10% of recycled fillers in new parts does not decrease the performance of a part drastically [19]. For applications requiring less structural performance this would allow for reuse of the entire fuselage.

Battery disposal

Due to the discharge cycles the actual battery capacity decreases over its lifetime. When the maximum capacity drops below 80 percent of the original capacity, the battery package is removed from service in the E-SPARC aircraft. The battery can then be sold as on ground energy storage unit (e.g. storing excess energy generated by solar panels or wind turbines) until its capacity is too low for useful applications.

Proper disposal of the battery is necessary to minimize the risk of fire (e.g. when dropped in a landfill) [20]. Whether batteries will be recycled depends on whether there is a commercial advantage associated. For the moment waste product sulfur is cheaper than recycling it form the battery. Recycled lithium is as much as five times the cost of lithium produced from the least costly recycle process. Thus it is not competitive for recycling companies to extract lithium [21].

II

Preliminary Aircraft Design

6 FINAL DESIGN

In this chapter an overview of the design will be given. First of all some drawings of the configuration are given in Section 6.1. All the subsystems that are designed will have to be fit together in one aircaft. The integration of these subsystems is given in Section 6.2. Next the results from the Class I method that were used in the conceptual design phase as a first estimate are given. Thereafter the refined methods that were used in Class II are provided, which are used to predict the weight and aircraft dimensions to a level that is sufficient for the preliminary design phase. This weight budget breakdown as wel as a cost budget breakdown and a power budget breakdown are shown in Section 6.4.

6.1 CONFIGURATION LAYOUT

In order to develop a design for the E-SPARC, the whole packaging of the aircraft has to be analyzed first. The E-SPARC is a complex system, consisting of a number of subsystems. This chapter presents the top level packaging of the E-SPARC and the interfaces between the subsystems.

6.1.1 PACKAGING

The top level packaging defines where the most important subsystems of the E-SPARC will be placed. Since the fuselage needs to connect and protect the components, the top level packaging (TLP) is of major importance for the fuselage design. The chosen TLP canard pusher configuration can be seen in Figure 6.1. The center of gravity is fixed throughout the flight, because the power units do not loose or gain weight.The electric motor, propeller and the battery are located in the back. The battery has been shifted around to shift the center of gravity location as such that the stability requirements and the structural requirements on ground and in flight are met. The pilot is seated as close as possible to the center of gravity to provide comfort in fast movements of the aircraft. Also, he/she is positioned to provide maximum visibility. While placing every component the pilot and the battery had to be shifted forward in order to achieve the correct center of gravity. This was located 2.34 m measured from the front. This posed a problem for the nose landing gear. Shifting the pilot forward reduced the space in the front, which also minimized the space needed for a retractable landing gear. It has been decided to retract the nose wheel under the seat of the pilot. This also provided more room for the controls.

6.1.2 E-SPARC DRAWINGS

This section provides all the drawings of the E-SPARC. Figure 6.1 gives the configuration layout and the positioning of the main components. Figure 6.2 shows the internal lay-out of E-SPARC with the avionics panel, the control stick and the accumulator.

6.2 SUBSYTEM INTEGRATION

The subsystems have to be integrated in such a way that they can interact if required. Therefore, the interfaces and the relations between them are analysed.

The integration and interaction of the subsystems have to be performed carefully. What requirements do the subsystems impose on the E-SPARC design or the other way around? All interfaces and connections have to be taken into account during the early stages of the design to prevent unforeseen problems during assembly. A list of the interfaces and their effect on the design is given in Table 6.1.

Table 6.1: E-SPARC subsystem interfaces

Subsystem	Connected to	Description	Influence
Main wing	Fuselage	The wing generates the required lift and in return carries all aerodynamic loads. The interface between wing and fuselage needs to be designed to transfer these loads and the created moments.	The fuselage needs to be locally stiff enough and offer the space needed for the wing integration.
Canard	Fuselage	The canard generates a control force to keep the aircraft in moment equilibrium. It can be loaded heavily and the loads need to be transferred through the fuselage.	The fuselage needs to be locally stiff enough at the canard intersection and transfer the canard loads.

Winglets	Main wing	Rudders are needed for directional control. The E-SPARC design integrates the Rudders in the winglets attached to the main wing tips.	The resulting forces from directional control need to be transferred from the wing tips through the wing. The wing needs to be stiff enough to carry these additional loads without deforming in an unfavorable way. Also the wing tips chord and airfoil need to allow for the installation of large winglets and rudder actuators.
Ailerons	Main wing	For roll control the E-SPARC uses ailerons installed on the main wing.	The main wing needs to support the static and dynamic loads from the ailerons. The airfoil shape need to provide enough thickness at the trailing edge to allow for the installation of the ailerons and actuators.
Propeller	Fuselage	The propeller is providing the thrust needed during flight. It is fixed to the back of the fuselage and transfers all rotational propeller loads and thrust via the interface to the fuselage.	The back of the fuselage needs to be rigid enough to support the loads and moments from the propeller and provide enough space for the installation of the transmission and maintenance.
	Motor	The propeller is connected to the electric motor by a direct transmission shaft.	The motor needs to be build and positioned such that a short and lightweight shaft transmission can be realized. It has to provide the required power at the rotational speeds that the constant-speed propeller is designed for.
Motor	Accumulator	The electric motor is driven by the energy stored in the batteries. The current is transferred at a high voltage to minimize energy losses and provide the required power.	The accumulator needs to provide a high voltage current at the discharge rate required by the motor to provide sufficient power to the propeller. Its position has to allow for a safe positioning of cables and low energy losses.
Accumulator	Fuselage	The batteries need to be protected from heat and structural damage. They make for a significant weight component and need to be securely fastened to the fuselage.	The fuselage needs to provide enough space for appropriate placement of the battery. It needs to be locally rigid enough to support the battery weight and provide protection from external heat or damage.
	Battery Management System	The batteries need to be continuously monitored and the charge or discharge current controlled by the Battery Management System (BMS). A close integration of the two is therefore essential.	The BMS needs to be connected or integrated in the accumulator in a safe way providing redundancies in case of component failure.
Landing gear	Fuselage	The landing gear is producing drag and carrying high loads during landing that need to be transferred into the fuselage. A lightweight but safe integration is required. Proper placement is essential to avoid tip-over, enable rotation during take-off and minimize the structural weight.	The fuselage needs to provide the space and local stiffness to allow for landing gear integration and load transfer.

6.3 WEIGHT ESTIMATION

In this section the estimation of weight and aircraft sizing is given based on Class I methods which were used for the conceptual design phase. These results were refined in the preliminary design phase with Class II methods. The difference between the two is that Class I is only based on weight requirements, the mission profile and statistics. Therefore Class I does not distinguish between different aircraft configurations. Class II is based on a combination of statistics and conceptual aircraft parameters and allows to estimate component weights.

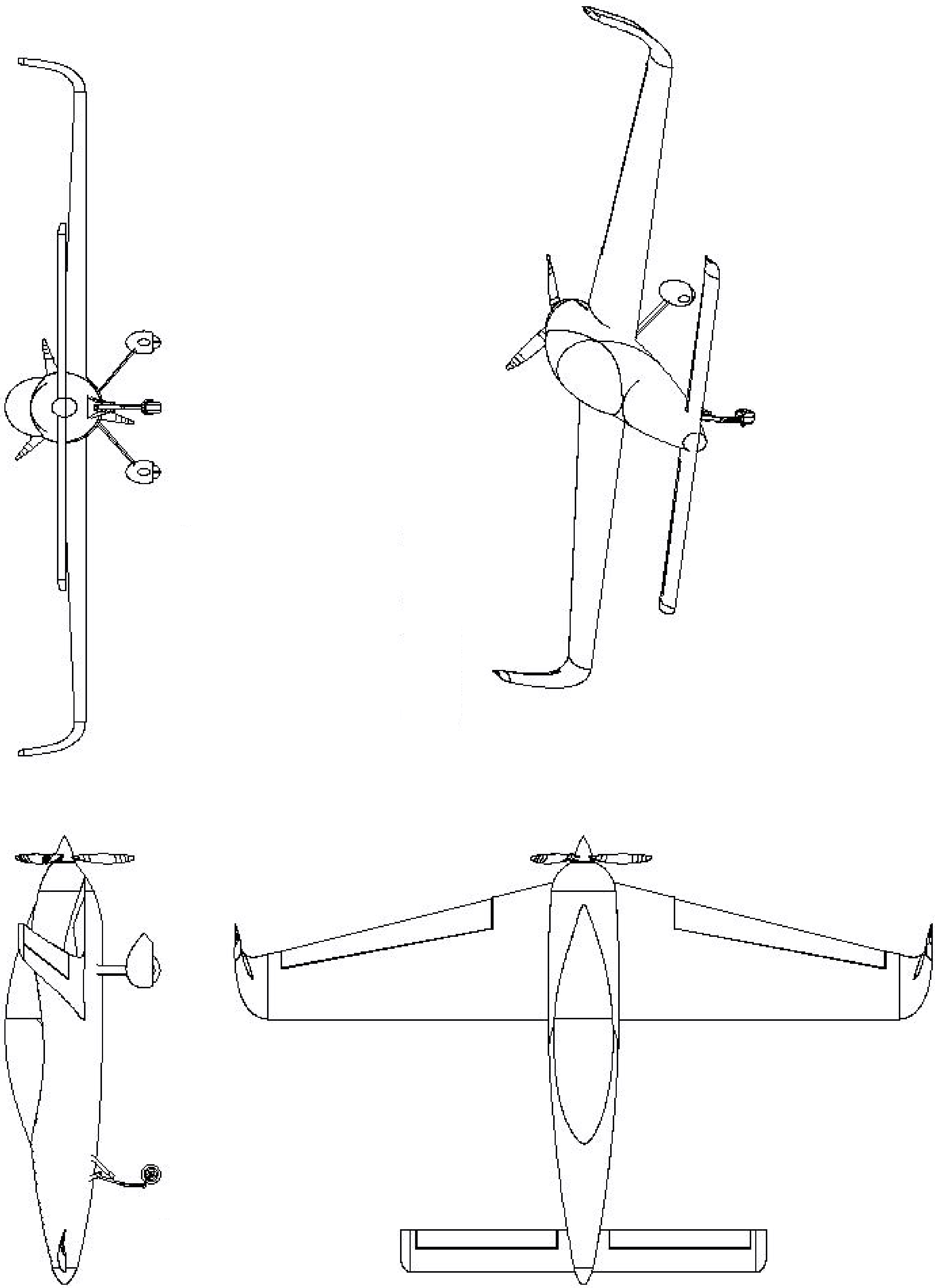

Figure 6.1: Three view drawing of the E-SPARC

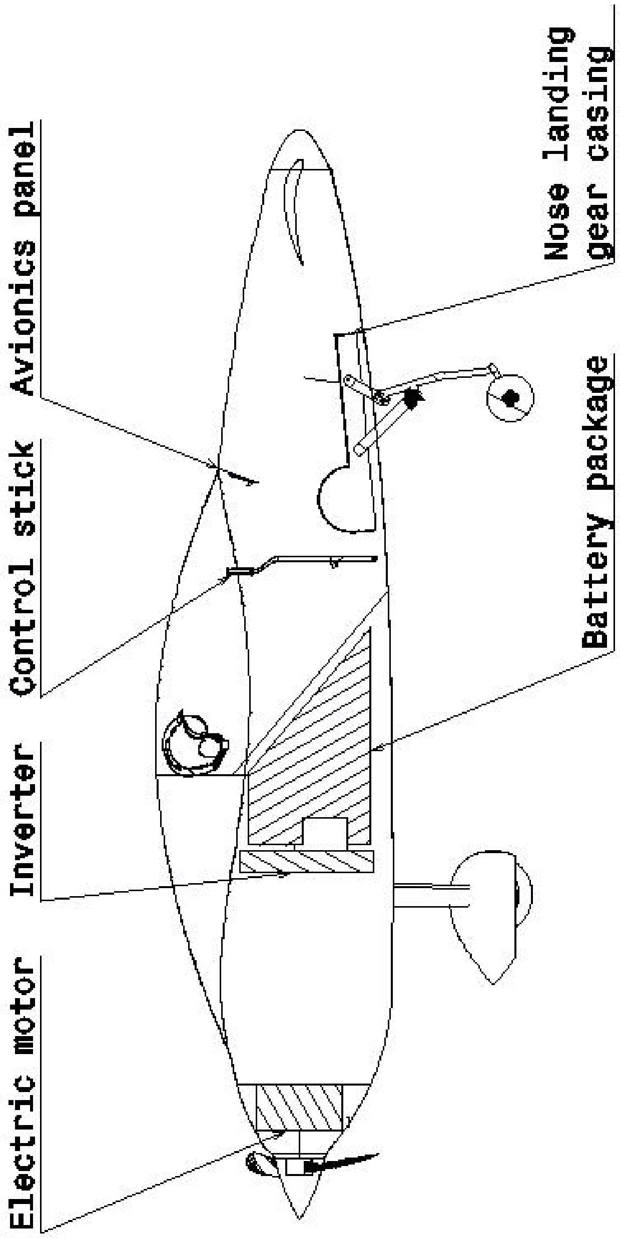

Figure 6.2: Cut through drawing of the E-SPARC

6.3.1 CLASS I

Using the theory shown below, a first estimation of the weight, wing planform and power characteristics of the aerobatic racing aircraft E-SPARC is given. These are based on statistical data found from reference aircraft and on basic performance equations.

DESIGN POINT ESTIMATION

This section elaborates on the general method used, the input parameters for this method and the results of the analysis of the wing and power loading of the E-SPARC aircraft.

Design Point Method

The general principle of the Class I determination of E-SPARCs design point is based on performance with respect to stall speed, takeoff and landing distance, climb rate and gradient as well as a sustained turn, which are dictated by the requirements. For each of these requirements equations exist that relate the required wing and power loading (see [22]), which can be used to compare wing and power loading in a $\frac{W}{S}$-$\frac{W}{P}$ plot, as shown in Figure 6.3. In order to meet all the requirements a design point should be chosen that is below and to the left of all curves. In terms of propulsive and aerodynamic efficiency one wants to find an as high as possible wing loading and an as high as possible power loading. A higher wing loading means a smaller wing, which also has consequences on the cost and weight of the whole aircraft. Besides, a smaller wing also generates less drag because the wetted area is smaller. A higher power loading means that less power and therefore smaller batteries (or less fuel) and smaller propellers are required to perform the mission. Using the chosen design point and the weight estimation that will be performed a first estimate of the wing surface and required power can be determined.

Design Point Inputs and Results

All input values used to construct the $\frac{W}{S}$-$\frac{W}{P}$ plot for E-SPARC, which is given in Figure 6.3, are tabulated in Table 6.2. Some of the values were purely based on reference aircraft while others were obtained from the mission requirements (Red Bull and CS-23 Experimental Aircraft Category). Therefore some of the original Class I inputs have become outdated in later design phases. It should also be stated that all constraints are based on sea-level conditions. Some input values are elaborated on below.

Table 6.2: Original input values for performance objectives

Parameter		Value	Description
A	[-]	6	Aspect ratio
V_{stall}	[m/s]	31	Stall speed
$V_{takeoff}$	[m/s]	34.1	takeoff speed
TOP	[Ns/m^3]	38.6	Takeoff parameter
$s_{landing}$	[m]	500	Landing distance
η_{prop}	[-]	0.8	Propeller efficiency
c	[m/s]	7	Sustained climb rate
$\frac{c}{V}$	[-]	0.083	Sustained climb gradient
e	[-]	0.8	Oswald factor
C_{d0}	[-]	0.025	Zero lift drag coefficient
$V_{max,turn}$	[m/s]	80	Maximum speed during sustained turn
$n_{max,turn}$	[-]	3.5	Maximum load factor during sustained turn
$C_{L,max,clean}$	[-]	1.5	Maximum lift coefficient in clean configuration
$\Delta C_{L,max,landing}$	[-]	0.3	Maximum lift coefficient increase in landing configuration

The aspect ratio is purely based on reference aircraft. The requirements for stall speed indicate that this speed shall not exceed 61 knots or 31 m/s [23]. The lift-off speed for a normal takeoff is 1.1 times the stall speed. A $C_{L,max,clean}$ of 1.5 is chosen based on the same reference aircraft. In order to allow for a more aerodynamically efficient aircraft it is assumed that E-SPARC will have some simple high lift devices (HLDs) in order to generate an increase in $C_{L,max}$ of 0.3. As stated in Chapter 13 it was decided to have wings which are able to generate a $C_{L,max,clean}$ of 1.8 for hihg-g turns, therefore eliminating the need for HLDs.

The zero drag coefficient of 0.025 is based on a skin-friction drag coefficient for the category of "Light aircraft - single engine" multiplied with the ratio of wetted area over reference area [24]. During later design phases a more accurate estimate of the zero drag coefficient (of 0.034) was performed as can be read Chapter 13. Using this final value results in lower power loading of 0.037 $\frac{N}{W}$, which is comparable to the power loading of the final design of 0.035 $\frac{N}{W}$.

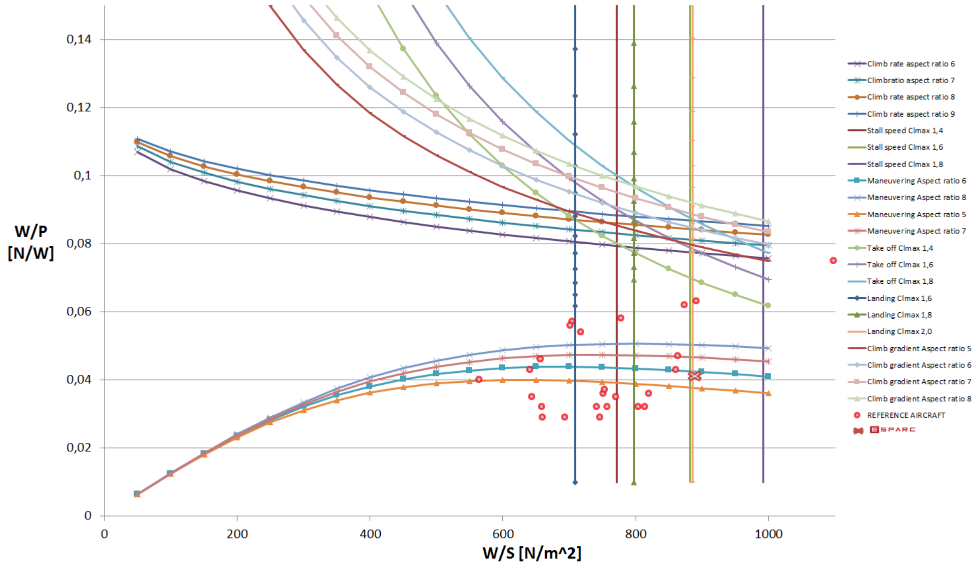

Figure 6.3: Wing- and power loading plot illustrating the E-SPARC design point space

For a sustained turn the aircraft will experience a load factor close to 3.5 with a maximum speed of around 80 m/s, which is equivalent to a turn at 73° bank angle. The takeoff parameter is taken to be 38.6 for a takeoff distance of 500 m, which follows from the RBAR regulations [25]. A relation has been found between the TOP, which combines all primary parameters that influence takeoff distance, for several reference aerobatic racing aircraft and their landing distance in Figure 6.4. From this statistical data the TOP parameter for E-SPARC was determined using a linear least square solution, which provided the best fit for the aircraft under consideration. Using Figure 6.3 a design point can be chosen. The resulting design point is found at $\frac{W}{S} = 790$ and $\frac{W}{P} = 0.043$,

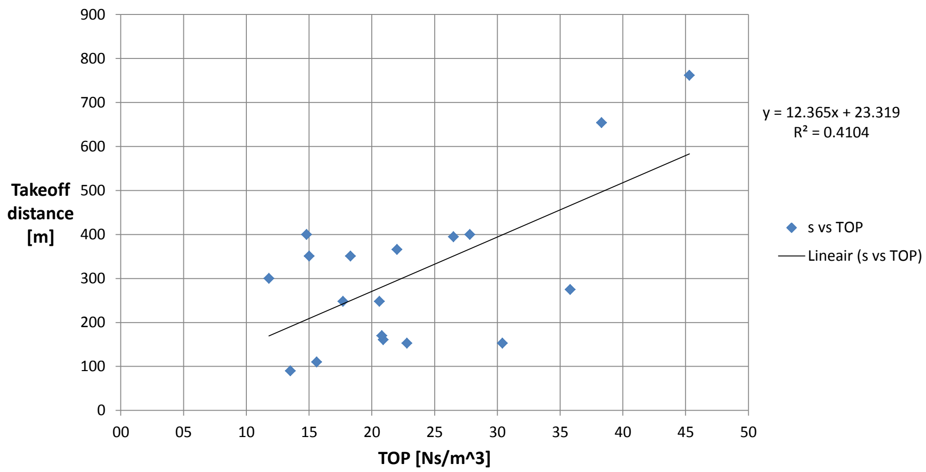

Figure 6.4: Statistical relation between landing distance and takeoff parameter

referring to the characteristic values shown in Table 6.2. As follows from Figure 6.3 the design point is dictated by the maneuvering and landing distance requirements, therefore E-SPARC will perform better than required on the four remaining performance requirements. Combining the chosen design point and equations [24] used to construct the curves the expected performance based on these requirements can be calculated. Table 6.3 shows all the expected performance values of E-SPARC.

WEIGHT ESTIMATION

After the design point has been chosen, the Class I weight estimation can be performed. A new Class I method has been developed to estimate main weight characteristics of an electric, battery-powered aircraft. First, this method will be explained, followed by the inputs and obtained results. Finally, the sensitivity of the results with respect to the main input values is also discussed.

Table 6.3: Required and expected performance values for E-SPARC design point, $\frac{W}{S}$ = 790 and $\frac{W}{P}$ = 0.043

Parameter		Required Value	Expected Value
$n_{max,turn}$	[-]	3.5	3.5
$V_{max,turn}$	[m/s]	80	80
$s_{landing}$	[m]	500	500
V_{stall}	[m/s]	31.0	29.3
TOP	[Ns/m^3]	38.6	22.6
$s_{takeoff}$	[m]	500	303
c	[m/s]	7.0	15.3
$\frac{c}{V}$	[-]	0.083	0.518 (31.2°)

Weight Estimation Method

The basis for the Class I method is Equation 6.1, where the maximum takeoff weight (W_{TO}) has been written as a function of its main fractions: the structural weight (W_{struct}, which is assumed equivalent to the empty weight without the engine weight), the electric motor weight (W_m), the battery weight (W_{bat}) and the payload weight ($W_{payload}$). For conventional aircraft W_{struct} and W_m would be combined in the empty weight. Since electric power trains are significantly lighter than the conventional combustion engines the two weights are shown separately for the battery powered aircraft method.

$$W_{TO} = W_{struct} + W_m + W_{bat} + W_{payload} \tag{6.1}$$

In order to estimate W_{TO}, all terms on the right side of Equation 6.1 will be replaced by either a number or a function of W_{TO} in order to solve the remaining equation for W_{TO}. The structural weight is related to W_{TO} via Equation 6.2a, where A_{bat} and B_{bat} are coefficients based on a set of reference aircraft. These parameters determine the trend of the linear relation between the takeoff weight and the structural weight. W_m depends on the required power P, the propeller efficiency η_{prop} and the specific power of the electric motor p_m, as can be seen in Equation 6.2b. The required power can be replaced by the takeoff weight divided by the power loading $\left(\frac{W}{P}\right)$. Equation 6.2c gives the relation between W_{bat} and W_{TO} which also includes the motor efficiency η_m, the battery discharge efficiency η_{bat} and the specific energy of the battery e_{bat}. The required energy E_{req} from Equation 6.2c can also be rewritten in terms of the takeoff weight, power loading and mission time t.

$$W_{struct} = A_{bat} \cdot W_{TO} + B_{bat} \tag{6.2a}$$

$$W_m = \frac{P}{\eta_{prop} \cdot p} = \frac{W_{TO}}{\left(\frac{W}{P}\right) \cdot \eta_{prop} \cdot p_m} \tag{6.2b}$$

$$W_{bat} = \frac{E_r}{\eta_{prop} \cdot \eta_m \cdot \eta_{bat} \cdot e_{bat}} = \frac{W_{TO} \cdot t}{\left(\frac{W}{P}\right) \cdot \eta_{prop} \cdot \eta_m \cdot \eta_{bat} \cdot e_{bat}} \tag{6.2c}$$

Substituting the relations from Equation 6.2a 6.2b and 6.2c in Equation 6.1 and rewriting to solve for W_{TO} results in Equation 6.3. Therefore, combining reference aircraft data, efficiencies and required power loading and payload weight a first estimate of the weight of the battery powered E-SPARC can be determined.

$$W_{TO} = \frac{B_{bat} + W_{payload}}{1 - A_{bat} - \frac{1}{\left(\frac{W}{P}\right) \cdot \eta_{prop} \cdot p_m} - \frac{t}{\left(\frac{W}{P}\right) \cdot \eta_{prop} \cdot \eta_m \cdot \eta_{bat} \cdot e_{bat}}} \tag{6.3}$$

Finally some important additional remarks have to be made that should be respected to make proper use of the Class I method explained above:

- The reference aircraft used to derive the statistical coefficients should be a conventional aerobatic (racer) aircraft or general aviation aircraft of similar size. The weight difference between a conventional and electric drive-train is taken into account by using W_{struct} instead of W_E for the battery powered method. Electric reference aircraft are mainly used to verify the feasibility of the estimation, e.g. by comparing the $\frac{W_{bat}}{W_{TO}}$.
- The time t in Equation 6.2c should be interpreted as the 'equivalent flight time at full power', e.g. when flying 20 minutes at 50% power and 10 minutes at full power, t should be 20 minutes. This includes the assumption that the efficiency of the electric motor is constant, not depending on the delivered power. For the E-SPARC t should be substituted by $t_{race} + \frac{1}{2} t_{loiter}$. Here t_{loiter} also accounts for takeoff, taxiing and landing etc.

Weight Estimation Inputs & Results

The inputs for the developed Class I estimate of the weights of E-SPARC are given in Table 6.4, followed by the results for both the battery powered and hydrogen fuel-cell powered version of E-SPARC in Table 6.5. A more elaborate description of the parameters is presented in the following.

Table 6.4: Input values for Class I weight estimation

Input	Value (SI units)		Value (popular units)		Source
$W_{payload}$	929	N	94.7	kg	[26]
A_{bat}	0.430				Fig. 6.5
B_{bat}	570.89	N	58.195	kg	Fig. 6.5
p_m	530.1	W/N	5.2	kW/kg	[27]
e_{bat}	$14.7{\cdot}10^4$	J/N	500	Wh/kg	Ch. 7
η_{prop}	0.80				[28]
η_m	0.95				[29]
η_{bat}	0.90				-
t_{race}	180	s	3	min	-
t_{loiter}	1800	s	30	min	-
$\frac{W}{P}$	0.043	N/W	4.4	kg/kW	-
A	6.0				-

Table 6.5: Results from Class I weight estimation

Output		Battery
W_{TO}	$[kg]$	485.3
$W_{payload}$	$[kg]$	94.7
P	$[W]$	110.7
S	$[m^2]$	6.03
b	$[m]$	6.01
W_{struct}	$[kg]$	266.9
W_m	$[kg]$	26.6
W_{bat}	$[kg]$	97.1
V_{bat}	$[L]$	88.3

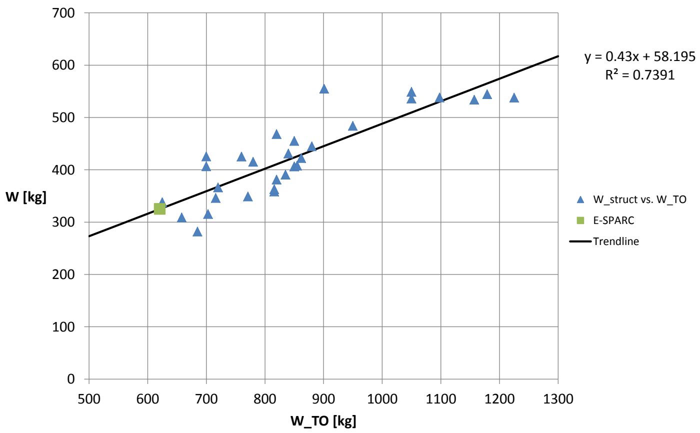

Figure 6.5: Scatter plot of empty weight, structural weight and takeoff weight for reference aircraft from Appendix A, including the corresponding linear regressions

The input value for the payload weight was based on the Red Bull requirements [26], which state that a minimum pilot weight of 82.0 kg is required. An additional 12.7 kg is added to account for the suit, helmet and parachute.

The statistical parameters A and B are the coefficients belonging to the linear correlation between W_{struct} (which is assumed equal to the empty weight without the engine) and W_{TO} for a battery powered aircraft. The plot in Figure 6.5 shows the relevant weights of the reference aircraft from Appendix A. To determine the coefficients a linear least-square solution was found. The results from Table 6.5 are also plotted for comparison.

The battery performance parameters like e_{bat} are based on the first trade-off of battery technologies, which resulted in a Lithium-Sulfur battery (for more detail see Chapter 7).

Weight Estimation Sensitivity Analysis

As some of the inputs above are estimated, changes to these parameter values are still possible. Therefore it should also be investigated how sensitive the results from the weight estimation are to minor changes in the input values. The resulting sensitivity analysis in summarized by the plot in Figure 6.6. For all main input parameters it was investigated what the W_{TO} would be if the value was 10% lower, 5% lower, 5% higher and 10% higher.

The W_{TO} is most sensitive to changes of the value of the statistical coefficient A_{bat}. The only reason for A_{bat} to change would be using a new (bigger) set of reference aircraft. Since almost all aerobatic racers for which information is available are already in the list of reference aircraft in Appendix A there is little chance A_{bat} is

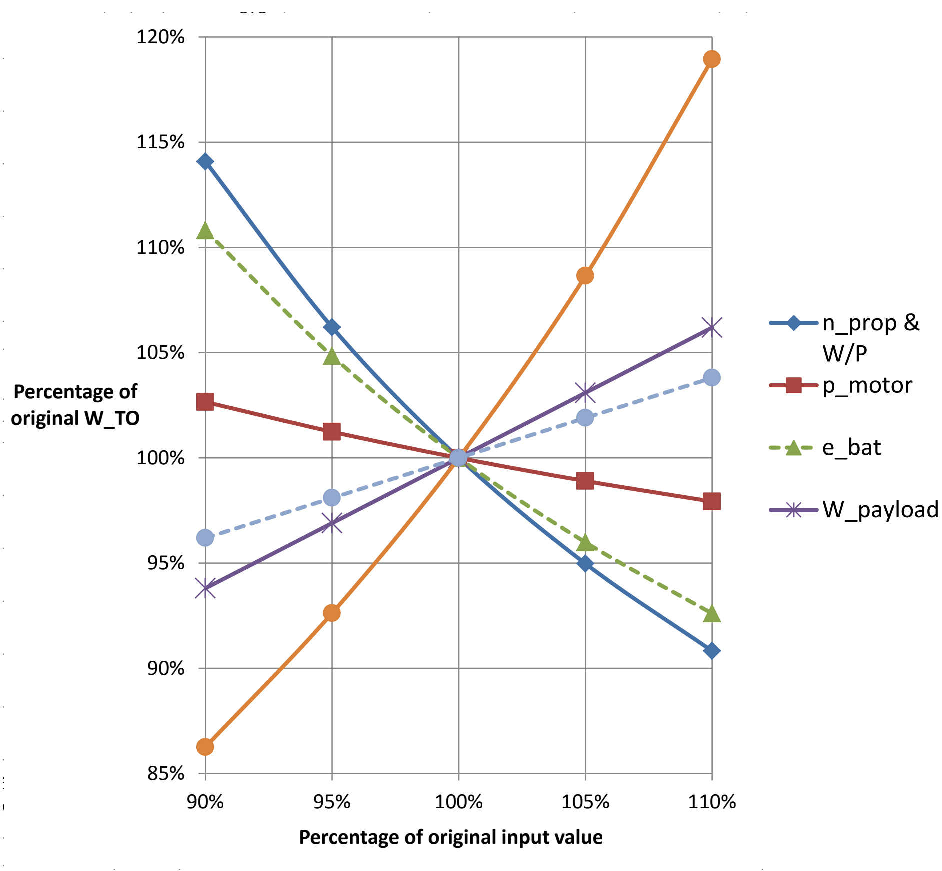

Figure 6.6: Results of the sensitivity analysis of the Class I

going to be changed. Therefore the high sensitivity of W_{TO} with respect to A_{bat} is not considered to be a big risk.

Two other parameters that have a big influence on the Class I weight estimation are η_{prop} and $\frac{W}{P}$. η_{prop} mainly depends on whether a contra-rotating propeller will be used, which could improve the propulsive efficiency and therefore decrease the weight. It has to be mentioned that the current value of 0.8 is conservative, as propeller efficiency generally varies between 0.8 and 0.9, and therefore there is little risk of a weight increase due to a change of η_{prop}. The power loading $\frac{W}{P}$ has been carefully selected, so for now, no apparent reason for a change of its value exists. The estimated takeoff weight is less sensitive to the remaining input parameters.

6.3.2 CLASS II

Following the Class I weight estimation, a more detailed component weight estimation was performed. Such a Class II weight estimation method is essential for the sizing and positioning of the various subsystems in the preliminary design phase. In addition to presenting the outcome of the Class II estimation, this Section will elaborate on the approach used and the methods used to verify the Class II outcomes.

CLASS II APPROACH

Since the Class II estimation was not as forthcoming for E-SPARC as it would be for conventional internal combustion engine aircraft, the used approach requires some additional explanation. For a given category of aircraft, the equations with which the component weights are computed are based on large quantities of reference aircraft within that particular category. The E-SPARC design, being an all electric aerobatic racing aircraft with a canard configuration, inherently does not comply with any of the existing categories and hence requires various assumptions.

First, it was decided that the category for general aviation lies within closest proximity of the E-SPARC design. This decision was mainly based on the fact that the approximated maximum take-off weight obtained from the Class I estimation matches the MTOW range of general aviation aircraft the closest, e.g. Piper Cub and Cessna 152 [30][31].

Secondly, the Raymer method [24] was used to approximate the component weights. This decision was based mainly on a comparison of the component weights obtained from the Raymer method with the component weights obtained from the Torenbeek method which was also used [32]. Based on engineering intuition, the results obtained from Raymer seemed more sensible, especially for the weight of the wing, and therefore also the wing dimensions. Thus, it was decided that the Raymer method would be more applicable for an aircraft as lightweight as E-SPARC. Additionally, the Raymer method was considered more user-friendly, based on the clear overview of the method.

Since at this stage of the design process, many of the actual aircraft parameters are yet to be determined, many parameters are obtained from reference aircraft. Although various canard aircraft have been developed, e.g. Berkut Long EZ and Velocity Aircraft [33] [34], most of these aircraft were designed as recreational aircraft, rather than as a race aircraft. Therefore, the assumption was made that more accurate weights would be obtained by using specifications from purpose built race aircraft. Hence, in addition to the Class I outputs, parameters from the following aircraft were used: Slick 360 [35], Extra 300 [35], Zivko Edge 540 [35] and MXS [35]. Out of these four aircraft, two are renowned for their current use in Red Bull Air Races [36]. However, it should be noted that neither of these aircraft are canards. Additionally, limited information regarding aircraft specifications was found for the aforementioned canard aircraft, which information was available for the aforementioned purpose build race aircraft.

Based on the fact that E-SPARC would have an electric motor and battery provision, the engine and fuel system weights were not determined using the equations provided by the Raymer method. Rather the engine weight was determined using the power and energy densities of an electric motor and battery respectively, as mentioned in Table 6.4 in Section 6.3.1 of the Class I method. Hence, these weights were computed using Equations 6.2c mentioned in Section 6.3.1. More detailed information regarding the power and propulsion systems is provided in Chapter 7. However, one is required to provide a weight of the fuel contained in the wings in order to compute the wing weight according to Raymer. Thus, it was decided to use a fuel weight of 0.01 pounds as input for the wing weight estimation. The error introduced by this is considered minimal.

Given the race nature of the E-SPARC design, the following components are not on the aircraft and hence left out of the Class II estimation: furnishing, anti-ice and airconditioning, avionics, electrical systems and hydraulics. Furnishing is left to a minimum, consisting solely of the pilot seat. Airconditioning and anti-ice are not required for racing, rather an oxygen supply system is included. Avionics are present in the aircraft, but as these too are left to a minimum, it was assumed that a more accurate approximation could be made based on the weights of the cockpit equipment in current race aircraft. The hydraulics weight depends on the exact nose landing gear that is chosen. Control surfaces will be actuated using either push-rods or wiring.

Finally, also the equation for the horizontal tail weight according to Raymer was not used in the Class II approximation, the reasoning being that the canard acts as a second wing, producing positive lift. Hence, the wing weight estimation equation according to Raymer was used instead, using input parameters from existing canards to estimate the weight of the canard [33]. The assumption was made that the canard will provide ten percent of the total required lift. Using the same wing loading as obtained from the Class I, one can compute the required area of the canard. Provided the assumption that the canard produces ten percent of the lift, this will result in a canard area which is ten percent of the total wing area. At later stages in the design process a different, more accurate method was used, see Chapter 9.

CLASS II RESULTS

Based on the aforementioned alterations, the structural weight of the aircraft is computed using the Raymer method, rather than the complete operational empty weight. The engine and battery weights are computed using Equations 6.2c and 6.2b from Section 6.3.1. The remaining subsystem weights (e.g. avionics) are computed based on results obtained from literature study. An overview of the outcome from the Class II method is given below in Table 6.6. An overview of the weight distribution is given by the pie chart in Figure 6.7. For convenience, the weights have been converted from pounds to kilogram. In Appendix B an overview is given of the input variables used for the Class II weight estimation according to the Raymer method. It should be noted that the input values used for the Class II estimation are preliminary values, mostly estimated or taken from reference aircraft. As such, for most parameters these values will change during the design process.

To reduce the initial discrepancy between the maximum take-off weight obtained from Class I (485.3 kg) and Class II (448.5 kg), various iterations were performed in which the maximum take-off weight from Class II was used as input. Iterations were performed using the equations from Raymer to compute the structural weights, as well as the aforementioned Equations 6.2c and 6.2b to estimate the battery and electric motor weights. Weights of other subsystems obtained from literature study were considered constant during these iterations. Both the initial and the final component weights are included in Table 6.6. The iterative process was continued until the error between the take-off weights of two consecutive iterations was less than 0.1 percent. This was obtained after nine iterations.

The cockpit weight as mentioned in Table 6.6 includes the weight of the avionics in the cockpit[37], the seat and seatbelt of the pilot[38], an oxygen supply system [39], a parachute [40] and the control stick and rudder pedals. The pilot weight includes the weight of his gear, e.g. g-suit and helmet, and an estimated value for the actual weight of the pilot himself of 82 kg as obtained from Roskam [41].

Table 6.6: Component weights Class II weight estimation

Component	**Initial value [kg] Raymer**	**After iterations [kg] Raymer**	**After iterations [kg] Torenbeek**	**Difference** [%]
Wing	61.9	49.5	44.2	+12.0
Canard	14.3	11.5	15.9	-27.8
Vertical tail	11.8	11.1	5.1	+116.8
Fuselage	62.1	60.2	59.3	+1.5
Main gear	30.0	26.2	25.0	+4.9
Nose gear	7.5	6.8	12.3	-44.8
Flight controls	9.1	7.6	9.5	-19.6
Structural Weight	196.9	172.8	171.3	+0.9
Engine	25.0	20.9		
Propeller	23.0	[42] 23.0		
Battery	91.4	76.4		
Wiring	3.0	3.0		
Cockpit	13.7	13.7		
Smoke generator	0.7	[43] 0.7		
OEW	353.8	310.5		
Pilot	94.8	94.8		
MTOW	448.5	405.3	424.3	-4.5

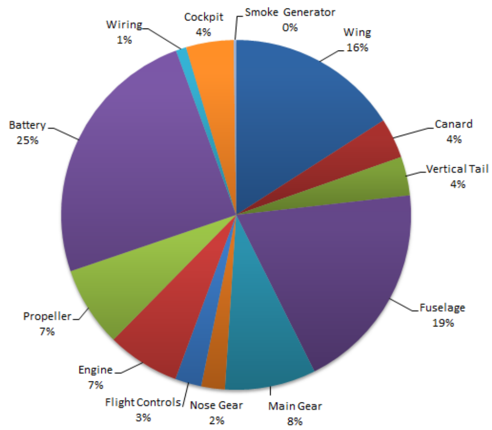

Figure 6.7: Pie chart showing the component weights as fraction of the Operational Empty Weight

Based on the wing loading of 790 N/m^2 from Class I, the wing area can be computed from the newly obtained total aircraft weight from the Class II estimation. Also, with the chosen aspect ratio and the computed wing area, the wing span can be determined. Using the wing span and area, and the chosen taper ratio of 0.45, the root chord length of the wing can be determined according to Equation 6.4[44]. From the taper ratio and root chord one can easily obtain the tip chord as well. Moreover, the mean aerodynamic chord length can be determined using the root chord and taper ratio according to Equation 6.5[44]. Finally, also the quarter chord sweep can be determined using the root chord and wing span, provided that the leading edge sweep was chosen to be zero, see Equation 6.6[44]. The same equations apply to the canard. A taper ratio of 1 was assumed for the canard. Thus, the sweep for the canard is zero over the entire chord length and the length of the mean aerodynamic chord is constant along the span of the canard and thus simply referred to as the chord of the canard, c_c. Furthermore, an aspect ratio of 10 was assumed based on reference aircraft [33]. However, for the canard area ten percent of the wing loading was used. An overview of the values obtained for these geometric aircraft parameters is given in Table 6.7. All values are based on the aircraft weight obtained from the final Class II iteration according to Raymer as mentioned in Table 6.6.

$$c_r = \frac{2S}{b(1+\lambda)} \tag{6.4}$$

$$MAC = \frac{2}{3} c_r \cdot \frac{1+\lambda+\lambda^2}{(1+\lambda)} \tag{6.5}$$

$$\Lambda_{0.25c} = arctan\left(tan(\Lambda_{LE}) - \frac{1}{4}\frac{2c_r}{b}(1-\lambda)\right) \tag{6.6}$$

Table 6.7: An overview of the aircraft's main geometric values based on the Class II weight estimation

Parameter	Value	Unit
S	5.03	m^2
b	5.50	m
c_r	1.26	m
c_t	0.57	m
MAC	0.96	m
$\Lambda_{0.25c}$	-3.6	deg
S_c	0.50	m
b_c	2.24	m
c_c	0.22	m
$\Lambda_{c_{0.25c}}$	0	deg

CLASS II VERIFICATION

The above mentioned results are initial estimates of the component weights and as such will be used during the preliminary design phase for more specific sizing and positioning of the subsystems. Although the results from the Class II are estimated weights, verification of the method and results was applied to ensure some level of accuracy.

In order reduce the computational strain imposed by the iterations, a PYTHON script was written to perform all desired outputs. First, the accuracy of this script had to be verified, to ensure that the equations had been correctly copied from literature and that no errors were introduced by the script. This part of the verification was performed by calculating the first iteration (which uses the maximum take-off weight directly from Class I) analytically. By comparing the analytical results with the outputs of the first iteration it was proven that the analytical and numerically computed outputs had only minor discrepancies of less than one percent. These errors are most likely the results of rounding in the analytical computations.

Secondly, the Raymer method had to be verified. As aforementioned, both the Torenbeek and Raymer method were used to compute the component weights. Since, based on engineering sense, Raymer provided more accurate results, the Raymer method was used. Nevertheless, by comparing the outcomes from Torenbeek and Raymer, the Raymer method could be verified. The results obtained from Torenbeek are also given in Table 6.6 above, as well as the difference with respect to the Raymer method in percentages. For the Torenbeek method the weights were iterated until a difference of less than 0.1 percent was achieved between two consecutive take-off weights, just as was done with the Raymer method. These results from the Torenbeek method were then compared to the results obtained from the Raymer method. The computation of the battery and engine weights, as well as the weights of the other subsystems was identical for both methods and hence was not included. For some structural components the difference is significant. However, based on the small difference of the structural weights, the Raymer method was considered verified.

Finally, the Raymer method was further verified by taking one of the reference aircraft used and estimating its maximum take-off weight, using the same program (with Raymer equations) as was used for the component weight estimation of E-SPARC. The reference aircraft selected for this was the Slick 360 [35]. The engine and battery weight were replaced by weights for the fuel and engine specified for the Slick 360. Also, geometric parameters were changed such that they represented the Slick 360. The Slick 360 has a maximum take-off weight of 680 kg, which was used as initial input. The final maximum take-off weight obtained from the Raymer method after iterations is 658.3 kg. Based on this difference of just 3.3 percent between the actual take-off weight and the estimated weight, further verification of the Raymer method was provided.

6.4 BUDGET BREAKDOWN

This section discusses the budget breakdown of the aircraft. Power, cost, mass and inertia breakdowns will be provided to give an overview of the aircraft.This chapter also includes the power budget breakdown and shows how much the battery provides and how much power each component needs. It is divided in two sections the high voltage system and the low voltage system.

6.4.1 POWER BUDGET BREAKDOWN: HIGH VOLTAGE SYSTEM

The high voltage system consists of the battery and the engine which is connected to the propeller. Table 6.8 gives a brief overview what those values are. The necessary power needed from the battery is derived from the required power for the propeller.

Table 6.8: High Power System Budget

Component	**Power [kW]**
High Voltage Battery	164.72
Power out High Voltage Battery	148.25
Power in Electric Motor	148.25
Power out Electric Motor	136.39
Power in Propeller	136.39
Power out Propeller	115.52

Table 6.9: Low Power System Budget

Component	**Power [W]**
In	
Low Voltage Battery	660
Out	
Altimeter	7 [45]
Turn And Slip Meter	7 [46]
Vertical Speed Meter	7 [47]
Battery Cooling System	26.4 [48]
Battery Heating System	462 [49]
Motor Control	3 []
Motor Pump	80[50]
G3X Touch	40 [51]
GSU 25 ADAHRS	25 [52]

Table 6.10: Cost Estimation for E-SPARC Components, Material and Manufacturing

Component	**Cost [€]**
Wing Material	[53] 2,200
Canard Material	961
Winglets Material	131
Fuselage Material	1372
Main gear	3,080
Nose gear	[54] 3,696
Electric Motor	[55] 10,769
Controller/Inverter	9,000
DC/DC Converter	1,100
Battery	[56] 14,667
Battery Cooling System	[48] 194
Battery Heating System	[49] 2,420
Propeller System	[57] 8,448
Smoke Generator	[58] 957
Wire Connections	[59] 66
Altimeter	[45] 176
Turn and Slip Meter	[45] 48
Vertical Speed Meter	[45] 166
G3X Touch Dual Screen	[51] 8,096
GSU 25 ADAHRS	[52] 703
Flight Control Connections	[60] 128
Seat	[61] 54
Control Stick	[62] 54
Pedals	[63] 323
Components acquired by pilot	
Parachute	[40] 418
G-Suit	[64] 418
Helmet	[65] 528
Oxygen Mask	[66] 418
Oxygen Tank	[67] 110
Manufacturing	
Wing Manufacturing	14310
Canard Manufacturing	6246
Winglets Manufacturing	853
Fuselage Manufacturing	8921
Assembly & Labour Cost	[68] 195624
Total	296518

Table 6.8 shows the power input and output of each component. During the determination of these values it was assumed that the wiring losses and the losses due to the shaft are negligible.

6.4.2 POWER BUDGET BREAKDOWN: LOW VOLTAGE SYSTEM

The voltage system consists of the low voltage battery which is charged from the high voltage battery, avionics and measurement instruments. How much power each component consumes is showed in Table 6.9.

6.4.3 COST BUDGET BREAKDOWN

This section shows all the costs needed to produce the aircraft. It gives an overview of all the component costs, material cost, manufacturing cost and labour costs. Table 6.10 contains all the respective costs divided in each section.

Table 6.11: Operation Costs

Operation	**Cost [€ per year]**	**Cost [€ per 1500 Flight Cycles]**
Hangar	3,500	
Inspection	1,500	
Insurance	1,200	
Battery Replacement		14,667
Repair	[69] 4,400	
Charging Costs		31,538
Total	15,600	46,205

The calculation for the labour cost has been divided into three groups: production employee, engineer and a supervisor. First the gross salary for a month has been determined, which is 2700€, 3800€and 3890€ [70] respectively. After that the labor cost that need to be paid by the company is calculated. in the Netherlands the gross salary is 69 % [71] of the labor cost. Those costs are also used to estimate the development costs. The price is given in euros, the exchange rate used from USD to EURO is 0.88. It is also assumed that the aircraft will be assembled in the assigned time schedule mentioned in the manufacturing schedule. However each company pays more depending in which country it is located, such costs are vacation leave, pensionable salary, travelling costs, expense allowance, extra allowance and taxes. The battery needs to be replaced after 1500 flight cycles which is included in the operation cost. For the estimation of the manufacturing costs Figure 6.8 has been used. This is done by first estimating the cost of the raw materials and then the total manufacturing cost, which is based on the weight of each component. While estimating the charging costs it is assumed that price for the energy is 0.2233 $€/kWh$.

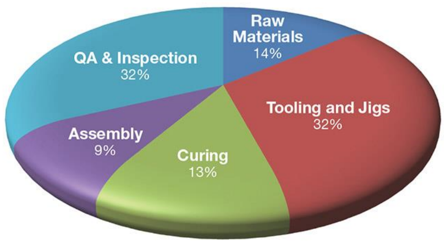

Figure 6.8: Piechart showing the manufacturing cost of composites

Besides estimating the cost to manufacture and assemble the aircraft, an estimate has been made for the cost of the design and engineering budget of the E-SPARC. Table 6.11 includes all the costs assuming a proper engineering team is used. During the estimates it is assumed that the students are working voluntarily and that a working area, office supply and programs are offered by TU Delft. If the engineering team consist out of students than there is no payment. The cost estimate for the supervisor is mentioned before and that he is required to come by the team 1 day a week. The cost estimates are done from two views. One view is outside of TU Delft and the other view, is how much the TU Delft needs to pay for the project. For both views it is estimated that one year is needed for the development.

6.4.4 MASS AND INERTIA BUDGET BREAKDOWN

Initially the Class I and Class II methods provided an early weight and inertia estimation of the overall aircraft and components. Based on the Python program for the Class II estimation (see Section 6.3.2), a systems engineering tool was developed, specifically designed to iterate the component weights (and inertias) based on design changes in the aircraft and subsystem parameters. A flowchart of the systems engineering tool is depicted in Figure 6.9.

Table 6.12: Design and Engineering Budget

	Total Cost with TU Delft [€]
Development Cost	
Programs [Catia [72], Matlab [73], ABAQUS [74]]	42,560
Equipments [Computer, Office Supply]	25,000
Working Area	4,700
Engineering Team [Students]	(Voluntary) 0
Supervisor	13,312
Additional	2,500
Total Development cost	88,072
Series Production Start Up Cost	250,000[75]
Total investment	338,072

The flowchart of the cg and inertia tool is shown in Figure 6.10. Using the outputs from the systems engineering tool and setting the component cg locations to meet the target cg required for stability and control (see Section 9), the aircraft inertia around the body axes can be determined.

Design iteration were continued throughout the preliminary design phase. An overview of the mass and inertia budget obtained from the final design, which resulted from using the last iteration as input for all subsystem design tools, is given in Tables 6.13 and 6.14. All cg location in Table 6.13 are with respect to the nose of the aircraft. The wing group contains both the wings and the smoke generator, as the latter is assumed to be located in one of the wings. The fuselage group includes the flight control connections, control surfaces and the actual fuselage. The electronics group contains the inverter as well as the wiring. The cockpit consists of the avionics, seat and seatbelt, control stick and rudder pedals as well as the oxygen supply and parachute.

Table 6.13: Weight and cg locations of all subsystems resulting from the final design iteration

Component	Weight *kg*	CG *m*
Wing Group	50.7	2.83
Canard	21.8	0.16
Vertical tail	3.0	2.65
Fuselage Group	40.7	2.20
Main gear	18.5	2.85
Nose gear	12.2	0.4
Structural Weight	144.9	2.1
Motor	26.2	3.72
Propeller	17.6	3.92
Electronics Group	17.1	2.36
Battery Group	100.7	2.54
Cockpit	13.7	1.93
OEW	322.2	2.46
Pilot	94.8	1.93
Total	417.0	2.34

Table 6.14: Overview of inertias about three axes, all values are in $kg \cdot m^2$

I_{xx}	I_{yy}	I_{zz}
234	386	590

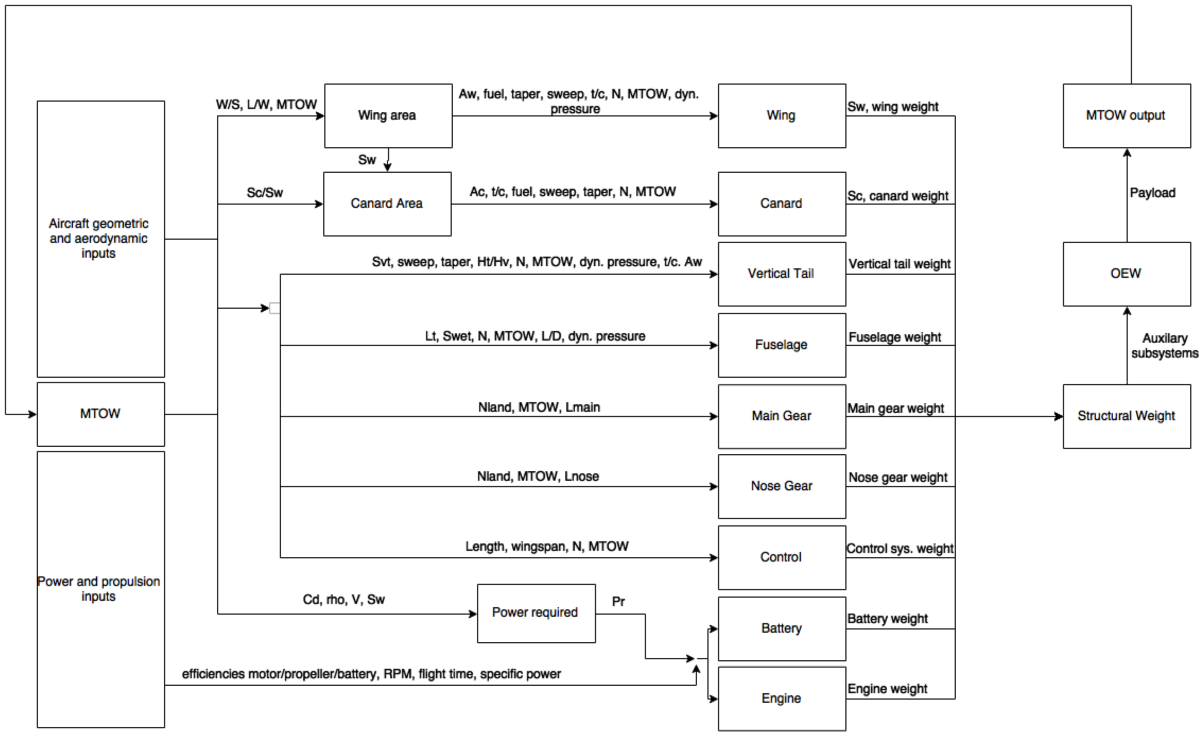

Figure 6.9: Flowchart of the Systems Engineering tool

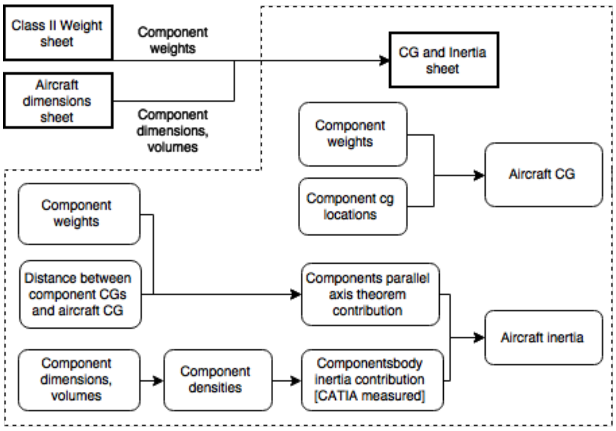

Figure 6.10: Flowchart of CG and Inertia estimation tool

7 Powertrain

This chapter describes the design choices related to the powertrain. The focus of the design process will be on the sizing of the propeller, electric motor and battery as these form the main components of this subsystem. Section 7.1 will describe the relations between the main powertrain components and explains the chosen design process and steps. Section 7.2 then elaborates on the first part of the design process, the propeller design. The propeller is sized first based on the required power and thus thrust during race and then the most efficient off-design point for cruise will be found. Based on the resultant torque and power requirements the electric motor can then be sized, which is done in Section 7.4. Finally, since the battery is a major component of the aircraft in terms of weight, the battery pack is sized based on individual cell properties. The sizing procedure is further elaborated on in Section 7.5. This is followed by a thermal analysis of the module design in Section 7.6, the charging options in Section 7.7 and an overview of the electrical power systems in Section 7.8.

7.1 Powertrain Overview

This section will elaborate on the main components included in the powertrain of the electric aircraft. They can be seen, together with in- and outputs used in the design process, in the flow diagram in Figure 7.1. The arrows within the dashed box show the design direction of the three main components. Important considerations are the links between the propeller, electric motor and battery system. These are the subsystems that will actually be designed or sized in the following sections.

The design process was initialized by the required power input P_r. Optimizing the propeller for the race and thus using the race entry velocity results in a required thrust (with corresponding coefficient C_T) that has to be delivered by the propeller. A major factor for determining the P_r is the drag coefficient C_D. Another consideration is the need for sufficient clearance, resulting in the need to limit the propeller diameter. After the design process in XRotor, propeller variables such as the thrust coefficient, torque, power and the propeller efficiency are known. The latter three variables influence the driveshaft and electric motor sizing.

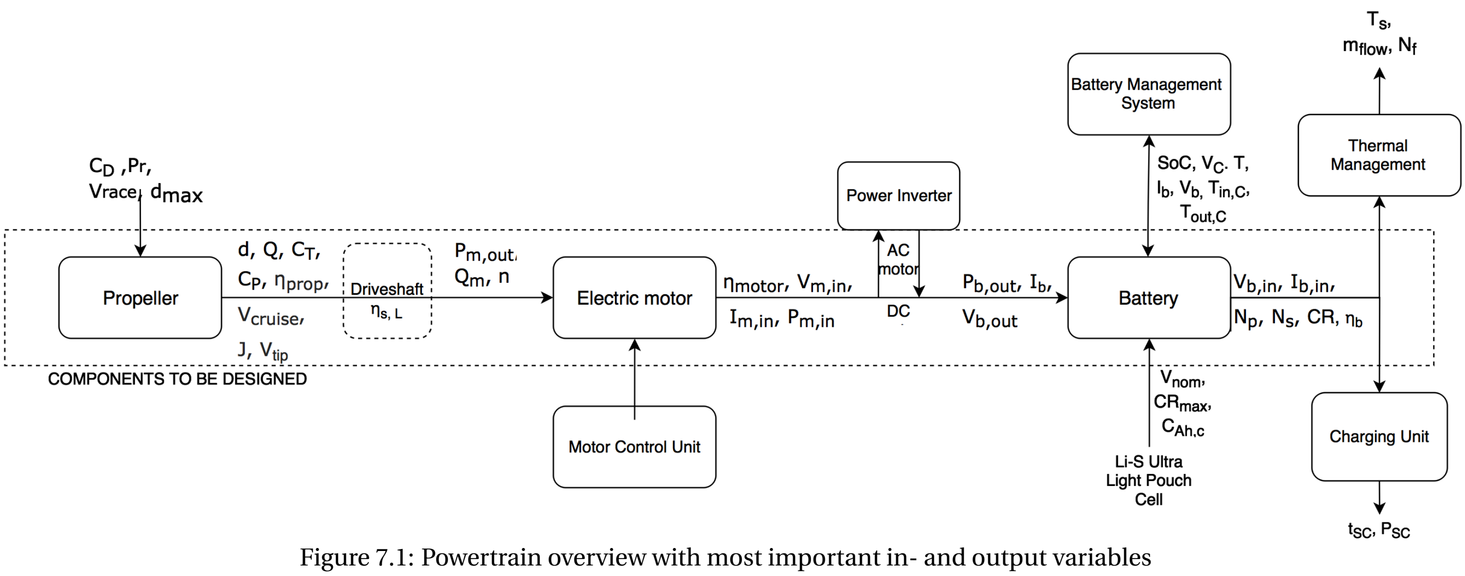

Figure 7.1: Powertrain overview with most important in- and output variables

The electric motor needs to deliver a certain power and torque continuously for three minutes based on the propeller requirements and propeller/driveshaft efficiencies. The angular velocity (n) of the propeller will be fixed to 2750 RPM. At 2750 RPM the chosen electric motor has the highest efficiency and outputs the maximum power. An electric motor requires a motor controller and a power inverter if it uses alternating current (AC). The combined weight can be determined after sizing the motor. The sizing will yield more information on motor characteristics, the efficiency η_m, motor voltage $V_{m,in}$, amperage $I_{m,in}$ and input power $P_{m,in}$. The weight and general size of the electric motor can also be determined.

The next step in the process is the sizing of the battery, which is based on the Li-S Ultra Light Pouch Cell of which production and delivery starts in 2019 by the UK-based company Oxis Energy. The limitations of the cell technology should be kept in mind and the sizing is done based on the required output power $P_{b,out}$, amperage I_b and voltage V_b.

Figure 7.1 shows the battery management system (BMS). This will not be designed but is of major importance for a safe and reliable battery pack. The aim is the design of a so-called smart battery pack, which consists of a BMS as well as a data-transferring protocol standard such as CANbus. These are automotive standards, which is the vehicle industry where EVs are already much further integrated. The usage of a BMS will reduce the risk of short-circuits, elongate the battery life and also avoid overcharging the batteries by controlling the amperage flow direction in individual cells or modules using MOSFET transistors.

After the design and integration -which is done in parallel- of the battery modules, the charging possibilities as well as the thermal management of the individual modules need to be studied. An air cooling system would be beneficial for the weight and complexity and thus cost of the system. Limitations that could arise are low heat conductivity coefficients of the cell-air interaction and uneven cooling. Series and parallel cooling are two possibilities for this system, which will be elaborated on in Section 7.6. Multiple automotive brands have adopted parallel cooling for more even cooling of the individual cells.

As mentioned, another aspect of the feasibility is the charging time (due to limited ground time on race days) and therefore the fastest possible charging time based on cell limitations will be determined. It will be shown that the possible charging times are sufficiently low but the required charger unit requires a high power output. The reader will be provided an overview of the electrical power flow in Section 7.8, which may also be worth looking at while reading the preceding sections.

7.2 PROPELLER DESIGN

Designing the propeller is a complex process since it is connected to several parameters. To find the desired diameter, the number of blades and RPM have to be determined first. When designing a propeller, the blades need to endure the centrifugal stresses and the tip speed should not have a high mach number to avoid formation of shock waves at the tips, reducing generated thrust.

The result of the trade-off between a contra-rotating propeller, with a higher efficiency and more clearance, and a single open propeller turned out to be non-decisive. The main reason for a contra-rotating propeller remains the clearance. In order to make a decision between a single open propeller and contra-rotating propeller, the diameter and the weight of each possibility has been determined. For both configurations, two-bladed and three-bladed propellers were investigated. These are most commonly used for this purpose. A lower number of blades increases overall efficiency, whereas a multi-blade propeller can deliver the same thrust with a smaller diameter. The next section explains which steps were taken to determine the diameter.

7.2.1 PROPELLER SIZING

This section explains the steps taken to determine the diameter of the propeller. The steps that are conducted are found in [76] which are based on the methods of McCormick (1979). During Class I the required power was determined and the RPM provided by the electric motor is assumed to be 2750 RPM. This is done because of the performance and characteristics of the YASA-750 electric motor, which has the highest efficiency at 2750 RPM for a much larger torque range. This means that the electric motor has the highest efficiency at full and half power. By knowing the RPM at which the propeller needs to turn, the speed power coefficient is determined for a propeller with 2 blades and 3 blades. This is done with Equation 7.1. Figures 7.6a and 7.6b were used to determine the advance ratio, with the calculated speed power coefficient.

$$C_s = V \frac{\rho}{(P_{m,out} n^2)^{1/5}} \tag{7.1}$$

$P_{m,out}$ is the power which will be provided by the motor and is thus the required power P_r divided by the propeller and shaft efficiencies η_p and η_s. The efficiency of a two bladed and three bladed propeller is also determined from Figure 7.4a and 7.4b. With the help of these two figures the pitch angle of each blade and the advance ratio is determined. With the advance ratio the propeller diameter is calculated with Equation 7.3. Since the main goal of this design is optimizing it for the race, an airspeed of 85 $\frac{m}{s}$ is used, which is the average speed during the race. For the design of the propeller the average speed is used, however to determine the required power a maximum speed of 100 $\frac{m}{s}$ is used. At the never exceed speed the drag is calculated which is used to determine the necessary power, this is done with Equation 7.2. The used cd_0 is 0.034 at a c_l of 0.2.

$$P_r = D \cdot V = c_d \cdot \frac{1}{2} \cdot \rho \cdot V^2 \cdot S \cdot V = (c_{d_0} + \frac{C_l^2}{\pi \cdot A \cdot e}) \cdot \frac{1}{2} \cdot \rho \cdot V^3 \cdot S \tag{7.2}$$

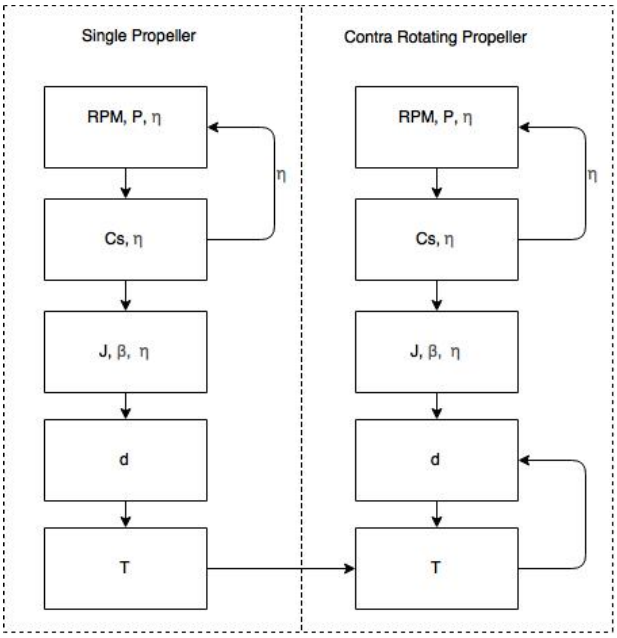

Figure 7.2: Flowchart of the steps conducted to determine the diameter of a single and contra-rotating propeller

$$J = \frac{V}{nd} \tag{7.3}$$

An overview of the parameters and found values are provided in Table 7.1. These values were calculated with the initial aircraft parameters to give an indication of the possibilities that different configurations offer.

Table 7.1: Overview of the single two and three bladed propeller

	Efficiency [-]	$\mathbf{C_s}[-]$	$\beta_{\mathbf{0.75R}}[\mathbf{deg}]$	**Advance Ratio** [-]	**Diameter** [m]
Two Bladed Propeller	0.87	2.24	35	1.41	1.71
Three Bladed Propeller	0.85	2.22	40	1.61	1.49

Now that the advance ratio and the speed power coefficient have been determined for a two bladed and three bladed propeller, the thrust coefficient (C_T) and the power coefficient (C_P) are determined with Figures 7.3 until 7.5. With those values the thrust was calculated according to Equation 7.4.

$$T = c_T \rho n^2 d^4 \tag{7.4}$$

The next step is finding the diameter for a contra-rotating propeller. This has been conducted by finding the ratio between the thrust coefficient in the first and second propeller. It was assumed that the thrust coefficient of the first propeller has the same value as for a single propeller, since the airflow is the same. With this ratio, C_T is determined for the second propeller. The ratio has been determined from Figure 7.7a and 7.7b [77]. Here it shows the thrust coefficient from the rear and front propeller calculated with different methods at an RPM of 700. The symbol on the y-axis shows the thrust coefficient and the symbol on the x-axis shows the position on the propeller blade, given as an angle. It is assumed that the ratio is the same at a higher RPM. The ratio for each method is calculated and the average is used. Then an iterative process was conducted by reducing the propeller size step by step until the thrust of the contra-rotating propeller is same as the single propeller. This has been done twice: once for a two bladed contra-rotating propeller and once for a three bladed propeller. During both processes it was also assumed that the ratio of the front and rear C_T is the same for a two and three bladed propeller. Since the second propeller receives an accelerated airflow it increases efficiency that is why the efficiency of the contra-rotating propeller equals to the efficiency of the single propeller increased by 10 % [78]. The results of these steps are listed in Table 7.2. When comparing the diameter to that of Table 7.1 it is clear that a two-bladed contra-rotating propeller performs slightly better and a three-bladed contra-rotating propeller performs much better than the single propellers. The next question that arises is how these systems perform in terms of weight due to added complexity.

Figure 7.2 shows the steps that were conducted to find the initial diameter size of a single and contra-rotating propeller.

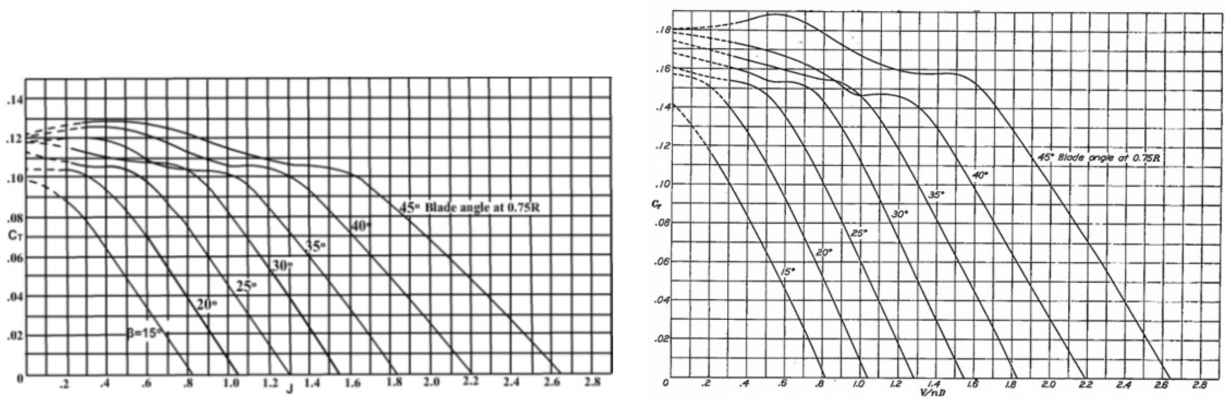

(a) Two blades (b) Three blades

Figure 7.3: Influence advance ratio J on the thrust coefficient C_T

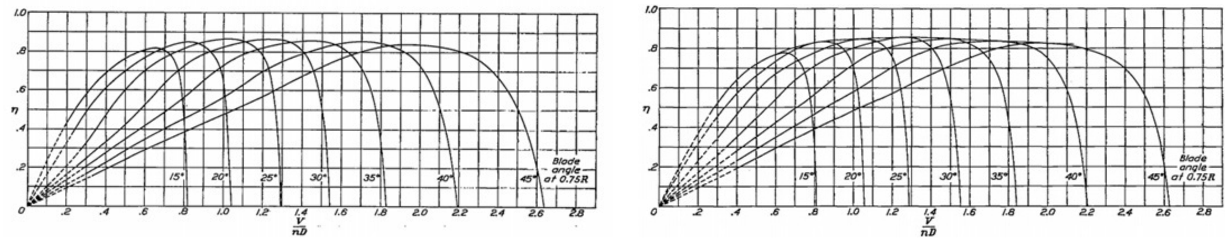

(a) Two blades (b) Three blades

Figure 7.4: Influence speed power coefficient on efficiency

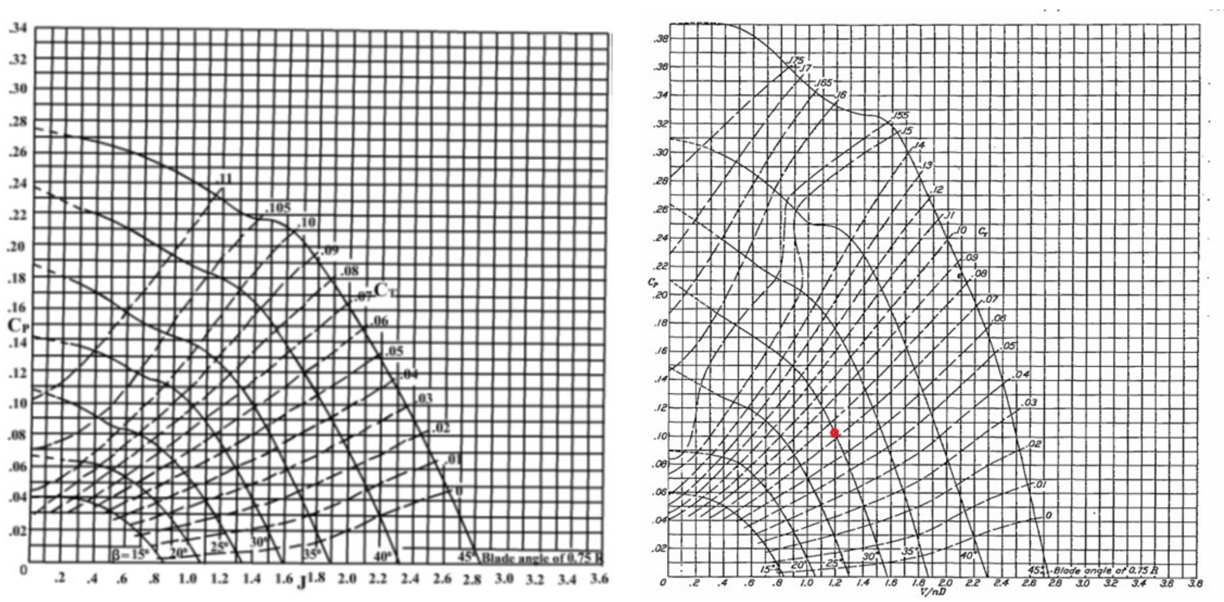

(a) Two blades (b) Three blades and the current design point

Figure 7.5: Influence advance ratio on power coefficient C_P

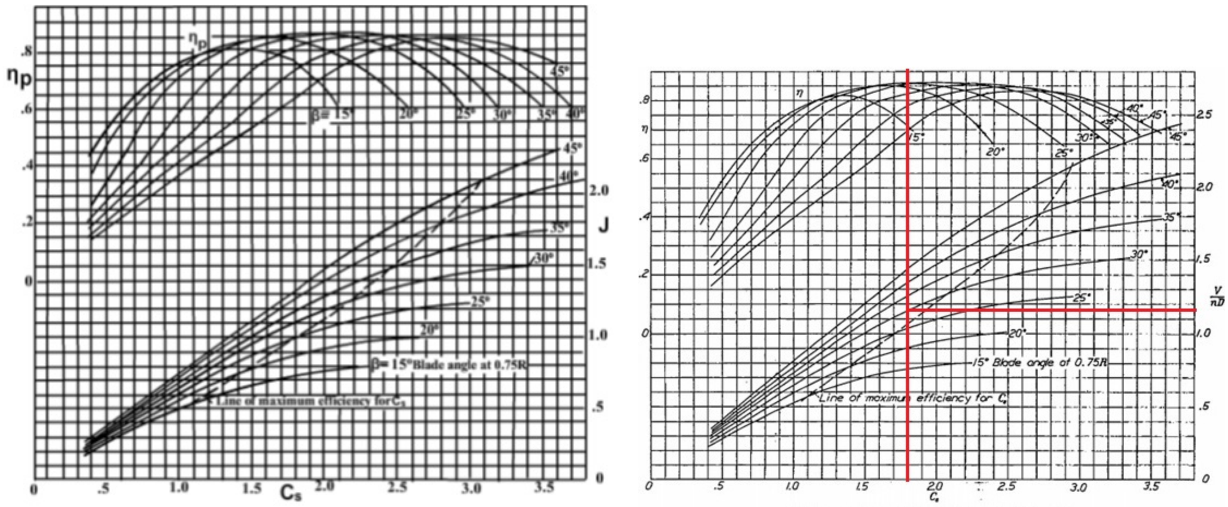

(a) Two blades (b) Three blades and the current design point

Figure 7.6: Efficiency and advance ratio J influence on speed power coefficient C_S

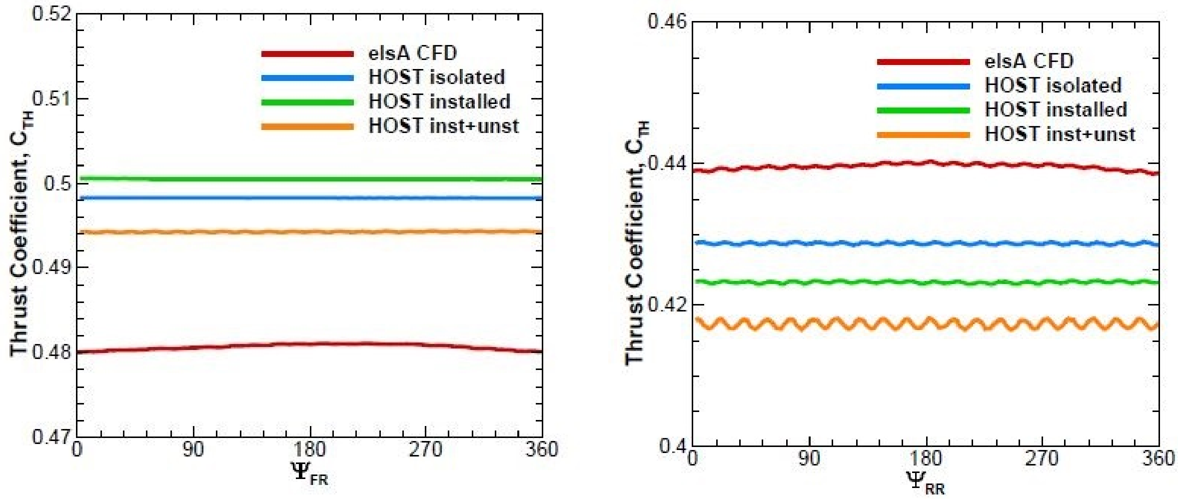

(a) Front thrust Coefficient (b) Rear Thrust Coefficient

Figure 7.7: Thrust Coefficient [77]

Table 7.2: Overview of the single two bladed and three bladed contra-rotating propeller

	Efficiency [-]	**C_s[−]**	**$\beta_{0.75R}$[deg]**	**Advance Ratio [-]**	**Diameter [m]**
Two Bladed Contra-Rotating Propeller	0.957	2.28	35	1.45	1.41
Three Bladed Contra-Rotating Propeller	0.935	2.27	40	1.65	1.25

7.2.2 PROPELLER SELECTION

In the previous section the diameter for several propeller configurations has been calculated. In order to do a proper selection the mass of each configuration has been calculated and compared. While calculating the mass the focus is on the reduced battery size, the mass of the propeller hub and the mass of the propeller blades. However when choosing a propeller configuration there is the possibility to chose for a fixed, variable pitch or constant speed (CS) propeller. A fixed propeller means that the pitch angle of the propeller is constant during the entire flight. When having a variable pitch propeller the pilot can choose what the blade angle should be during the flight. A constant speed propeller changes the pitch automatically by measuring the speed and the RPM. For each of these possibilities the mass has also been determined and the values are included in Table 7.3. Here η_r is the efficiency during race and η_{cr} is the efficiency during cruise. The equivalent efficiency η_{eq} is scaled with the time duration of those two flight phases. In Table 7.3 NP stands for *Not Possible*. These options were not possible because the battery weight increased to much.

Table 7.3: Weights and efficiencies of different propeller types for two- and three-bladed single and contra-rotating propellers

Single		**Fixed**				**Variable**				CS	
	d [m]	W [kg]	η_r,β_{45}	η_{cr},β_{45}	η_{eq}	W [kg]	η_r,β_{45}	η_{cr},β_{15}	η_{eq}	W [kg]	η_{eq}
2B	1.71	4.66	0.87	0.25	0.31	9.76	0.87	0.8	0.81	13.66	0.87
3B	1.49	6.10	0.85	0.42	0.46	12.4	0.85	0.77	0.78	17.6	0.85
Motor		26.6				26.6				26.6	
Battery		NP				95.8				83.8	
2B Total		-				132.2				124.1	
3B Total		-				134.8				128.0	
Contra		**Fixed**				**Variable**				**CS**	
	d[m]	W [kg]	η_r,β_{45}	η_{cr},β_{45}	η_{eq}	W [kg]	η_r,β_{45},	η_{cr},β_{15}	η_{eq}	W [kg]	η_{eq}
2B	1.41	7.69	0.96	0.28	0.34	17.9	0.96	0.88	0.89	26	0.957
3B	1.25	10.23	0.94	0.46	0.51	22.8	0.94	0.85	0.86	33	0.935
Motor		26.6				26.6				26.6	
Battery		NP				81.2				71.7	
2B Total		-				125.7				124.0	
3B Total		-				130.6				131.5	

With the help of Table 7.3 the decision was made to choose a single constant pitch propeller with three blades. The weight estimation of each configuration includes the major components which are necessary for the different propeller types. The values used to find the propeller blade weights are based on the first estimation of the propeller size. Table 7.3 is used to see if there are large weight differences between the configurations. If a configuration with contra-rotating propellers is slightly lighter than a single propeller configuration the latter is chosen. Having a contra-rotating propeller is more complicated and the two propellers need to be placed and adjusted properly. If that is not the case, the efficiency will reduce [78].

7.2.3 PROPELLER IN CRUISE CONDITIONS

During cruise it is set that the E-SPARC flies at half power. It is assumed that when the electric motor is running at half power that it is still the most efficient at 2750 RPM[17]. This means that the torque reduces when the motor is performing at half power. Table 7.4 shows what the parameters at cruise speed are going to be. The cruise speed is determined by calculating the required power at several speeds with Equation 7.5. The speed is found when the available power during cruise equals to the required power. This speed changes during each iteration process. The C_d value used in Equation 7.5 is taken from the drag polar in chapter 13. Th C_d is taken at the aircraft speed when flying horizontally at 100 $\frac{m}{s}$ The current values in 7.4 are the new values after the last iteration.

$$P_r = C_d \cdot \frac{1}{2} \cdot \rho \cdot V^3 \cdot S \tag{7.5}$$

Further analysis has been conducted with XRotor. It is a program that is based on an extension of the classical

Table 7.4: Final results of the propeller design

	Efficiency	**Thrust [N]**	$\beta_{\mathbf{0.75R}}$ [deg]	**Torque [Nm]**	**Speed [m/s]**	**Diameter [m]**
Race	0.90	1224	30	401	85	1.62
Cruise	0.833	1080	21	201	45	1.62

blade-element/vortex formulation. The propeller diameter that has been determined with the previous steps is used as an input for XRotor. The sizing has been further optimized with XRotor by increasing the efficiency until 0.9 during the race at the average speed of 85 $\frac{m}{s}$. However the maximum speed of the aircraft is 100 $\frac{m}{s}$, which is when the required power equals to the available power. This results in the same torque -since the available power is the same- and a different propeller efficiency. The results from XRotor are listed in Table 7.4.

The inputs that were required for XRotor in order to calculate the power and the blade pitch at several positions are: tip radius, hub radius, hub wake displacement, airspeed, RPM, power and the lift coefficient used at each section. Most inputs are obtained during the first steps explained in the beginning. The inputs that are required are hub radius, the hub radius wake displacement and the lift coefficient at each section.The hub radius is estimated to be $0.14m$ which is based on a reference propeller [57]. The hub wake displacement is set to be $0.05m$ and the lift coefficient is assumed to be 0.5. These values are obtained from XRotor which gives initial values.

In order to still perform efficiently, the pitch angle of the blade needs to reduced. The new value of the pitch angle is found with the help of XRotor, using an iterative process. At first the three bladed single propeller is entered in XRotor, with the initial values from which it calculates the parameters of the propeller. After that the RPM is set fixed and only the airspeed is reduced systematically. Reducing the airspeed, reduces the power and the torque, this is done until the power was half of the required power during the race.

7.3 SHAFT DESIGN

The shaft connects the electric motor with the propeller and attention needs to be paid for energy losses due to the twist of the shaft. It is desired to have the shaft as light as possible, yet still having a low twist. For the analysis Equation 7.6 has been used, which calculates the polar moment of inertia of the shaft. Since the electric motor and the propeller are adjusted to each other, no gear is needed to provide the correct torque from the electric motor to the propeller. The twist is calculated with Equation 7.7, after which the weight of the shaft is determined.

$$J = \frac{1}{2}\pi((c_{out})^4 - (c_{in})^4) \tag{7.6}$$

$$\theta = \frac{ML}{GJ} \tag{7.7}$$

Since the length was not known the lightest option was calculated for each length ranging from 0.05 to 0.6 m. The outer diameter of the shaft c_{out} was fixed to be maximum 184 mm, which is the maximum diameter the shaft can have for the chosen electric motor. The inner diameter c_{in} The analysis has been done to give a preliminary indication which material would perform the best. This has been done for aluminium, steel, titanium and composite. The results are shown in Figure 7.8, choosing a composite shaft is the lightest option.

After that the allowable twist was determined, by determining the energy needed to twist the shaft. This has been calculated with Equation 7.8.

$$E_{s,loss} = \frac{M \cdot \theta}{2} \tag{7.8}$$

The maximum allowable twist for the shaft was set to be 1°, which resulted in a shaft efficiency of 0.999%. For further calculations it was assumed that the power output of the electric motor and the power received at the propeller is the same, thus having a shaft efficiency η_s of 1.

7.4 ELECTRIC MOTOR SIZING

Before performing a motor sizing, it is important to get an overview of what is available on the market in terms of motor types and technologies, as well as to get an understanding of the motor characteristics. Hence, this will be discussed in Subsection 7.4.1 first.

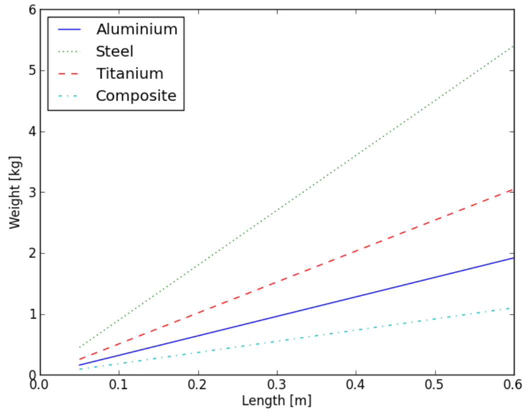

Figure 7.8: Weight vs Length of the shaft for different materials from 0.05 to 0.6 m

7.4.1 AVAILABLE ELECTRIC MOTORS

A wide variety of electric motors exist and choosing a suitable motor depends on several parameters. Therefore a literature study has been conducted to get a better overview of all parameter relationships which helps with deciding on a suitable electric motor.

There is the possibility to choose between alternating current or direct current. Having an electric motor with alternating current is most of the times cheaper, but the torque has a small delay. The output of the battery is direct current, so it would need a DC/AC inverter. Table 7.5 contains the differences between AC and DC motors.

Table 7.5: Comparison AC and DC motors

AC Motor	**DC Motor**
Single-speed transmission	Multi-speed transmission
Light weight	Heavier at equivalent power
Less expensive	More expensive
95 % Efficiency at full load	85-95% Efficiency at full load
More expensive controller	Simple controller
Motor/controller/inverter more expensive	Motor/controller less expensive

Another selection is between synchronous or asynchronous electric motors. Synchronous means that the stator and the rotor have the same rotational speed. The principle here is that when the electricity flows into the stator windings it produces a rotating electromagnetic field, which induces the windings of the rotor when it starts rotating. An asynchronous motor works in a similar way as the synchronous motor, but it has no external exciter. The rotor does not receive any electric power by conduction. The rotor speed depends on the varying magnetic induction, which results in that rotor rotates at a lower speed than the magnetic field of the stator. The difference in rotational speed is called 'slip'. The advantage of a synchronous electric motor is that these motors operate at leading power and operate at constant speed irrespective of load. Since these motors can be constructed with air gaps, they are mechanically better. However the motor cannot be used for variable speed jobs and cannot be started under load and stops when it is over-loaded. An external DC source is required to lock the rotors.

The number of phases in an electric motor is also an important variable. Having more phases improves the reliability and minimizes the torque pulsations. Furthermore, the casing of an electric motor can also differ. The squirrel cage and a wound rotor casing are commonly used. A squirrel cage is often found in induction (asynchronous) motors. They are robust, simple to construct and inexpensive. Wound rotor casing are well suited for low inertia loadings. The construction enables lower rotor weight, centrifugal force and windage losses.

7.4.2 ELECTRIC MOTOR CHOICE

This section elaborates on the chosen electric motor and elaborates further on its specifications. Outputs such as the torque Q_m and motor efficiency η_m will determine the output power $P_{m,out}$, input power $P_{m,in}$ and corresponding input voltage $V_{m,in}$ and amperage $I_{m,in}$. The required electric motor torque follows directly from the required torque by the shaft for both the race and cruise condition. The motor torque should match the propeller torque ($Q_m = Q_p$) as well as possible for an efficient system. Therefore, the electric motor should provide an output power $P_{m,out}$ that results in this particular motor torque Q_m. The relationship between torque and power is given by Equation 7.9 resulting in a motor power corresponding to the chosen angular velocity and required torque for a certain pitch angle and flight speed of the aircraft.

$$P = \tau\omega \tag{7.9}$$

Electric motors are relatively simple systems compared to internal combustion engines but remain relatively complex in terms of design. A preliminary design of an electric motor was considered too extensive and therefore an off-the-shelf electric motor was chosen, with proposed alterations. The decision was made to use a 75kW AC motor by YASA Motors as reference, the YASA 750 Axial Flux Electric Motor [17]. The advantage of this electric motor is that the flat torque region in lower RPM regions - which is a characteristic of the majority of current motors - continues until the chosen propeller RPM. Until this point, the power linearly increases according to Equation 7.9 in which τ is the torque (Nm) and ω the angular velocity (rad/s). The maximum power can be found in the RPM region slightly behind the point where the flat torque region comes to a halt. These characteristics are beneficial for the flight profile at the chosen RPM of 2750 RPM. The same can also be seen when studying the RPM-Torque/Power curve provided by YASA Motors, shown in Figure 7.9. A clear issue that arises is that the

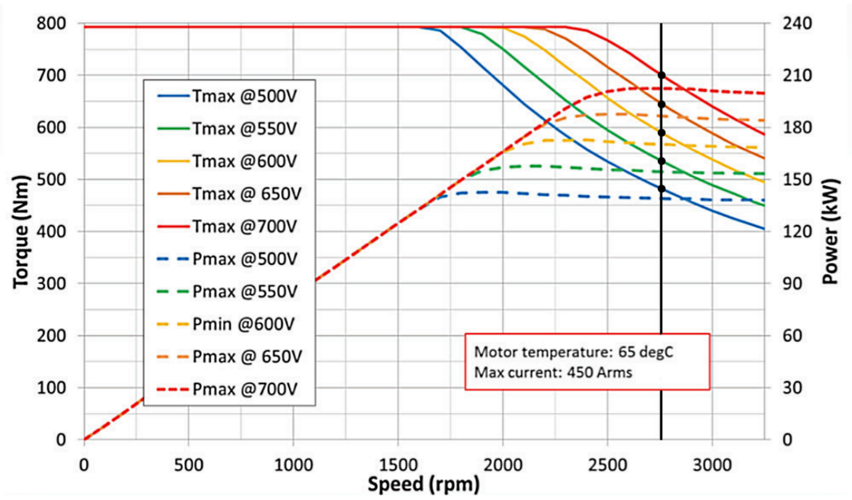

Figure 7.9: YASA Motors RPM vs torque graph

required power provided by the propeller, equal to 115.5 kW, is already much higher than the rated continuous power of 75 kW for the YASA 750. Taking into account the propeller, driveshaft and electric motor efficiencies, the motor continuous output and input power $P_{m,out}$ and $P_{m,in}$ become 136.4 and 148.2 kW respectively. This means that the YASA 750 does not provide the required continuous power output. Before continuing to the proposed solution, it is worth looking at the parameters for the proposed method. These are shown in Table 7.6. Note that given torque requirements ($Q_{p,race}$ and $Q_{p,cr}$) are direct results of the propeller sizing.

The proposed solution was to derive the characteristics of the electric motor inside the peak region, above continuous power. This was based on the specifications sheet of the YASA 750 motor [17]. Some assumptions were made with respect to scaling the electric motor. At higher voltages and with a more sophisticated controller, the maximum power and torque output can be extended with the YASA 750, which is seen in Figure 7.9. It was then assumed that until 2020-2025 the motor could be adjusted for the power needs of the aircraft. This means that these peak settings would then become the continuous power and torque rating of the custom-made electric motor. Following the pattern of Figure 7.9, the relationship between the motor torque Q_m and the input voltage $V_{m,in}$ was estimated through the approach of Figure 7.9.

$$Q_m = \frac{P_r}{\eta_p \cdot \eta_s} \cdot \frac{60}{2\pi n} = \frac{60 P_{m,out}}{2\pi n} \tag{7.10}$$

Since the RPM is fixed, the electric motor voltage can now be derived from Figure 7.9. The motor torque was calculated based on Equation 7.9, resulting in Equation 7.10. The correlation between voltage and torque Q_m at an angular velocity n of 2750 RPM was found to approximate a linear relationship, according to Equation 7.11 and the adjusted YASA 750 performance graph as can be seen in Figure 7.10. The output torque Q_m was found to be 482.4 Nm The input motor voltage $V_{m,in}$ required for a steady continuous power input of 149 kW at 2750 RPM was then determined to be approximately 502.4 V. For the cruise phase the voltage remains at this level but the amperage is reduced to only half of the maximum continuous current, resulting in half power. The resulting Q_m

Table 7.6: Parameters for electric motor sizing

Parameter	**Value**	**Unit**
P_r	115.5	[kW]
η_m	0.92	[-]
η_p	0.847	[-]
η_s	1.00	[-]
$Q_{p,race}$	401	[Nm]
$Q_{p,cr}$	201	[Nm]
$Q_{m,race}$	482	[Nm]
$P_{m,out}$	136.4	[kW]
$P_{m,in}$	148.2	[kW]

during the cruise phase is then 241 Nm. This proved to be sufficient for the propeller.

$$V_m = Q_m + 20 \tag{7.11}$$

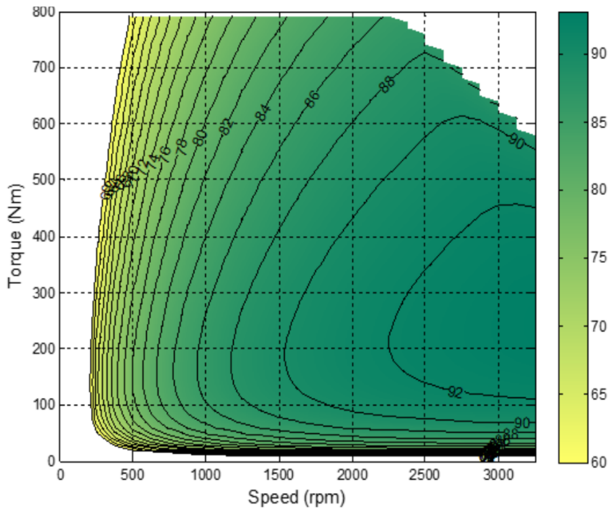

Figure 7.10: Efficiency range of YASA 750

When comparing the propeller torque Q_p with the motor torque Q_m they are well matched, when taking the propeller and shaft efficiencies η_p and η_s into account. Finally, the size and weight of the motor has to be determined. Instead of scaling the YASA 750's weight with the increased continuous power, the power density was based on upcoming electric motor technology. It is assumed that these can be reached before 2025. Siemens manufactured a prototype electric motor for aircraft with a power density p of 5.2 kW/kg [27]. Based on the motor output power $P_{m,out}$ of 136.4 kW, this yields a motor weight of 26.2 kg. The dimensions were scaled based on the YASA 750 however, which led to the values provided in Table 7.7. Also, the motor efficiency was based on the YASA 750 data sheet, resulting in a 0.92 efficiency [17]. The efficiency range of this motor can also be seen in Figure 7.10.

Table 7.7: Electric motor dimensions and weight

Parameter	**Value**	**Unit**
d_m	0.35	[m]
l_m	0.20	[m]
W_m	26.2	[kg]
p	5.2	[kW/kg]

7.4.3 MOTOR CONTROLLER

The chosen electric motor requires AC input, whereas the battery pack delivers a DC output. An inverter is required for this particular need. A lightweight motor controller was therefore chosen that can handle the high DC voltage of 502.4 V from the battery and functions as both an inverter and controlling unit. A very suitable and lightweight controller/inverter combination is the Sevcon Gen 4 Size 10. The specifications fit the power requirements of the electric motor extremely well [79]. The unit specifications are shown in Table 7.8.

Important considerations are the operating voltage range, maximum continuous power as well the maximum amperage at both continuous and peak power settings. The controller input power of 148.2 kW equal to $P_{m,in}$ (the motor efficiency includes the controller[17]), is lower than the rated continuous power of the controller, as can be seen in Table 7.8. However, the amperage (based on $P_{m,in}$ and $V_{m,in}$) during the full power of the aircraft equals 295 A. The continuous amperage rating $I_{C,rms}$ is, however, only 200 A. According to Table 7.8 a peak amperage $I_{P,rms}$ of 400 A can be sustained for a total duration of two minutes. However, given the fact that it can sustain a peak power of 300 kW at an amperage of 400 A for two minutes, it is assumed that the controller will also be suitable at 148.2 kW and 295 A for three full minutes.

Table 7.8: Motor controller specifications

Parameter	**Value**	**Unit**
Operating Voltage	50-800	[V]
Continuous Power	150	[kW]
Peak Power	300	[kW]
$I_{C,rms}$	200	[A]
$I_{P,rms}$	400	[A]
Duration $I_{P,rms}$	120	[s]
Communication	CANopen bus	[-]
Operating T	-40 to +85	[°C]
Nominal Power Supply	12-24	[V]
Coolant	Water/Glycol	[-]

7.5 BATTERY SIZING AND INTEGRATION

The battery sizing and integration is one of the major issues with an EV from a systems engineering standpoint. The main reasons are the sheer volume of the modules and complete packs, the cell limitations as well as thermal management issues. Cell properties such as the internal resistance change with an uneven temperature distribution, causing differences in discharge rates. This increases the risk of short-circuits and reduces the battery cycle life.

In order to size the battery pack one therefore needs to go back to the chosen cells for the battery modules and derive their characteristics. The cells that have been chosen based on an extensive trade-off are Li-S cells which will be manufactured by Oxis Energy around 2019. One issue is that test results are unavailable and the test results of the current prototype (with worse specifications) are confidential. However, Oxis Energy provides a road map with expected specifications in 2019. These are given in Table 7.9 [80].

The goal of the battery sizing is to find a low-weight battery module design, while considering the limitations of the Li-S cells and different pouch cell sizes. The result should comply with the required output power $P_{b,out}$, DC voltage $V_{b,out}$ and amperage $I_{b,out}$. Therefore the battery efficiency η_b which results in a power - and thus voltage - loss should be taken into account.

Table 7.9: Oxis Energy Li-S Ultra Light Pouch Cells

Parameter	**Value**	**Unit**
Gravimetric specific energy	500	[Wh/kg]
Peak gravimetric power	3000	[W/kg]
Volumetric energy	550	[Wh/L]
Peak volumetric power	3300	[W/kg]
Maximum continuous discharge	5	[C]
Cycle life	1500	[Cycles]
Discharge temperature range	-30 to 70	[°C]
Capacity	6.5-50	[Ah]

7.5.1 BATTERY SIZING TOOL

A tool was written that determines the low weight battery options, based on a given electric motor input voltage and current. This voltage is then increased as a result of battery efficiency, thus taking into account the voltage drop occurring due to power losses. The outputs of this tool are the number of cells in series (N_s), cells in parallel (N_p), the weight of the pack (kg), the total capacity (kWh), the discharge rate (or C-Rate), the individual cell capacity $C_{Ah,c}$ (Ah), the total current (A) and total voltage (V). The latter two function as a check and will be slightly off due to the need of rounding. Each series connection adds the cell nominal voltage to the pack voltage, whereas parallel connections add capacity (in terms of Ampere-hours) to the pack. The latter allowing for either a higher discharge current or a lower discharge rate in terms of C. C, or C-Rate, indicates the discharge current based on the cell capacity. 1C stands for the current that can be discharged for a full hour, whereas a 2C continuous discharge is only possible for half an hour.

Since extensive test results of the chosen Li-S battery were not available, some assumptions have been made with respect to the cell properties. For this reason, cell characteristics of the commonly used Panasonic NCR18650B Li-ion cells were used to derive the influence of temperature and C-rate on the capacity [81]. According to Figure 7.11a the C-rate has a negative effect on the usable capacity. However, if the C-rate is reduced during the flight the unused capacity can still be discharged[82]. For that reason, the effect of the lower C-rate during cruise should be considered when taking into account the capacity reduction. The program calculates the number of

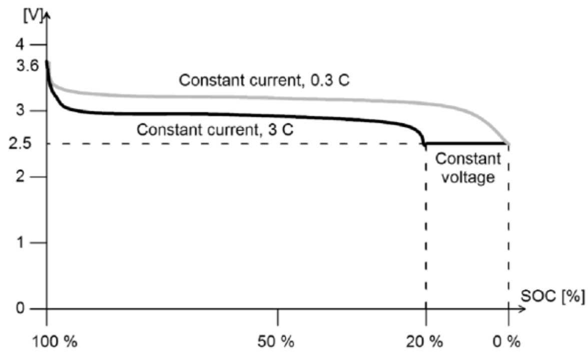

(a) Influence C-Rate on the capacity of battery cells [82]

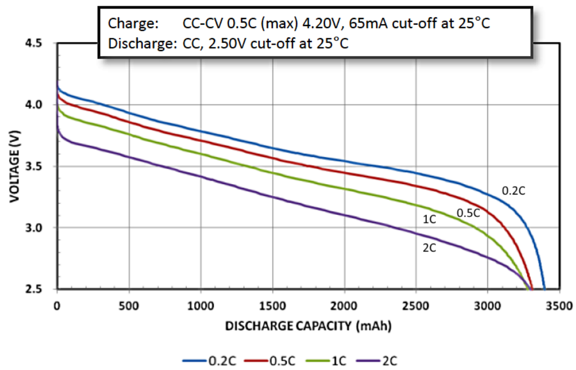

(b) Influence C-Rate on the capacity of NCR18650B cells[81]

Figure 7.11: C-Rate influence on capacity

cells in series and parallel for different pouch cell sizes (6.5-50Ah) and C-rates ranging from 0.1 to 5.0. For each combination the number of series and parallel connections are calculated. To find suitable low-weight configurations, some constraints were included. These are constraints on the total pack capacity (should be equal or larger than the required energy for the flight profile), weight, difference in amperage output and required motor amperage input as well as a check on the voltage difference. These are immediate checks on the output values. The required energy from the flight profile is equal to 49.42 kWh according to Equation 7.13a. The total pack capacity C_{tot} (kWh) is calculated using Equation 7.13b, which should be larger than E_r (kWh). The number of cells in series and parallel can be determined using the required pack amperage I_p (A) and voltage V_p (V) and rewriting Equations 7.12a and 7.12b.

$$I_p = N_p \cdot C_{Ah,c} \cdot CR \tag{7.12a}$$

$$V_p = N_s \cdot V_{nom} \tag{7.12b}$$

$$E_r = \frac{P_r(\frac{1}{2} \cdot t_{cr} + t_{race})}{60\eta_p\eta_s\eta_b} \tag{7.13a}$$

$$C_{tot} = \frac{N_p \cdot N_s \cdot V_{nom} \cdot C_{Ah,c}}{1000} \tag{7.13b}$$

The results of this method showed that the low weight options were all at a maximum C-rate (CR) during the race of approximately 3.0-3.5C and that all possible solutions have individual cell capacities $C_{Ah,c}$ of 6.5-8.5Ah. This means that the smaller cells yield the best possible results in terms of weight. This is because smaller cells match the required amperage of the motor in the best way. The C-rate should preferably be lower based on the reduced capacity at high discharge rates. The maximum charge- and discharge rates the cells allow is 5C. Analysis proved that restricting the C-rate had a major effect on the battery weight and thus also its sheer size. The reason is that reducing the effects of the C-rate on the capacity requires a C-rate that is lower than 1C. Because limiting the C-rate to ≤ 1 did not result in any feasible results, the program includes a CR correction factor κ_{CR} resulting in a race single cell amperage that is calculated according to Equation 7.14. The correction factor is based on the capacity change between low and high C-rates of the Panasonic 18650 cell (Li-ion), which has a 3% reduction of the total capacity. Also see Figure 7.11.

$$I_c = CR \cdot C_{Ah} \cdot \kappa_{CR} \tag{7.14}$$

Taking the considerations of cell size, effects of the C-rate and weight into account, the program yields a low-weight result of which the pack specifications are provided in Table 7.10.

Table 7.10: Battery Pack Specifications

Specification	Value	Unit
Cells Parallel	12	[-]
Cells Series	273	[-]
C-Rate	3.3	[-]
κ_{CR}	1.03	[-]
Total Ah	90.0	[Ah]
$C_{Ah,c}$	7.5	[Ah]
I_p	297	[A]
V_p	559.65	[V]
C_{tot}	50.37	[kWh]
Pack Weight	100.74	[kg]

7.5.2 BATTERY MODULE DESIGN

As there are volume restrictions within the aircraft, the battery pack needs to be separated in modules. The decision was made to have 12 separated modules attached in parallel, each consisting of 273 cells in series. This decision was quickly made based on the fact that there are 12 cells in parallel according to the results presented in Table 7.10. This means that all 12 modules will be connected in parallel. The chosen module configuration allows for some center of gravity flexibility and an easier fit in the confined fuselage volume. The integration of the modules inside the fuselage was conducted in parallel with the module design to ensure an allowed centre of gravity location. This was done in CATIA which also helped with coping with the volume restrictions.

A program was written that explores the size of the entire battery module. Since the height of the individual pouch cells is known, the configuration from the top view was determined with this tool. The top view configuration that resulted from this can be seen on the left side of Figure 7.12.

The configuration approach (top view) consisted of a few steps. First of all, the decision was made to find all configurations that yield a rectangular top view, for which a frame would be easier to produce. Then, an estimate was made regarding the cell thickness, which is shown in Table 7.11. More importantly, with air cooling in mind, channels were added allowing for a larger cell surface area. The dimensions of these channels are from now on fixed and the feasibility of the design in terms of thermal management is investigated in Section 7.6. The current channel dimensions are given in Table 7.11.

In terms of thermal management it would be advantageous to have large channels and to separate the cells from each other. However, the integration of subsystems in CATIA showed that this would require too much volume. A logical step was to create groups of cells as can be seen in Figure 7.12. The configuration shown in this figure proved to be the lowest volume option, with 39 cells divided over four groups and 7 cells in the longer direction. Four groups with a spacing of 3 mm between each group turned out to be feasible in terms of fuselage integration. A channel width of 3 mm was also chosen based on feasibility. Whether this is possible in terms of thermal management by air cooling will be studied in Section 7.6. The current group setup of 10-10-10-9 cells (as shown in Figure 7.12) can be changed but in this report a 4-group configuration will be maintained due to volume limitations.

Table 7.11: Battery channel dimensions and cell thickness estimate

Dimension	Meaning	Value	Unit
w_{ch}	Channel width	3	[mm]
h_{ch}	Channel height	148	[mm]
t_c	Cell thickness	3	[mm]
s_g	Group spacing	3	[mm]
N_g	Number of groups	4	[-]

7.6 THERMAL ANALYSIS BATTERY MODULE

One of the most important parts of the battery is the thermal management. The operating range of the Li-S cells lies within -30 to +70 °C. Due to a battery efficiency η_b of 90% each cell has waste heat that amounts to 10% of the cell power. The main risk will be overheating the battery during the 3-minute race in which the C-rate is 3.3 and the heat loss per cell equals 5.1 W according to Equation 7.15. The heat loss per group can easily be determined by multiplying it with N_i, the number of cells in group i.

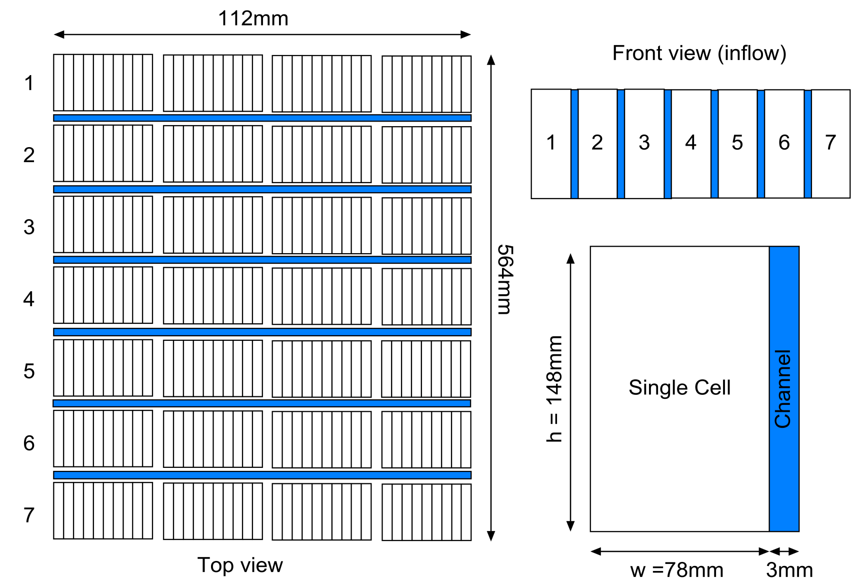

Figure 7.12: Initial lay-out of chosen configuration: the blue channels indicate the mass flow direction for air cooling

$$\dot{Q}_{l,c} = V_{nom} \cdot CR \cdot C_{Ah,c} \cdot (1 - \eta_b) \tag{7.15}$$

The main risks for the battery are thermal runaways when exceeding the safe operating temperature and uneven temperatures within the battery modules and pack. Uneven temperatures within a module will change the characteristics of each cell, resulting in different resistance, efficiency and discharge rates along cells. This means that the battery pack relies heavily on the battery management system. Thermal management by means of liquid- or air cooling is the solution to this issue.

7.6.1 THERMAL MANAGEMENT APPROACH

Thermal management is usually done by flowing a fluid along the battery cells which absorb the energy and moves it away from the battery pack. One of the options is liquid cooling. This would however require a pump system which adds weight to the aircraft. The liquid has to be cooled again, which also adds more weight. Another option is to use the ambient air as a fluid: air cooling. This can be done passively, by means of an inlet in the aircraft and fans that either push or pull the mass flow through the modules. As long as each module gets its separate inlet with an equal or similar inflow temperature, the entire battery pack can be modeled with single battery modules.

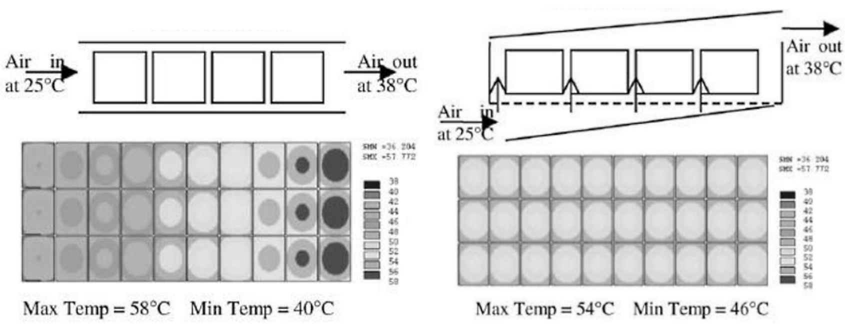

Figure 7.13: Difference air cooling philosophies

There are two different air cooling methods, which are shown in Figure 7.13 [83]. These methods can be applied on pack as well as module level. It is clear that the temperature increase of the air flow in series cooling results in a more uneven distribution of module or cell temperatures. For this reason, the chosen air cooling direction is as shown in Figure 7.12, following the parallel method. The major challenge in detailed design would be to get similar inlet temperatures as the parallel approach is harder on pack level.

The thermal management system also needs to be able to heat up the battery modules when ambient temperatures are below the efficient operating temperature. The air is first heated before pushed through the battery module. This will not be further discussed.

7.6.2 THERMAL ANALYSIS MODEL

This section elaborates on the analysis method for the thermal management. It studies the surface temperature and flow temperature inside the channels of the battery modules using an analytical solution method [84]. The heat conductivity of the cell-air interaction, heat radiation and different mass flows are considered in this analysis. The flow regime of the fluid flow needs to be considered as the Reynolds number changes with increasing mass flow $\dot{m}$. An important consideration of thermal management is the increase of air flow temperature along the channel length. The result is a smaller temperature difference between the cell (group) surface and the air temperature, resulting at a heat flow equilibrium at a higher cell surface temperature. This section elaborates on a simplified approach that studies the cell temperature for several group configurations. It is based on the equilibrium Equation 7.16.

$$\dot{Q}_l = h_c A\left(T_s - \frac{T_{b_1} + T_{b_2}}{2}\right) + \sigma\epsilon F_{sh} A_s\left(T_s^4 - T_b^4\right) = \dot{m}C_p \cdot \left(T_{b_2} - T_{b_1}\right) \quad (7.16)$$

The radiation term is neglected in the further analysis because this is very small for temperatures inside the operating range of the battery cells [85]. The symbol $\dot{Q}_l$ indicates the heat losses (W) per group, h_c the heat conductivity coefficient (W/m^2K), A the surface area of a group, T_{b_1} the begin temperature of a section, T_{b_2} the end temperature. For the heat flow through air the mass flow $\dot{m}$ through the channel and the specific heat C_p are required.

For the following approach, Figure 7.14 has been used. The temperatures before and after each cell group are calculated as well as the surface temperature T_s of each group. It is assumed that each group has homogeneous properties. The number of cells per group will be changed. The channels perpendicular to the flow are assumed not to have any influence on the fluid mass flow, but do add to the heat conductivity surface.

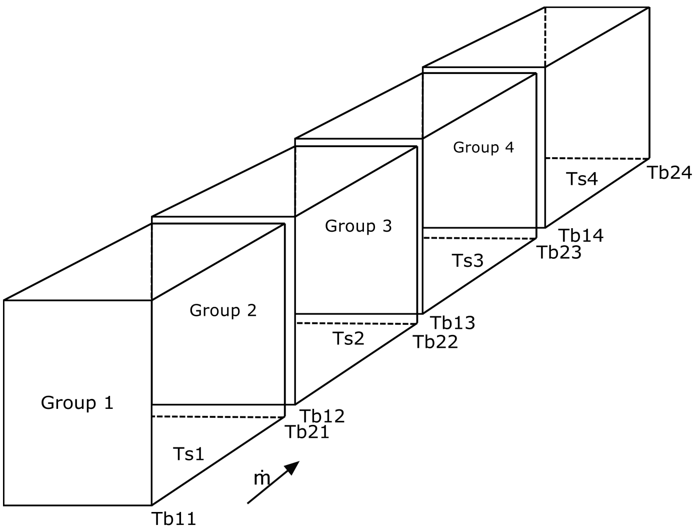

Figure 7.14: Battery thermal management approach

FLOW PROPERTIES

Before continuing with the analysis, it is required to derive the flow properties inside the channel. A range of mass flows will be studied in the tool which relate to the channel flow velocity according to Equation 7.17. The fluid velocity in the channel will determine whether the flow regime is laminar or turbulent. The flow regime has an effect on the heat conductivity coefficient as will be shown later.

$$\dot{m} = \rho \cdot w_{ch} \cdot h_{ch} \cdot V \quad (7.17)$$

The critical Reynolds number is approximately 2000. Equation 7.18 is used to calculate the Reynolds number within the channel, in which D_h is the hydraulic diameter and v the kinematic viscosity coefficient.

$$Re = \frac{V \cdot D_h}{v} \quad (7.18)$$

$$D_h = 2\left(\frac{w_{ch} \cdot h_{ch}}{w_{ch} + h_{ch}}\right) \quad (7.19)$$

The hydraulic parameter can be calculated with Equation 7.19 for rectangular channels. The next step is to find the appropriate heat conductivity coefficient. Due to the airflow through the channel, there is forced conductivity instead of free conductivity, allowing for a higher heat conductivity coefficient and thus a lower required temperature difference between the block surface T_s and the average air temperature $(T_{b1}+T_{b2})/2$ in the blocks. The heat conductivity coefficient h_c can be approximated using the Nusselt's number, which takes the flow regime effects into account. The heat coefficient was calculated according to Equation 7.20, in which k is the thermal conductivity of air.

$$h_c = \frac{k \cdot Nu}{D_h} \tag{7.20}$$

The Nusselt's number is then calculated using Equation 7.21, which is different for the laminar or turbulent flow regime. Because RBARs are held around the globe, two different inlet temperatures for the modules are analysed. A moderate and high inlet ambient temperature T_{b11} of 20 and 40 °C were considered in the analysis. Table 7.12 gives an overview of the air properties at these air temperatures [86].

$$Nu(Re) = \begin{cases} 1.86(Re \cdot P_r)^{0.33} \frac{D_h}{L}^{0.33} \cdot \frac{\mu_{50}}{\mu 20}^{0.14}, & \text{if } Re < 2000. \\ 0.023Re^{0.8} \cdot P_r^{0.3}, & \text{if} Re \geq 2000. \end{cases} \tag{7.21}$$

Table 7.12: Properties of air at 20 and 40 °C and general parameters

Variable Parameters	**Meaning**	**T = 20 °C**	**T = 40 °C**	**Unit**
C_p	Specific Heat	1005	1005	$[J/kgK]$
k	Thermal Conductivity	0.0256	0.0271	$[W/mK]$
ρ	Density	1.2047	1.1275	$[kg/m^3]$
v	Kinematic Viscosity	1.51E-05	1.70E-05	$[m^2/s]$
P_r	Prandtl Number	0.716	0.712	[-]
Fixed Parameters	Meaning	Value		Unit
μ_{20}	Dynamic viscosity air at 20 °	1.82E-05		$[kg/ms]$
μ_{50}	Dynamic viscosity air at 50 °	1.91E-05		$[kg/ms]$
D_h	Hydraulic parameter	0.00588		[m]
L	Channel Length	0.1121		[m]

SURFACE TEMPERATURE ANALYSIS

Determining the surface temperature is quite straightforward at this point. First of all, it should be cleared up what surface area is used for the heat conductivity from the cell group/block surface. Each channel is surrounded by two blocks, each fully surrounded by air. For now, it is assumed that half the surface area of both of the surrounding groups will transfer heat to the channel. This results in the following conductivity surface per group, with a number of N cells per group, according to Equation 7.22.

$$A_b = 2(w_c \cdot h_c + N \cdot t_c \cdot w_c + h_c \cdot N \cdot t_c) \tag{7.22}$$

Defining the temperature between the surface and the average fluid flow temperature along a block as $\Delta T2$ and the temperature difference between the beginning and end section of each group $(T_{b2} - T_{b1})$ as $\Delta T1$ results in Equations 7.23 and 7.24. In these equations $\dot{Q}_l$ is the heat flow out of a single block and A_b is the block surface area. The subscript j is the block number of which there are four according to Figure 7.14. The subscript i only takes the values 1 and 2 as these indicate the block in- and outflow respectively.

$$\Delta T_{2,j} = \frac{\dot{Q}_{l,j}}{h_c \cdot A_b} = T_s - \frac{T_{b_{i+1,j}} - T_{b_{i,j}}}{2} \tag{7.23}$$

$$\Delta T_{1,j} = \frac{\dot{Q}_{l,j}}{\dot{m} \cdot C_p} = T_{b_{i+1,j}} - T_{b_{i,j}} \tag{7.24}$$

Based on these temperature differences the average surface temperature of each block can be calculated using Equation 7.25.

$$T_s = \Delta T_{2,j} + \left(\frac{T_{b_{i,j}} + T_{b_{i+1,j}}}{2}\right) \tag{7.25}$$

Four different group distributions were now analysed, starting with the 10-10-10-9 configuration of Figure 7.12. The other distributions are 15-11-8-5 and the outputs are checked by a far from non-optimal result 5-8-11-15.

The last version is an optimized configuration in which the surface temperature difference between the fourth and first cell ($T_{s4} - T_{s1}$) is low, the 16-10-7-6 configuration. Two constraints were set:

- T_{s4} should be lower than 60°C to make sure the core temperature does not exceed the maximum operating temperature.
- Surface temperature difference between the first and last block $T_{s4} - T_{s1}$ should be smaller than 15°C

The results of this analysis can be seen in Figures 7.15 and 7.16. Note that the axes are slightly different due to these two constraints. The undashed lines have an inflow temperature of 20°C and the dashed lines 40°C. Furthermore, the bottom line shows the surface temperature of the first block (lowest temperature) and the line on top the surface temperature of the fourth and last block the fluid flow reaches.

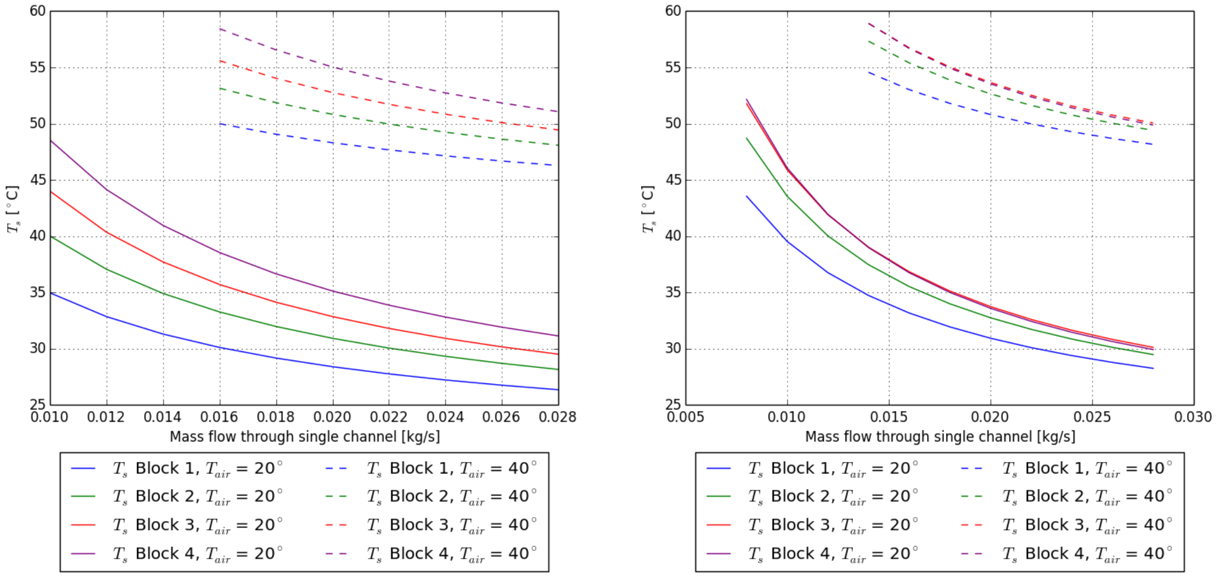

(a) 10-10-10-9 Group Configuration (b) 15-11-8-5 Group Configuration

Figure 7.15: T_s for all four blocks for $T_{b_{11}}$ of 20 (undashed) and 40°C (dashed)

The original configuration (Figure 7.15a) shows a relatively large difference between block 1 and block 4. The main reason is that each block has a similar heat loss to area ratio, but the last block sees a smaller temperature difference between mass flow and surface. The 15-11-8-5 configuration (Figure 7.15b) shows much better results as the heat loss to area ratio gets better along the channel. The opposite was added as a check as part of the model verification. Figure 7.16a shows the 5-8-11-15 configuration which has large temperature difference. This is the expected result. Finally, a small adjustment was made to the 15-11-8-5 configuration which is shown in Figure 7.16b. This 16-10-7-6 configuration shows very similar results.

It should be noted that this simplified model comes with major limitations. First of all, the larger blocks will see a much greater core temperature increase than the smaller blocks. The core temperature cannot be estimated well without test results of the Li-S cells. However, even the current analytical method could be improved by studying the surface temperature of each individual cell instead of the blocks as a whole. Further analysis may prove that decreasing the number of cells per block may not be ideal due to a significant rise of core temperature for larger groups.

The method does show however that the potential of (parallel) air cooling is feasible even with relatively small channel dimensions. These are limited due to fuselage volume restrictions.

AIR COOLING FANS

Based on Figure 7.16b and Figure 7.15b a mass flow per channel $\dot{m}_{ch}$ of approximately 0.015 kg/s is the minimum mass flow per channel for ambient temperatures ($T_{b_{11}} = T_{air}$) of 40°C. Each battery module has a total of 6 channels (N_{ch}), resulting in a total mass flow of 0.09 kg/s. The specifications of the chosen fan show a mass flow of 0.035 kg/s [48]. This means three (N_f) of these low power fans (P_f = 2.4 W) are required per module. These fans add 25 mm w_f to the width of the modules. Table 7.13 shows these values.

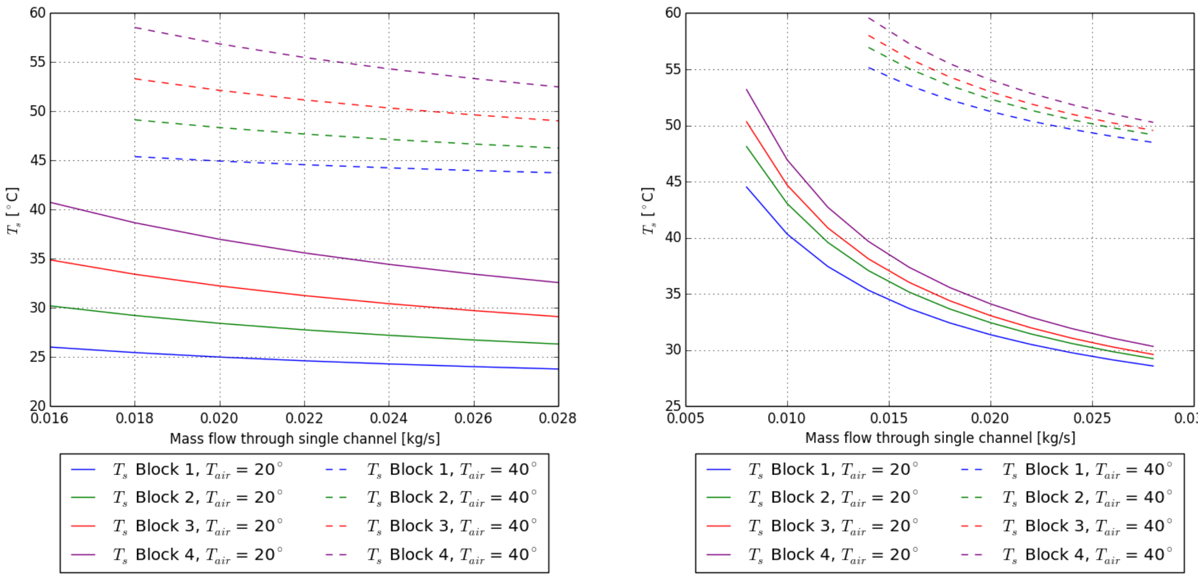

(a) 5-8-11-15 Group Configuration

(b) 16-10-7-6 Group Configuration

Figure 7.16: T_s for all four blocks for $T_{b_{11}}$ of 20 (undashed) and 40°C (dashed)

Table 7.13: Air cooling final overview of each battery module

Parameter	**Value**	**Unit**
N_{ch}	6	[-]
$\dot{m}_{ch}$	0.015	$[kg/s]$
$\dot{m}_f$	0.035	$[kg/s]$
N_f	3	[-]
w_f	25	$[mm]$
P_f	2.4	$[W]$
$T_{s_4} - T_{s_1}$ (20°C)	ca. 4	[°C]
$T_{s_4} - T_{s_1}$ (40°C)	ca. 4	[°C]

7.7 CHARGING POSSIBILITIES

When considering the feasibility of the aircraft, a major consideration is charging. The time between landing and take-off on race days is short and the charging time should therefore be limited to a bare minimum. This section therefore studies the theoretical minimum charge time based on the Li-S cell limits and charging options. The main reason is that a regular grid will not be able to deliver enough power for reasonable charging times. High voltage lines at airports may be an option but the AC input would have to be transformed and rectified by a large charging unit. The exact charging options for regular usage needs to be studied to a greater extent.

On race days fast charging is required due to limited time between landing and take-off. The theoretical charging time was calculated using a maximum 5C charge-discharge rate. With 12 separate modules of 7.5Ah each, this results in a current of 450 A into the battery. The corresponding voltage from the charger unit needs to be at the same level – equal to 569.65 V - or slightly under the total battery pack voltage. The reason is, based on Figure 7.11 that with lower voltages the cells cannot be charged fully. The result is a total power input of 251.8 kW into the battery. Such a power input would not be feasible with small charger units on-board of the aircraft that transform and rectify from AC to DC. A supercharger, similar to that of Tesla would be necessary to install. These do not go through an on-board charging unit but have twelve 10kW chargers inside the exterior charging station, allowing for a power input of 120kW. The DC from these 12 chargers go directly into the battery. The same approach seems to be the most feasible option for this aircraft, with charger specifications that are given in Table 7.14. However, it is clear that the supercharger needs to deliver over twice the power of the Tesla supercharging stations. This then results in a theoretical charging time t_{sc} of only 12 minutes. As the current drops in the final stages of charging, it is estimated that the practical duration of charging is approximately 20 minutes. Slower charging is preferred due to a reduced C-rate and a longer battery cycle life.

While integrating the batteries into the fuselage, the volume constraints resulted in slightly fragmented battery module positions. The result is that battery swapping would not be a feasible or fast option. The detailed design phase should therefore consider the end of life replacement possibilities only.

Table 7.14: Supercharging specifications

Charging Specification	Value	Unit
I_{SC}	450	[A]
V_{SC}	569.65	[Vdc]
C-rate (CR)	5	[C]
P_{SC}	251.8	[kW]
Theoretical Charging Time t_{SC}	12	[min]
Estimated Practical t_{SC}	20	[min]

7.8 ELECTRICAL POWER FLOW DIAGRAM

The majority of the powertrain components, functions and specifications are known at this point. The integration of these systems and the flow of electrical power should be known before going into the detailed design phase. An overview of all the electrical components and corresponding amperage, voltage and power is given in Figure 7.17.

The undashed lines indicate the electricity flows whereas the dashed lines show the data flow between control units. The protocol used is CANbus, a standard in several vehicle industries. EFIS also functions as the central logic controller which all CANbuses are leading to. The vehicle exterior shows the charging options and time. The charging time of a regular socket has been added, leading to 4-20hr charging time. Note that the high voltage lines at airports will allow for faster charging. The battery pack output power (149 kW) is including the battery efficiency. The subsequent voltage drop towards the electric motor is due to power losses that occur in the battery. The motor efficiency of Table 7.6 includes the controller/inverter efficiency. While charging the main battery pack, the DC-DC converter allows for charging the 24V pack for the low voltage circuit as well.

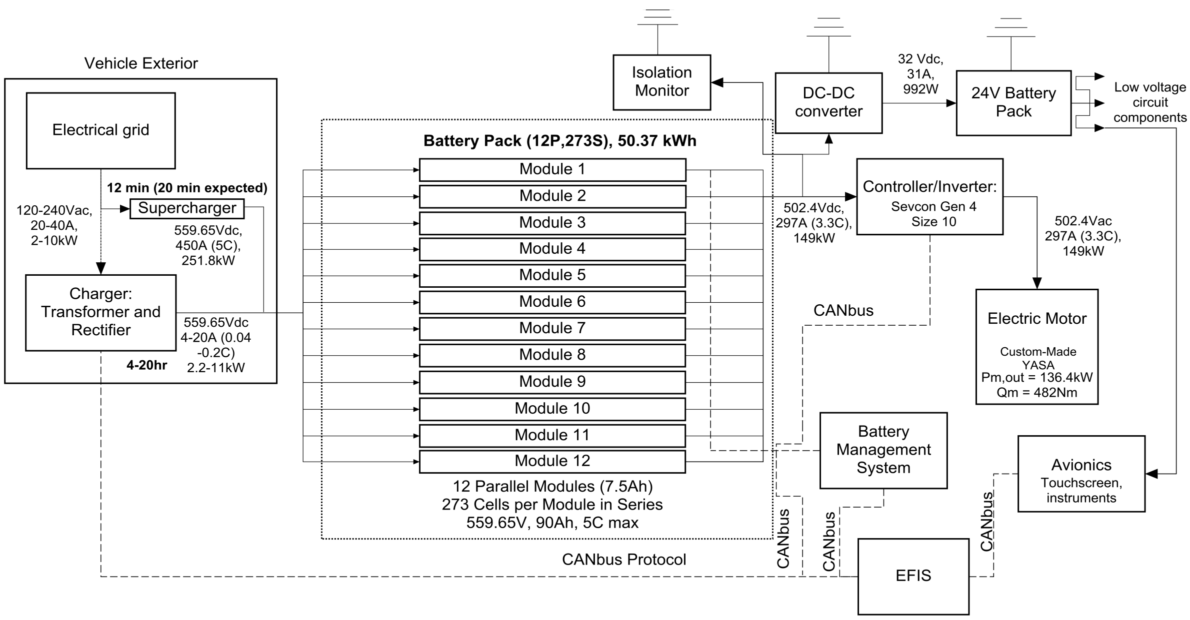

Figure 7.17: Powertrain flow diagram including power flow, local voltage/amperage and data flow from processing units

7.9 ENERGY RECOVERY SYSTEM

For the energy recovery system, kinetic and thermal energy sources were identified as feasible. Kinetic energy could be recovered by regenerative braking. Kinetic energy is released when throttling down. However during the flight the throttle setting is decreased only at cruise descent and landing approach, so this energy source is very limited. Thermal energy could be recovered from the battery and electric motor waste heat by the use of thermoelectric generators or a Rankine cycle. However, as the analysis in the Mid-Term Report shows [87], the added mass, cost and complexity of such systems are not covered by a sufficient mass decrease at the predicted or theoretical conversion efficiencies. Thus aircraft performance would only deteriorate.

7.10 VERIFICATION

While designing the powertrain several tools were built for the analysis. The first program was created for the sizing and estimation of the propeller weight and performance for each configuration. The outcome values of the tool were, checked by calculating it analytically and then compared with actual propellers, with the same design conditions. Some values were retrieved from graphs which can cause discrepancies. Calculating the diameter size analytically and with the tool, with the same input values, resulted in the same diameter of the propeller. The tool was thus verified. During the design of the propeller the program XRotor has been used. This program was developed by MIT and used in several successful projects. With the help of XRotor the outcome of the tool was checked and improved.

The next tool that has been used is a script for the shaft design programmed in Python. The script was based on an analytical method of which the outcome could be easily recalculated and checked. This showed no discrepancies and thus the program has been verified.

The tool for calculating the battery weight and dimensions consists of several units. Each step was checked analytically and showed that the results had no discrepancies with the set constraints. These constraints played both a major role in determining the best configuration as well as in the verification process. During the verification it was noticed that the battery weight is very sensitive to the total drag of the aircraft, requiring a larger number of iterations. For this reason the tool to estimate the battery weight was incorporated with the tool that determines aircraft and component weights using an iterative process. This tool returned the same values after the implementation of the battery sizing script.

Also, the outcome showed that smaller battery cells were favoured by the program. This is a logical result as these have a lower rounding effect. Besides, the C-rate of the low weight battery pack configurations was always in the region of 3.0-3.5 and C-rates under approximately 2 were not feasible at all. This is a logical result as a lower C-rate automatically means that one does not use the entire potential of the cells, hence resulting in a much higher weight. Higher C-rates also did not show any feasible results. Even though the required power can be easily reached with higher C-rates, the total pack capacity is not sufficient due to a much smaller number of cells in the pack. The flight profile could in no way be fulfilled as the total capacity C_{tot} is in this case lower than the required energy E_r (kWh). Therefore, these results are deemed as logical.

The last program that has been used was for the thermal management of the battery. The proposed solution method is a simplified analytical solution of which a single result was checked. Furthermore, the different results in Figure 7.15a to 7.16b showed expected results. Figure 7.16a was added to show that an illogical configuration shows exactly what was expected.

7.11 VALIDATION

Even though the tools cannot be fully validated at this moment, there are still some steps that could be taken in the detailed design phase. These validation processes will be briefly elaborated on in this section.

The propeller design characteristics can be validated using wind tunnel tests. The electric motor should first be manufactured after which its performance can be tested using a custom made test bench. The next step would be to test and validate the propeller and electric motor integration.

The battery pack weight estimation could already be validated in the very near future by analysing currently available battery cells and arbitrary voltage/amperage/power requirements. Since the tool also works for smaller battery packs this could be a cheap validation method. The output of a smaller pack can be measured and the program can be validated.

For the thermal analysis validation the current tool may not be sufficient. Since the current methodology has some major limitation (core temperature estimation is not possible for different group sizes) the effect of the group size on the core temperature needs to be studied first. The result could show that equally sized groups are more beneficial in terms of even cooling and that instead a higher mass flow might be required to maintain a low temperature difference between the blocks. The results of the 10-10-10-9 configuration may therefore be the most reliable at this moment, as the four blocks are almost equal in size. This could then be verified using for example ANSYS' *Battery Cell Electrochemical and Thermal Modeling* software. Cooperation with the Li-S cell manufacturer will be necessary at that point. These models could then be validated using extensive module testing. Testing the complete battery pack will be expensive and most likely not necessary.

8 WING AND CANARD

In this chapter the wing and canard subsystem will be presented first from the aerodynamic point of view in Section 8.1 and then from the structures point of view in Section 8.2. The aerodynamic design is mainly focusing on the efficiency of the aircraft. It was the goal to optimize the airfoil, minimize interference effects and to select a planform that results in a good lift distribution and the desired stall characteristics. For the structural design the aerodynamic characteristics were used to analyze the forces and stresses that are applied on the structure.

8.1 AERODYNAMIC DESIGN

This section deals with the aerodynamic design of both the wing and canard. The airfoils are selected, the wing planform is determined, a 3D analysis is performed and the results are presented and discussed. The aerodynamics section is divided in two parts. The first part elaborates on 2D airfoil design and the second part on the 3D wing analysis. However, there is a great overlap between the two parts, because they are both based on DATCOM and the wing planform uses the airfoil from 2D as input for the design.

8.1.1 AIRFOIL SELECTION 2D

One of the main design parameters of the wing, besides the overall dimensions, is the airfoil. The shape of the airfoil decides how much lift the wing sections can produce at how much drag and how the the wing will behave in a stall. Choosing a proper airfoil shape is therefore crucial in designing an aircraft and optimizing its wing for a range of specific flight situations. The airfoil optimization is done in 2D, accounting for 3D effects using correction factors. Later, a 3D analysis is used to improve the design and verify the 3D corrections.

ASSUMPTIONS

For the 2D airfoils non-finite wing assumptions apply. No span-wise flow is therefore assumed. The calculations are based on a panel-method, as implemented in the program XFoil[88]. In general the program uses a panel solution with Karman-Tsien correction added for compressibility[89]. Far from the airfoil the program assumes inviscid, incompressible, irrotational and steady flow. Strong interaction with the potential boundary layer is modelled with a surface transpiration model and drag is calculated from the wake momentum thickness far downstream and often underestimated. Up to shortly after the stall angle the $C_{l_{max}}$ and C_{l_α} predictions are very accurate. Even though the drag estimation is not very accurate and can not be trusted in a quantitative sense, the values of C_d can be seen as a good indication of the qualitative influence that the individual parameters have on the design.

METHOD

For selecting an airfoil, first the requirements have to be known in terms of $C_{l_{max}}$, C_{l_α}, C_m, C_d. The wing has to provide enough lift during all flight situations during the race to allow the aircraft to perform as good as possible and achieve a good lap time.

Input/output parameters

The input parameters for the optimization are therefore the minimum required $C_{l_{max}}$ value for the airfoil, the maximum negative C_m value that the airfoil needs to stay above and the $C_{l_{design}}$ values for cruise, level racing and steep turns where the C_d should be as low as possible to allow the aircraft to loose as little velocity or to accelerate as fast as possible. Equation 8.1 is used to calculate the C_L values and corrected for 3D effects using Equation 8.2 with correction factors from the DATCOM methods[90] for compressibility effects. For cruise, the required C_l is calculated using n=1, V=45m/s, sea level density, the wing loading from Chapter 6.3.1 and a 3D correction from Equation 8.2 yielding $C_{l_{cruise}}$=0.71. For level racing V=100m/s is used, yielding $C_{l_{race}}$=0.36. Finally for steep turns the load factor is increased. Small radii at high speeds allow for shorter lab times, but require a higher load factor. During the competitions the maximum load factor is limited to 10g. Using n=10 and V=85m/s due to the increased drag and loss of velocity during a steep turn, a (2D) $C_{l_{turn}}$ of 2.1 is found. This results from the 3D C_L of 1.78 and is almost the same as for landing (see Chapter 6.3.1). At landing the Reynolds number is lower, but also compressibility effects can be neglected, so that the required 2D $C_{l_{land}}$ is lower than $C_{l_{turn}}$. A value of 2.1 is therefore taken as the minimum required $C_{l_{max}}$ for the airfoil selection. A list of input parameters for the airfoil optimization is given in Table 8.1.

$$C_L = \frac{W \cdot n \cdot 2}{\rho V^2 S} \tag{8.1}$$

$$C_L = \left[\frac{C_{L_{max}}}{C_{l_{max}}}\right] C_{l_{max}} + \delta C_{l_{max}} \tag{8.2}$$

Because main wing stall leads to a deep stall that the aircraft can not recover from, the stall characteristics for

Table 8.1: Input parameters for airfoil optimization

Parameter	Need
$C_{l_{10g}}$	achieve $C_{l_{10g}}$
$C_{m_{min}}$	stay above $C_{m_{min}}$
$C_{l_{10g}}$	minimize corresponding C_d
$C_{l_{levelrace}}$	minimize corresponding C_d
$C_{l_{cruise}}$	minimize corresponding C_d

the main wing are of no major importance. Stall of the main wing in general has to be avoided. The desired output from an optimization procedure is an airfoil shape. During earlier design already the modified NACA 4-series airfoil was chosen[87]. Besides camber, camber position and maximum thickness, the modified version also allows changing the nose radius and the position of the point of maximum thickness. This gives a large design space and a challenge for the optimization. A list with the airfoil shape output parameters is given in Table 8.2.

Table 8.2: Output parameters for airfoil optimization

Parameter	Description
t/c_{max}	Maximum thickness
xt/c_{max}	Position of max thickness
f/c	Camber
xf/c	Position of camber
R/c	Leading edge radius

Optimization strategies

The number of (5) airfoil shape parameters allows for an enormous number of combinations that makes it impossible to calculate aerodynamic properties even with the simplified 2D equations implemented in XFoil for all possible shapes on a standard machine within a reasonable time.

With camber from 0.0 to 0.16 (f/c) and maximum thickness from 0.1 to 0.2 (t/c) in steps of 0.01, camber and thickness locations from 0.1 to 0.9 (x/c) in steps of 0.01 and nose radius from 2 to 10 (R/c) in steps of 0.1 the modified NACA 4-series already gives $16 \cdot 20 \cdot 80 \cdot 80 \cdot 80 = 163{,}840{,}000$ possible shapes. With an average calculation time of 5 seconds for the aerodynamic properties using XFoil it would take the author's personal i7 machine 26 years to try all combinations of shape parameters and find the optimum. Because most aerodynamic properties depend on multiple airfoil shape parameters, standard parametric optimization strategies do not apply or are impossible to implement without getting stuck in a local minimum that does not represent the global optimum solution. The strategy chosen was therefore a genetic algorithm, which tries to mimic evolution and breed an optimal result. Genetic algorithms (GA) can be applied for a large field of applications and seem particularly useful for airfoil optimization. The principle behind GAs is explained in the following section.

Genetic algorithms

The principle of genetic algorithms is universal but needs to be implemented and tailored for every optimization problem individually. The genetic algorithm for the E-SPARC airfoil optimization is written as a Python script and consists of multiple parts, including a number of tools for aerodynamic calculations and airfoil generation. First the script generates airfoil coordinates from input parameters on thickness(location), camber(location) and nose radius. The algorithm then hands the airfoil coordinates to XFoil in order to calculate the aerodynamic output properties. The genetic algorithm part itself takes care of initializing a number of first airfoils from random parameters, judging the airfoils' fitness based on the calculated aerodynamic properties and breeding new generations from the initial airfoils based on their fitness. An overview over the algorithm layout is given in Figure 8.1 and the individual components shortly explained in the following. First an initial (parent) population is generated by initializing a number of airfoils as objects of the airfoil class, defined in Python (Figure 8.2). Every airfoil, or member of the population, is described solely by its genetic code. The genetic code holds the encoded information of the airfoil shape as can be seen in Figure 8.2. Because modified NACA-4 series airfoils are described using the five input parameters stated above, the genetic code of every airfoil holds those values in an array. During the initialization a random value is chosen within specified boundaries for each parameter of the individual airfoils. Every airfoil object is then drawn, meaning that a list of points (x,y coordinates) is generated describing the airfoil shape. This is done using the formulas specified in the mod NACA-4 series

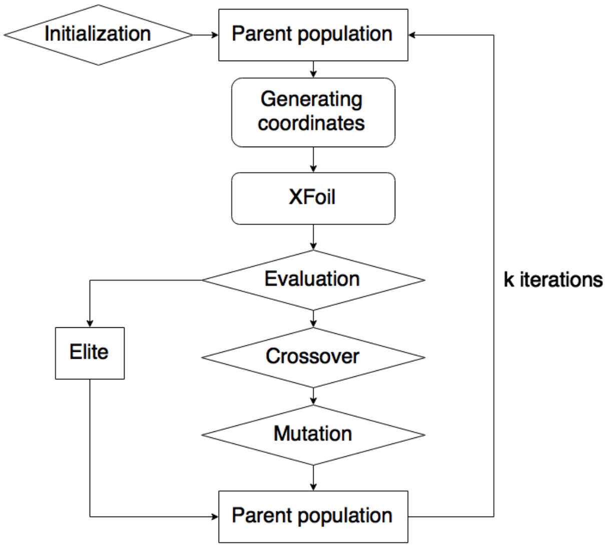

Figure 8.1: Airfoil optimization flow diagram

```python
class member:

    def __init__(self,DNA):
        self.DNA = DNA
        self.MM  = float(DNA[0]) #Camber
        self.PP  = float(DNA[1]) #Camber position
        self.TOC = float(DNA[2]) #max thickness
        self.IP  = float(DNA[3]) #nose radius
        self.TT  = float(DNA[4]) #thickness pos
```

Figure 8.2: Shape parameters encoded in DNA array

definition[91] stated below for points in front (8.3a) and after (8.3a) the point of maximum thickness. From the boundary conditions the parameters can be derived and the curves evaluated for given airfoil shape parameters from Table 8.2.

$$\frac{y}{c} = a_0\left(\frac{x}{c}\right)^{1/2} + a_1\left(\frac{x}{c}\right) + a_2\left(\frac{x}{c}\right)^2 + a_3\left(\frac{x}{c}\right)^3 \tag{8.3a}$$

$$\frac{y}{c} = d_0 + d_1\left(1-\frac{x}{c}\right) + d_2\left(1-\frac{x}{c}\right)^2 + d_3\left(1-\frac{x}{c}\right)^3 \tag{8.3b}$$

The coordinates for every airfoil are then loaded in XFoil and the desired individual aerodynamic output parameters calculated. The Reynolds number used is $5.5 \cdot 10^6$ as calculated in Equation 8.4 with L the chord length at MAC, v the airspeed and μ the dynamic viscosity of air. The airfoil is analyzed in XFoil for angles of attack between -8 and 25 degrees. The algorithm determines the maximum C_l value, the C_d and C_m at that angle of attack and the C_d values at the $C_{l_{race}}$ and $C_{l_{cruise}}$ values.

$$Re = \frac{\rho V L}{\mu} \tag{8.4}$$

The fitness of every airfoil is then calculated based on the aerodynamic parameters. The weights for the different C_d values that should be minimized are stated in Table 8.3. They are included in the fitness equation as stated in (8.5), which is maximized during the optimization routine. The weights are based on the assumption that maintaining speed during high-G maneuvers and accelerating in level flight are equally important. Cruise is given a lower weight, as the aircraft is mainly designed for flying a short lap time at the Red Bull Air Races. The cruise phase before and after the race is considered a secondary optimization goal.

Table 8.3: Weights for airfoil drag optimization

Parameter	**Weight**
C_d at $C_{l_{10g}}$	0.41
C_d at $C_{l_{levelrace}}$	0.41
C_d at $C_{l_{cruise}}$	0.18

$$fitness = \left(\frac{1}{7C_{d_{10g}} + 7C_{d_{levelrace}} + 3C_{d_{cruise}}}\right)^{1.5} \tag{8.5}$$

The $C_{l_{max}}$ and $C_{m_{min}}$ values are hard requirements for the airfoil. The fitness is therefore significantly decreased if one of those values is too low by multiplying the fitness with the ratio between the required and the real value to the power of 100. The fitness is then normalized (adding up to one) and the members of the population sorted by fitness. To make sure that no good genetic code is lost during the optimization the best member of each population (Elite) is passed to the next (children)population without modification as can be seen in Figure 8.1. The rest of the children population is derived from the parent population by a method called cross-over, where for every two new members two parents are selected from the old generation. This selection is done based on the old members fitness, so that members with a higher fitness produce more children and therefore propagate their properties more than members with lower fitness. The members of the children population then derive their genetic code (airfoil shape) from the selected parents. Finally 15% of all members are modified (mutation) by randomly changing one of their parameters to make sure that the algorithm explores the whole design space and does not get stuck in a local minimum. The algorithm generates a number of k populations before it stops and presents the member of the last generation with the highest fitness as result.

2D RESULTS

After the general layout of the optimization strategy is stated, this section presents the results. The algorithm turns out to converge with a high confidence to one result for a population size of n=20 members and k=100 iterations. More iterations increase the confidence that the optimum of the entire design space is found, but the time needed by XFoil to calculate the aerodynamic properties limits the amount of airfoils that can be tested on a standard machine within a reasonable time. Allowing very small mutations during cross-over also decreased the time needed to explore the design space.

The code was run for both the main wing and canard airfoils with different input values. For the main wing using a $C_{l_{max}}$ of 2.1, $C_{l_{cruise}}$ of 0.71, $C_{l_{race}}$ of 0.36 and $C_{m_{min}}$ of -0.15 lead to the NACA 9216-42 in Figure 8.3. The $C_{m_{min}}$ is needed for controllability, as the pitch down moment needs to be countered by the lift of the canard. In order to allow for a small canard, producing less drag, and a short canard arm (less structural weight) this value should not be too negative. The airfoil uses a maximum thickness of 16% at 29% chord length, 9% camber at 29% chord and 1.5% leading edge radius. The 2D plots for the aerodynamic lift, drag and moment characteristics of the

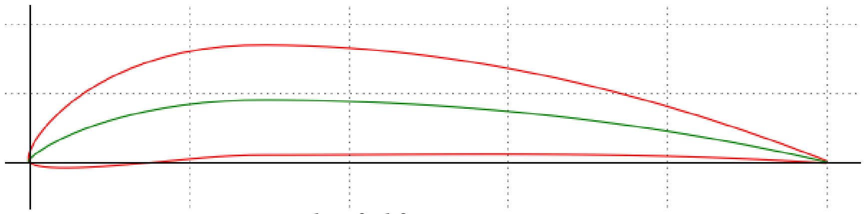

Figure 8.3: Final airfoil for main wing: NACA 9216-42

NACA 9216-42 are plotted in Figure 8.4. From Figure 8.4a the high $C_{l_{max}}$ of 2.1 can be seen. Low lift coefficients for level racing flight are achieved at negative angles of attack, meaning that the airfoil is mounted at a negative angle of incidence of about -6 degrees. The moment coefficient stays above -0.15, which is important for stability and controllability of the aircraft. From Figure 8.4b it can be seen that the C_d is rather high at low C_l, but stays low over a wide range of high C_l values, which is crucial for minimizing the decrease in speed during high-G maneuvers that can now be performed efficiently at high Cl/Cd ratios. Figure 8.5 shows pressure distributions from XFoil from which the trailing edge stall can be seen at around between 10 and 15°. For stability and control reasons the canard usually operates at slightly higher C_l values and therefore the design C_l values for the canard are taken slightly higher than for the main wing. A 3D $C_{L_{max}}$ of 2.0 is required for the canard from stability analysis in Chapter 14. Using Equations 8.1 and 8.2 the required 2D $C_{l_{max}}$ is then calculated to lie at 2.45. It also poses no restrictions on the C_m value, as this only has a minor contribution to the overall aircraft stability. Structural reasons might require a minimum thickness value to allow for a high aspect ratio, but at this point the construction method is not known so that the requirement is disregarded and considered later. The maximum value for the maximum thickness is set to 0.12 t/c during the optimization in order to assure that the stall of the canard is fast enough to prevent main wing stall. It should not be too sharp however to allow for a smoother nose drop that is desirable during high-G maneuvers. The Reynolds number for the canard is taken at $85m/s$ to lie at $3 \cdot 10^6$. The final airfoil can be seen in Figure 8.6 and uses a maximum thickness of 11% at 22% chord length, a camber of 12% at 36% chord and 1.6% nose radius.

DISCUSSION

The initial airfoil design is based purely on 2D tools. This section gives a short discussion on the results and their validity. The airfoils are designed based on input parameters that are derived from both individual performance of the airfoils and required stability and controllability constraints for the canard. The number of iterations

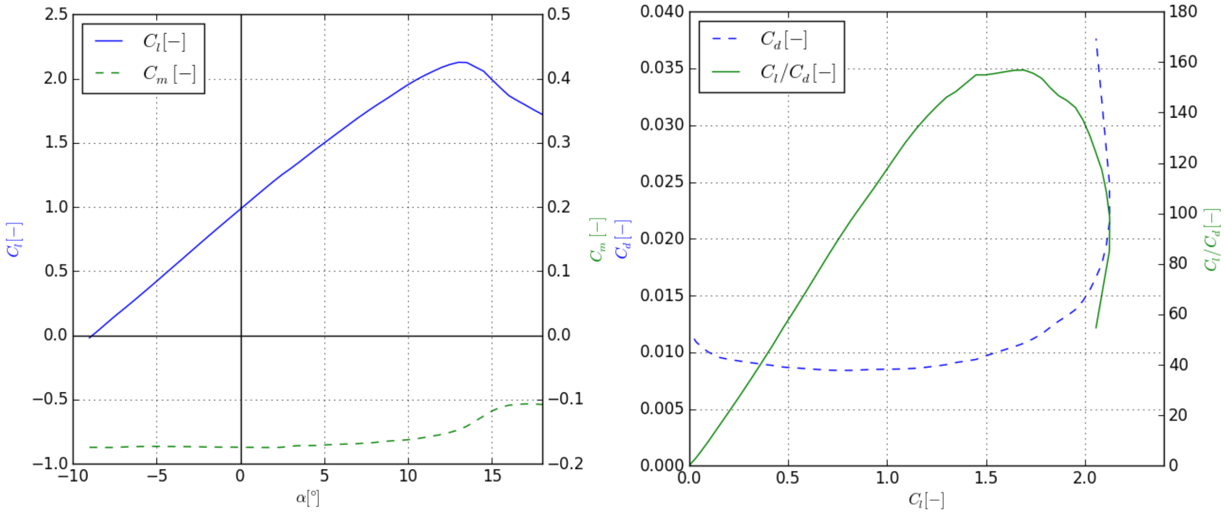

(a) Lift and moment curve (b) Drag polar

Figure 8.4: Lift, drag and moment polars for the NACA 9216-42

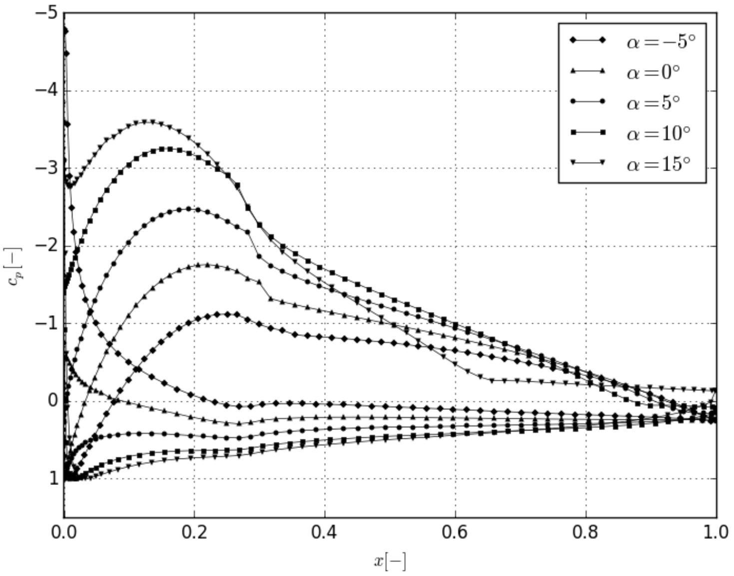

Figure 8.5: Pressure distribution for the NACA 9216-42 at different angles of attack

needed for a proper optimization can not be done with a proper 3D simulation that does not come with problematic simplifications. The 2D simulation was therefore chosen for the initial optimization step, as it can be verified and validated (see Section 8.1.3) to give reliable results for this case. Although the values need to be corrected for 3D they give qualitative results and reliable correction factors can be used to account for most 3D effects. A more in depth analysis of those effect however, is crucial, especially for a canard configuration where interaction of the two wings plays a major role in aircraft stability and safety. This follows from Chapter 14. The drag prediction is based on very crude assumptions and therefore too optimistic. For the power sizing another approach for the overall aircraft drag is used (Section 13.1).

For a canard aircraft it is essential that the canard stalls before the main wing. This means that the stall angle of the canard needs to be smaller than the stall angle of the main wing. The stall angle can be calculated from the 3D lift slope, the maximum 3D lift coefficient and the angle of attack at which the airfoil generates no lift, $\alpha_{L=0}$ using Equation 8.6.

$$\alpha_s = \frac{C_{L_{max}}}{C_{L_\alpha}} + \alpha_{L=0} + \delta\alpha_{C_{L_{max}}} \tag{8.6}$$

With $C_{L_{max}}$ calculated earlier, $\alpha_{L=0}$ can be read from the $C_l - \alpha$ plots for the two airfoils and C_{L_α} can be estimated

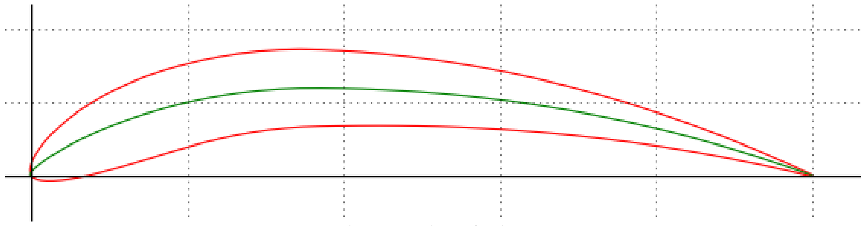

Figure 8.6: Final canard airfoil: NACA 12311-62

using Equation 8.7 with $\beta = \sqrt{1 - M_\infty^2}$ to account for the derivation from 2π caused by the finite wing effects.

$$C_{L_\alpha} = \frac{2\pi A}{2 + \sqrt{4 + \left(\frac{A\beta}{\eta}\right)^2 \left(1 + \frac{tan^2 \Delta_{0.5C}}{\beta^2}\right)}} \tag{8.7}$$

$\delta\alpha_{C_{Lmax}}$ is then found using the DATCOM methods[90] and the flight situation to lie at 0.4 for landing[90]. Inserting the values in Equation 8.7 and finally in 8.6 yields an α_s of 14.1°for the wing and 11.6°for the canard during turning flight. This means that the canard stalls before the main wing. As mentioned before this also means that the main wing does never reach its maximum C_L value. At the stall angle of the canard the main wing reaches a C_L of 1.7. The high $C_{L_{max}}$ of the canard however leads to the overall $C_{L_{max}}$ of 1.78 for landing and high-G turns. Due to it's low thickness it stalls very suddenly, ensuring that no deep stall can happen. An incidence angle of -5 is chosen for both the canard and the main wing, to allow the aircraft to fly at 0°angle of attack during level cruise flight.

The 3D correction DATCOM methods[90] were used as first estimates to calculate the requirements for the 2D aerodynamic airfoil properties. In Section 8.1.2 more advanced 3D tools are used where the results will be compared with the empirical DATCOM methods in order to verify the results.

8.1.2 WING ANALYSIS 3D

For the 3D case of a finite wing the assumption of no spanwise flow can not be made and the situation becomes more complex. This greatly affects the results that were found for 2D airfoils. The 3D effects are analyzed with different tools, which methods are discussed in Section 8.1.2. First in Section 8.1.2 the effect of design parameters and the selection of the wing planform for E-SPARC will be discussed. Then in Section 8.1.2 the assumptions used for the model tool are discussed. The final results are given in Section 8.1.2. Thereafter a discussion and recommendation will be given in Section 8.1.2. Finally, verification and validation of the tools is done in Section 8.1.3.

WING PLANFORM

The wing planform main design parameters are listed below and a description is given on the influence of the parameters. The parameters are used as input for the 3D model and a sensitivity study is performed during the 3D analysis. A final overview of wing's and canard's planform and aerodynamic properties is given in Table 8.4.

1. **Aspect ratio**; The aspect ratio mainly determines the efficiency and stall characteristics of the wing. The aspect ratio of 6 for the wing was determined from the design point in the W/S-W/P plot in the class I estimation 6.3.1. For the canard a higher aspect ratio was chosen to have the canard stall before the main wing without the drag penalty of an incidence angle. An aspect ratio of 8 was therefore chosen for the canard[87].
2. **Sweep angle**; Sweep for a canard configuration has different advantages and disadvantages than for a conventional configuration. With the rudders mounted on the wing tips, sweep increases the moment arm for directional control. For aerodynamic reasons however, sweep lowers the efficiency of the wing and has no advantage in terms of compressibility effects at the relatively low velocities of the E-SPARC. Instead, sweep increases the tendency to tip stall, which can especially be critical for the heavily loaded wing tips of a canard aircraft. Forward sweep can decrease this effect, but introduces other difficulties such as flutter. For structural and aerodynamic reasons the leading edge sweep is therefore set to zero, allowing for a straight spar parallel to the leading edge. The same is done for the canard, in order to achieve a high lift slope (Equation 8.7).
3. **Taper ratio**; The goal of introducing taper is to have a lift distribution that closely resembles that of an elliptical wing for maximum aerodynamic efficiency. The most suitable taper ratio for the E-SPARC is 0.45 [24] which results in an as much as possible elliptical lift distribution. This is confirmed later during the 3D analysis, however the wing encounters effects of the canard and wingtips. For the canard a non-tapered

Table 8.4: Main wing design parameters

Parameter	Value	Unit	Description
A_w	6	$[-]$	Aspect ratio of the main wing
A_c	8	$[-]$	Aspect ratio of the canard
i_w	-5	[°]	Wing incidence angle
i_c	-5	[°]	Canard incidence angle
b	5.56	$[m]$	Wing span
S_w	5.156	$[m^2]$	Wing area
S_c	1.14	$[m^2]$	Canard area
C_r	1.279	$[m]$	Root chord length
C_t	0.575	$[m]$	Tip chord length
MAC	0.972	$[m]$	Mean Aerodynamic Chord
$\Lambda_{w_{LE}}$	0.0	$[rad]$	Sweep at leading edge main wing
$\Lambda_{c_{LE}}$	0.0	$[rad]$	Sweep at leading edge canard
λ_w	0.45	$[-]$	Taper ratio of main wing
λ_c	1.00	$[-]$	Taper ratio of canard
Re_r	$7.5 \cdot 10^6$	$[-]$	Reynolds number at the root section of the main wing
Re_{MAC}	$5.6 \cdot 10^6$	$[-]$	Reynolds number at MAC of the main wing
Re_t	$3.0 \cdot 10^6$	$[-]$	Reynolds number at the tip section of the main wing
Re_c	$2.5 \cdot 10^6$	$[-]$	Reynolds number at the canard
$NACA\,9216-42$	$[-]$	$[-]$	Airfoil type main wing
$NACA\,12311-62$	$[-]$	$[-]$	Airfoil type canard

wing is used[87].

4. **Twist**; Tip stall can be very dangerous for a canard aircraft. The downwash of the canard leads to a decrease in wing loading at the inboard section of the main wing and an increase at the outboard section. There is an increase in the angle of attack that the wing locally sees and could therefore lead to tip stall. It also results in a loss of the main wing's lift as is explained in Section 8.1.2. If the main wing stalls before the canard, the aircraft can pitch up very fast and enter a dangerous deep stall. In order to avoid this behavior, a slight negative twist could be applied to a wing with a high torsional stiffness to have slightly less high angles of attack at the outboard section of the wing. For E-SPARC at this phase no twist is applied to the wing, since the airfoil design was such that the canard will stall before the main wing.

ASSUMPTIONS

1. The fuselage generates a lift contribution about the same as the contribution that is lost by the part of the wing that is inside the fuselage. Different experimental studies on wing-body configurations that take into account different values of span and fuselage width have demonstrated that [44]. *The maximum lift coefficient that the aircraft can reach differs within a certain limit that should be determined with a more advanced CFD tool, because the analysis tools used at this stage of the design are not able to give accurate results of the fuselage lift.*
2. No drag prediction was given based on XFLR5, since an inviscid analysis was performed. *The lift slope does not show a maximum lift coefficient and the results on drag will be inaccurate to represent the real physics, therefore an independent method will be discussed in Chapter 13.*
3. The loss in lift of the main wing due to the downwash of the canard equals the lift that the canard generates. *No extra net lift is created by the wing and the wing area is the reference area calculated from the wing loading.*

METHOD

The aerodynamic coefficients of the three dimensional wing are obtained with the DATCOM method and supported by the use of analysis tools named XFLR5 and ESDU. The 2D airfoil that was found by the genetic code was implemented in the analysis tools and simulated in a 3D analysis. An overview of the strategy used for 3D analysis and optimization is given in Figure 8.7.

Both the lift slope and maximum lift coefficient values were verified with the DATCOM methods previously described in Section 8.1.1. The 3D results are compared with the required values for design lift coefficients, as was described in Section 8.1.1, derived for steep turns and landing. If the 3D results were found not to satisfy these requirements, the geometric input parameters are modified and the design is iterated until a solution was found for the planform. A more elaborate description of each tool is given in the following sections.

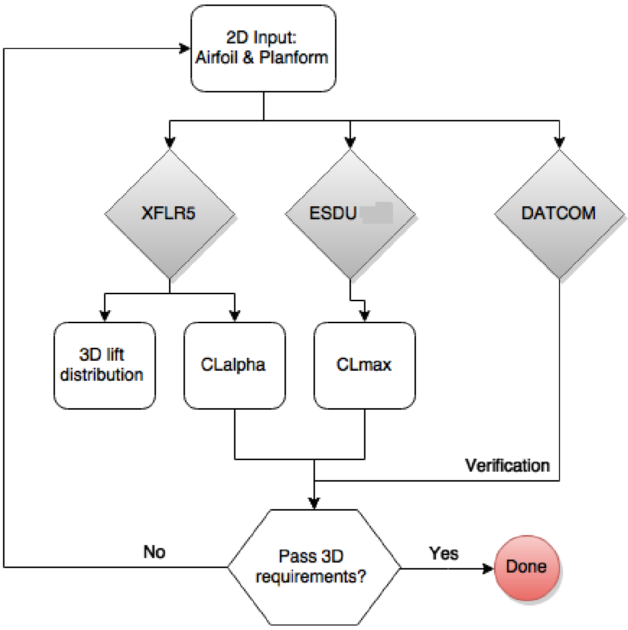

Figure 8.7: Flow chart of the 3D analysis

XFLR5

The aerodynamic analysis carried out using XFLR5 is a good starting point for contructing the desired lift distrubtion over the wing and induced drag and other planform induced effects. The values of the aerodynamic derivatives obtained using XFLR5 seem to be reasonable for the lift slope and zero-lift angle of attack. They agree with the physics of flight dynamics and therefore support the DATCOM theory. However, the analysis tool is not able to model viscous drag effects in 3D. The drag model is therefore inaccurate to predict a maximum lift coefficient and should be improved using flight data from real tests, however this was not possible in the preliminary design phase, so another tool that estimates the maximum lift coefficient was used. ESDU provided this validated engineering analysis tool. The use of it will be described in Section 8.1.2. For this reason XFLR5 served mainly to have more qualitative data in the design of E-SPARC that shows the interactions of the canard and wingtips on the wing, rather than quantitative data. As quantitative results the DATCOM method is most reliable for E-SPARC. The analysis will identify potential problem areas, for example the shape of the canard and winglets that might have adverse or desired effects on the aerodynamic efficiency of the aircraft.

XFLR5 is able to use different methods to calculate the lift distribution, the difference in the methods is mainly the viscous part of the analysis. The three methods that the analysis tool can simulate are the Lifting Line Theory (LLT), the Vortex Lattice Method (VLM1) and a 3D panel method analysis. The VLM is a extension of Prandtl lifting line theory, where the wing of an aircraft is modeled as an infinite number of Horseshoe vortices. Therefore the VLM method was used for E-SPARC aerodynamic analysis because the results represent a more precise simulation. VLM divides the lifting surfaces into a fine mesh of panels. The user is able to refine this mesh as much as possible, however increasing the amount panels will not give better results after a while because the computer converges to the same values and it will only take much longer time to calculate. Each panel is surrounded by a horseshoe vortex, that extends from the chord length to infinity. With a few boundary conditions the tool is able to calculate the lift contribution of each vortex. It then sums up all the vortices to have a result of the performance of the whole surface that was given as input by the user.

ESDU maximum lift coefficient

For the calculation of maximum lift coefficient the engineering tool ESDU 93015 provided by IHS ESDU was used, which is written for the calculation of maximum lift coefficients of plain modern aerofoils and wings at subsonic speeds. For 3D wings ESDU 89034 is used which was given by the author to generally compute the maximum lift coefficient within 10% of accuracy. It uses ESDU 84026 for 2D airfoils which was verified with a standard deviation of 0.08 [92]. The program combines the above mentioned engineering tools for aerofoils (2D) and wings (3D) at different span-wise sections as input together with corresponding Reynolds numbers. The method uses empirical formulas for airfoil calculations, based on parameters such as nose sharpness and maximum thickness. Empirical corrections are applied for sweep, taper, aspect ratio and twist effects and for the influence of Mach number and Reynolds numbers in order to calculate the $C_{L_{max}}$ of the 3D wing. The method was tested against wind-tunnel data for a wide range of wing geometries [92].

3D RESULTS

As already discussed in the previous section, for the determination of the aerodynamic coefficients of the wing and canard the DATCOM method is used as basis. Furthermore XFLR5 and ESDU are used to verify these results and support the data. The analytical results from DATCOM are summarized in Table 8.5 and the equations that are used are given in the verification Section 8.1.3.

Table 8.5: Analytical results of aerodynamic coefficients from DATCOM

	Maximum lift coefficient	**Lift slope**	**Stall angle**
DATCOM	1.78	4.71 $[rad^{-1}]$	12.45 [°]

The aerodynamic coefficients that were used from the 3D analysis tool XFLR5 are the lift slope of the wing and canard together, the zero lift angle of attack and quantitative results that show the interaction of the canard and vertical wingtips on the wing. The same airfoil was used over the whole wing span in all sections. The lift slope and zero lift angle of attack are shown in Figure 8.8, however this figure does not show a maximum lift coefficent, since XFLR5 performed an inviscid analysis. For the calculation of the maximum lift coefficicent an ESDU tool was used as was explained in Section 8.1.2. The final results found with this tool are given in Table 8.6. The lift slope was taken 2/3 of the total range of angles of attack, from -8.2 to 4 degrees, because in the high angle of attack regions the program normally underestimates the decrease in lift [93].

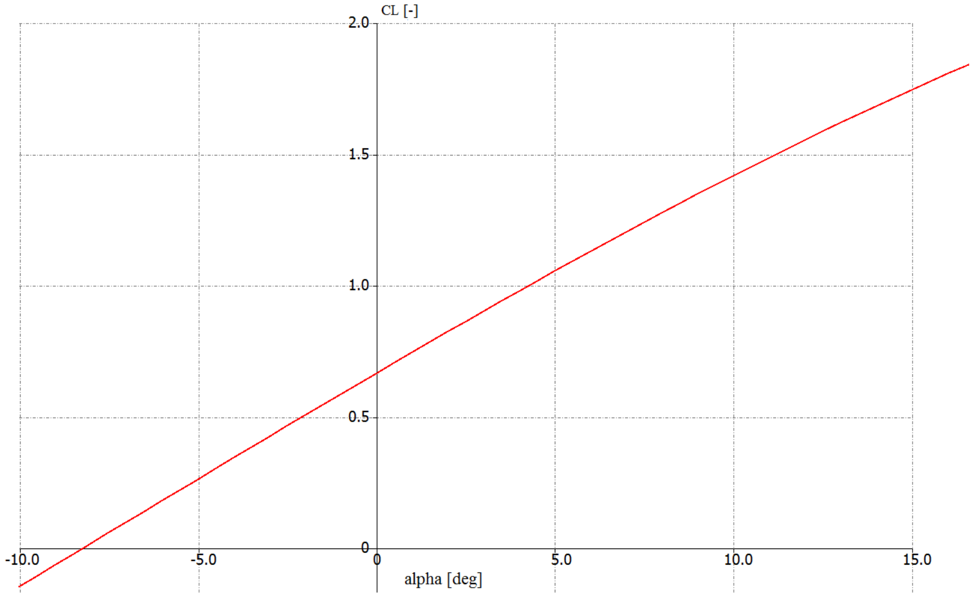

Figure 8.8: Lift slope and zero-lift angle of attack of wing and canard in XFLR5

Table 8.6: Zero-lift angle of attack and lift slope results from XFLR5

	Zero-lift angle of attack	**Lift slope**
XFLR5	-8.2 [°]	4.69 $[rad^{-1}]$

The Reynolds numbers are different for each section of the wing, because they are dependent on the local chord length. The free stream speed was taken 85 m/s, as this is the turning speed of the aircraft for which it is designed and is most constraining. The Reynolds number at the root is around $7.5 \cdot 10^6$ and at the tip $3 \cdot 10^6$ for the main wing. The canard encounters Reynolds number around 2.5E6. Figure 8.9 shows the effect of the wingtips in obstructing the airflow going from the lower to the upper side of the wing. The wing is analyzed in XFLR5 for angles of attack between -10 and 20 degrees. The figure is given at an angle of attack of 12 ° since this best represents the flow close to the stall angle that was calculated with DATCOM. The 3D values for C_L will reach the required value as was set as criteria for the turning performance at 10g. Only at the top of the wingtip there is a small flow going to the outboard sections of the wing. The canard has no wingtips and here the vortex flow is clearly visible going from lower to upper side. These vortices greatly affect the inboard sections of the main wing. These sections straight behind the canard show lower pressure areas at the leading edge. Also the vortex that the canard introduces makes the flow behind it very turbulent resulting in locally high pressure gradients on the wing leading edge. This is better shown in Figure 8.10, but it should be kept in mind that this figure serves as qualitative results to show the interactions rather than quantitive since the flow is simulated inviscid.

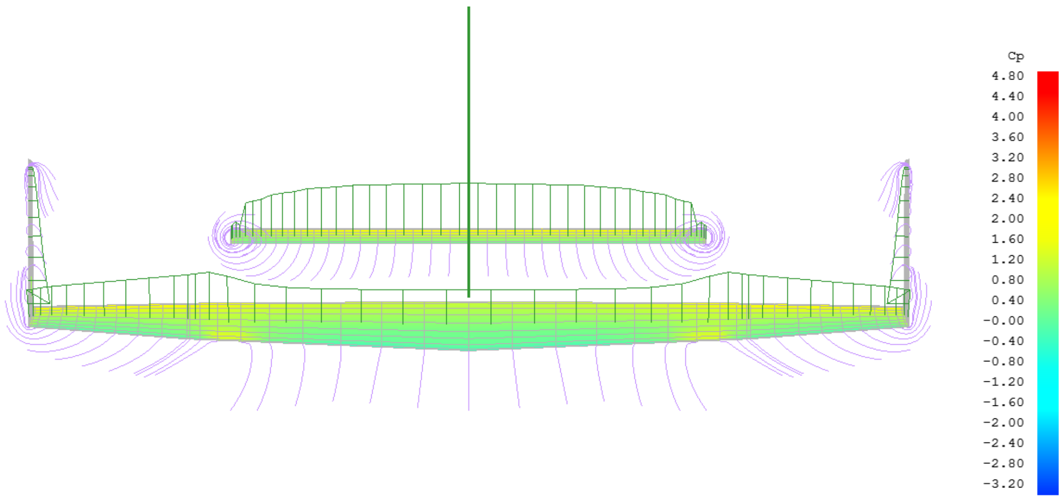

Figure 8.9: Qualitative results showing the effect of wingtips on induced drag at α= 12 °

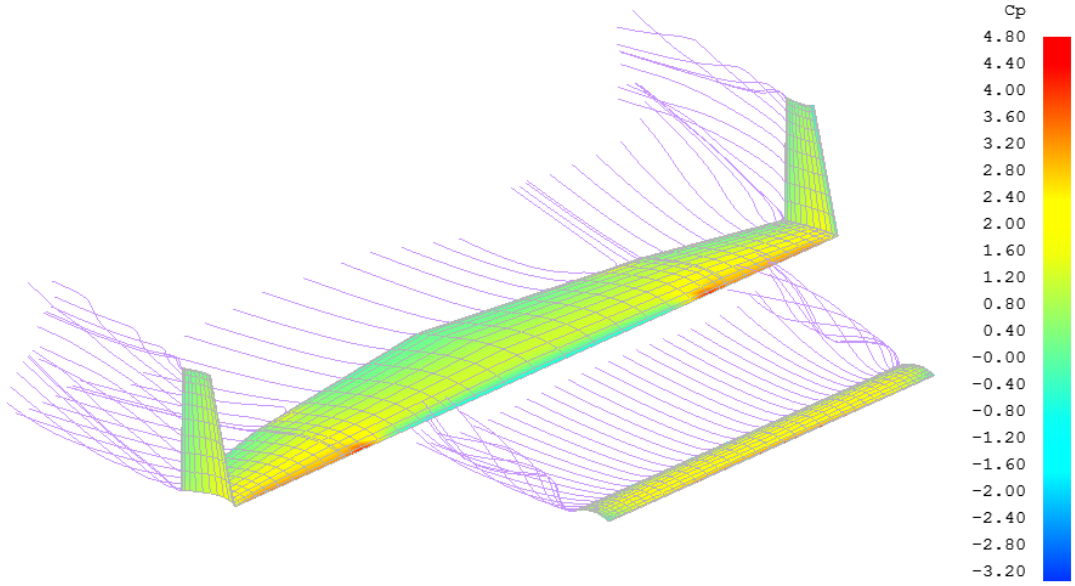

Figure 8.10: Qualitative results showing the interaction of the canard on the main wing at α= 12 °

The ESDU method calculated the maximum lift coefficient and the zero-lift angle of attack. The 2D airfoil coordinates, the wing aspect ratio, taper ratio and the Mach number at race condition were given as input values. As output the maximum lift coefficient was given for a range of different Reynolds numbers. The Reynolds number corresponding to the MAC position of $5.6 \cdot 10^6$ was taken. As explained before, both main wing and canard produce positive lift in a canard configuration. This comes with a downside however, namely the decrease in efficiency of the main wing caused by the downwash of the canard. The air is deflected downwards by the canard and the effective angle of attack at the main wing therefore decreases, generating less lift. As a result the elliptical lift distribution decreases on the inboard section of the main wing as can be seen in Figure 8.11. The quantitative results are given in Table 8.8. An XFLR5 analysis is run to compare the two cases of a wing without downwash and a second wing with a canard in front. From the analysis it is concluded that the loss in main wing lift due to the downwash almost equals the lift generated by the canard. The main wing is therefore sized to carry

Table 8.7: Zero-lift angle of attack and maximum lift coefficient results from ESDU

	Zero-lift angle of attack	**Maximum lift coefficient**
ESDU (93015)	-7.96 [°]	1.72 [-]

the entire required lift, assuming that positive lift of the canard and lift losses due to downwash are equal. The required total lifting surface area is therefore 5.17 m^2 for the wing as a result from the wing loading and 1.14 m^2 for the canard, using the factor $\frac{S_h}{S}$ = 0.22 from the stability analysis. This confirms the earlier assumption that the canard avoids negative control lift, as produced by a horizontal tail. No extra net lift however is generated by the canard as the negative effect on the main wing equals the lift from the canard.

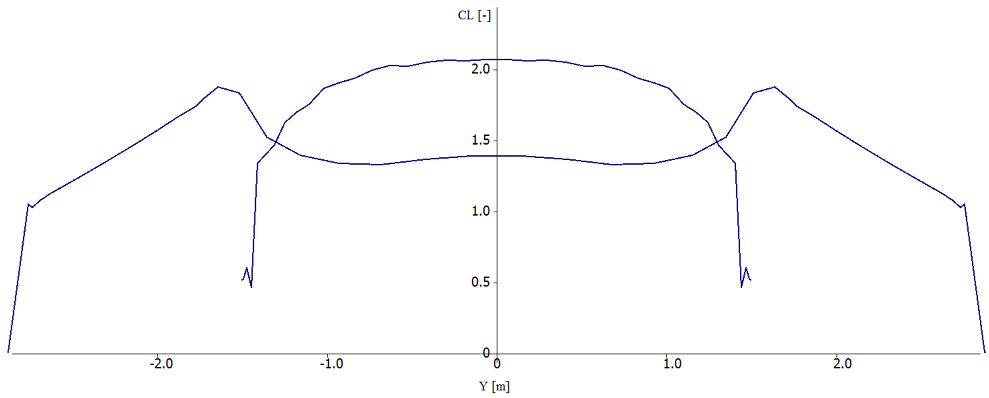

Figure 8.11: Lift distribution of the wing and canard at α= 12 °

Table 8.8: Lift coefficients as a function of the wing span for the wing and canard

Wing	x[m]	0	0.5	1.0	1.5	2	2.5	2.84
	C_L	1.4	1.3	1.35	1.8	1.6	1.3	0
Canard	x[m]	0	0.5	1.0	1.5	1.52	-	-
	C_L	2.1	2.0	1.86	1.2	0	-	-

DISCUSSION & RECOMMENDATION

The validation data does not coincide perfectly with the numerical solution obtained from DATCOM, the chosen analysis tool should be discussed to check if deviations from reality and on DATCOM can be explained. Also recommendation for further design will be proposed.

All methods predict a value close to reality for the zero-lift angle and the lift slope in 3D and give a rather good estimation of the lift distribution on the wing and canard. However the methods underestimate the decrease in lift at high angles of attack. Also the viscous drag is underestimated more than the induced drag and could be due to several reasons. First, the VLM algorithms computes the lift coefficient, moment coefficients and the center of pressure's position in a 2D analysis (Xfoil). Then the viscous variables from the 2D analysis are extraplated from the C_l value of the previously XFoil-generated polars in the 3D analysis. This raises the issue that the value can run out of the flight envelope, because the Reynolds numbers are too high for the given C_L value in 3D. Secondly, the flow transitions from laminar to turbulent at some point along the wing's chord could be wrong determined, because inadequate values for N_{crit} are used in Xfoil polar mesh. This explains the limitation to use XFLR5 for refined drag estimations, however it gives a rather good prediction on the lift distribution of the wing and canard and is therefore be used to support DATCOM.

In the analysis it is assumed that the part of lift that the fuselage will generate is the about the same contribution of the part of the wing that is mounted into the fuselage. Based on this assumption the fuselage-wing interaction was not considered in the analysis of XFLR5. In reality the influence of the fuselage on the characteristics creates an extra upwash induced by the presence of the fuselage at the wing root sections of the wing. Also in case of a side slip angle, dependent on the wing position, the left and right wing experience different angles of attack. This creates a rolling moment, which is an important characteristic for the stability of the aircraft. In the detailed design, a more advanced CFD analysis could also help to refine the design and verify the analysis tools that were used at this stage. Thereafter the data predicted should be validated against results from its first flight test as is also specified in the Project Design & Development (PDD) logic.

The zero leading edge sweep helps to avoid tip stall. Without sweep less spanwise flow can develop and the wing tips are less heavily loaded. The downwash of the canard at the inboard section of the main wing however, might still lead to a higher tip loading and tip stall tendency. It is recommended to test this behavior in a CFD analysis combined with a FEM model to analyze the influence of wing twist angles. If tip stall should turn out to be problematic, a small twist angle of about -2° can be used. For the design this relatively minor change does not pose a major challenge, as the carbon fiber wings allow for much shape freedom. The small twist can also help to distribute the wing loading over the main wing in the canard downwash more evenly.

8.1.3 VERIFICATION

In order to verify the tools that were used during the 2D optimization and 3D analysis, different verification approaches are used. An overview of the final results of the three different methods is given in Table 8.10.

XFoil

The aerodynamic calculations from XFoil based on panel methods can not easily be verified by analytical calculations that would be beyond the scope of this report. Instead the calculations are validated using lift and drag polars for the same airfoils made available from NASA[94]. Those polars are based on experimentally obtained data from the Langley two dimensional low turbulence wind tunnels. Lift and drag polars for a NACA-4 series airfoil (4415) are compared to the XFoil polars for the same airfoil calculated at the same Reynolds number. Besides very accurate C_m values show the predicted underestimation of drag and overestimation of maximum lift coefficient. All discrepancies however, are within 10% error margin and the graphs match closely in terms of shape and slope.

Genetic algorithm

The convergence of the code is verified using multiple runs to make sure that they converge to the same result and that the procedure is repeatable. This verifies the assumption that the global optimum for the given optimization function is found and the algorithm does not get stuck in a local maximum for the fitness (Equation 8.5). The script is run five times for a population size of 20 and 100 iterations each, to see whether each run would yield the same result. Table 8.9 presents the airfoils chosen by the program in the five different runs and their aerodynamic properties and fitness. The airfoil is presented as its genetic code in the format:

$$\left[\text{Camber, Camber pos., Max thickness, LE radius, Pos. of max thickness}\right]$$

as explained in Section 8.1.1. It can be seen that the algorithm only converges to the same airfoil for Run 2 and Run 3. The fourth run results in a very similar airfoil with only slight differences in thickness, max thickness location and nose radius. The first run deviates a bit more and the fifth run final selects an airfoil with very different parameters such as higher drag during high-G turns and lower drag for level racing conditions and cruise. The script converges to the same or similar airfoils and therefore has a sufficient reliability for a good optimization. It should be kept in mind however, that the procedure is not 100% repeatable. It is therefore advised to run it with more iterations or a higher mutation rate to make sure that it covers the whole design space and finds the global optimum.

Table 8.9: Optimization results for five independent runs

Parameter	Run 1	Run 2	Run 3	Run 4	Run 5
Airfoil	$[9,3.0,15,3.8,2.6]$	$[9,2.6,13,5.5,3.3]$	$[9,2.6,13,5.5,3.3]$	$[9,2.6,12,4.4,2.9]$	$[4,8.4,9,3.9,2.4]$
$C_{l_{max}}$	2.15	2.12	2.12	2.12	2.11
C_m at $C_{l_{max}}$	-0.15	-0.15	-0.15	-0.15	-0.1
C_d at $C_{l_{max}}$	0.021	0.017	0.017	0.018	0.039
C_d at $C_{l_{levelrace}}$	0.0086	0.0089	0.0089	0.0091	0.0066
C_d at $C_{l_{cruise}}$	0.0081	0.0083	0.0083	0.0082	0.0075
Fitness	1.74	1.76	1.76	1.76	1.65

XFLR5

The verification process of XFLR5 determines if the simulation is simulating the problem correctly. Especially in the analysis of aerodynamics of wings and body the results are likely to differ from reality, because the physics are very complex and include a lot of uncertainties and errors. Uncertainties are deficiencies due to lack of information about the system. For example unanticipated behaviour of the flow due to the interaction of fuselage and wing, or the interaction of the canard on the wing. Errors are deficiencies due to approximations used, for example because sub-models have been used for phenomena which are difficult to compute. The model no longer represents the real physical system anymore and is just a prediction based on a system of horseshoe vortices with boundary conditions. Due to the time scope of this project it was not possible to carry out a full verification of the tool by analytical calculations. The methods used for calculating the maximum lift coefficient, the lift slope and the stall angle however are verfied using DATCOM methods (Equations 8.8 to 8.10).

DATCOM

The DATCOM verification values are analytically computed using Equations 8.8 to 8.10, that were already used for the estimation of the required 2D values in Section 8.1.1. Equation 8.8 calculates the 3D maximum lift coefficient from the earlier determined 2D airfoil lift coefficient. It uses correction factors for geometric and flow-related 3D effects[90]. Similarly, the 3D C_{L_α} is determined in Equation 8.9. Finally the stall angle α_s is calculated from the 3D lift curve using this lift slope that was just calculated. The $C_{L_{max}}$ and zero lift angle of attack $\alpha_{L=0}$ use the correction factor $\delta\alpha_{C_{L_{max}}}$ from [90].

$$C_L = \left[\frac{C_{L_{max}}}{C_{l_{max}}}\right] C_{l_{max}} + \delta C_{l_{max}} = [0.9]\cdot 2.1 - 0.11 = 1.78 \tag{8.8}$$

$$C_{L_\alpha} = \frac{2A\pi}{2+\sqrt{4+\left(\frac{A\beta}{\eta}\right)^2\left(1+\frac{tan^2\Delta_{0.5C}}{\beta^2}\right)}} = \frac{2\cdot 6\cdot 1.2\pi}{2+\sqrt{4+\left(\frac{6\cdot 1.2\cdot 0.97}{0.95}\right)^2\left(1+\frac{tan^2 0}{0.97^2}\right)}} = 4.71\ rad^{-1} \tag{8.9}$$

$$\alpha_s = \frac{C_{L_{max}}}{C_{L_\alpha}} + \alpha_{L=0} + \delta\alpha_{C_{L_{max}}} = 57.3\cdot\frac{1.78}{4.71} - 8 - 1.2 = 12.45° \tag{8.10}$$

The simulated values from XFLR5 and ESDU differ from DATCOM results by less than 10%. This was also tested for other wing geometries and Reynolds numbers. The results from XFLR5 and ESDU 93015 are presented together with the DATCOM results in Table 8.10 and can taken as verified at this phase of the design.

Table 8.10: Verification of lift calculations with DATCOM methods

Method	$C_{L_{max}}$ [-]	C_{L_α} $[rad^{-1}]$	$\alpha_{C_{L0}}$ [°]	α_s [°]
XFLR5	[-]	4.69	-8.2	[-]
ESDU (93015)	1.72	[-]	-7.96	
DATCOM	1.78	4.71	[-]	14.0
Difference	3.37 %	1.26 %	2.93 %	[-]

8.1.4 VALIDATION STRATEGY

For validation experimental data of a first flight test should be compared with the results that XFLR5 gives. However, since modelling of viscous effects is the biggest uncertainty of this program, a more advanced CFD simulation tool is adviced to use in the detailed design phase. Also wind tunnel tests on model scales of the aircraft could be done to validate the analysis tools.

8.2 STRUCTURAL DESIGN

In this section the structural design of the wing will be examined. To make a model some assumptions have to be made, these are listed in Section 8.2.1. Section 8.2.2 explains the method that was used to construct the model and design the wing. The results can be found in Section 8.2.3. The wing will be constructed as one big sandwich panel with a foam core and a carbon fiber reinforced polymer (CFRP) facesheet. The sandwich panel design is chosen because there is no fuel that has to be stored in the wings. This means that the wing is almost empty except for some connections from the control stick to the control surfaces. The minimal facesheet thickness is assumed to be 0.5 mm. This differs from the minimal facesheet thickness that is used in the fuselage design in Chapter 11. This is because impact has less influence here because it is a sandwich panel. Since there is a foam core, there is less need for a thick facesheet to resist impact damage, because the foam core also has some resistance against impact.

8.2.1 ASSUMPTIONS

To make an analytical model, some assumptions are necessary. These assumptions are listed here. The impact that they will have on the model is also explained.

- Constant lift distribution. *The true lift distribution of the wing by itself is elliptical but due to the canard the lift in the middle of the wing is lower and the winglets increase the lift at the wingtips. This means that the true lift distribution of the wing in the complete aircraft will not be that different from a constant lift distribution.*
- The drag of the fuselage and the wing in chordwise direction is neglected. *At the speeds that E-SPARC will encounter, the drag will be small compared to the lift. Therefore there will be no big differences.*
- The CFRP facesheet carries all the loads. No loads are carried by the foam. *In reality, the foam will carry a small amount of the shear loads. This amount is so small that the wing will only be slightly over designed when assuming it does not carry loads. This means that the only function of the foam core is to prevent local buckling of the facesheet.*
- The wing is modelled as a box. with a symmetrical and rectangular cross-section. *This means that the values used for area and moment of inertia used for these calculations will be lower than the actual values. This will result in a wing that is slightly over designed.*
- The deflections resulting from the loads are negligible *There will be some deflections but they will all be small.*
- Only static loads were taken into account.

8.2.2 METHOD

The methods for the analytical model for the design of th wing and the canard are very similar. The outline of this tool can be seen in Figure 8.12. There are some small differences between both models. First of all, the chord of the canard is constant which means that there is no equation for C(x) needed. A second difference is that the elevator spans the whole canard, unlike the aileron which has a smaller span than the main wing. This results in a different torsion distribution. The starting point is to calculate all the loads that are acting on the wing.

Loads

First of all, the loads acting on the wing have to be calculated. There are several loads that constrain the wing design:

- Bending moment
- Shear force
- Torsion

The lift force is constant over the whole wing. This means that $L(x) = L_0$ and L_0 is calculated with Equation 8.11.

$$W_{ac} = 2 \cdot \int_0^{b/2} L_0 \, dx \tag{8.11}$$

This results in a constant lift distribution of 16059 N/m. The weight distribution is calculated in more or less the same fashion, except for the assumption that the weight varies parabolicaly with chord. The weight distribution can be calculated by stating that $w(x) = \lambda * C(x)^2$. Then λ can be calculated using Equation 8.12.

$$W_{wing} = 2 \cdot \int_0^{b/2} \lambda \cdot C(x)^2 \, dx \tag{8.12}$$

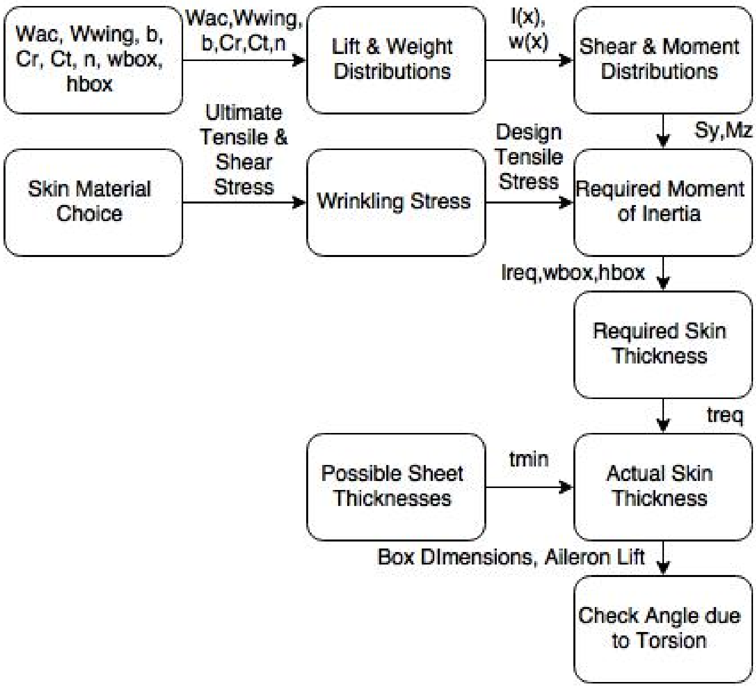

Figure 8.12: Flow diagram of the analytical wing model

In order to calculate this, a function for C(x) is needed as well. This function is found to be:

$$C(x) = C_r oot - x \cdot 2 \cdot \frac{C_{root} - C_{tip}}{b} \tag{8.13}$$

Using these lift and weight distributions, the shear and moment forces can be calculated.

$$q(x) = \frac{dS_Y(x)}{dx} \Leftrightarrow S_Y(x) = \int q(x)dx \tag{8.14a}$$

$$S_Y(x) = \frac{dM_Z(x)}{dx} \Leftrightarrow M_Z(x) = \int S_Y(x)dx \tag{8.14b}$$

With Equations 8.14a and 8.14b the shear and moment forces due to both the lift and weight of the wing can be calculated. In order to obtain the total shear and moment force, these need to be summed.

$$S_{Y,total} = S_{Y,lift} + S_{Y,weight} \tag{8.15a}$$

$$M_{Z,total} = M_{Z,lift} + M_{Z,weight} \tag{8.15b}$$

Based on these shear and moment forces, a required moment of inertia can be calculated. This moment of inertia will vary with the local chord.

$$I_{req,shear} = \frac{S_{Y,wing} \cdot h_{box}}{(4 \cdot \tau_{max,face}) \cdot (w_{box} + h_{box}/2)} \tag{8.16a}$$

$$I_{req,moment} = \frac{M_{Z,wing} \cdot h_{box}}{(2 \cdot \sigma_{design,face})} \tag{8.16b}$$

It is known that for a rectangle: $I = \frac{b \cdot h^3}{12}$. Based on this and Equations 8.16a and 8.16b the required facesheet thickness can be calculated.

$$t_{req} = \frac{12 \cdot I_{req}}{h_{box}^2 \cdot (2 \cdot h_{box} + 3 \cdot w_{box})} \tag{8.17}$$

The aileron will induce some torsion in the wing. To make sure that the deformation resulting from this torsion is acceptable the angle of the wing at the tip is calculated. The aileron has a chord of 25% of the local chord. Since the wing box spans from 0.2 of the chord to 0.75 of the chord, the torsion arm ($r_{L,aileron}$) is always $0.4 \cdot C(x)$. The extra lift that the aileron generates is assumed to be constant over the span of the aileron. This constant can be calculated by Equation 8.18.

$$l_{0,aileron} = \frac{\Delta L_{aileron}}{b_{aileron}} \tag{8.18}$$

It is known that the torsion is calculated by $T = F \cdot d$. In this case F is the shear force generated by the lift of the aileron and d is the torsion arm. To calculated the shear force due to the lift, Equation 8.14a can be used. This yields Equation 8.19.

$$T(x) = r_{L,aileron} \int l_0 dx \tag{8.19}$$

This equation applies for x-positions between the beginning and the end of the aileron. On the inboard side of the aileron, the torsion is equal to the torsion at the last position of the aileron and on the outboard side the torsion is equal to zero. Now that the torsion is known, the angular deflection in the wing can be calculated with Equation 8.20.

$$\theta = \frac{1}{G} \int \frac{T(x)}{J(x)} dx \tag{8.20}$$

In Equation 8.20 the term J is the polar moment of inertia. This constant can be approximated by Equation 8.21 [95].

$$J \approx ab^3 \left(\frac{1}{3} - 0.21 \frac{b}{a} \left(1 - \frac{b^4}{12a^4} \right) \right) \tag{8.21}$$

Failure Modes

There are several failure modes that could be critical.

- Facesheet strength failure (compressive/tensile)
- Facesheet wrinkling
- Adhesive failure

Facesheet failure will not be fatal to the sandwich panel because the required thickness is calculated based on the maximum stress of the facesheet material.

To prevent facesheet wrinkling, the stress in the facesheet should be lower than the wrinkling stress. Because the foam core is rather thick (thicker than 5 mm) it can be assumed that asymmetric wrinkling will not be the most critical case. The symmetric wrinkling stress can be calculated with Equation 8.22.

$$\sigma_{wr} = 0.43 \cdot (E_f \cdot E_c \cdot G_{xz})^{1/3} \tag{8.22}$$

Ideally, this wrinkling stress would have to be higher than the ultimate stress of the facesheet material. To achieve this, the Young's and Shear modulus of the core have to be so high, that the density of the core is also high and thus the core would not be lightweight. Therefore a compromised value for the wrinkling stress was accepted. This value of 264 MPa will be used for all calculations instead of the ultimate tensile stress of the facesheet material which is 440 MPa.

8.2.3 INPUTS AND RESULTS

In this section the results from the method as explained in Section 8.2.2 will be shown. Firstly the input values can be seen in Table 8.11. The material properties that were used for the calculations can be seen in Table 8.12.

INPUTS

Table 8.11: Input parameters

(a) Wing design

Parameter	Value	Unit
Mass of the aircraft	414.95	$[kg]$
Mass of both wing (from Class II)	50.74	$[kg]$
Mass of both winglets (from Class II)	2.98	$[kg]$
t/c-ratio	0.16	$[-]$
Wing area	5.156	$[m]$
Radius of the fuselage	0.5	$[m]$
Ultimate load factor	18	$[g]$
Root chord	1.279	$[m]$
Tip chord	0.575	$[m]$
Begin of aileron (from centerline)	0.8	$[m]$
End of aileron (from wing tip)	0.14	$[m]$
Chord ratio of aileron vs wing	0.25	$[-]$

(b) Canard design

Parameter	Value	Unit
Mass of the aircraft	414.95	$[kg]$
Mass of the canard (from Class II)	21.83	$[kg]$
t/c-ratio	0.11	$[-]$
Wing area	1.14	$[m]$
Radius of the fuselage	0.086	$[m]$
Ultimate load factor	18	$[g]$
Chord	0.3775	$[m]$
Begin of elevator (from centerline)	0.086	$[m]$
End of elevator (from wing tip)	0	$[m]$
Chord ratio of elevator vs wing	0.4	$[-]$

Most of these values are outputs from the aerodynamic design of the wing as presented in Section 8.1. This includes the t/c-ratio, the chord and the wing span.

The size of the aileron and the elevator is an output of the stability and control department. These will be presented in Chapter 14.

Table 8.12: Material properties of the facesheet and the core material as seen in EduPack

Parameter	Facesheet	Core	Unit
τ_{max}	372.32	0.45	$[MPa]$
σ_{max}	440	0.45	$[MPa]$
E	69 000	84	$[MPa]$
G	28 000	40	$[MPa]$
ρ	1 500	40	$[kg/m^3]$
cost	31.1	18.6	$[€/kg]$

RESULTS

When using these input values and material properties, a required thickness can be calculated with the formulas from Section 8.2.2. The results can be seen in Figure 8.13. It can be seen that the moment is the most constraining. This is because instead of the material ultimate tensile and compressive stress, the wrinkling stress was used as a maximum stress and the wrinkling is only about 60 % from the material ultimate stress. Note that this graph only shows the part of the wing that is not in the fuselage. Therefore the graph begins at the edge of the fuselage. Also, a check for torsion was performed to ensure that the angle at the tip is not too big. When using the torsion

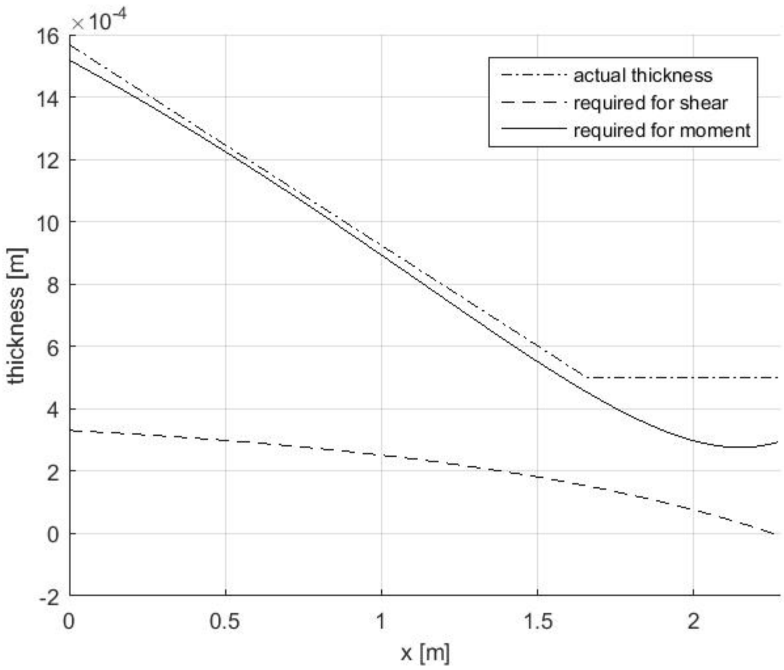

Figure 8.13: Actual and required facesheet thickness vs spanwise position for the wing

equations in Section 8.2.2. These equations result in an angle θ at the wing tip of 0.0087 rad or 0.49°.

With the thickness of the facesheet known, the mass and thus the cost of the wing can be calculated. At this point only the mass of the simplified box will be calculated as an indication of what the actual wing will weigh, it is still to be considered as a very rough estimate. The mass can be calculated by simply multiplying the volume with the density from Table 8.12. This is done for both the core and the facesheet, summing them results in the mass of one wing.

WING FUSELAGE CONNECTION

As part of requirement ESP-MIS-018 E-SPARCs wings should be detachable for transportation. Therefore the wing-fuselage integration should provide the possibility to detach the wings. A detailed design of the wing-fuselage connection is beyond the scope of this project and impossible to perform without numerical methods,

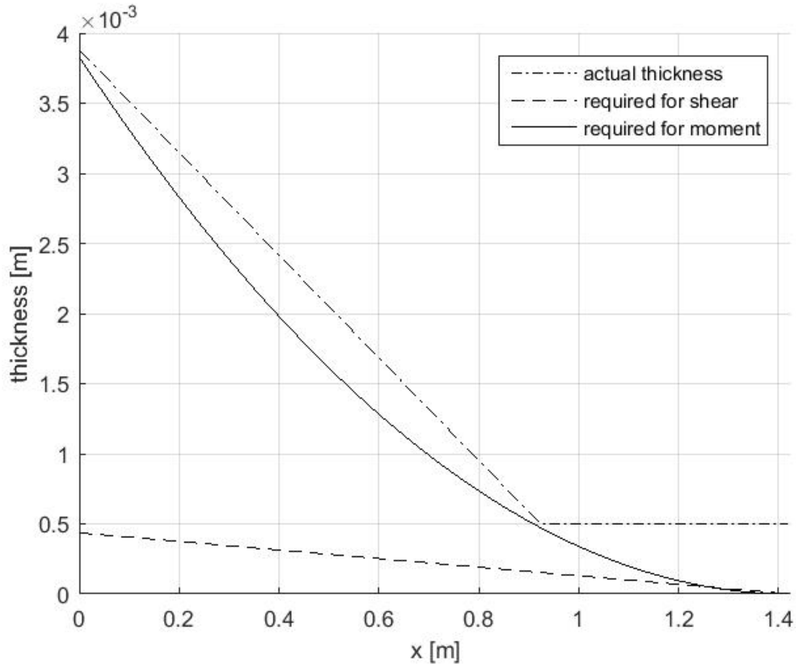

Figure 8.14: Actual and required facesheet thickness vs spanwise position for the canard

Table 8.13: Mass and cost of the core, facesheet and the total wing and canard (These values are only for one wing)

	Wing		Canard	
	Mass	**Cost**	**Mass**	**Cost**
Facesheet	4.19 kg	€130.25	1.68 kg	€52.2
Core	6.57 kg	€122.3	0.5 kg	€9.17
Total	10.76 kg	€252.55	2.17 kg	€61.39

however, Figure 8.15 shows technical drawings of the current concept for the connection.

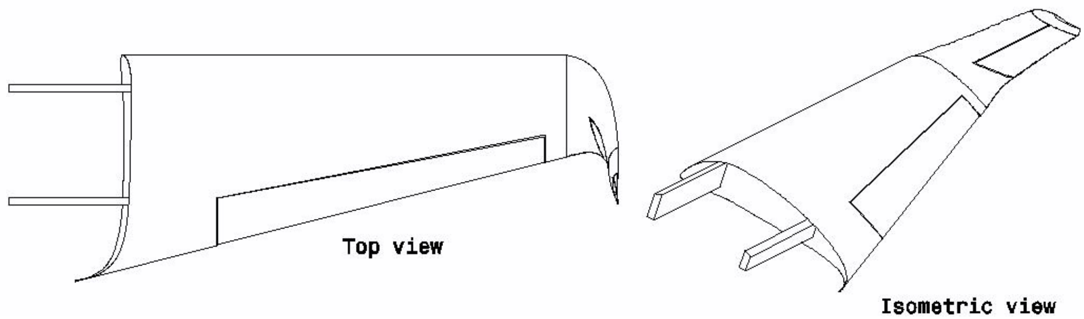

Figure 8.15: Technical drawing of conceptual wing fuselage connection

The basic idea is that both wing will have two parallel spars that extend from the edge of the wing into the fuselage. The length of the spars from the root of the wings should be slightly larger than the fuselage radius, which results in a overlap of the spars from the left and right wing in the middle of the fuselage. Using bolts the spars from both wings can be connected, resulting in two uninterrupted equivalent spars connecting both wings through the fuselage. The spars also partially extend into the wing along the front and back skin of the wing box.

The reason to have two spars instead of one per wing extending into the fuselage is in order to improve the torsional stiffness of the connection. Structurally, it would be ideal to have the complete sandwich panel wing box extend into the fuselage, however, the combination of low fuselage volume and high battery volume make this an infeasible option. The reason to have the wings detach separately instead of in one piece is that the wing span in larger than the fuselage length, which would mean the required container size for transportation is determined by the span instead of the fuselage length.

RECOMMENDATIONS

- In order to get more precise results, the exact area and moment of inertia of the airfoil can be calculated. This will result in slightly different required thicknesses. In the current design, the thickness is calculated by expressing the moment of inertia as a function of thickness. Therefore it is not useful to get these values from a modeling program.
- The simplified wing was designed using a quasi-isotropic CFRP. To get a more optimized design, the plies can be oriented in a more desirable way. This will result in a higher maximum stress and Young's modulus in a certain direction which will result in a lighter structure.
- If the aileron sizing would be carried out in more detail, the torque it creates would be more precise which would result in a more precise estimate of the deflection angle of the wing.
- A first concept of the wing-fuselage connection is provided above, during later design stages, using more elaborate methods, a proper structural design for this connection should be made. Also, a elaborate trade-off should be performed in order to definitively determine the wing-fuselage connection concept.
- It has to be checked whether the canard fits in a regular transportation container. If this is not the case, the canard will also have to be detachable.

8.2.4 VERIFICATION AND VALIDATION

The design of the wing and canard is done with an analytical MATLAB-tool. This tool needs to be verified and validated. This section contains the verification methods that were used and some plans for possible validation strategies.

One of the ways in which the tool is verified is by doing a simple sanity check on all the results. This includes for example checking that the shear force due to the lift at the root is exactly half of the total amount of lift acting on the wing. It can also be checked that the shear force due to the lift at the tip of the wing is exactly zero.

Another verification strategy is based on a sensitivity analysis. This means increasing and decreasing major input parameters such as the total lift or the weight of the aircraft to see whether the result is as expected. If the total weight of the aircraft is doubled, it can be seen from the results in the program that the total lift doubles as well which doubles the shear force due to the lift. This is exactly what was expected to happen.

Validation can only be done when test pieces are produced. The first test that will have to be performed is testing the material itself to make sure that its properties are the same as they are assumed in the model. This can be done by making a simple square panel and testing it until it fails.

After the material properties are validated, the wing and canard will have to be validated as well. This is done by building them and doing a stress test which simulates the actual loading to see how the structure behaves and if it behaves as expected. If this test is successful, a destructive test can be done to check the ultimate loads that the structure can withstand.

9 Stabilizer Sizing and Stability

The empennage of the aircraft incorporates the stabilizers that shall provide the aircraft with aerodynamic stability and make it controllable during flight. Both the canard and the vertical stabilizer are considered in this design. Also, the vertical and horizontal stabilizers house important control surfaces.

9.1 Horizontal Stabilizer Design and Longitudinal Stability

The horizontal stabilizer is used to provide a lift force to allow for pitch control. Additionally, the aircraft needs to be controllable and, if possible, aerodynamically stable. As will be shown, this is a challenge because of the canard configuration. However, since the aircraft is designed for aerobatic racing and the pilot is assumed to give constant control inputs, a marginally stable or even slightly unstable aircraft is accepted in this stage of the design.

9.1.1 Design Approach

In order to design the canard, the stability characteristics of the aircraft have to be considered. Thereby, the location of the centre of gravity plays an important role, since both lateral and longitudinal motions will be performed around that point. In this respect, the electric aircraft has several advantages. Since no fuel is burned and the power units do not gain or lose weight, the centre of gravity can be fixed at a certain location. Also, there is no payload added before the flight, apart from the pilot's weight and the power units. Thus, on ground stability only depends on the stability of the empty aircraft, the aircraft with internal systems and finally with the pilot in the cockpit, while the in-air centre of gravity can be fixed precisely, which allows for an accurate prediction of the behaviour of the aircraft over the course of a flight.

A superior race performance requires a very maneuverable aircraft. The aircraft's centre of gravity shall thus be close to a point where the aircraft is neutrally stable to allow fast maneuvers. No stability margin (SM) is assumed between the centre of gravity and the neutral point of the entire aircraft, meaning that they coincide (SM=0). This can also offer better controllability characteristics than a conventional configuration, since the canard can be used up to higher values of C_{L_c} [96].

The stability is dependent on the stabilizer size with respect to the wing area. The relation of the two is plotted over the location of the centre of gravity with respect to the leading edge of the mean aerodynamic chord. The derivation of the corresponding requirements for stability and controllability for the canard can be found in [96] and [97]. The results are presented in Equations 9.1a and 9.1b. Equation 9.1a shows the relation of the centre of gravity and the tail size within the limits of stability, resulting from the fact that in the neutral point the aerodynamic moment should not change with a disturbance in angle of attack. Equation 9.1b depicts the relation of the centre of gravity and the tail size in controllability, with the underlying idea that, for a controllable, trimmable aircraft, the moment around the neutral point in trimmed condition should be zero.

Due to the fact that the canard configuration has a negative additional lifting surface (or canard) arm and that the canard produces positive (upwards) lift, the allowable centre of gravity range for stability is drastically decreased and shifted forward as compared to a conventional configuration. This limits the design flexibility, but since the centre of gravity does not change during the flight this will not cause problems when considered early in the design process.

$$\frac{S_c}{S} = \frac{1}{\frac{C_{L\alpha_c}}{C_{L\alpha}}\left(1-\frac{d\epsilon}{d\alpha}\right)\frac{l_c}{c}\left(\frac{V_c}{V}\right)^2} x_{cg} - \frac{x_{ac}}{\frac{C_{L\alpha_c}}{C_{L\alpha}}\left(1-\frac{d\epsilon}{d\alpha}\right)\frac{l_c}{c}\left(\frac{V_c}{V}\right)^2} \tag{9.1a}$$

$$\frac{S_c}{S} = \frac{1}{\frac{C_{L_c}}{C_{L_w}}\frac{l_c}{c}\left(\frac{V_c}{V}\right)^2} x_{cg} + \frac{\frac{C_{m_{ac}}}{C_{L_w}} - x_{ac}}{\frac{C_{L_c}}{C_{L_w}}\frac{l_c}{c}\left(\frac{V_c}{V}\right)^2} \tag{9.1b}$$

Using these equations requires to make several assumptions.

- $\mathbf{\frac{d\epsilon}{d\alpha} = 1}$ A canard is assumed to not produce significant downwash effects in this analysis and has the same angle of attack as the main wing [96]. However, if the trailing edge of the canard is too close to the leading edge of the main wing, closer than 2 times the root chord length, the design becomes close coupled and this assumption cannot be made any more [96]. The canard experiences an upwash and stall characteristics have to be considered.

- $\mathbf{\frac{V_c}{V} = 1}$ The velocity faced by both wings is assumed to be equal.
- The effect of the canard on the main wing can be neglected for the empennage design phase. However, in later stages, numerical analysis and wind tunnel tests have to be performed to assess whether there is an effect of the canard on the main wing in reality. Should the wing be located too closely to the canard, negative aerodynamic effects may occur and the $C_{L_{\alpha_w}}$ of the wing is decreased, according to Equation 9.2. This Equation is used to determine the altered C_{L_α} of the main wing when the airfoil is determined [96]. However, this will only play a role if the canard is very close to the main wing (if the distance between the two is less than 2 times the MAC of the main wing).

$$C_{L_{\alpha-duetocanard}} = C_{L_{\alpha_w}}(1 - \frac{2C_{L_{\alpha_c}} S_c/S}{\pi A_w k}) \tag{9.2}$$

The stability analysis after several design iterations is shown in Figure 9.1. Contrary to the depiction of the stability and controllability lines shown by LaRocca [96], the lines are not straight but curved. This is due to the fact that the canard arm depends on the centre of gravity position according to $l_c = x_{ac} - x_{cg}$, which is why it has to be updated with every centre of gravity position. Thus, the denominator in Equation 9.1a and 9.1b decreases with the centre of gravity moving forward, which increases the negative value of the slope of the curves. Figure 9.1 shows the stability and controllability requirements for the centre of gravity location with

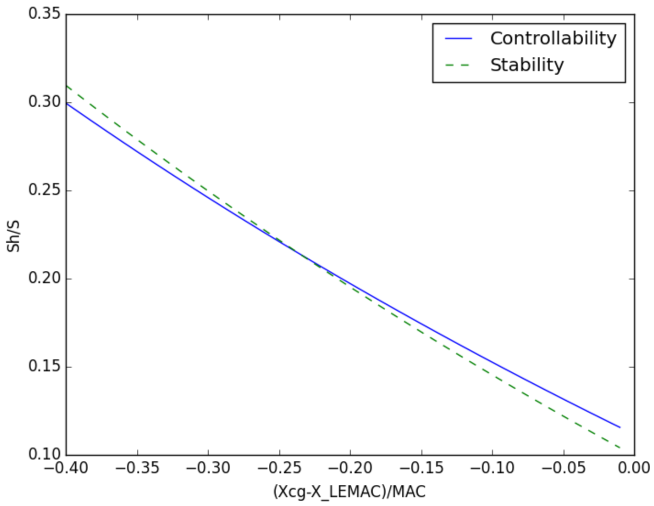

Figure 9.1: Stability and controllability over different positions of the centre of gravity.

respect to the main wing for a certain canard area with the configuration parameters presented in Table 9.1. The C_L values in this table are not the actual maximum lift coefficients but rather the ratio of lift coefficients that is achieved. The ratio of the canard area with respect to the main wing area may not lie under the control line or above the stability line for a particular centre of gravity location for the aircraft to be both stable and controllable. To minimize drag and possible influences on the main wing, a small canard surface area is beneficial. A design point close to the intersection of the lines in Figure 9.1 is preferred. The centre of gravity can be fixed at this point since no weight deviations are assumed to occur. This is because of the electric propulsion system.

Since the $\frac{S_c}{S}$ ratio should not become too big the design is limited at $\frac{S_c}{S} = 0.25$ for this stage of the design. Smaller canard areas are favourable. For the selection of a canard area, the controllability curve in Figure 9.1 is leading since it dictates the minimum required canard to main wing area fraction. The graph shows that, for the maximum area ratio of 0.25, the controllability and stability lines have crossed. Thus, the aircraft is statically stable and controllable when the centre of gravity is located at this point and the S_c/S ratio is chosen between the lines. The most aft centre of gravity location where both controllability and stability are possible lies 0.23 times the length of the MAC in front of the wing, requiring a $\frac{S_c}{S}$ ratio of 0.2114. While this would be possible to fly efficiently, it is decided that the centre or gravity should lie slightly in front of the point. Thus, the centre of gravity location is fixed at 0.25 times the MAC length in front of the leading edge mean aerodynamic chord. This x_{LEMAC} is at 2.58 metres from the nose of the aircraft. As a result, the centre of gravity position is at 2.34 metres from the nose, leading to an S_c/S ratio of 0.22. The design is summarized in Table 9.3. This updates the area assumed previously through the Class II method.

9.1.2 POSITIONING OF THE CANARD

The canard is positioned far in the front of the fuselage to allow for a long moment arm around the centre of gravity of the aircraft. The further forward the canard can be placed, the smaller its area and its weight can be. However, a canard working too efficiently and generating a lot of lift with increasing angle of attack can introduce a moment destabilising the aircraft. The canard is required to have a higher lift coefficient than the main wing.

Table 9.1: Factors used for determining the longitudinal stability and control characteristics

Factor	Symbol	Value	Unit
Lift coefficient, main wing	C_{L_w}	1.78	-
Lift coefficient, canard	C_{L_c}	2	-
Moment coefficient about aerodynamic centre	$C_{m_{ac}}$	-0.1214	-
Lift gradient, main wing	C_{L_α}	4.71	$\frac{1}{rad}$
Lift gradient, canard	$C_{L_{c\alpha}}$	4.83	$\frac{1}{rad}$
Position of aerodynamic centre, main wing	x_{ac_w}	2.83	m
Position of aerodynamic centre, canard	x_{ac_c}	0.16	m

This is necessary to not make the aircraft too unstable. Additionally, the slope of the lift curve, represented by C_{L_α} and C_{L_α}, is similar for both wings, as suggested by Phillips [98]. However, it is preferable that the canard has a higher lift slope since it will then stall earlier without a large angle of incidence. Canard stall is very important since the nose will then drop, leveling out the aircraft under high angles of attack and avoiding tail slipping, meaning the drop of the main wing of the aircraft, leaving the aircraft uncontrollable and non-recoverable.

9.2 VERTICAL STABILIZER DESIGN AND DIRECTIONAL STABILITY

The size of the vertical stabilizer area depends on the required directional stability characteristics of the aircraft and the conditions encountered over the course of a mission. Therefore, the main requirements for the vertical stabilizer have to be analysed and evaluated.

9.2.1 REQUIREMENTS

The following mission characteristics during which the vertical stabilizer and rudder control are required were analyzed for E-SPARC.

Crosswind Landing

Depending on the centre of gravity location and the aerodynamic forces acting on the fuselage and the vertical tail, the aircraft will either experience a stabilizing weathercock effect or will be unstable. This will lead to a rotation about the centre of gravity and a sideslip of the aircraft. Thus, it is important that the vertical stabilizer can be used to achieve and maintain a certain orientation towards the runway and the incoming wind direction, meaning that the aircraft is stable and “trimmable” in lateral motion as well. A straight approach to the runway is aimed at. According to CS23 regulations, the aircraft has to be able to cope with wind at 0.2 times the landing velocity, coming in at 90 degree [99]. For E-SPARC, assuming a landing velocity of 1.1 times the stall speed of 29.3 $\frac{m}{s}$, this means that crosswinds of at least 6.45 $\frac{m}{s}$ have to be coped with.

Recovery from Spin

Spin occurs after the stall of the main wing. Since the aircraft is designed to not enter a spin because the canard will always stall first and thus lower the angle of attack by dropping the nose, spin is not a leading design consideration. This limits the aerobatic application of the aircraft, but is considered to not be detrimental for the race performance. Wind tunnel tests on a model have to be performed in order to find the exact aerodynamic characteristics of the aircraft to evaluate the eventual spin recovery abilities [100].

Asymmetric Thrust

Asymmetric thrust plays a role in case of an engine failure when more than one engine is used. This is not the case for E-SPARC and can thus be neglected.

Adverse Yaw and Coordinated Turn

The aircraft has to be able to perform a coordinated turn and the vertical stabilizer has to equal out the effects of the ailerons. Wind tunnel model tests have to yield the exact aerodynamic characteristics [100].

9.2.2 DESIGN APPROACH

Designing the vertical tail is an iterative process. Often, vertical stabilisers are still changed in later stages of the design when wind tunnel tests and more precise aerodynamic analysis are performed.

For small and single engine aircraft, the crosswind landing is often assumed to be the leading requirement [100]. Thus, it has to be assured that the aircraft is stable and trimmable in directional orientation. For designing, several options are available. Raymer suggests to consider reference aircraft for sizing the vertical tail at this stage [24]. For this, the vertical tail volume coefficient $c_{V_{vt}}$, as calculated in Equation 9.3, is used. However, the other racing aircraft often feature overdesigned tails since they are not optimised for racing but also have a focus on performances in aerobatics.

$$c_{V_{vt}} = \frac{l_{vt} S_{vt}}{bS} \tag{9.3}$$

Another approach would be to take historical reference data into account [101] and calculate the corresponding vertical tail area based on formulas found from these historical relations of vertical tail planes to main wing area and arm lengths. However, this approach is based on aircraft that are not necessarily comparable to the aircraft under consideration. Thus, the same approach is taken as for the sizing of the horizontal stabilizer [96, 97]). Equations 9.1a and 9.1b can be altered accordingly and Equations 9.4a for the stability characteristics and 9.4b for the controllability characteristics can be found. Notice that the wing area has been replaced by the side area of the fuselage of the aircraft, S_f, which, under a sideslip angle, will create an outboard force. This introduces a moment about the centre of gravity that has to be counteracted by the vertical stabilizer. From the stability and control requirements the ratio of the vertical stabilizer area S_v to the fuselage side area can be determined. Also, the aerodynamic moment $C_{m_{ac}}$ is not present in Equation 9.4b since the fuselage of the aircraft is assumed to not have such a moment. This approach, however, only works as long as the aerodynamic centre of the fuselage lies in front of the centre of gravity. Otherwise, another approach has to be considered.

$$\frac{S_{vt}}{S_f} = \frac{x_{cg}}{\frac{C_{Y_{\beta_{vt}}}}{C_{Y_{\beta_f}}} \frac{l_{vt}}{b} \left(\frac{V_{vt}}{V}\right)^2} - \frac{x_f}{\frac{C_{Y_{\beta_{vt}}}}{C_{Y_{\beta_f}}} \frac{l_{vt}}{b} \left(\frac{V_{vt}}{V}\right)^2} \tag{9.4a}$$

$$\frac{S_{vt}}{S_f} = \frac{x_{cg}}{\frac{C_{Y_{vt}}}{C_{Y_f}} \frac{l_{vt}}{b} \left(\frac{V_{vt}}{V}\right)^2} - \frac{x_f}{\frac{C_{Y_{vt}}}{C_{Y_f}} \frac{l_{vt}}{b} \left(\frac{V_{vt}}{V}\right)^2} \tag{9.4b}$$

In this case, the lift force depicted by subscript Y acts in the lateral direction. Using the results of Equations 9.4a and 9.4b, a scissor plot can be generated, as shown in Figure 9.2. In this plot, the area of the vertical stabilizer with respect to the side area of the fuselage of the aircraft is plotted over the centre of gravity location as was done in Figure 9.1. In order to keep the size and thus the weight of the vertical stabilizer small, a high ratio of $\frac{C_{L_{\beta_{vt}}}}{C_{L_{\beta_f}}}$ has to be found. Then, placing the centre of gravity at the same position as for the horizontal stabilizer sizing, a vertical stabilizer size can be found.

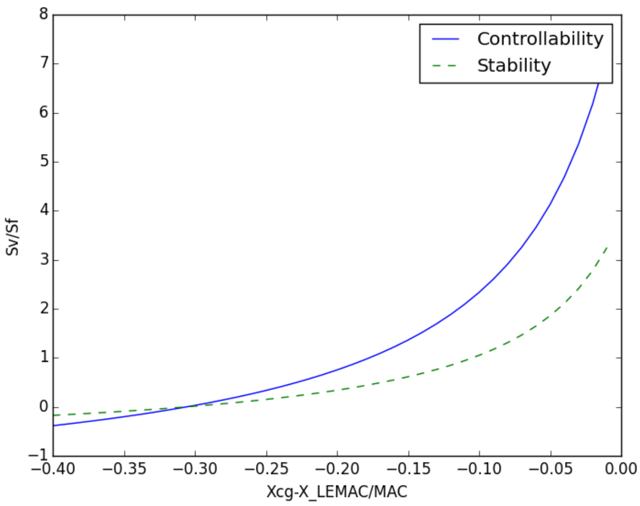

Figure 9.2: Directional stability and controllability over different positions of the centre of gravity.

The centre of gravity of the aircraft that is selected to find the size required for lateral stability and control has to match the centre of gravity selected for the canard wing. However, the centre of gravity should lie as far forward as possible in order to minimize the tail area. A far forward centre of gravity would require the canard to increase in size (see Figure 9.1). Also, as can be seen, the possible space for centre of gravity is very limited to avoid that the centre of gravity lies before the aerodynamic centre of the fuselage. The most forward point would be at 2.29

metres from the front. The selected centre of gravity location of 2.34 metres from the front is thus stable and controllable and can be used for further steps. It yields a vertical stabilizer size of $0.3m^2$. The small area can be explained by the small distance between the centre of gravity and the aerodynamic centre of the fuselage. Thus, the moment introduced by the fuselage is small, meaning that the moment from the winglets can be smaller. Also, this does not include the use of control surfaces yet. Therefore, it is even possible for the vertical stabilizer to decrease in size in later design steps. Table 9.2 shows the parameters used to determine the vertical stabiliser size. The factor of side force coefficients is determining the minimum size of the vertical stabilisers. Without

Table 9.2: Factors used for determining the directional stability and control characteristics

Factor	Symbol	Value	Unit
Force coefficient, fuselage	$C_{Y_{\beta_f}}$	-0.03	-
Force coefficient, vertical stabiliser	$C_{Y_{vt}}$	-0.2	-
Force gradient, fuselage	C_{Y_f}	-0.001	$\frac{1}{rad}$
Force gradient, vertical stabiliser	$C_{Y_{vt}}$	-0.003	$\frac{1}{rad}$
Velocity ratio	$\frac{V_{vt}}{V}$	1	-
Fuselage side area	S_f	2.00	m^2

wind tunnel tests it is difficult to determine these values accurately. However, it is found from literature that the vertical stabiliser has by far the largest effect on the lateral force [24]. Precise tests have to be performed in later stages and a resizing may be required. The incorporation of control surfaces can also improve the overall performance of the vertical stabiliser and thus allow for smaller sizes.

9.2.3 POSITIONING OF VERTICAL STABILIZER

In order to allow a high efficiency of the vertical stabilizer during flight it should be placed where the airflow it faces is influenced as little as possible. In a conventional configuration, a wake created by the horizontal tail can already influence the vertical stabilizer heavily under small angles of attack. This is particularly a problem for the canard since the main wing is positioned in the back and thus introduces an even bigger wake that could potentially mitigate the positive effects of a conventional vertical tail on the fuselage. In order to keep the vertical stabilizer small, its distance to the centre of gravity has to be kept as large as possible which means that moving the vertical stabilizer on the fuselage before the wing, as proposed by Torenbeek in [102] is not an option.

An even more important influence on the positioning arises from the fact that the effectiveness of the pusher canard configuration highly depends on the effective performance of the propeller and the electric engine. Since a conventional vertical stabilizer in front of the propeller would influence the airflow through the propeller and disturb it dramatically, especially under high angles of attack for the vertical tail, the propeller would work less efficiently where the tail is positioned and thus deliver thrust asymmetrically on the top and bottom of the aircraft. Also, a vertical stabilizer on both top and bottom of the fuselage would not solve this problem since the tail would disturb the flow “against” the rotation of the propeller on one side and “with” the rotation of the propeller on the other side. This would even increase the negative effects.

Therefore, it was decided to use blended winglets with the equivalent size of the vertical stabilizer to allow for directional stability. These have to be able to incorporate rudders to grant more control. Also, winglets can use aerofoils other than symmetrical ones and add additional lift and drag contributions to the performance of the aircraft. Another benefits of winglets is that they are optimised for one velocity [24]. Since the velocity requirements for E-SPARC are known precisely, this can be done with more extensive analysis. The precise effects of this have to be assessed in further steps and wind tunnel tests. The exact dimensions also have to be refined for the optimal use. For the preliminary design, it is only assumed that the root chord of the winglet is the tip chord of the main wing. Proven working concepts of this type of configuration exist, as shown by Kumar and Rao in 2002 [103]. The resulting longitudinal moment arm l_{vt} of the winglets is 0.31 meters. The outboard arm and moment generated by the drag component, resulting from the fact that the vertical stabilizer is not on the centre line of the fuselage anymore, is not taken into account yet since it requires a more elaborate estimation of the size and airfoil of the winglet.

The findings presented in this chapter have to be proven to be correct in later stages of the design process by performing wind tunnel tests or other means of investigation.

Table 9.3: Design parameters of the horizontal and vertical stabilizer as well as general design choices resulting from the analysis.

Parameter	Symbol	Value	Unit
Canard area to wing area ratio	$\frac{S_c}{S}$	0.221	-
Vertical stabilizer area to fuselage side area ratio	$\frac{S_{vt}}{S_f}$	0.15	-
Canard area	S_c	1.14	m^2
Combined winglet area	S_{vt}	0.3	m^2
Centre of gravity position from front	x_{cg}	2.34	m

9.3 KEEL AREA AND LATERAL STABILITY

According to [104], the aircraft is laterally stable if the majority of the aircraft's side area, also called 'keel area', is above and behind the c.g. centerline. An example is demonstrated in Figure 9.3. In the side view drawing given in Section 6.1, it can be seen that this condition is satisfied. Thus E-SPARC is laterally stable.

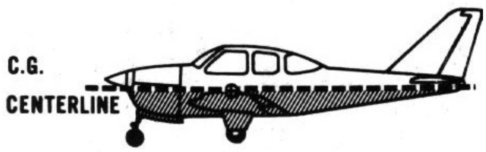

Figure 9.3: Lateral stability and keel area distribution [105].

Recommendations

Since the centre of gravity range is very limited in order to fulfill both the longitudinal and directional stability and controllability characteristics, it will be crucially important to manage the distribution of the subsystems correctly and pay attention during production to maintain the c.g. in the correct position.

Also, further investigation has to be undertaken to determine the behaviour of the aircraft in lateral direction and the effect the vertical stabilisers have on lateral motions. This can be done best when models are present and the interchange between the different lifting surfaces becomes apparent.

9.4 VERIFICATION AND VALIDATION

The sizing of the tail surfaces was performed using two tools, one for the horizontal stabiliser analysis and one for the vertical stabiliser analysis. Both tools have to be verified. Also, suggestions will be made on how to validate the outcome of the tools in later stages of the design process.

9.4.1 VERIFICATION

The first tool, the analysis of longitudinal stability and controllability over different positions of centre of gravity, can be verified by checking the tools performance when other values for another aircraft are plotted. However, first unit tests were undertaken to prove the correct working of the individual calculations. For this, the canard arm for different centre of gravity locations was determined. As expected it decreases with the c.g. moving forward. Furthermore, the trend of the stability and controllability curves for changing centre of gravities was compared to plots found by LaRocca [97]. Thereafter, the entire program was analysed by using the aerodynamic characteristics and dimensions of the Cessna Ce500 Citation that were presented by in't Veld [106]. Since this is a conventional aircraft, the plot should switch, with the stability curve increasing and the controllability curve still decreasing from forward to aft centre of gravity locations. This allows for a broader design space, as is to be expected for conventional aircraft. The plotted results show precisely this trend. For the provided centre of gravity location of $0.3\bar{c}$, the plots showed enough stability region for centre of gravity shifts due to fuel. Since the general trend that has to be expected is depicted both for canard and for a conventional configuration, it was concluded that the tool can be called verified.

To verify the tool for vertical stabiliser sizing, the trend over a wider range of c.g. locations is considered. There, it can be seen that the required area for the vertical stabiliser becomes negative for a c.g. moving forward, as can be expected since the centre of gravity passes the aerodynamic centre of the aircraft at a certain point. From this point forward, the vertical stabiliser has to generate a force and moment opposing the direction of the force of the fuselage. With the same aerodynamic characteristics this is only possible with a negative surface. A further investigation of the graphs show that the lines cross precisely at the location of the aerodynamic centre of the fuselage. This proves the correct working of the tool in longitudinal direction. Additionally, it was concluded that the graphs direction should not change when considering a conventional aircraft, in contrast to the verification performed for the horizontal stabiliser tool. The general trend should remain the same. By considering the dimensions for the Cessna Ce500 Citation from [106] again, it was found that the graphs still show the same tendency, with the only difference that the design space for the Citation moved aft considerably, which also makes sense since the c.g. in reality lies further back than for E-SPARC. Since the tool can account for different centre of gravity locations as well as changing aircraft configurations it was deemed verified.

9.4.2 VALIDATION STRATEGY

Validation has to be performed to show that the tool determines stabiliser sizes that are actually sufficient to achieve stability and controllability. For this, in later stages of the design process wind tunnel tests or actual flight tests have to be performed. These show the behaviour of the aircraft. Also, when the aircraft is actually built and tested, the dimensions and aerodynamic coefficients used in the model can be updated as soon as the correct values are known. Then, the actual comparison to real life performance and thus verification can take place.

10 Landing Gear

This chapter includes the description of the current main landing gear design for E-SPARC, as well as the used method to size and select components. A section on verification and validation of the design method and design itself is also included. The nose gear design is not yet finished at this stage, but the recommendations will include some required properties that should form the basis for an actual nose gear design.

The current main gear design is based on the trade-offs performed prior to the Mid Term Review [87], which include the decision to have a tricycle non-retractable landing gear. Also, the design is based on the structural requirements and therefore the aerodynamic optimization of the gear, e.g. adding wheel fairings, is not included at this stage. During the designing of the landing gear it was decided to make effective use of compatible off-the-shelf products in order to simplify and shorten the design process.

10.1 Method

This section will be dedicated to elaborate on the method used to design the main landing gear, which is summarized by the work flow chart in Figure 10.1. The actual values used for the parameters shown in this section are given in Section 10.2. The nose gear has not been fully designed at this stage, but the results in Section 10.2 also include some constraints on the nose gear design.

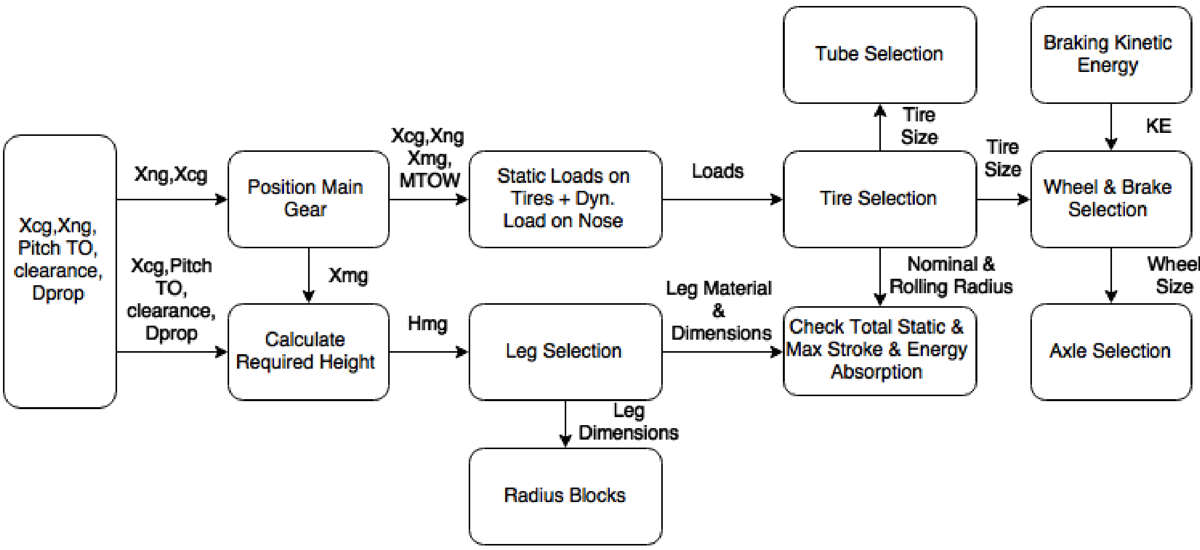

Figure 10.1: Work Flow Diagram for the main gear design process

The first step was to derive the main gear position x_{mg}, which was performed using Equation 10.1.

$$x_{mg} = x_{cg} + WF_{ng} \cdot \frac{x_{ng} - x_{cg}}{WF_{ng} - 1} \tag{10.1}$$

Here x_{cg} is the total c.g. location, x_{ng} the chosen nose gear location and WF_{ng} the fraction of the weight carried by the nose gear during static loading of the landing gear.

Using the derived location of the main gear the static loads on the landing gear, $F_{mg,static}$ and $F_{ng,static}$, were evaluated using Equation 10.2a and 10.2b. Since these values are needed to choose the type of tires, the forces are calculated per wheel. The max static load the nose gear needs to be able to carry is a combination of the fraction of the aircraft weight and an additional vertical load during braking to counteract the nose-down moment generated by main gear braking during landing.

$$F_{mg,static} = W_{TO} \cdot \frac{x_{cg} - x_{ng}}{x_{mg} - x_{ng}} \cdot \frac{S.F._{static}}{N_{mg}} \tag{10.2a}$$

$$F_{ng,static} = \left[\underbrace{W_{TO} \cdot \frac{x_{mg} - x_{cg}}{x_{mg} - x_{ng}}}_{\text{static loading}} + \underbrace{a_x \cdot (H_{ng} + r_{f,ng}) \cdot \frac{W_{TO}}{g \cdot (x_{mg} - x_{mg})}}_{\text{braking contribution}} \right] \cdot \frac{S.F._{static}}{N_{ng}} \tag{10.2b}$$

In these equations W_{TO} is E-SPARCs take-off weight, N_{mg} and N_{ng} are the number of wheels on the main and nose gear and a_x is the deceleration after landing. In addition, H_{ng} and r_f are the nose gear height with respect to the bottom of the fuselage and the fuselage radius at the nose gear location. The equations also include a safety factor $S.F._{static}$. E-SPARCs fuselage should be level during static loading of the main gear, therefore $H_{ng} + r_{f,ng}$ was later replaced by $H_{mg} + r_{f,mg}$. In addition, the maximum force a main gear tire will ever experience, $F_{mg,max}$, is derived using Equation 10.3, which does not include N_{mg} because the landing gear should not fail in case the aircraft touches down on one of the main gear tires.

$$F_{mg,max} = W_{TO} \cdot n_{gear} \tag{10.3}$$

Where n_{gear} is the max loading gear load factor, which is experienced at the end of the deflection stroke. Based on the calculated static and maximum loads the tire selection can be performed using a tire book [107]. For E-SPARC Goodyear tires have been selected. The chosen tires for the main gear should have a rated load higher than $F_{mg,static}$ and a bottoming load, the load at which the wheel and tire radius are equal, higher than $F_{mg,max}$. Compatible tubes were also selected from the tire book.

Using the known parameters of the selected tires, compatible off-the-shelf wheels, brakes and axles can be selected from an aerospace warehouse. In the case of E-SPARC this is Grove Aerospace Landing Gear Systems Inc. [108]. The manufacturer of the brakes, which are sold in a package with the wheels, provided the maximum amount of kinetic energy that can be absorbed (per wheel), ΔKE_{max}. This value can be compared to actual amount of (horizontal) kinetic energy, $\Delta KE_{x,req}$, that needs to be absorbed per wheel to brake E-SPARC. This actual value was calculated using Equation 10.4 with m_{TO} being the take-off mass and V_{stall} the stall speed.

$$\Delta KE_{x,req} = \frac{1}{2}\frac{m_{TO} \cdot V_{stall}^2}{N_{mg}} \tag{10.4}$$

Another check to be performed on the brakes is whether the maximum braking torque is sufficient to achieve the assumed deceleration a_x, which is true if the condition from Equation 10.5 holds.

$$\frac{T_{brake}}{R_r} \geq \frac{1}{2} m_{TO} \cdot a_x \tag{10.5}$$

Where T_{brake} is the torque generated by one brake and R_r the loaded rolling radius of the tire.

Another task that can be performed after the position of the main gear has been determined, is to calculate the required height of the main gear, $H_{mg,req.}$, to provide enough ground clearance for the pusher propeller during landing and take-off. The required main gear height is calculated using Equation 10.6, which assumes E-SPARCs CG to lie on the fuselage centre-line.

$$H_{mg,req.} = \frac{\frac{1}{2} \cdot D_{prop} \cdot \cos(\theta_{stall}) + \left(x_{prop} - x_{mg}\right) \cdot \sin(\theta_{stall})}{\cos(\theta_{stall})} - r_{f,mg} \tag{10.6}$$

Here D_{prop} is the propeller diameter and x_{prop} the propeller location with respect to the nose of the aircraft. $H_{mg,req.}$ is calculated for the highest possible fuselage pitch angle during touch-down, θ_{stall}. Based on the required landing gear height, a set of off-the-shelf leaf spring landing gear legs can be selected from Grove Aerospace Landing Gear Systems Inc. The provided height of the legs is the unloaded height, therefore the actual landing gear height during static ($H_{mg,static}$) and dynamic ($H_{mg,dynamic}$) loading should also be checked, which is done using Equations 10.7a and 10.7b.

$$H_{mg,static} = H_{leg,unloaded} + R_{tire,unloaded} - S_{mg,static} - S_{tire} \tag{10.7a}$$

$$H_{mg,dynamic} = H_{leg,unloaded} + R_{tire,unloaded} - S_{mg,dynamic} - S_{tire} \tag{10.7b}$$

Where $H_{leg,unloaded}$ is the provided landing gear leg height and $R_{tire,unloaded}$ the unloaded tire radius. Additionally $S_{mg,static}$ and $S_{mg,dynamic}$ are the static and dynamic strokes of the gear legs and S_{tire} is the tire stroke, which is assumed equal to the difference between R_r and the unloaded radius for both the dynamic and static case. In order to calculate $S_{mg,static}$ and $S_{mg,dynamic}$ a simplified version of the landing gear and loading is assumed, as shown in Figures 10.2a and 10.2b. It is assumed that the stroke under static loading of the landing gear leg is caused only by the deflection of beam A and B (δ_A) and the rotation of the ends of beam C ($\Delta\theta_C$) due to moments inflicted at those location via beams A and B. For the dynamic stroke the same assumptions apply, only in this case beam C is loaded by a single moment at the right end (instead of equal opposite moments on both ends). Using these assumptions and Euler-Bernoulli beam theory $S_{mg,static}$ and $S_{mg,dynamic}$ can be

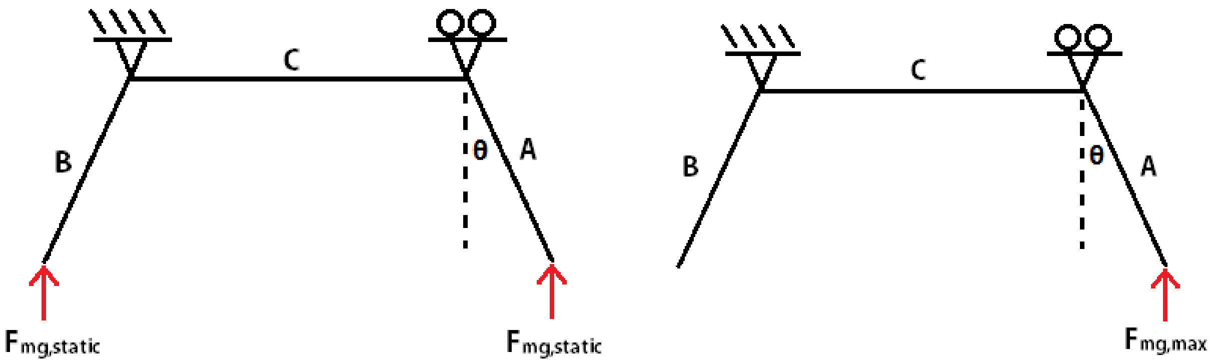

(a) Static loading; aircraft weight on all three wheels (b) Dynamic loading; hard landing on one wheel

Figure 10.2: Illustration of simplified landing gear and loading used for stroke calculations

calculated, using Equations 10.8 and 10.9.

$$S_{mg,static} = (\delta_A + \Delta\theta_C \cdot L_A)\sin\theta = \left(\frac{F_A L_A^3}{3EI_A} + \frac{M_C L_C}{2EI_C} \cdot L_A\right)\sin\theta \quad (10.8a)$$

$$\text{with } F_A = F_{mg,static} \cdot \sin\theta \quad (10.8b)$$

$$\text{and } M_C = F_A \cdot L_A \quad (10.8c)$$

$$S_{mg,static} = (\delta_A + \Delta\theta_C \cdot L_A)\sin\theta = \left(\frac{F_A L_A^3}{3EI_A} + \frac{M_C L_C}{3EI_C} \cdot L_A\right)\sin\theta \quad (10.9a)$$

$$\text{with } F_A = F_{mg,max} \cdot \sin\theta \quad (10.9b)$$

$$\text{and } M_C = F_A \cdot L_A \quad (10.9c)$$

Where L stands for length, F for force, E for the materials Young's modulus and I for area moment of inertia.

For the chosen landing gear leg, $H_{mg,static}$ and $H_{mg,dynamic}$ should be larger than $H_{mg,req.}$, otherwise the propeller might hit the runway during a hard landing at high pitch angle. In case the chosen landing gear leg meets these requirements, the radius block used to attach the gear to the fuselage, can be selected. Radius blocks also prevent the bending moments in the main gear leg to be transferred to the fuselage, which would require reinforcements to prevent local skin buckling.

Finally it should be noted that some of the inputs for the landing gear selection, e.g. x_{cg}, depend on the landing gear location and weight. Therefore the first landing gear design is based on estimated Class II values, afterwards the complete process is iterated till the input values remain constant for the first actual design. Since the input values are continuously updated based on more accurate designs of the other subsystems, the compatibility of the selected landing gear should also be checked once in a while. This process was simplified by also adapting the method to MATLAB-code.

10.2 INPUTS AND RESULTS

This section provides the inputs for the selection of the landing gear following the method from Section 10.1, as well as presenting the selected landing gear and some of the results belonging to the selected landing gear.

INPUTS

The most important input values are tabulated in Table 10.1. WF_{ng} is based on Raymers chapter for conceptual landing gear sizing [24]. The $S.F._{static}$ is also based on Raymers method, which states 7% should be added to the load for regulations and 25% to account for later increase of the MTOW (both during the design phase as well as E-SPARCs operational life). Since E-SPARC has a relatively low MTOW (compared to most general aviation) two main wheels and one nose wheel should suffice, keeping the landing gear weight as low as possible. In order to derive the braking deceleration a typical braking coefficient of $\mu_{brake} = 0.3$ was assumed [24], which results in the used value of $a_x = 2.94$, using $a_x = \mu \cdot g$. By combining the given values for V_{stall} and a_x it can be concluded that E-SPARC is expected to have a ground run of almost 150 m. n_{gear} is also based on Raymers sizing method.

The θ_{stall} is based on E-SPARCs canard stall and incidence angle of 11.6° and -5.0°, see Chapter 13. ΔH_{SM} is

Table 10.1: Main input parameters and values for selection of landing gear components

Input parameter	Value		Source
WF_{ng}	20.0	[%]	Raymer [24]
$S.F._{static}$	1.34	[-]	Raymer [24]
N_{mg}	2	[-]	
N_{ng}	1	[-]	
a_x	2.94	$\left[\frac{m}{s^2}\right]$	Raymer [24]
n_{gear}	3	[-]	Raymer [24]
V_{stall}	29.3	$\left[\frac{m}{s}\right]$	
θ_{stall}	16.6	[°]	
x_{ng}	0.3	[m]	

based on CS23 [109] regulations, which state that the ground clearance should be at least 0.18 m during static loading of the landing gear.

The input variables related to E-SPARCs geometry, like x_{cg}, are provided in Table 6.13 in Section 6.4.4. The values for E-SPARCs geometry changed continuously during the project, therefore (as stated earlier) the selected landing gear was checked for compatibility with the latest values several times. x_{ng} is currently set at 0.4 m from the nose, just behind the canard, but there is some margin for moving the nose gear either back- or forwards in case this is required by the nose gear design.

RESULTS

The main landing gear will be located at 2.85 m. E-SPARC will have Type III 5.00-4 tires from Goodyear based on a $F_{mg,static}$ of 2178 N (489 lb) and a $F_{mg,max}$ of 12.2 kN (2744.4 lb). Goodyear 5.00-4 TR67 tubes were selected based on their compatibility by the tires. From Grove Aerospace Landing Gear Systems Inc. the wheel and brake kit 40-102 (with wheel number 40-1A and brake pad number 066-106) were selected, which has the most powerful brakes of the two compatible options (while costing an equal amount of US Dollars). Each brake pad is design to absorb 97.6 kJ of kinetic energy, while the required amount is 89.1 kJ. The brakes also provide a large enough braking torque in order to achieve the calculated a_x. The selection of wheels and brakes immediately fixes the axle decision to a P/N 5030-axle.

The selected landing gear is the Lazer / Stephens Acro gear, which is made from 7075-T6 aluminum. The manufacturer's offer to add a gundrill for the brake-hydraulics has also been selected. For latest iteration of E-SPARCs design, the chosen landing gear leg and tires will result in $H_{mg,static} = 0.72\,m$ and $H_{mg,dynamic} = 0.64\,m$, therefore meeting the required $H_{mg,req.} = 0.63\,m$. Four compatible radius blocks were also selected.

Table 10.2 summarizes all selected components and the corresponding mass and costs.

Table 10.2: Overview of mass and cost of the main landing gear components

Component	Mass [kg]	Cost [$]	Cost [€] *($1.00 = €0.88)*
1 x Grove Lazer / Stephens Acro Leg	11.5	1775.00	1562.00
2 x Grove Wheels & Brakes model 40-102	1.89	619.00	544.72
2 x Grove P\N 5030 Axle	0.36	98.00	86.24
4 x Grove Radius Blocks	1.588	124.00	109.12
2 x Goodyear 5.00-4 6 Ply Tire	1.81	670.00	589.60
2 x Goodyear Inner Tubes	1.36	205.40	180.75
Total	18.54	3491.40	3072.43

RECOMMENDATIONS FOR FUTURE DESIGNS

- The current method of landing gear selection results in an over-designed design. The selected landing gear could be used as a starting point for an own, optimized, landing gear design which would weigh less than the current design.
- The current landing gear design is only based on the structural requirements. Wheel fairings could be designed in order to decrease the drag. Also, the shape of the legs could be optimized not only for structural performance but also for contributing to the lift or minimizing the drag.
- The nose gear has not been designed at this stage, therefore of course a nose gear should be designed. Although the main gear is fixed, initial studies have shown there are several off-the-shelf retraction mech-

anisms available for nose gears which weigh approximately 5 kg, therefore greatly decreasing the zero-lift drag. Also, in contrary to the main gear, there is more available space in the nose of the fuselage. Based on these arguments it was decided to have a retractable nose gear in the CATIA model, but a in future design stages a more elaborate quantitative trade-off should be performed to make a definitive decision. Currently, the only required values for the nose gear design are a height w.r.t. the bottom of the local fuselage of 1.01 m and a location w.r.t. the nose of approximately 0.3 m. It should also be able to carry a static load of 1550 N (348.4 lb).

10.3 VERIFICATION AND VALIDATION

This section includes the applied verification methods for the landing gear selection and sizing MATLAB-tool as well as some remarks on the planned validation of the actual landing gear.

The general approach for verification of the landing gear sizing tool is based on simple sensitivity analyses. This included increasing and decreasing all major inputs and checking whether the changes to the outputs were as expected with respect to sign and order. As an example, decreasing the stall fuselage pitch to 5° instead of 8.5° decreases the required main gear height from 0.66 m to 0.59 m. This is as expected since a lower pitch angle during landing means the ground clearance increases and thus the landing gear height can be decreased.

In addition to the sensitivity analysis the calculations on the main gear leg strokes can be verified using an energy method. Using the gear load factor (and therefore the vertical deceleration during touchdown) the maximum vertical velocity prior to touchdown can be derived, which is equal to 1.98 m/s: resulting in a vertical kinetic energy prior to touchdown of 813 J. Using the equations for potential energy in Euler-Bernoulli beams, which happens in the form of strain energy, it can be calculated how much energy is absorbed by the gear legs during touchdown. In case both the deflection and energy method are carried out correctly the absorbed kinetic energy by the gear is exactly equal to the required value, therefore verifying correct implementation of the deflection method.

Validation of the main landing gear will be performed during the production stage of development. At that stage several tests can be performed on the actual selected landing gear legs, wheels, brakes and tires. Drop tests with dummy weights could be performed with the complete landing gear to validate the calculated stroke. The static stroke could be derived by statically loading the gear. A dynamometer could be used to validate the tires as well as test whether the brakes are able to perform the required (and stated) torques.

11 FUSELAGE

Ideally the fuselage would be designed as a pure monocoque structure because a monocoque is lightweight and very damage resistant [110]. However, since the length is 4 m, the required thickness to withstand buckling would be significant, resulting in a heavy design. Therefore, some stiffeners in the longitudinal direction and some frames are added to the structure. The stiffeners and frames are assumed to be evenly spaced in the structure. The number of stiffeners will be determined during the design. The number of frames is already set to four in order to keep the design relatively simple. For now the fuselage was designed to be made of quasi-isotropic CFRP. The minimum skin thickness is taken to be 1.65 mm this is also the value that is used in the industry based on impact resistance. The method for the design of the fuselage will be explained in Section 11.1. The results will then be presented in Section 11.2. Finally, some recommendations for further developments are made in Section 11.2.

11.1 METHOD

In order to be able to perform a preliminary design for the fuselage, the shape is simplified to the shape shown in Figure 11.1. The smallest radius on the side of the nose is 0.05 m and the smallest radius on the side of the tail is 0.1 m. The radius of the middle section is 0.5 m. This shape resembles the actual shape of the fuselage.

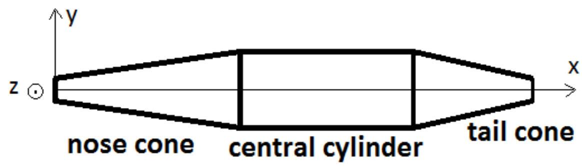

Figure 11.1: Simplified fuselage shape

This simplified representation of the fuselage means that cut-outs are not accounted for and therefore the fuselage will be under-designed in the region around these cut-outs. Four frames will be laced in the fuselage to add extra strength to the fuselage. The four frames are placed at the nose and tail as well as on both sides of the central cylinder.
For the calculations concerning the fuselage, a non-inertial reference frame was considered. The reference frame origin is located at the nose of the airplane with the x-axis running through the symmetry axis of the simplified fuselage.

Figure 11.2 shows a flow chart which visualizes the MATLAB-tool created for the fuselage design.

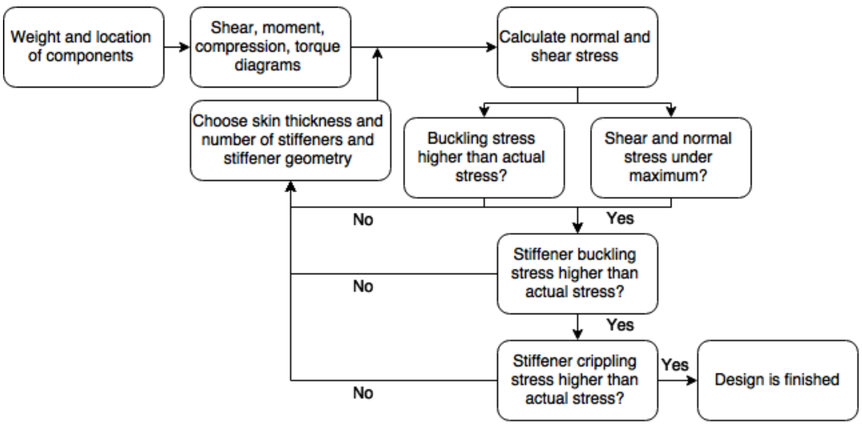

Figure 11.2: Flow chart explaining the layout of the program written for the fuselage design

The first step of the solution to this problem is to determine the loads on the fuselage. The fuselage design is based on the following loads.

- Shear loads due to the weights of all the components and the lift acting on the canard and main wing.
- Bending moments due to the weight of all the components, the lift and the aerodynamic moment of the canard and the main wing.
- Torsion due to aileron deflection during roll acceleration.
- Compression due to the thrust of the engine and the drag that act in opposite directions.

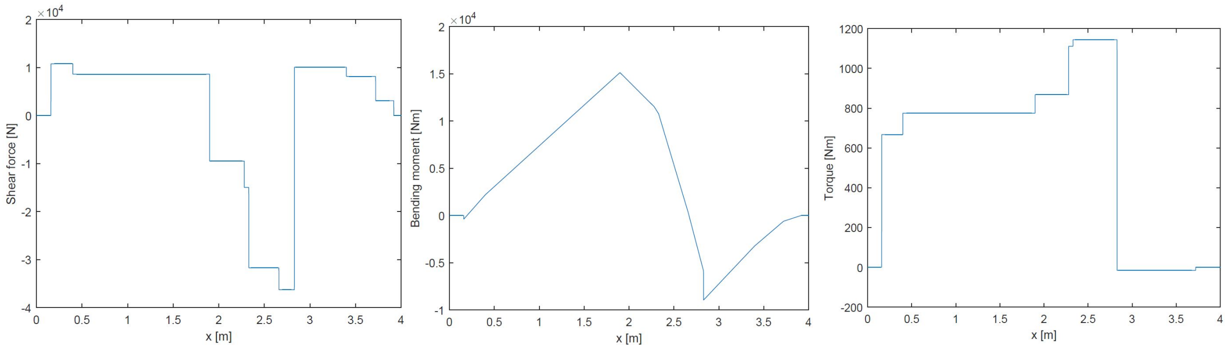

(a) Shear force diagram (b) Bending moment diagram (c) Torsion diagram

Figure 11.3: Force and moment diagrams for the fuselage

The weights and locations of all the components are known. To calculate their shear force, the respective weights are multiplied by the ultimate load factor of 18. From these shear forces a shear force diagram can be derived. This diagram can be seen in Figure 11.3a

Now that the shear force is known over the whole fuselage, the moment diagram can be calculated with Equation 11.1. Note that this formula calculates the slope of the moment curve for any given location along the beam. The aerodynamic moments of the canard and main wing are still to be added at their respective locations. The moment diagram can also be seen in Figure 11.3b.

$$S_Y(x) = \frac{dM_Z(x)}{dx} \Leftrightarrow M_Z(x) = \int S_Y(x)dx \tag{11.1}$$

In this equation $S_Y(x)$ is the shear force in y-direction and $M_Z(x)$ the bending moment about the z-axis along the fuselage. Now that all the forces are known, the skin thickness and the stiffener design can be determined. This is done by making an initial guess. The torsion was calculated by using Newton's second law applied to rotation.

$$T = \dot{\alpha} \cdot I = \dot{\alpha} \cdot (I_f + I_w) \tag{11.2}$$

The torque introduces by the wing is the torque that is generated by the ailerons at maximum aileron deflection, this is 3933 Nm. This torque is counteracted by each component due to its inertia. Summing all these yields the torsion diagram in Figure 11.3c.

The compressive force is only created by the thrust of the propeller and the drag acting on the airplane. For simplicity it is assumed that the drag is acting on the nose. This means that there is a constant compressive force in the fuselage which is equal to the trust of 1224 N. The next step is to see if the current design has enough strength to sustain the applied loads. There are four important failure modes that need to be considered and thus four checks that need to be performed.

- Strength failure
- Plate buckling of the skin
- Column buckling of the stiffeners
- Crippling of the stiffeners

To check for strength failure it is enough to check whether the maximum occurring shear and normal stresses do not exceed the yield shear and normal stress of the material. If this requirement is not met, the chosen design will have to be reconsidered. The maximum normal and shear stress can be calculated using Equation 11.3a and 11.3b. Here $r_f(x)$ and $I(x)$ are the local fuselage radius and area moment of inertia, which is calculated using thin-walled assumptions. This is a valid assumption because the initial estimate of the thickness is 1.65 mm, which is 0.33% of the fuselage radius of 0.5 m

$$\tau_{max,shear} = \frac{S_Y(x) \cdot t \cdot r_f(x)}{I(x)} \tag{11.3a}$$

$$\sigma_{max} = \frac{M_Z(x) \cdot r_f(x)}{I(x)} \tag{11.3b}$$

The torsion also induces a shear stress, which can be derived using Equation 11.4, which should be added to the value calculated using Equation 11.3a. Where $T(x)$ and $A(x)$ are the local torsion on the fuselage and its area. It is assumed that the torsion is carried by the skin only.

$$\tau_{torsion} = \frac{T(x)}{2 \cdot A(x) \cdot t} \tag{11.4}$$

In order to check for the plate buckling failure mode of the skin, the plate buckling stress will have to be calculated. This can be done using Equation 11.5 [111].

$$\sigma_{CR} = \frac{k\pi^2 E}{12 \cdot (1-\nu^2)} \left(\frac{t}{b}\right)^2 \tag{11.5}$$

In this equation b is the short side of the plate, thus the distance between two stiffeners. k is the buckling coefficient which is determined as a function of $\frac{a}{b}$, where a is the long side of the plate. The most conservative value that is used for k is 4, so this is the value that will be used in the fuselage design. In addition E and ν are the Young's modulus and Poisson ratio of the fuselage material. To make sure that the design does not fail under plate buckling, the critical buckling stress should be higher than the actual normal stress acting on the fuselage.

After these two checks are performed, it can be said that the skin will not fail before it is allowed to fail. Now the stiffeners still need to be checked for column buckling and crippling. Crippling of a stiffener means that it will fail after local buckling in one of the webs.

For column buckling, the Euler buckling equation can be used, shown in Equation 11.6 [111]. The crippling stress needs to be calculated for each member of the stiffener individually. But because both members of the stiffener design have the same area and Young's modulus, as can be seen in Figure 11.4, the load in both members will be equal. The L-shaped stiffener design was chosen because this is the most simple design. The crippling stress can be calculated with Equation 11.7, which then needs to be compared to the actual maximum stress in a stiffener.

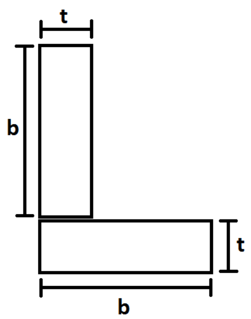

Figure 11.4: Cross-sectional view of the stiffener design

$$P_{CR} = \frac{\pi^2 EI}{l^2} \tag{11.6}$$

$$\sigma_{crippling} = \frac{1.63}{\frac{b}{t}^{0.717}} \cdot \sigma_{ult} \tag{11.7}$$

When all these checks are performed and the design did not fail any of the checks, the current design can sustain all the loads. However, it is still possible that the fuselage will be over-designed. In order to judge this several ratios have been defined.

$$\frac{\tau_{actual}}{\tau_{max}}, \frac{\sigma_{actual}}{\sigma_{max}}, \frac{\sigma_{buckling}}{\sigma_{actual}}, \frac{I_{stiff}}{I_{stiff,req,buck}}, \frac{\sigma_{crippling}}{\sigma_{stiff}} \tag{11.8}$$

Note that all these ratios are defined in such a way that if they are all bigger than or equal to one, the design is sufficient. Ideally they would all be equal to one because this would mean that the design is not over-designed at all. Using these ratios, the design can be optimized on a trial and error basis.
To simplify the whole design process, a MATLAB-code was written that incorporates all of the above mentioned equations. The verification strategy for this MATLAB-code can be found in Section 11.3.

11.2 INPUTS AND RESULTS

The most important inputs for the fuselage design are all the forces that act on the fuselage and thus the weight and location of all the components. An overview of weight and position of each subsystem is provided in Table 11.1. It was found that when the skin thickness is 1.7 mm and there are 5 stiffeners on each half of the fuselage (10 in total) with an area of 43 mm^2 each, the design is optimal with a mass of 26.1 kg. This is the mass of the simplified fuselage and thus not equal to the exact mass of the fuselage. Therefore the Class II estimation will be used for reference at this stage of the design. The stiffener thickness is assumed to be the same as the skin thickness. This means that the width of the flanges is 12.6 mm.

Table 11.1: Weight and cg locations of all subsystems resulting from the final design iteration

Component	**Weight [cg]**	**CG [m]**
Wing Group	50.7	2.83
Canard	21.8	0.16
Nose gear	12.2	0.4
Payload + Cockpit	108.5	1.93
Fuselage Group	40.7	2.20
Electronics Group	17.1	2.36
Battery Group	100.7	2.54
Vertical tail	3.0	2.65
Main gear	16.5	2.82
Motor	26.2	3.72
Propeller	17.6	3.92
MTOW	415.0	2.34

Recommendations

The proposed structural design of the fuselage is not finalized yet. This implies that there are still means to further improve the design and make it more complete. This includes:

- Consider cut-outs in the design. Taking cut-outs into consideration will imply some local skin thickening or adding local stiffeners to support the local stress concentrations due to these cutouts. Several major cutouts ought to be included, such as a cut-out for the cockpit, several cut-outs for the wing-fuselage connection and various cut-out for maintenance and inspection hatches.
- Consider a method to join the stiffeners and the shell. This could be done by using bolts or other fasteners, an adhesive layer, stitching or co-curing of the different parts.
- Vibrations and fatigue loading were not considered in this design. To complete the design, a fatigue analysis should be performed and the dynamic loading of the fuselage should be analysed as well.
- In order to minimize the drag of the fuselage, an aerodynamic design of the fuselage should be performed.
- The current fuselage cross section is symmetric, meaning that the skin thickness is constant and all (equal area) stiffeners are equally spaced. However, the stresses are not constant along the cross section and therefore many parts of the cross section are over-designed based on the current loading. In order to minimize the fuselage weight, an elaborate fuselage design optimization should be performed. It is expected that this would result in a smaller stiffener spacing in the bottom and top of the fuselage and larger stiffener spacing around the centre-line in order to maximize the contribution of the stiffeners to the area moment of inertia. This might decrease the number of stiffeners needed and therefore reduce the fuselage weight.
- The current fuselage design is highly simplified and designed using only some structural requirements. The actual final fuselage design should be a compromise between a structural and aerodynamic optimization in order to decrease fuselage drag as well.

11.3 VERIFICATION AND VALIDATION

In this section the verification strategy for the MATLAB-tool used to design the fuselage is presented, as well as the planned validation techniques for future stages of development.

First of all, the resulting loading plots from the tool were analysed in order to verify that the boundary conditions were met. $M_Z(x)$, $S_Y(x)$ and $T(x)$ should all be zero at the ends of the fuselage. The loading diagrams were also analysed by checking whether each load "jump" could be explained with respect to the inputs.
As with all structural design tools, also a sensitivity analysis was performed by varying the input values and checking whether the changes in results made sense with respect to sign and order.
During future stages of development the analytically determined stresses from our MATLAB-tool could be verified using more advanced numerical finite-element methods (FEM). It is however also recommended to use FEM to come to the final design for E-SPARCs fuselage.

The validation of the fuselage is slightly more advanced than most other subsystems. First of all, test should be performed on plates, so-called coupons, of the chosen material to validate the theoretical yield stresses. In addition, load test ought to be performed on separate fuselage sections, as well as on the complete fuselage. During these tests, the strains should also be monitored because it is possible that the fuselage does not fail under the loads, but that bending moments result in unwanted incidence angles for the wing or canard.

III

AIRCAFT ANALYSIS

12 Performance Analysis

Now that a preliminary design of the aircraft has been completed, it is possible to find out how the E-SPARC would perform in a Red Bull Air Race, compared to its current competitors. This is done by performing a track analysis. Such an analysis takes the aircraft parameters and the coordinates of a track and calculates the time required for the aircraft to race around the simulated track. In addition to the track analysis, a noise footprint has been computed for E-SPARC as well as a performance diagram to compute the aircraft's service ceiling.

The method used to define the track analysis is described in Section 12.1, the results of the analysis and the comparison to the current aircraft is described in Section 12.2. Section 12.3 shows the steps conducted to calculate the noise footprint and Section 12.4 shows the performance diagram.

12.1 Track Analysis

A Python program was written to perform the track analysis. This program is used to provide an expected track time for an aircraft with given aircraft parameters. The program is also able to check whether the aircraft is able to fly the provided track by checking the load factor of the aircraft in each turn. Section 12.1.1 gives a summary of the program layout and its features. Sections 12.1.2 and 12.1.3 present the equations used in the track analysis program.

12.1.1 Program Layout

Figure 12.1 shows the general program layout of the Python program. The big block with double lines shows the content of the main program, used for the computations of each discretized track segment. The discretization of the track is done prior to running the main program as indicated some of the blocks in the top left corner of the flow diagram and as further explained in detail in Section 12.1.3.

Within each track segment firstly the load factor is calculated. This is done based on the radius of curvature of the current segment of the track and the current airspeed (see Section 12.1.2). Following this, the angle of attack is computed, after which the forces acting on the aircraft are determined for a given track segment. Using these forces the acceleration of the aircraft can be calculated, which in combination with the required time for the current segment of the track results in the calculation of the airspeed for the next segment. This new airspeed is used as the starting parameter for the next discretized segment.

By summing the time required for each discretized track segment, the total track time can be computed.

12.1.2 Equations Of Motion

The movement of the aircraft is determined by the forces that act upon it. For this reason it is important to be able to calculate the lift, weight, drag and thrust. To calculate these forces the angle of attack and the load factor are required.

The load factor is the relation between the lift and the weight ($N = \frac{L}{W}$). The load factor is used to calculate the angle of attack, which is in turn needed for the lift and drag calculations. Figure 12.2 shows the forces that act on the aircraft when it is in a turn. For these turns it is assumed that the aircraft does not lose altitude during its manoeuvre. Therefore L_v, the vertical component of the lift force, is equal to the weight (Equation 12.1). L_h in the figure is the horizontal component of the lift force and is equal to the centripetal force of an object in circular motion with speed, V, and a radius of curvature, R, as is seen in Equation 12.2.

$$L_v = W \tag{12.1}$$

$$L_h = \frac{m \cdot V^2}{R} \tag{12.2}$$

From the lift forces and the weight the load factor can be determined using the Pythagorean theorem, as seen in Equation 12.3.

$$L = \sqrt{L_v^2 + L_h^2} \Rightarrow N = \frac{L}{W} = \frac{\sqrt{W^2 + \frac{m \cdot V^2}{R}^2}}{W} \tag{12.3}$$

The radius of curvature of a particular point in the track can be calculated using the current, previous and next xyh coordinates of the track as shown in Equations 12.4 through 12.8. However, this does means that a problem occurs at the start and finish of the track as only two points are available. For this reason two points should be added in line with the starting/finish gate heading, one before entering the track and one after finishing to also

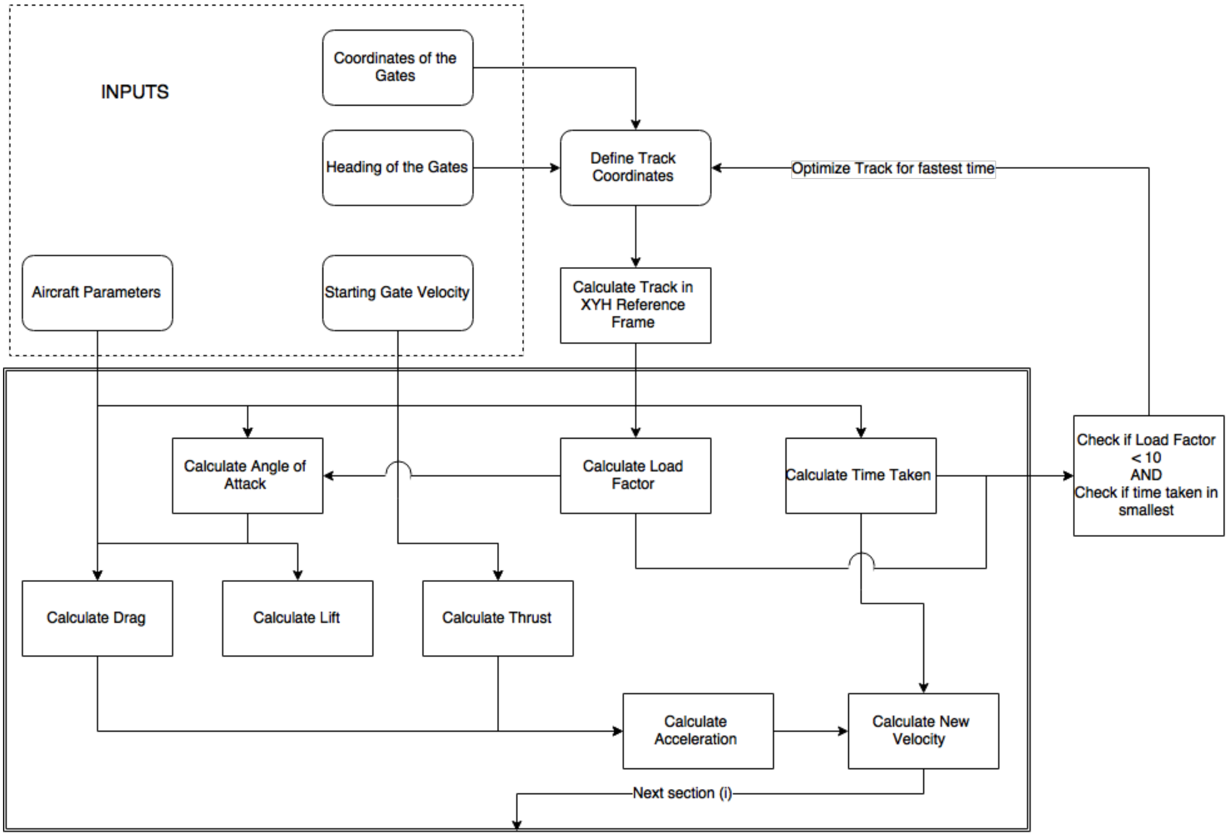

Figure 12.1: Program Layout of the Track Analysis Program

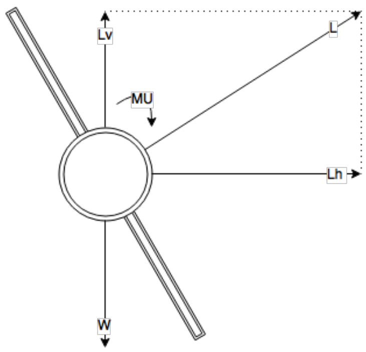

Figure 12.2: Illustration of the forces acting on the aircraft in a turn

allow for computation of the radius of curvature for the first and last discretization steps.

$$A = \left\| \begin{bmatrix} x_{i-1} \\ y_{i-1} \\ z_{i-1} \end{bmatrix} - \begin{bmatrix} x_i \\ y_i \\ z_i \end{bmatrix} \right\| \tag{12.4}$$

$$B = \left\| \begin{bmatrix} x_{i-1} \\ y_{i-1} \\ z_{i-1} \end{bmatrix} - \begin{bmatrix} x_{i+1} \\ y_{i+1} \\ z_{i+1} \end{bmatrix} \right\| \tag{12.5}$$

$$C = \left\| \begin{bmatrix} x_i \\ y_i \\ z_i \end{bmatrix} - \begin{bmatrix} x_{i+1} \\ y_{i+1} \\ z_{i+1} \end{bmatrix} \right\| \tag{12.6}$$

$$s = \frac{A+B+C}{2} \tag{12.7}$$

$$R = \frac{A \cdot B \cdot C}{A \cdot \sqrt{s \cdot (s-A) \cdot (s-B) \cdot (s-C)}} \tag{12.8}$$

Now that the load factor is known, the angle of attack is calculated using Equation 12.9 which is a function of the velocity, load factor, the lift slope (C_{L_α}) and the wing area (S). Since the differences in height during a race are relatively small the air density, ρ, is assumed constant. The angle of attack is used to calculate the lift and the drag.

$$\alpha = \frac{2 \cdot W \cdot n}{C_{L_\alpha} \cdot \rho \cdot V^2 \cdot S} \tag{12.9}$$

For an electric aircraft such as E-SPARC the weight, W, remains constant. For other aircraft it is assumed that, since the race is over a short period of time, the weight remains constant as well for the duration of the flight.

The lift, L, that the aircraft produces is calculated using Equation 12.10 and is a function of the angle of attack, α, and the velocity, V.

$$L = C_{L_\alpha} \cdot \alpha \cdot \frac{1}{2} \cdot \rho \cdot V^2 \cdot S \tag{12.10}$$

The drag, D, acting on the aircraft is calculated using Equation 12.11. Besides using the lift coefficient the equation for the drag uses the zero-lift drag coefficient, C_{d0}, which is constant.

$$D = \left(C_{d0} + \frac{\left(C_{L_\alpha} \cdot \alpha\right)^2}{\pi \cdot A \cdot e} \right) \cdot \frac{1}{2} \cdot \rho \cdot V^2 \cdot S \tag{12.11}$$

The thrust, T, that the aircraft produces is dependent on the power available, P_a, of the aircraft and the velocity of the aircraft as is seen in Equation 12.12.

$$T = P_a \cdot V \tag{12.12}$$

The velocity for the next section is calculated using the acceleration as shown in Equations 12.13a and 12.13b. The time derivative, dt, is calculated based on the current airspeed and the distance traveled in the track over the current discretized segment.

$$\frac{dV}{dt} = \frac{T}{m} \cdot cos(\alpha) - \frac{D}{m} - g \cdot sin(\gamma) \tag{12.13a}$$

$$V = \frac{dV}{dt} \cdot dt \tag{12.13b}$$

12.1.3 DEFINING THE TRACK

The track selected for the track analysis is based on the 2008, San Diego, Red Bull Air Race track. From literature study both the coordinates of all the gates, as well as the required headings to fly through each gate were obtained for this specific track [112]. These coordinates are defined based on the Geodetic system, using latitudinal and longitudinal angles to describe their respective position with respect to the center of the Earth.

As it is desirable to have the origin of the reference frame located at the position of the starting gate of the track, a transformation was required from the inertial reference frame to a vehicle carried reference frame, the vehicle being the stationary starting gate. This first required the definition of the vectors of the Earth fixed reference frame based on the angles of latitude and longitude, see Equations 12.14a to 12.14c. Following this definition, the transformation from the Earth fixed reference frame to the desired reference frame at the starting gate position could be performed. By fixing the reference frame to the position of the starting gate, the Earth's rotation will be ignored in the track analysis, an assumption that can be made given the relatively low velocity of the aircraft with respect to the Earth's velocity and the relatively short time period to fly around the track. Ignoring the Earth's rotation implies that the Earth rotating frame (C-frame) and Earth fixed inertial frame (I-Frame) coincide. This entails that the Z-axis of the Earth inertial frame is aligned with the Earth's rotational axis and that the X-axis is directed towards Greenwich, zero longitude [113]. The goal of the transformation is to obtain a reference frame located at the Earth's surface, with an axis system such that the z-axis points away from the Earth's surface, the y-axis pointing towards the east and the x-axis pointing south.

$$x = R_{Earth} \cdot cos(\tau) \cdot cos(\delta) \tag{12.14a}$$

$$y = R_{Earth} \cdot sin(\tau) \cdot cos(\delta) \tag{12.14b}$$

$$z = R_{Earth} \cdot cos(\pi - \delta) \tag{12.14c}$$

To obtain this desired reference frame, three rotations and one translation are required. First a rotation about the z-axis is performed to align with the desired latitude. Provided that San Diego lies on the Western hemisphere, this is achieved by a negative rotation about the z-axis, with the required angle τ equivalent to the latitudinal angle of the first gate. Following are two rotations about the y-axis. First, a negative rotation about the y-axis with the angle δ to align the reference frame with the desired longitudinal position of the first gate of the San Diego track. This will result in the x-axis pointing away from Earth, rather than the z-axis. Hence, a final positive rotation about the y-axis of 90 degrees will result in the desired orientation of the reference frame. An overview of the transformation matrices for the required rotations is given below by Equations 12.15 and 12.16.

$$F_E = T_y(\pi/2 - \delta) \cdot T_z(-\tau) \cdot F_C \tag{12.15}$$

$$F_E = \begin{bmatrix} sin(\delta) & 0 & -cos(\delta) \\ 0 & 1 & 0 \\ cos(\delta) & 0 & sin(\delta) \end{bmatrix} \cdot \begin{bmatrix} cos(\tau) & -sin(\tau) & 0 \\ sin(\tau) & cos(\tau) & 0 \\ 0 & 0 & 1 \end{bmatrix} \cdot F_C \tag{12.16}$$

With the required transformation known, all gates coordinates as obtained from literature can be transformed to the desired reference frame located at the starting gate of the track. What remains is to position the reference frame at the Earth's surface, rather than at the center of the Earth. This is done by subtracting the values of the x, y and z coordinates of the starting gate from all gates (including the starting gate itself) such that the coordinates of all gates are defined with respect to the first gate. With the relative locations of the gates known, a first simplified track trajectory can be plotted by simply connecting the gates with vectors that form straight lines in between the gates. This simplified track is not flyable as the changes in heading are instantaneous and too large to be physically possible. Hence, the next step of the track definition is to find the optimal flight trajectory, such that the track time is minimized. To accomplish such a track optimization two different approaches have been applied, of which only one proved successful. Nevertheless, both approaches will be elaborated upon to serve as a basis for future third parties that desire to improve these approaches.

First Approach

The methodology of the first approach is illustrated in Figure 12.3. The approach first discretizes the straight line between the gates in small segments by defining a large quantity of points on this straight line, for example by using linear spacing. As aforementioned, this straight line track between each of the gates is not flyable. Hence, the problem to be solved is to define a track such that the heading change from one segment of track to the next becomes flyable. Whether or not a segment of track is flyable depends directly on the bank angle μ and the load factor. Therefore, one possible reason for a non flyable trajectory would be that the change in heading is larger than what can be achieved while the aircraft is flying knife-edge, or with 90 degrees of bank. Another possibility is that the aircraft can fly the required heading change, but that in doing so the maximum allowable load factor as predicated by Red Bull Air Races is exceeded in order to do so.

In order to obtain a flyable track with small enough changes in heading in between the discretized steps, an approach was developed by which the discretized points are displaced gradually until the location of two consecutive points is such that the respective change in heading becomes flyable. Using the headings of the entry and exit gate of one section of track, unit vectors were defined with a specific orientation for each of the discretized points, see the dotted lines in Figure 12.3. The discretization points are displaced by adding the length of the vector to its original position. The code of the program was developed such that whenever the load factor

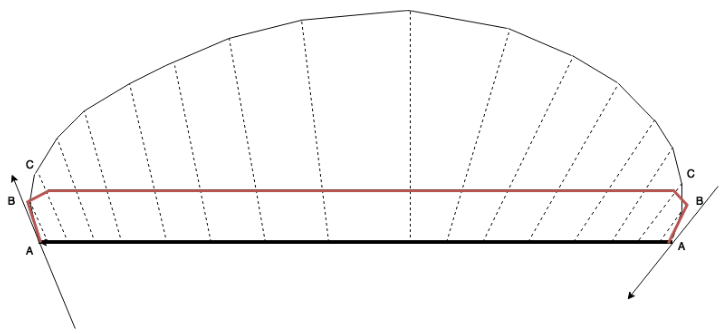

Figure 12.3: A schematic representation of approach 1 in the track optimization

would be exceeded or whenever the required bank angle is larger than 90 degrees for a given point, an error would be identified for that particular point. This error would trigger the response to displace the point next to the error by adding the length of the unit vector corresponding to that point. These iterations then continue until the error is removed, at which point the heading change has been reduced such that this segment of the track has become flyable.

For example, the very first iteration would give errors at two locations, namely the two gate locations. The reason being that the heading of the gates is significantly different from the heading of the straight line in between the gates, and thus from the heading of the first and last discretization points on the straight line. This will trigger the program to displace the first and last discretization points, as well as all points lying in between it, until this error is removed. Once this error is removed, errors will occur for the two most outward points and hence the points next to these have to be displaced. This is illustrated by the red line shown in Figure 12.3. One can see that the for the outer most points, indicated by A, the errors have been resolved. However, there still exists an error for the points indicated by B, which has to be resolved by displacing points C. By this method the displacement moves inward until all errors are removed. The black track outline would be an estimate of what the optimized track could look like.

This approach proved successful for a simplified track analysis of just 10 points. However, upon using this approach for the actual track, iterations continued indefinitely. This would entail that the heading errors were not resolved by the program for a given point and as such it kept increasing the length of the vectors for these points. This error may be attributed to various possible causes. It could be there is an error in the computation of `dCHidt`. This would imply that the program does not correctly calculate the change in heading between two consecutive discretization points. Another possibility would be that the list `errors` is not properly refreshed with each iteration, meaning that the present error locations would remain in the list even when the errors should be removed. Another possibility is a bug in the segment of code where the unit vector is added. A possible bug would be that this segment of code only works for the first two discretization points, but not for the rest of the discretization points. This would imply that the even when the error is removed, the unit vector keeps being added these first two locations. All of these causes would imply that the program enters an infinite loop, rather than progressing from one discretization point to the next. Efforts to find the exact cause and resolve this coding error were unsuccessful in the given time span and ultimately this approach was abandoned for the more simplified but successful second approach.

Second Approach

The second approach is not so much focused on obtaining the optimal track trajectory, but rather on obtaining a feasible trajectory that might have been flown during the 2008 San Diego Red Bull Air Races. Thus for this approach, an initial estimate of the trajectory of the track in between the gates was obtained using literature study, see Figure 12.4[114][112]. With the coordinates of and headings at the gates, as well as using the trajectory shown by literature, a trajectory was estimated by estimating the locations of points on that trajectory. Google Earth was used to assists in estimating the locations of these points based on the prior mapped gate locations. In Appendix C an overview is given of the coordinates of all of the points used to define the track trajectory.

Thus, similar to approach 1, also for this approach the track was discretized with points, but now the locations of these points were simply estimated using literature, rather than determining the optimal location of each point as was planned for approach 1. Using the same transformation as had yet been applied to the gate coordinates,

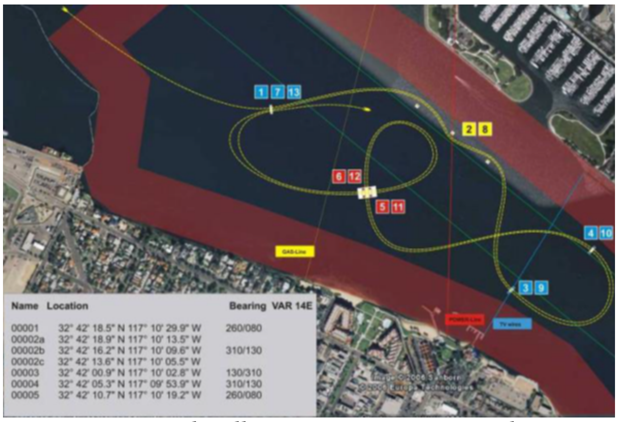

Figure 12.4: Red Bull Air Race San Diego track (2008) [114]

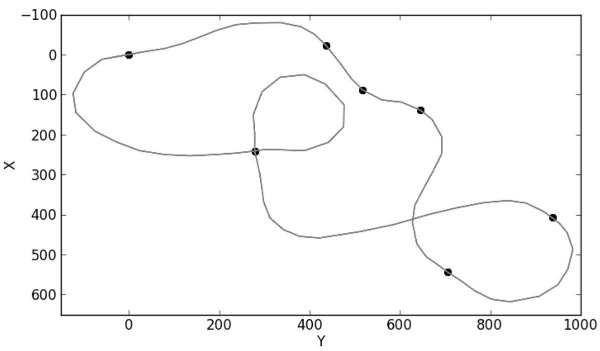

Figure 12.5: Estimated trajectory of 2008 San Diego Red Bull Air Race track as implemented in Python

all discretization points were also transformed to the same reference frame. Figure 12.5 shows the resulting track as used in the further computations of the track analysis. Important to note is that the track as shown in Figure 12.5 is merely an estimation of a possible trajectory that might have been flown during the 2008 Red Bull Air Races. It is by no means optimized yet for optimal track time. Some minor alterations were made to coordinates to ensure that the load factor would not exceed the maximum allowable load factor of ten, as predicated by Red Bull Air Race regulations. In addition to the locations in the x and y frame, also an estimate for the height at each point on the trajectory was made. This was estimated from race videos [112]. Additionally, the assumption was made that the height at which the aircraft passes through the gates is always 14 meters. This assumption is based on Red Bull race regulations that stipulate that the flying window for the gates is in between ten and fifteen metres [115].

12.2 Track Analysis Results

Perhaps the most significant performance analysis parameter is the time required to complete the track. As aforementioned for a given discretization step on the trajectory all input variables, such as velocity, acceleration and forces are considered constant. This results in a time for each discretization step, which, when summed, results in the total track time. Furthermore, as in the Red Bull Air Races two laps are flown around the track, two consecutive laps are also simulated with the track analysis. Thus the time count is started at the starting gate and stopped after completing two full laps.

Provided that the track coordinates are not altered, the track time is an objective method to compare the performance of E-SPARC with other existing aircraft. From literature a different track simulation was found, which was based on the aircraft characteristics of the Extra-300S [116]. This aircraft also participated in the actual 2008 San Diego Red Bull Air Races, flown by French pilot Nicolas Ivanoff [117][118]. Therefore, the Extra-300S was selected as reference aircraft to compare its performance around the track with the performance of the E-SPARC.

The track analysis program requires several aircraft parameters as input. The inputs for the EXTRA-300S and the E-SPARC can be found in Table 12.1. In this table it can be seen that the EXTRA-300S requires more input parameters than the E-SPARC. This is due to the fact that the lift slope was not known for the EXTRA-300S and had to be calculated using Equation 12.17. The variables β, η and F are defined by Equations 12.18 through 12.21. For the power available of both aircraft it has to be noted that the motor and propeller efficiency are already included. The effective aspect ratio of E-SPARC in Table 12.1 is the aerodynamic aspect ratio rather than the geometric aspect ratio, this value takes into account the winglets that E-SPARC uses [44, p. 47].The entrance velocities of the EXTRA-300S and E-SPARC are based on the maximum entrance speed according to RBAR regulations. It was, however, checked to see if the aircraft could reach this speed. For E-SPARC reaching a starting gate velocity of $102.89 m/s$ requires a small dive as its maximum level velocity is $101.6 m/s$.

The resulting track times for the Extra-300S and E-SPARC are given in Table 12.2.

Table 12.1: Input aircraft parameters for the EXTRA-300S and the E-SPARC [116]

Parameter	**EXTRA-300S**	**E-SPARC**
Gravitational constant $[m/s^2]$	9.81	
Air density (sea level) $[kg/m^3]$	1.225	
Entrance velocity $[m/s]$	102.9	102.9
Aircraft mass $[kg]$	612.2	415.0
Power available $[W]$	211,560	115,520
Wing area $[m^2]$	10.44	5.16
Effective aspect ratio [-]	5.39	7.2
Oswald factor [-]	0.89	0.78
Zero-lift drag coefficient [-]	0.02587	0.034
Maximum 3D lift coefficient [-]	1.535	1.78
Lift slope [1/rad]	4.62	4.71
Additional values required for EXTRA-300S		
Wing span $[m]$	7.5	-
Fuselage diameter $[m]$	1.0	-
Mach number [-]	0.30	-
Sweep angle at thickest point on the airfoil $[rad]$	0.0	-
Exposed wing area $[m^2]$	10.14	-

$$C_{L_\alpha} = \frac{2\pi \cdot A}{2 + \sqrt{4 + \frac{A^2 \cdot \beta^2}{\eta^2}\left(1 + \frac{tan(\Delta_{max_t})}{\beta^2}\right)}} \cdot \frac{S_{exp}}{S} \cdot F \quad (12.17)$$

$$\beta^2 = 1 - M^2 \quad (12.18)$$

$$C_{l_\alpha} = 2\pi \quad (12.19)$$

$$\eta = \frac{C_{l_\alpha}}{\frac{2\pi}{\beta}} = \beta \quad (12.20)$$

$$F = 1.07 \cdot \left(1 + \left(\frac{d_f}{b}\right)^2\right) \quad (12.21)$$

Table 12.2: Track times for the Extra-300S and E-SPARC

	Extra-300S	**E-SPARC**
Track time [s]	87.17	95.28

From Table 12.2 it can be seen that the E-SPARC aircraft is 8.1 seconds slower than the Extra-300S. This difference also becomes visible in the graphs in Figures 12.6 and 12.7 depicting the velocity with respect to time as well as the load factor as a function of the trajectory points. The time difference is a result of the difference in velocities, as shown in the velocity graph. The main reason for the velocity difference is the lower available power and higher form drag of the E-SPARC aircraft. From Table 12.1 it can be seen that the E-SPARC only has 80 percent of the power to weight ratio of the Extra-300S. Furthermore, the lower form drag of the Extra-300S implies that the overall drag is larger for the E-SPARC aircraft. The higher velocity of the Extra-300S also implies a higher centripetal acceleration, which results in a higher load factor for a given point on the track, which is visible from the graph in Figure 12.7. Although a higher load factor also implies more drag, this additional drag is outweighed by the higher power to weight ratio of the Extra-300S. Thus, overall the Extra-300S has a larger resultant force in the direction of flight, resulting in a higher acceleration and thus a higher overall velocity throughout the track. Based on these results, it may be concluded that in further design iterations the power to weight ratio of the E-SPARC design should be increased to achieve more competitive results.

As aforementioned the Extra-300S participated in the 2008 Red Bull Air Races in San Diego. One of the contestants flying the EXTRA-300S was Nicolas Ivanoff who finished 10th in that particular race with a track time of 83.14 seconds[117]. This is roughly four seconds faster than the current time the Extra 300S achieves around the simulated track. If the track would be fully optimized it is to be expected that the Extra-300S would achieve a faster track time than what it achieved in the real life race. This is due to the fact that the simulation does not account for, e.g. wind and pilot error. The current time difference between the the real life race and simulated track is that the trajectory of the track currently being flown is not optimized. Rather, it is a flyable track for both the Extra-300S and the E-SPARC aircraft. It is therefore safe to assume that a much better track time would be achieved when the track is further optimized. The optimization of the trajectory is a trade-off between the load factor and the distance to be flown. Increasing the radius of curvature further than needed would reduce the load factor and thus the drag, however this comes at the expense of a longer distance. Alternatively, increasing the load factor by following a tighter trajectory than currently being used would shorten the distance to be flown, but at the expense drag penalties.

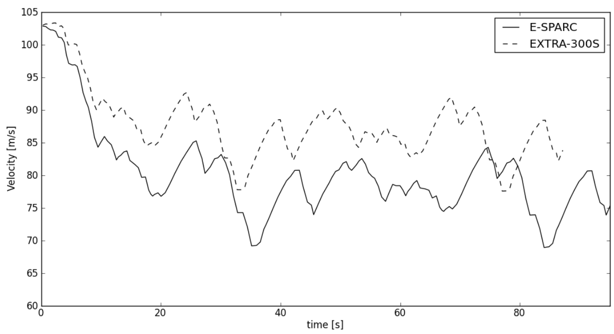

Figure 12.6: The velocities of E-SPARC and the Extra-300S as a function of time for two laps

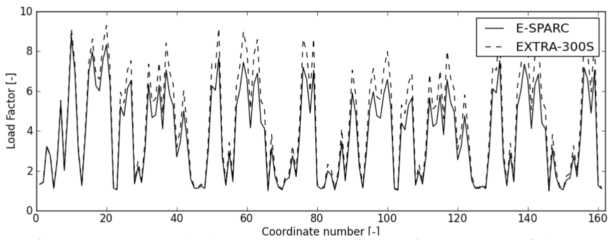

Figure 12.7: The load factors of E-SPARC and the Extra-300S as a function of the points on the track for two laps

12.2.1 RECOMMENDATIONS

Several technical and non-technical recommendations can be made to improve the quality of the track analysis tool. First and foremost, it is highly recommended to start the development of the track analysis tool as soon as possible. Although a non-technical recommendation, a better planning would have allowed a much more detailed track analysis tool than currently presented. Moreover, the results from the track simulation may then also be used as input for further design iterations. The comparison between E-SPARC and one of the current Red Bull Air Race aircraft showed for example the need to increase E-SPARC's power to weight ratio, as well as the need to reduce the form drag.

When starting earlier the track analysis tool can be developed such that the optimal flight trajectory can be found. As already mentioned, the optimization will be a trade-off between flying faster by slightly increasing altitude in tight turns or to fly a tighter turn slower by maintaining altitude. Thus, the optimized track would provide the best possible flight path in order to minimize the track time, while staying within the limits of the aircraft, Red Bull Air Races and physics. Optimizing the track would also include refining the discretization steps further. Even when the optimisation is done manually, it is recommended to use more points to get more accurate results. Currently about 80 points have been defined on the entire trajectory. Although this is a significant amount, better more realistic results are obtained when these discretization step sizes are further decreased by using more points on the trajectory. By doing so the assumption that changes in bank angle, velocity, acceleration, forces etc. occur instantaneous becomes more accurate.

Another recommendation to further improve the accuracy of the actual track times would be to find out what atmospheric conditions were present that day and to incorporate these in the model. In particular the effect of wind plays a significant role on the flight path of the pilots, thus also affecting the track times. This recommendation would require more advanced equations of motion which also incorporate the force of the wind, which will have a varying orientation with respect to the body reference frame of the aircraft for different positions around the track and may therefore proof to be difficult to incorporate. In general looking into more advanced equations of motions is recommended for a more realistic result.

Finally, for calculating the load factor the vertical lift component was assumed to be the same as the weight. This assumption was used to simplify the equations but, when making a more accurate analysis should include the actual vertical force. This force can be calculated from the change in height of the aircraft.

12.2.2 VERIFICATION AND VALIDATION OF THE MODEL

To make sure the track simulation code works for all cases the code was verified. This was done in a number of ways. Firstly unit tests were performed for each function in the program, this included a sanity check, an analytical comparison and a singularity check. Next the code to compose the track was verified by changing the gate locations input to a completely different track. Lastly the overall code was checked by running the program for two different aircraft. The latter two were specifically used to check the code for robustness.

UNIT TESTS

Each of the functions in the program can be seen as a unit, for example each of the equations of motion has its own function but there is also a `GateLocations` function that turns the input geodetic coordinates into a XYH coordinate system. Most of the units were verified without issues, for example the `drag` function, which is just an equation. As long as the user puts in reasonable input variables the program will give the correct output, e.g. a negative aircraft length will yield incorrect results.

For the following functions some singularities have been found that are worth discussing; `alpha`, `GateLocations`, `LoadFactor`.

`GateLocations`

During the verification process it became clear that the function that converts coordinates to XYH coordinates is not robust to all possible tracks. If the track partly is above the equator and partly is below the equator, the geodetic latitude coordinates are suffixed partly with a N and partly with a S. However, the program requires the user to make a choice between N and S for the whole group of coordinates. The same is the case for the meridian with east and west. Since the chance that this situation occurs is very small, it was chosen to leave the responsibility for correctly implementing the coordinates with the program user. For example, in case of the occurrence of both N and S the user will need to add a minus sign in front of all coordinates that lie on the other hemisphere. The same is true for the meridian.

`alpha`

The Equation for lift (Equation 12.10) assumes a linear C_{L_α} curve. This assumption is valid for low angles of attack but when the aircraft gets close to its stall angle this assumption is no longer valid. For this reason an error message was implemented in the code when the angle of attack that corresponds with stall, is reached.

`LoadFactor`

To calculate the load factor the radius of curvature has to be calculated. Equation 12.8 can lead to some singularities that could occur if another track would be used. The used track does not have any perfectly straight parts which means all points on the track have a valid R. However, if a straight track would be used as an input for the program, the radius of curvature would go to infinity. During the verification process this singularity was found and a fix for this problem was implemented.
Also it would have been an issue in the program if the track would have two consecutive points with exactly the same coordinates. This leads to a radius of curvature of zero, which raises an error. To make the program more robust in this respect, the code has been adjusted such that the program in case of two consecutive points have the same coordinates, the program will look back one extra discretization step to get rid of double points on the

same location.

PROGRAM ROBUSTNESS

The robustness of the track analysis program was tested by verifying that the program still functions as it should for different input variables. Hence, lack of robustness would entail that the program would produce an error when the input values are changed. This was tested by changing both the input values of the aircraft parameters as well as by changing the coordinates.

For the track robustness a completely different track was used as an input (see Table C.2. For this verification track and the real track it was checked whether the peaks in load factor made sense and if they truly occur at the steepest turns. The implementation of a new track and the added functionalities in the `GateLocation` and `LoadFactor` functions(as aforementioned), resulted in a program that is verified for track robustness.

Besides the track, the program should also be verified for use of different aircraft parameter inputs. This option was verified by using two different aircraft. Again, it was checked whether changes in certain aircraft parameters resulted in outputs that made sense. For example, lowering the power available resulted in a lower airspeed and longer track time, whereas lowering the zero-lift drag coefficient resulted in a higher airspeed and shorter track time. This approach was taken for all of the parameters.

VALIDATION PROPOSAL

In order to validate the track simulation model actual flight data is required from a race aircraft that flies along a particular track. This data could be obtained by installing required measurement equipment in an actual race aircraft. This equipment will register the aircraft's accelerations, position, altitude, G-loads, airspeed etc. with a given time step. By implementing the aircraft parameters of the aircraft used to obtain the validation data into the track analysis program and comparing the outcome from the track analysis with the actual flight data a proper validation of the track analysis tool can be performed.

12.3 NOISE CHARACTERISTICS

Since aircraft noise pollution should be kept to a minimum and at the same time, noise is one of the factors that draws attention to the aircraft in the air races, it is important to know the noise footprint of E-SPARC.

This section explains all the steps that were conducted to create a noise footprint of the aircraft. During these steps the fact that the E-SPARC has a pusher propeller is neglected. A pusher propeller receives more turbulent air compared to puller propeller, which results in more noise. A pusher prop has also a higher pitch sound compared to a puller propeller.

The method used to calculate the noise footprint is done using the steps of NASA's method to estimate noise from propellers [119]. The first step that was performed was finding the reference level of the noise, based on the power input of the propeller, this was done using Figure 12.8. Since the required power of 115kW (155hp) is known the reference value was estimated to be around 117 dB.

The next step was finding correction values for the propeller. The first correction value is found with Equation 12.22, where B is the number of blades. The second correction value depends on the diameter, D, in feet. This is shown in Equation 12.23.

$$C_{propeller_{blades}} = 20 \cdot log(\frac{4}{B}) \tag{12.22}$$

$$C_{propeller_{diameter}} = 40 \cdot log(15.5/D) \tag{12.23}$$

The third step is also finding a correction factor, which depends on the rotational speed of the propeller. This is done by first calculating the tip Mach number and finding the correction value using Figure 12.9. The reference point to the propeller disc, Z, is assumed to be 1 ft, this leads to a correction factor of -4 dB.

The next correction value depends on the angle of the propeller heading towards the observer. It therefore accounts for the directional characteristics of sound propagation from the propeller. The correction value can best determined with Figure 12.10. this has been done for an angle of 50° to 160° with steps of 10°. The final step is determining the correction factor at a certain distance. Here several distances are selected at each angle. The correction factor depending on the distance has been calculated with Equation 12.24, here S is the distance in feet from the centre of the propeller.

$$C_{distance} = -20 \cdot log(S-1) \tag{12.24}$$

Table 12.3 contains all the correction factors calculated for the fuselage, amount of blades, diameter and rotational speed. Summing all the correction factors up including the noise reference value at each angle and

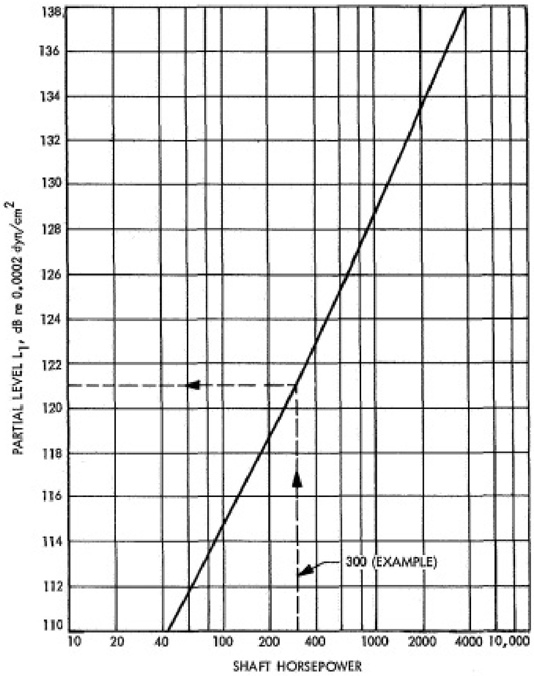

Figure 12.8: Reference Noise vs Shaft Horsepower

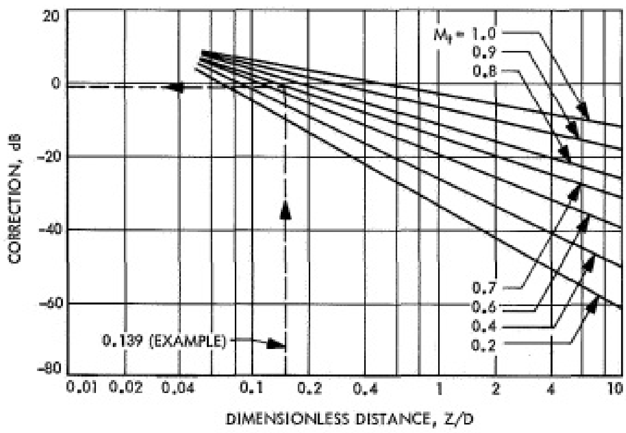

Figure 12.9: Correction for speed and radial distance

Table 12.3: Noise correction factors

Correction Factor	Noise [dB]
Correction Factor for number of blades	2.5
Correction Factor for blade diameter	18.6
Correction Factor for rotational speed	-4
Correction Factor with no fuselage	5
Correction Factor with fuselage	1
Distance 65ft	-36
Heading Angle 60°	-10
Total	93.0

distance results in a noise footprint shown in Figure 12.12. Figure 12.12 also includes an additional correction factor which is dependant on the position of the fuselage. The fuselage reduces the propeller noise, when the fuselage is between the observer and the propeller. This correction factor is determined with Figure 12.11 where it is assumed that the fuselage is a circular wall. While the selecting the correction factors the maximum and minimum values are selected in figure 12.11.

12.4 PERFORMANCE DIAGRAM

This section explains the performance diagram of the E-SPARC and how it is constructed. Figure 12.13 shows the power available against the required power. The required power has been determined with equation 12.25.

$$P_{required} = c_{D_0} \cdot \frac{1}{2}\rho V^3 \cdot S + \frac{W^2}{\frac{1}{2}\rho V \cdot S \cdot \pi A e} \tag{12.25}$$

The available power changes with altitude, due to the density. Therefore Equation 12.26 is used.

$$P_{available} = P_{available_0} \cdot \left(\frac{\rho}{\rho_0}\right)^{0.75} \tag{12.26}$$

Next the flight ceiling is determined. This is done by determining limiting factors, such as the stall speed, power limit and energy limit. The first curve that is determined is the stall speed at different heights for which Equation 12.27 is used.

$$V = V_0 \sqrt{\frac{\rho}{\rho_0}} \tag{12.27}$$

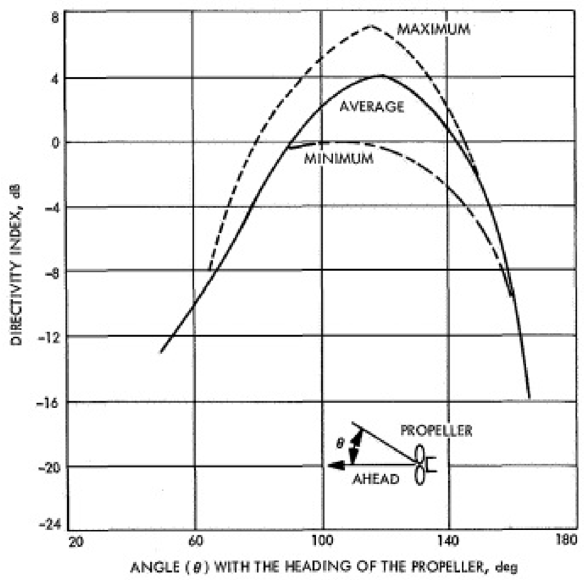

Figure 12.10: Polar distribution of overall noise levels for propellers

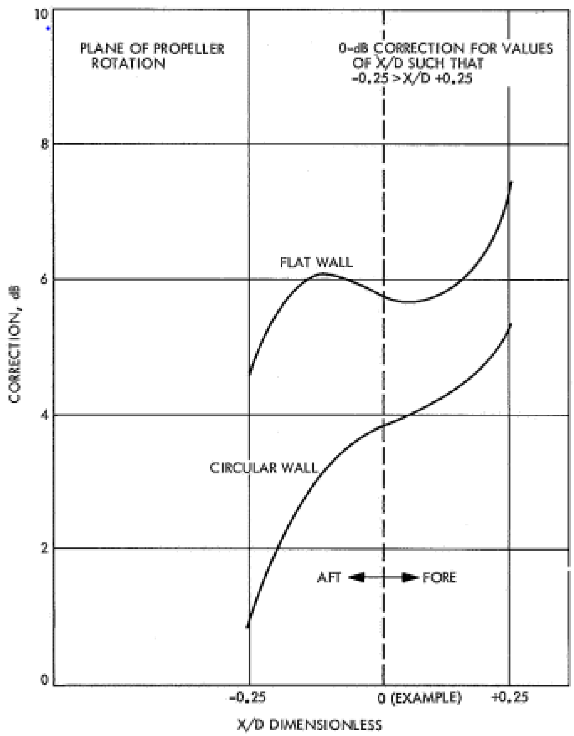

Figure 12.11: Effect of reflecting surfaces in pressure field

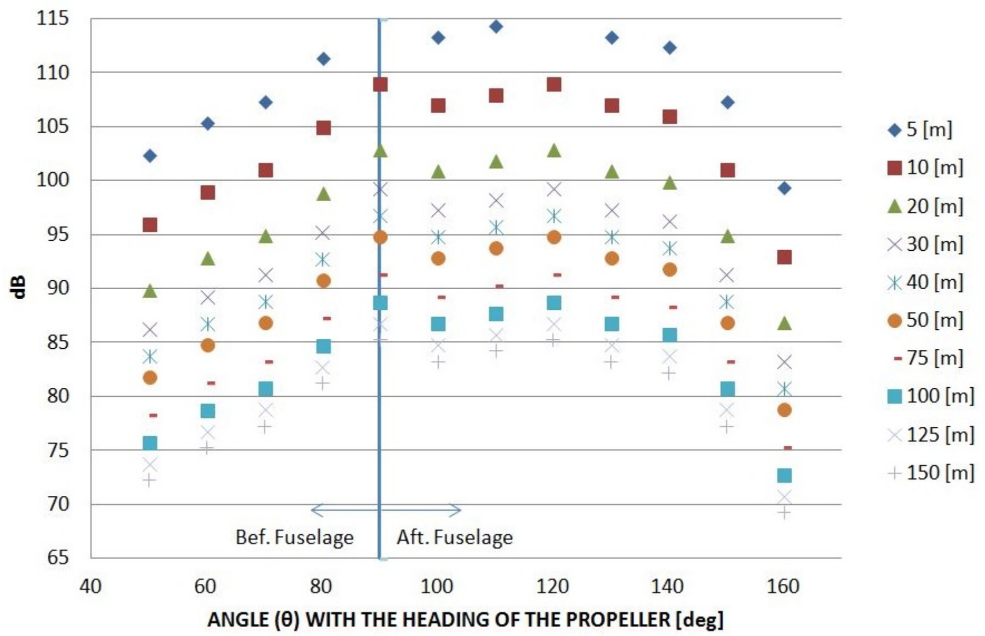

Figure 12.12: Noise footprint of the propeller

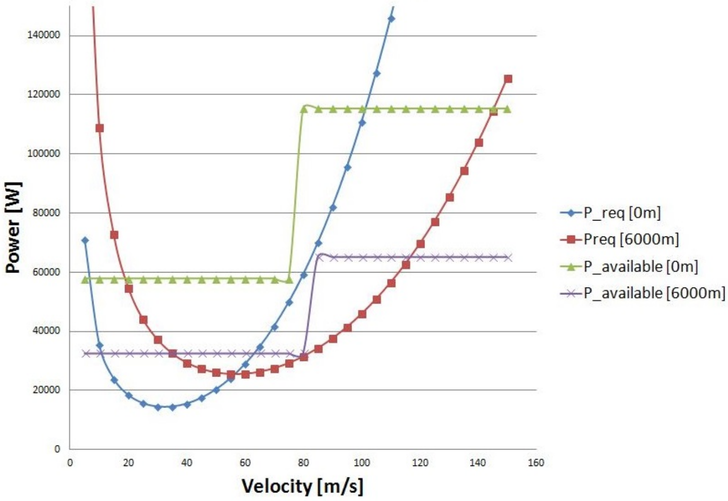

Figure 12.13: Performance Diagram of the E-SPARC

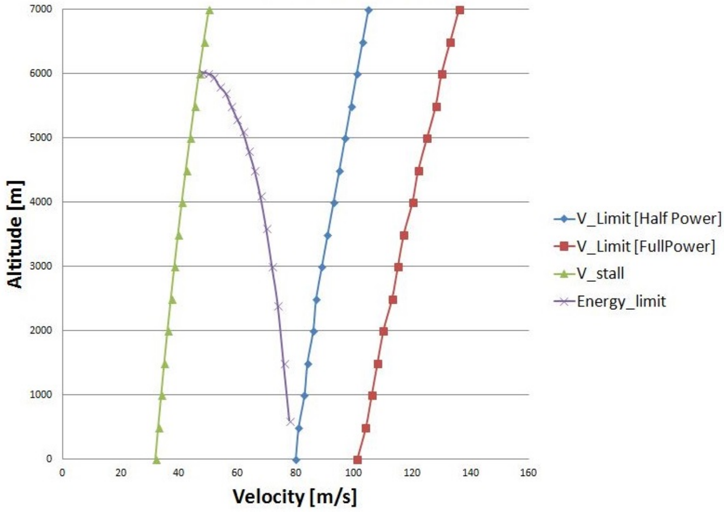

Figure 12.14: Performance limits of the E-SPARC

The second and third curves represent the power limit at half and full throttle. The limit is reached when the required power and the available power are the same. Figure 12.13 shows the performance at ground level and at 6000 m and the limiting speed at that height for the different power setting. The same is done for the height between 1000 m and 6000 m, with intervals of 500 m.

The final curve represents the energy limit, which is calculated by determining the required energy needed to fly to a certain altitude. The total available energy for the total flight is 4567115 J. In order to determine the maximum altitude, the energy allowed to climb is set to half of the total available energy. Descending requires less energy, but some energy is required to fly to an airstrip and loiter this is done for safety reasons. Since the rate of climb changes, for each 500 m an average RC and the time needed to climb 500 m is determined using Equation 12.28. The needed energy is calculated with Equation 12.29, where the available power also changes at different heights. The needed energy at each section of the climb is added up, until the allowable energy is reached. This is done for several initial speeds.

$$RC = \frac{P_{available_0} \cdot \left(\frac{\rho}{\rho_0}\right)^{0.75} - c_D \cdot \frac{1}{2}\rho V^3 S}{W} \tag{12.28}$$

$$E = \frac{100}{RC} \cdot P_{available} \tag{12.29}$$

Combining all the curves results in Figure 12.14, which shows the final service ceiling of 6000 meters.

13 AERODYNAMIC CHARACTERISTICS

After determining the race performances in Chapter 12, the aerodynamic characteristics will be given in this chapter. First, the drag estimation methods for each phase of the E-SPARC design will be discussed in Section 13.1. Thereafter, the drag polar is given in Section 13.2. The Oswald efficiency factor, which is a measure of the efficiency of lift production over the wing, will be elaborated upon in Section 13.3. In Section 13.4 an overview is given of the lift and moment coefficients. The chapter is concluded with some further recommendations.

13.1 DRAG ESTIMATION

Traditionally, the aircraft design process is divided into three phases: conceptual, preliminary and detailed design. In each subsequent phase, the level of detail of the analysis tools increases and an increasing number of design parameters is fixed. Similarly, the drag coefficient of E-SPARC has been estimated at different stages of the design. While progressing throughout these design phases, it was also possible to come up with a more refined estimate of the drag. Although aircraft design over the last decades has developed tools with increased sophistication like CFD, the prediction of aerodynamic drag is still a challenge during the design, because the methods to be used are only applicable for certain flight conditions or wing geometries. As is the case for the actual weight of the aircraft, the exact value of the drag can only be determined when the aircraft is built and flight test are performed. However, several methods exists that give a sufficient estimate of the drag based on reference aircraft that are within the same category and have similar geometric parameters. The different methods are characteristic to each design phase, with an increasing level of refinement and are explained in more detail below. The Class I drag estimation was based on Raymer [24], whereas the Class II method was based on Torenbeek [102]. At the end of the preliminary design phase a more refined method was used from Hoerner [120], which is based on the airfoil drag. An overview of the resulting zero lift drag coefficients obtained from these methods is given in Table 13.1. The method from Hoerner is used for the preliminary E-SPARC zero lift drag coefficient.

Table 13.1: Zero drag coefficient calculated at different design phases

	Raymer method (Class I)	**Torenbeek method (Class II)**	**Hoerner method (Final design)**
C_{D0}	0.025	0.032	0.034

CLASS I: INITIAL ESTIMATION OF AIRCRAFT DRAG

In the early conceptual design phase the zero-lift drag coefficient is only based on the ratio of wetted area to wing reference area ($\frac{S_{wet}}{S_{ref}}$). The method is based on Raymer and the result was used as input for the Class I method where it was used for the W/S - W/P plot. Equation 13.1 shows the relation of paramters that determine the zero lift drag coefficient. The skin-friction drag coefficient (C_{fe}) was taken to be 0.0050 for the category "Light aircraft - single engine" from Raymer [22]. Together with the estimated ratio of wetted area to wing reference area of 5, from the figure in the design book of Raymer, this gives an C_{D0} of 0.025. The decision was made to use wetted area ratios roughly between those of a Cessna Skyplane and the Beech Starship, since that is probably a good estimate of where a subsonic racing aircraft would be as a first estimate [121] based on reference aircraft.

$$C_{D_0} = C_{fe}\frac{S_{wet}}{S_{ref}} \tag{13.1}$$

CLASS II: ESTIMATION OF AIRCRAFT DRAG

During the conceptual design phase an improved estimation of the drag was performed for the different components of the aircraft. This estimation was iterated repeatedly given the changing nature of other design parameters. The total drag was assumed to be the sum of the drag contributions from the wing, fuselage, canard, propeller and landing gear. This method of Torenbeek is only applicable for a wing with thickness/chord ratios up to 20% and slender fuselages (length/diameter ratio greater than 4) [32], which will be the case for this aircraft. The computation of the total zerolift drag coefficient according to this method is given by Equation 13.2 below.

$$C_{D_0}S = r_{RE}r_{uc}\left(r_t\left((C_DS)_w + (C_DS)_f\right) + (C_DS)_n\right) \tag{13.2}$$

$$(C_DS)_w = 0.0054 \cdot r_w\left(1 + 3\,(t/c)\,(cos\Lambda_{0.25})^2\right)S \tag{13.3}$$

$$(C_D S)_f = 0.0031 \cdot r_f l_f \left(b_f + h_f\right) \tag{13.4}$$

$$r_{RE} = 47 \cdot Re_f^{-0.2} \tag{13.5}$$

Separately analyzing the wing drag (Equation 13.3) and fuselage drag (Equation 13.4) and then summing these values, results in an overall higher drag estimate. Therefore, a correction factor is taken into account in the first term of Equation 13.2 to correct for this phenomenon. This is given in the relation of Reynolds number in Equation 13.5. An overview of the parameters required to compute the zero lift drag according to this method is given in Table 13.2.

Table 13.2: Parameter input values for zero-lift drag coefficient based on Torenbeek

Parameter	Value	Unit	Description
$\frac{t}{c}$	0.16	$[-]$	Thickness/chord ratio main wing
$\Lambda_{0.25}$	-0.063	$[rad]$	Sweep angle at the quarter-chord line
S	5.156	$[m^2]$	Wing area
r_w	1	$[-]$	Type of wing support
r_f	1.15	$[-]$	Fuselage shape factor
l_f	4	$[m]$	Fuselage length
b_f	0.95	$[m]$	Fuselage maximum width
h_f	1	$[m]$	Fuselage maximum height
r_t	20	$[\%]$	Tail drag as percentage of wing and fuselage drag
r_{uc}	1.20	$[-]$	Fixed gear, streamlined wheel fairings and struts
Re_f	$2.27 \cdot 10^7$	$[-]$	Reynolds number fuselage at race speed
V	85	$[m/s]$	Race speed
A	6	$[-]$	Aspect ratio

E-SPARC: REFINED AIRCRAFT DRAG

A further improvement of the zero lift drag coefficient for the E-SPARC is based on Hoerner where the value is dependent on the minimum airfoil drag of the wing and canard and on the other subsystem parameters. The final values of the aircraft parameters fixed at the end of the preliminary design phase are used as input. The method has great overlapping with the Torenbeek method [120] and results are therefore very close. Torenbeek assumes that the drag of each component is a percentage of the overall fuselage drag, whereas Hoerner uses the dimensions of each single component and is also dependent on airfoil characteristics.

The resulting zero-lift drag coefficient is the summation of the C_{D0} values of each of the contributing components, including the wing, canard, fuselage and landing gear. It is taken into account that the nose landing gear is retracted during cruise and race and therefore only the main gear determines the overall landing gear drag. Since the the wingtips are lifting surfaces they are also dependent on their thickness ratio and wetted to wing reference area. Equations 13.6 to 13.9 given below, are used to compute the drag contribution of each of these components. Turbulent flow over the components is assumed, since the Reynolds numbers are higher than 2E6 [120], which is taken into account in the first parameter of Equation 13.6.

$$C_{D0_f} = C_f f_{LD} f_M \frac{S_{wet_f}}{S} \tag{13.6}$$

$$C_f = \frac{0.455}{log10\,(Re)^{2.58}} \tag{13.7}$$

$$f_{LD} = 1 + \frac{60}{(L/D)^3} + 0.0025\frac{L}{D} \tag{13.8}$$

$$f_M = 1 - 0.08M^{1.45} \tag{13.9}$$

The second parameter in Equation 13.6 is a function of the fuselage length-to-diameter (fineness) ratio. Since the wing, canard and wing tips are lifting surfaces, the drag of these components is computed in a similar way as is done for the fuselage, but for these lifting surfaces it also depends on the maximum thickness and the minimum drag coefficient of the airfoil of the respective lifting surface, which is computed using Equation 13.10. The selection of airfoils can be read in Chapter 8.

$$C_{D0_l} = C_f f_{tc} f_M \frac{S_{wet_f}}{S}\left(\frac{C_{d_{min}}}{0.004}\right)^{0.4} \tag{13.10}$$

$$f_{tc} = 1 + 2.7\left(\frac{t}{c}\right)_{max} + 100\left(\frac{t}{c}\right)_{max}^4 \tag{13.11}$$

An overview of the parameters that were used as inputs for the Hoerner method is given in Table 13.3. Table 13.4 gives an overview of the drag output of each component according to Hoerner. Also, the contribution given as a percentage of the total zero-lift drag of the aircraft is given in Table 13.4. As can be seen, the wing, canard and fuselage provide the largest contribution to the aircraft's overall zero-lift drag coefficient. For the majority of conventional aircraft, the wing and fuselage contribute to 30%-40% (totally 60%-80%) of the aircraft's C_{Do}, according to [120].

Table 13.3: Parameter input values for zero-lift drag coefficient based on Hoerner

Parameter	Value	Unit	Description
$Re_{fuselage}$	$22.6 \cdot 10^6$	[−]	Reynolds number fuselage at race speed
Re_{wing}	$5.6 \cdot 10^6$	[−]	Reynolds number wing at MAC in race speed
Re_{canard}	$2.5 \cdot 10^6$	[−]	Reynolds number canard at race speed
F	4	[−]	Fineness ratio
M	0.25	[−]	Mach number during race
V	85	$[m/s]$	Race speed
L	4	$[m]$	Fuselage length
$\frac{S_{wet_f}}{S}$	1.3	[−]	Wetted area fuselage
$\left(\frac{t}{c}\right)_{wing}$	0.16	[−]	Maximum thickness to chord ratio wing
$\left(\frac{t}{c}\right)_{canard}$	0.11	[−]	Maximum thickness to chord ratio canard
Cd_{min_w}	0.008	[−]	Airfoil minimum drag main wing
MAC_{wing}	0.972	$[m]$	Mean aerodynamic chord main wing
$\frac{S_{wet_w}}{S}$	1.96	[−]	Wetted area main wing
Cd_{min_c}	0.009	[−]	Airfoil minimum drag canard
MAC_{canard}	0.377	$[m]$	Mean aerodynamic chord canard
$\frac{S_{wet_c}}{S}$	2.1	[−]	Wetted area canard
Cd_{lg}	0.05	[−]	Drag coefficient of wheel
d_{gw}	0.337	$[m]$	Wheel diameter
w_{gw}	0.102	$[m]$	Wheel width

Table 13.4: Output zero-lift drag coefficient as refined drag estimation

Component	Zero-lift drag coefficient	Value	Unit	Percentage
Fuselage	C_{D0_f}	0.0062	[−]	19.4
Wing	C_{D0_w}	0.0126	[−]	36.8
Canard	C_{D0_c}	0.0091	[−]	26.7
Vertical wing tips	C_{D0_v}	0.0024	[−]	7.1
Landing gear (per wheel)	C_{D0_g}	0.0017	[−]	5.0
Total zero-lift drag	$C_{D0_{total}}$	0.034	[−]	100

13.2 DRAG POLAR

The total drag of E-SPARC is assumed to be the sum of two components; the drag at zero-lift and the induced drag dependent on the flight condition. The zero-lift drag was calculated in Section 13.1 and is the drag resulting from viscous shearing stresses over the contact surfaces of the components. Drag is dependent on the Reynolds number that the components encounter, assumed to be turbulent because of their high values. The total aircraft drag is given as a mathematical expression (Equation 13.12) where the variation of drag coefficient versus lift coefficient can be shown in a drag polar. The induced drag results from the generation of trailing vortices downstream of the lifting surface and at the wing tips. The downwash generated by the canard has a great influence on the local angle of attack that the main wing encounters. Furthermore, the wing is finite, which, compared to 2D-airfoils implies that air flows from the lower to upper wing surface which in turn also changes the local angle of attack that the main wing encounters at different sections along the wingspan.

$$C_D = C_{D0} + \frac{C_L^2}{\pi A e} \tag{13.12}$$

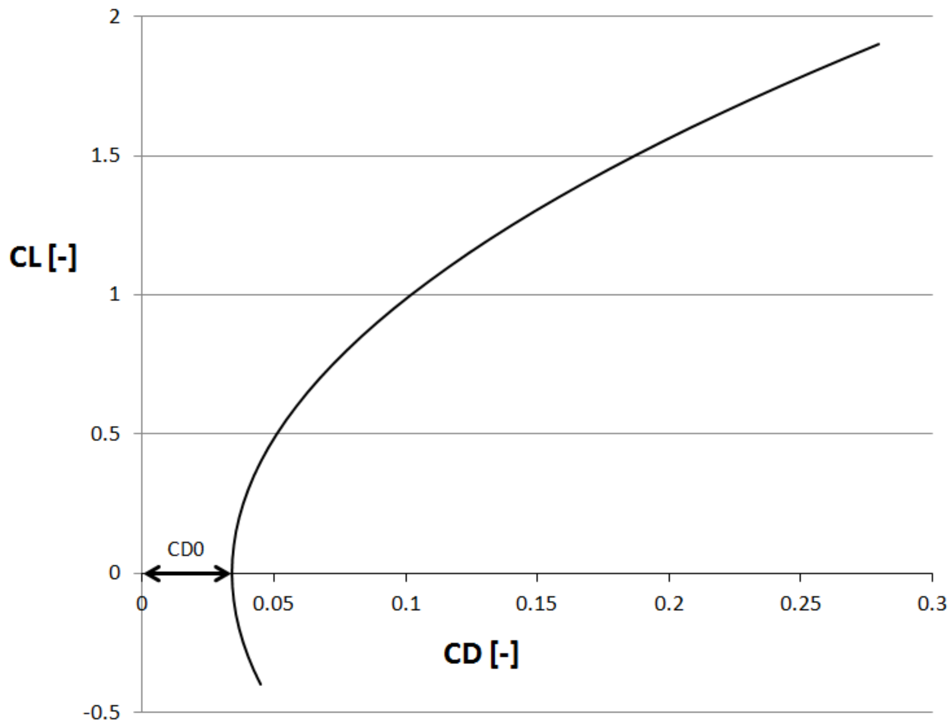

Figure 13.1: Drag polar: C_L versus C_D

In the drag polar, shown in Figure 13.1, the influence of induced drag as a function of the lift coefficient can be clearly shown. The steeper this curve the more the wing represents an infinite wing and the less interaction it encounters with other components. That is because more lift can be produced for the same amount of drag at a certain flight condition. The Oswald factor in Equation13.12 is mainly determined by the ellipticity of lift distribution and is greatly influenced by the canard wing. However, the wing tips again lower this effect and introduce more ellipticity, because the vortex flow is disturbed at the wing tip. An aspect ratio of 6 was taken for E-SPARC, which determines how much of the airfoil sections along the wingspan encounter the vorticity effects.

13.3 OSWALD FACTOR

The Oswald efficiency factor was determined at different stages of the design. Both methods are based on Torenbeek and an overview of the Oswald factors at each design phase is given in Table 13.5.

Table 13.5: Oswald lift curve factor calculated at different design phases

	Torenbeek (Class II)	Torenbeek (Final design)
e	0.80	0.78

CLASS II: ESTIMATION OF OSWALD FACTOR

As a first estimation an Oswald efficiency factor of 0.80 is determined with formula 13.13 using Torenbeek [32]. This is also a function of the aspect ratio which is taken to be 6 from the chosen design point in the W/S-W/P plot.

$$e = \frac{e_v}{1 + k_L C_{D_0} \pi A e_v} \tag{13.13}$$

Table 13.6: Parameter input values for Oswald factor (Equation 13.13)

Parameter	Value	Unit	Description
e_v	0.90	[−]	Span efficiency factor
k_L	0.20	[−]	Sweep correction factor
C_{D0}	0.034	[−]	Zero-lift drag coefficient
A	6	[−]	Aspect ratio

E-SPARC: REFINED OSWALD FACTOR

The Oswald factor mainly depends on the distribution of lift along the wing span. The factors S_{wet} and the wingspan are the design variables which are most important for the determination of this value and largely influence the drag of the aircraft. Therefore, another statistical approach for the determination of the Oswald efficiency factor was found and is given by equation 13.14. This is also based on Torenbeek [102], but more refined because the value is dependent on the aircraft dimensions and on the skin friction drag.

$$e = C_{fe} * 220 \left(\frac{S_{wet}}{bl_{ref}} \right)^{1/6} \tag{13.14}$$

The skin friction drag C_{fe} is a function of the Reynolds number from equation 13.7, therefore the size of the wing has an effect on C_{fe}. Also winglets increase the Oswald factor by 5 to 10% according to [32]. Because of the relative big size of E-SPARC' winglets the Oswald factor will increase significantly, however due to the fact that the configuration is a canard this value will be reduced again due to the interference from the canard to an Oswald efficiency factor of 0.78. The input values are shown in Table 13.7.

Table 13.7: Parameter input values for the refined Oswald factor (Equation 13.14)

Parameter	Value	Unit	Description
C_{fe}	0.00328	$[-]$	Skin friction drag of the wing
S_{wet}	8.61	$[m^2]$	Wetted area of wing
b	5.562	$[m]$	Wing span
l_{ref}	0.972	$[m]$	Mean aerodynamic chord length

13.4 MOMENT AND LIFT COEFFICIENT

During the airfoil selection and the 3D wing analysis in Section 8.1 the required lift and moment coefficients have been calculated. An overview of the 3D lift coefficients for the various flight situations, the lift slopes and the C_M of the main wing is given in Table 13.8. Both moment coefficient are taken at the maximum lift coefficient.

Table 13.8: 3D lift and moment coefficients and lift slope

Parameter	Value	Unit
$C_{L_{max,wing}}$	1.78	$[-]$
$C_{L_{max,canard}}$	2.0	$[-]$
$C_{L_{race}}$	0.13	$[-]$
$C_{L_{cruise}}$	0.64	$[-]$
$C_{M_{wing}}$	-0.14	$[-]$
$C_{M_{canard}}$	-0.21	$[-]$
$C_{L_{\alpha,wing}}$	4.71	$[rad^{-1}]$
$C_{L_{\alpha,can}}$	4.83	$[rad^{-1}]$

13.5 DISCUSSION & RECOMMENDATIONS

Every component, whether it has a large size such as the wing or with just a small size such as a rivet has direct contact with the air flow and thus contributes to the drag. The drag estimation for a new design is in general not a single exercise, but a continuous process from the early conceptual design, through to the preliminary design and and development. Drag estimations for these various design phases have been provided in this chapter. At this point in the design phase a more accurate estimation than the ones currently provided was beyond the scope of this assignment and design phase. Based on reference aircraft, like a glider (Schleicher ASW22) having a zero-lift drag coefficient of 0.016 and an agricultural aircraft (Dromader PZAL M-18) of 0.058, the zero-lift drag coefficient lies within the appropriate range and thus appears to be a good estimate for the drag of a race aircraft. Aerodynamic tools, like XFLR5 are able to calculate the drag for wing profiles, however it was decided not to rely upon the values obtained through such methods since these tools are not accurate in determining viscous drag [93]. For better accuracy, it is recommended to make use of a more advanced CFD tool software package which incorporates and computes the viscous effects on a total body as well as the interaction between various components.

14 Stability and Control Characteristics

The stability characteristics were already an important part of the horizontal and vertical stabilizer sizing process. Their areas were selected such that they provide longitudinal and lateral stability. It was described in Chapter 9. This chapter takes a step further and focuses on the design of the control surfaces, their analysis and the handling of the aircraft through the pilot. To achieve roll, pitch and yaw control, actuated control surfaces are used. The following strategy is followed to size these surfaces that are positioned on the wing and the horizontal and vertical stabilizer sized previously. First the size and disposition is estimated from reference aircraft and statistical data. Then using these sizes the performance of the aircraft is verified. The results indicate whether or not the surfaces are too small or too large. Furthermore the aircraft handling characteristics for the pilot are discussed for longitudinal control.

14.1 Reference Frames and Sign Convention

The reference frames and control deflection sign convention used in the stability and control analysis are shown in Figure 14.1 and 14.2. For the stability scissor plot the airplane reference frame is used. The body fixed reference frame with the CG as origin is also used. The airplane reference frame and the body fixed reference frame are shown in Figure 14.1 It is used in the aileron and rudder analysis. For the control deflection sign convention is shown in Figure 14.2. Note that elevator up is considered as positive. Together with the canard configuration, this allows to use the same sign conditions for the stick behaviour measures as in conventional aircraft.

14.2 Statistical Control Surface Sizing and Disposition

An initial estimate of the sizes of the control surfaces with respect to the wing they are installed on can be based on other aircraft. For this, racing aircraft are considered.

14.2.1 Size of Control Surfaces

Sizing the control surfaces at this stage of the process is based on area relations between the control surface and the respective wing it is placed on. The ailerons, elevators and rudders are placed on the main wing, the canard and the winglets, respectively. Analyzing the performance of the control surfaces in the next step allows to judge whether the found sizes are sufficient.

According to Torenbeek, in the preliminary design phase the ailerons can be sized by considering the area ratio from reference aircraft as presented in Equation 14.1a [102]. The variables are visualized in Figure 14.3. The same is assumed to be the case for the elevators and rudders, establishing Equations 14.1b and 14.1c. It is important

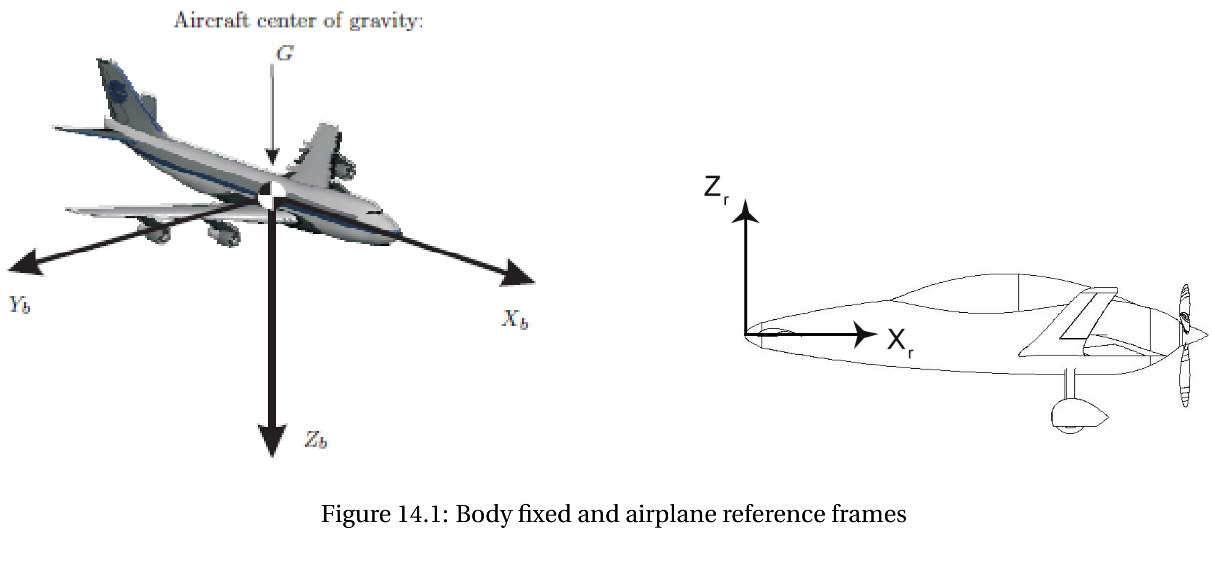

Figure 14.1: Body fixed and airplane reference frames

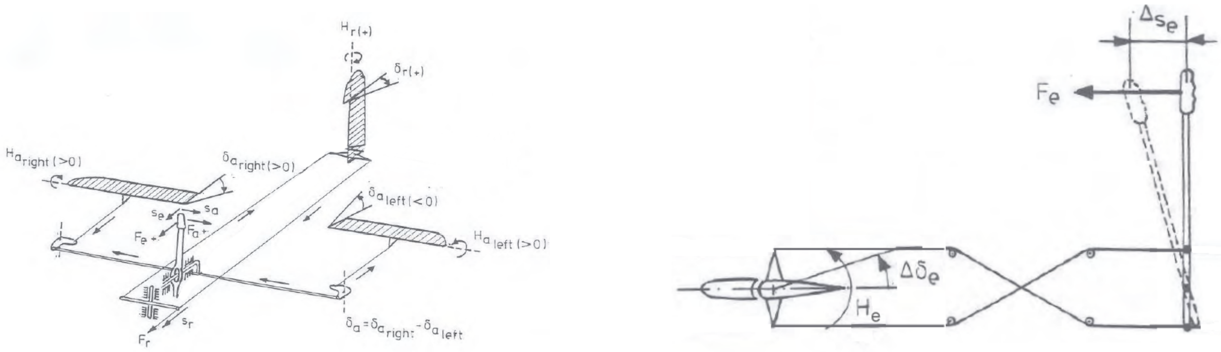

Figure 14.2: Aileron, rudder and elevator sign convention

to note that for the rudder only the area relation $\frac{S_r}{S_{vt}}$ is considered.

$$\frac{S_a l_a}{Sb} = constant \tag{14.1a}$$
$$\frac{S_e l_e}{S_c b_c} = constant \tag{14.1b}$$
$$\frac{S_r}{S_{vt}} = constant \tag{14.1c}$$
(14.1d)

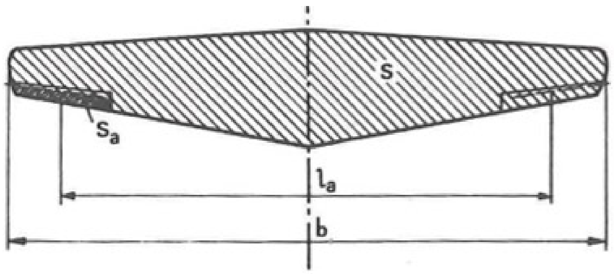

Figure 14.3: Area relation between main wing and ailerons [102].

Using two existing racing aircraft, the MXS-R and the Edge 540, as reference and considering their area ratio, the control surface area can be determined. The ratios found from the reference aircraft are averaged and applied to the areas of the lifting surfaces of E-SPARC. The results are presented in Table 14.1. Thus, a first estimation for the size of the control surfaces is found.

14.2.2 POSITIONING AND DEFLECTION OF CONTROL SURFACES

Next, the size and, position and deflection angles of the control surfaces are considered.

The control surfaces have to be positioned in such a way that they can affect the motion of the aircraft as effectively as possible. Ailerons are positioned spanwise outboard on the wings as far from the center-line as possible. The elevators are located on the trailing edge of the canard, so their distance from the centre of gravity depends on the position of the canard. Their spanwise position depends on the surface area and chord ratio. The rudders are positioned on the trailing edge of the winglets and should ideally cover the entire trailing edge to avoid becoming useless in case of a wake generated by the main wing.

Typical chord ratios and deflection limits suggested by literature are presented in Table 14.2. These values are taken over initially to check performance and are adjusted if due to wing span and area requirements the chord ratio should need to be changed.

Possible Adjustments

The size of the control surfaces depends on the area required, found as in Table 14.1, and whether an entire coverage is possible with these areas. If the control surfaces turn out to not provide sufficient controls, the area will first be increased by covering the entire trailing edges of their respective wing. If this is still not enough, they

Table 14.1: Area relations from reference aircraft and E-SPARC used to size the control surfaces.

Dimension	**MXS-R**	**Edge 540**	**Average of ratios**	**E-SPARC**
S $[m^2]$	9.48	9.10	-	5.16
b $[m]$	7.32	7.32	-	5.56
S_c $[m^2]$	1.88	2.08	-	1.14
b_c $[m]$	2.50	2.29	-	3.02
S_{vt} $[m^2]$	1.19	1.35	-	0.30
l_a $[m]$	3.66	4.75	-	3.38
l_e $[m]$	1.25	1.15	-	1.53
S_a $[m^2]$	0.68	0.72	-	**0.375**
S_e $[m^2]$	0.61	0.74	-	**0.386**
S_r $[m^2]$	0.72	0.90	-	**0.190**
Area fractions				
$\frac{S_a l_a}{Sb}$	0.0357	0.0516	0.0437	-
$\frac{S_e l_e}{S_c b_c}$	0.1615	0.1769	0.1692	-
$\frac{S_r}{S_{vt}}$	0.6026	0.6666	0.6346	-

Table 14.2: Typical control surface chord ratios and deflection ranges [102]

Control surface	**Chord ratio** c_f/c range [-]	**Deflection range** [deg]
Ailerons	0.25	-20/+20
Elevator	0.25-0.30	[-30,-25]/+[15,25]
Rudder	0.30-0.35	[-30,-25]/+[25,30]

will be improved aerodynamically or will be extended into the wing.

14.3 ANALYTICAL CONTROL SURFACE SIZING AND DISPOSITION

To judge whether the control surfaces are efficient, their performance has to be analysed. For this, several different methods are used. Aileron, elevator and rudder analysis are performed separately.

14.3.1 AILERON ANALYSIS

The goal of the aileron analysis is to determine the steady roll rate achievable with a given size and disposition. Equation 14.2 gives the equation of motion (EOM) for roll. The rolling moments due to the roll motion L_{damp} and the aileron deflection are shown in Equation 14.3 and Equation 14.4 respectively.

$$\dot{p} = \frac{L_{damp} + L_{aileron}}{I_{xx}} \tag{14.2}$$

$$L_{damp} = \frac{1}{2}\rho V^2 S b C_{l_p} \frac{pb}{2V} \tag{14.3}$$

$$L_{aileron} = \frac{1}{2}\rho V^2 S b C_{l_{\delta_a}} \delta_a \tag{14.4}$$

The EOM depends on the stability derivative C_{l_p} and control derivative C_{l_δ}. C_{l_p} is estimated from [106] using the following planform parameters: taper ratio, aspect ratio and sweep angle. The result is shown in Table 14.3. $C_{l_{\delta_a}}$ is estimated using a DATCOM method [122] based on aerodynamic reference data given in graphs and an analytical method from Sadraey[123]. These methods are compared below. Both are using the aileron size determined from the statistic method in previous section as input in the form of the $\left(\frac{c_f}{c}\right)_a$ flap-to-wing chord ratio and spanwise positions in dimensional form (y_{i_a} and y_{o_a}) or non dimensional form (η_{i_a} and η_{o_a}) determined from Equation 14.5. Given the area S_a, $\left(\frac{c_f}{c}\right)_a$ and an assumed maximum outboard position of $y_{o_a} = 0.95\frac{b}{2}$ of half

Table 14.3: C_{l_p} estimate [106]

Input	**Value**	**Output**	**Value**
λ	0.45	C_{l_p}	-0.4
Λ	0 deg		
A	6		

wing span, the inboard spanwise position can be determined using Equation 14.6 and selecting the root that is between zero and half wing span.

$$\eta = \frac{2y}{b} \tag{14.5}$$

$$y_{i_a} = \frac{-2C_r \pm 2\sqrt{C_r^2 - 4\frac{C_t - C_r}{b}\left(S_a\frac{c}{c_f} - \frac{C_t - C_r}{b}y_{o_a}^2 - C_r y_{o_a}\right)}}{4\frac{C_t - C_r}{b}} \tag{14.6}$$

DATCOM method

The DATCOM method for subsonic plain trailing edge flaps is used to find $C_{l_{\delta_a}}$. The ailerons are assumed to work in the same way as flaps at the trailing edge of the wing. Firstly, the rolling moment coefficient parameter $\frac{\beta C_{l_\delta}{'}}{\kappa}$ is determined for two ailerons that span the entire chord of the wing at a certain spanwise position. From this, the rolling effectiveness $C_{l_\delta}{'}$ for the full chord ailerons is determined by taking β and κ from graphs[122]. In order to find the rolling effectiveness for ailerons that only span part of the chord of the wing, Eqation 14.7 is used, where α_δ is the section lift effectiveness obtained from graphs[122]. The aileron size enters the method through the inboard and outboard spanwise position η_{i_a} and η_{o_a} and the aileron chord ratio $\left(\frac{c_f}{c}\right)_a$. The graph inputs are given in Table 14.4. A value of $C_{l_{\delta_a}} = -0.2027$ is found. The complete method can be followed step by step in [122].

$$C_{l_{\delta_a}} = C_{l_\delta}{'}|\alpha_\delta| \tag{14.7}$$

Table 14.4: Graph input values for DATCOM roll coefficient estimation.

Parameter	Value
β	0.95
A_w	6
$\Lambda_{0.25c_w}$	-0.063
$\left(\frac{t}{c}\right)_w$	0.16
$\left(\frac{c_f}{c}\right)_a$	0.25
η_{i_a}	0.3
η_{o_a}	0.95

Sadraey method

The analytical method suggested by Sadraey in [123] first calculates the $C_{l_{\delta_a}}$ and then determines the roll rate that is achievable. For the first step equation 14.8 is used.

$$C_{l_{\delta_a}} = \frac{2C_{L_{\alpha_w}}\tau c_r}{Sb}\left[\frac{y^2}{2} + \frac{2}{3}\left(\frac{\lambda - 1}{b}\right)y^3\right]_{y_i}^{y_0} \tag{14.8}$$

Here, y_i is the position of the aileron from the fuselage going outboards and y_0 is the end position of the aileron near the wingtips. The factor 2 is included to account for both wings and their deflected ailerons. τ is the control surface angle of attack effectiveness parameter. It is determined using the control-to-lifting-surface chord ratio from [100]. Thus, all variables can be determined and a value of $C_{l_{\delta_a}} = -0.0989$ is found. As can be seen, the estimated $C_{l_{\delta_a}}$ from both methods differ significantly. To get a feeling which one is either unreasonable or correct, both are used in the simulation and the responses compared.

Roll model

For a given flight condition and aileron position, size and deflection, the aircraft response in terms of roll rate can now be determined by numerically integrating Equation 14.2 using the coefficients determined above. The roll rate at each timestep is given by Equation 14.9.

$$p_{t+dt} = p_t + \dot{p}dt \tag{14.9}$$

The model inputs are shown in Table 14.5. The resulting roll acceleration, roll rate and rolling moments are calculated using a Python script and the output graphs are shown in Figure 14.4. The steady roll rate is achieved after 0.5 seconds and is 460 deg/s. When comparing the responses based on the estimated coefficients from Sadraey and DATCOM, there is a large difference in achieved steady roll rate. Given the fact that the aileron surface is based on reference aircraft and E-SPARC is lighter and has less inertia than those aircraft, the E-SPARC steady roll rate should be equal or higher than that of reference aircraft. This favors the coefficient estimate from the DATCOM method.

Table 14.5: Input variables used in the roll model.

Characteristic	Value	Characteristic	Value
dt [s]	1/250	S [m^2]	5.16
$\dot{p}_0$ [$\frac{rad}{s^2}$]	0	b [m]	5.56
p_0 [$\frac{rad}{s}$]	0	I_{xx} [kgm^2]	234
$\delta_{a_{max}}$ [deg]	-20	C_{l_p} [-]	-0.4
ρ [$\frac{kg}{m^3}$]	1.225	$C_{l_{delta a_{DATCOM}}}$ [-]	-0.2027
V [$\frac{m}{s}$]	103	$C_{l_{delta a_{Sadraey}}}$ [-]	-0.0989

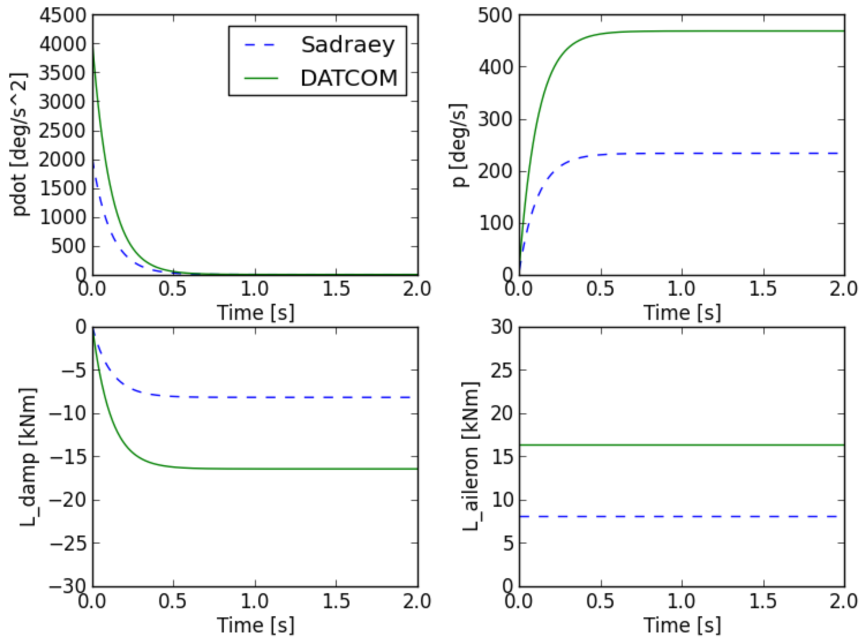

Figure 14.4: Roll response of the aircraft with full aileron deflection.

In order to compete in the Red Bull Air Races, it is desirable to achieve roll rates of at least the same amount as current racers, so around 420 deg/s [36]. The results might indicate an overdesigned aileron for the E-SPARC aircraft when using the aileron size determined with the Torenbeek statistical method. With a better estimation of the coefficients in the detailed design phase and what maximum roll rate is needed, the aileron size can be trimmed.

14.3.2 ELEVATOR ANALYSIS

Since no pitch rate requirement is known at this point which is needed during the race, the elevator analysis is focused upon the take off rotation manoeuvre. The elevator must be sized such that rotation is possible at take off. In Figure 14.5 the forces and moments acting on the aircraft in the phase just before rotation are shown. Using Equation 14.10, the rotational acceleration can be calculated when giving a certain elevator deflection. In Table 14.6 the inputs for this analysis are given. The rotation airspeed is assumed slightly above stall speed $V_r = 1.2V_s$ [123]. The 3D aerodynamic coefficients are used, except for C_{m_w} which is not available yet in 3D. The resulting rotational acceleration is $\ddot{\theta} = -56\frac{\circ}{s^2}$, thus nose up in this sign convention, when the pilot applies full elevator deflection. Take off rotation is thus possible.

$$\ddot{\theta} = \frac{-L_h(x_{mlg} - x_{ac_h}) + (T - D)l_{mlg} + W(x_{mlg} - x_{cg}) + M_w + L_w(x_{ac_h} - x_{mlg})}{I_{yy}} \tag{14.10}$$

14.3.3 RUDDER ANALYSIS

As suggested by Sadraey, the rudder has to provide stability during crosswind conditions [100]. According to CS23 regulations, at least a crosswind of 0.2 times the landing speed has to be compensated for using the rudders, allowing for a safe landing [99]. Under a crosswind at 90°, the rudder performance can be analysed. A

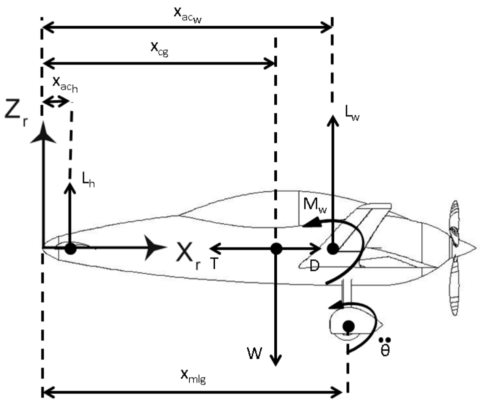

Figure 14.5: Moments and forces during takeoff rotation.

Table 14.6: Elevator analysis inputs.

Characteristic	Value	Characteristic	Value
$\rho[\frac{kg}{m^3}]$	1.225	$C_{N_{w_\alpha}}[-]$	4.71
$V_r[\frac{m}{s}]$	32	$C_{N_{h_\alpha}}[-]$	4.83
$S_h[m^2]$	1.14	$C_{N_{h_{\delta_e}}}[-]$	-3.39
$S[m^2]$	5.16	$\delta_e[deg]$	-20
$\bar{c}[m]$	0.990	$C_{D_0}[-]$	0.034
$A_w[-]$	6	$x_{mlg}[m]$	2.85
$e[-]$	0.78	$x_{ac_h}[m]$	0.16
$I_{yy}[kgm^2]$	386	$x_{cg}[m]$	2.34
$m[kg]$	415	$x_{ac_w}[m]$	2.83
$g[\frac{N}{kg}]$	9.81	$l_{mlg}[m]$	0.59
$i[deg]$	-5	$T[N]$	1224
$\alpha_{h_0}[deg]$	-12.5	$C_{m_w}[-]$	0.14
$\alpha_{w_0}[deg]$	-8		

maximum rudder deflection of 30°is assumed. Following Sadraey[100], the behaviour under crosswinds can be analysed by assuming that the fuselage and the vertical stabiliser create a force under crosswinds. Thus, two moments are created. The rudder has to balance the moment from the fuselage. The aerodynamic moment and the side force of the aircraft under a positive sideslip angle is calculated using Equations 14.11 and 14.12.

$$N_A = qSb(C_{n_0} + C_{n_\beta}(\beta - \sigma) + C_{n_{\delta_r}}\delta_r) \tag{14.11}$$

$$F_A = qS(C_{y_0} + C_{y_\beta}(\beta - \sigma) + C_{y_{\delta_r}}\delta_r) \tag{14.12}$$

To maintain moment and force equilibrium, these have to counteract the force of the crosswind, F_W, shown in Equation 14.13, as illustrated in Figure 14.6.

$$F_W = \frac{1}{2}\rho V_W^2 S_S C_{D_y} \tag{14.13}$$

For satisfactory rudder control, the required deflection to allow for a safe landing may not be larger than the actual possible deflection. Solving the equilibrium Equations 14.14 and 14.15 simultaneously yields a rudder deflection angle and thus serves as a check, where $q = \frac{1}{2}\rho V_T^2$ [100].

$$qSb(C_{n_0} + C_{n_\beta}(\beta - \sigma) + C_{n_{\delta_r}}\delta_r) + F_W d_c cos\sigma = 0 \tag{14.14}$$

$$-qS(C_{y_0} + C_{y_\beta}(\beta - \sigma) + C_{y_{\delta_r}}\delta_r) + \frac{1}{2}\rho V_W^2 S_S C_{D_y} = 0 \tag{14.15}$$

In order to perform these calculations, the coefficients C_{n_β}, $C_{n_{\delta_R}}$, C_{y_β} and $C_{y_{\delta_R}}$ have to be determined using Equations 14.16 through 14.19 [100].

$$C_{n_\beta} = K_{f1} C_{L_{\alpha_V}} \left(1 - \frac{d\sigma}{d\beta}\right) \eta_V \frac{l_{Vt} S_V}{bS} \tag{14.16}$$

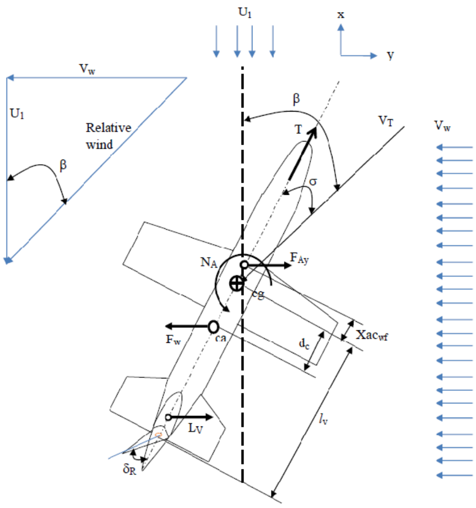

Figure 14.6: Moments and forces under incoming crosswind.[100]

$$C_{n_{\delta_r}} = -C_{L_{\alpha_V}} V_V \eta_V \tau_r \frac{b_r}{b_V} \tag{14.17}$$

$$C_{y_\beta} = -K_{f2} C_{L_{\alpha_V}} \left(1 - \frac{d\sigma}{d\beta}\right) \eta_V \frac{S_V}{S} \tag{14.18}$$

$$C_{y_{\delta_r}} = C_{L_{\alpha_V}} \eta_V \tau_r \frac{b_r}{b_V} \frac{S_V}{S} \tag{14.19}$$

Many of the coefficients in these equations cannot be known without wind tunnel tests. Therefore, only crude estimations can be made and their effectiveness and accuracy has to be validated later. However, a general trend can be found, meaning that it can be seen which parameters have an influence on the tail and rudder size. The variables are estimated from [100]. Solving Equations 14.14 and 14.15 simultaneously yields values for σ and δ_{Rudder}. Using the inputs shown in Table 14.7 it is found that the assumed winglet area is not large enough. Increasing the winglet area with the same parameters as before results in a sufficient area of 0.25 times the side area of the aircraft, which, with S_f of 2 metres^2, results in a total vertical stabilizer area of 0.5 metres^2. The values in Table 14.7 are adjusted accordingly. This is split over both winglets. The corresponding rudder deflection δ_R is then 29.65°. The results also show that the rudder deflection is negative and the heading angle σ is larger than the sideslip angle. This can be explained by the fact that the aerodynamic centre of the fuselage is assumed to lie in front of the centre of gravity. Since this is heavily dependent on the aircraft shape a redesign, bringing the aerodynamic centre of the fuselage closer to the centre of gravity, could decrease the required rudder size. In further steps, the assumed coefficients have to be validated through testing models or the actual aircraft. Also, due to the slight increase in size the winglets may increase in weight. The area fraction considering the rudder size presented in Section 14.2 will remain the same, leading to a rudder area of $0.32m^2$. This is still small, but since most comparable aircraft are designed for aerobatics as well, they require a larger vertical stabiliser and rudder to recover from spins. E-SPARC is designed as such that it will not enter a spin and can thus fly safely with a smaller rudder.

14.4 PILOT STICK BEHAVIOUR

The pilot handling characteristics of the aircraft are limited by certain requirements resulting in behaviour that makes the aircraft either difficult or easy to fly. In this section the longitudinal handling qualities are focused upon, since they are relevant during high g pull ups in the race. First the handling qualities beneficial for the pilot are described and their required magnitude and sign is stated. Then the E-SPARC values for these measures are shown and checked to be in compliance or not. Finally recommendations to improve handling qualities are described.

14.4.1 HANDLING QUALITY MEASURES

Elevator stick position and stick force stability

It is beneficial for the pilot if the initial and ultimate control displacements when performing a pitch up or pitch down manoeuvre are in the same direction. If the condition in Equation 14.20 is satisfied, the aircraft has elevator stick position stability [106].

Table 14.7: Variables used to determine the rudder deflection required under crosswind.

Characteristic	Value
C_{n_0} $[-]$	0.00
C_{D_y} $[-]$	0.35
$C_{L_{\alpha_{vt}}}$ $[1/rad]$	5.00
β $[rad]$	0.197
$\frac{d\sigma}{d\beta}$ $[-]$	0.50
τ_r $[-]$	0.52
η_{vt} $[-]$	1.00
d_c $[m]$	-0.145
l_{vt} $[m]$	0.324
x_{cg} $[m]$	2.34
S_S $[m^2]$	2.00
S_{vt} $[m^2]$	**0.5**
V_{land} $[m/s]$	32.23
V_{vt} $[-]$	0.00533
$\frac{b_R}{b_V}$ $[-]$	0.80
K_{f_1} $[-]$	0.6
K_{f_2} $[-]$	1.5

Characteristic	Value
Intermediate results	
F_w $[N]$	4287.5
C_{n_β} $[-]$	0.01
$C_{n_{\delta_R}}$ $[-]$	-0.014
C_{y_β} $[-]$	-0.655
$C_{y_{\delta_R}}$ $[-]$	0.252
Outputs	
δ_R $[rad]$	-0.52
σ $[rad]$	0.60

With elevator stick force stability, the stick has positive feeling: it feels like it is being pulled back to the center position by springs. Furthermore the stick forces and displacements are in the same direction. If the condition in 14.21 is satisfied in the trim condition, the aircraft has elevator stick force stability [106]. A quantitative limit set by military specifications is $\left(\frac{dF_e}{dV}\right)_{F_e=0} > 0.041$ [124].

$$\frac{d\delta_e}{dV} > 0 \tag{14.20}$$

$$\left(\frac{dF_e}{dV}\right)_{F_e=0} > 0 \tag{14.21}$$

Stick displacement and stick force per g in pull up
In the pull up it also beneficial for the pilot if the initial and final control displacements are in the same direction. For an increase in g this means a more negative control displacement, i.e. more aft. This is expressed in condition 14.22. No quantitative constraints were found, but the ratio between stick displacement and stick force per g, described next, is known to be determining the handling qualities [106].

For an increase in g the stick pull force should increase, i.e. become more negative according to the sign convention. This is described by the condition in Equation 14.23 as the stick force per g [106]. Furthermore the magnitude of the stick force per g is constrained to avoid either oversensitive or too heavy stick control. For trainer and fighter aircraft, according to military specifications, the constraints are a function of maximum load factor and defined by Equation 14.24 [124]. The maximum load factor of 12g is used.

$$\frac{d\delta_e}{dn} < 0 \tag{14.22}$$

$$\frac{dF_e}{dn} < 0 \tag{14.23}$$

$$-2.31kg < \frac{dF_e}{dn} < -1.37kg \tag{14.24}$$

14.4.2 E-SPARC STICK BEHAVIOUR

To calculate the different handling quality measures, first the positions of the neutral point stick fixed and stick free and the manoeuvre point stick fixed and stick free are calculated. These positions give an indication of the influence of the c.g. position on the handling quality measures. Magnitudes of the quality measures are then calculated with the respective equations from flight dynamics theory.

For the calculations the elevator hinge moment derivatives C_{h_α} and C_{h_δ} are required. These are estimated from DATCOM methods and the inputs are indicated in Table 14.8. The results are $C_{h_\alpha} = -0.2039$ and $C_{h_\delta} = -0.4200$.

In the following equations the assumptions are made for $\frac{d\varepsilon}{d\alpha} = 0$ and $\frac{V_h}{V} = 1$ due to the canard configuration. The equations are modified versions of [106]. The neutral point stick fixed $x_{n_{fix}}$ is linked to the elevator stick position

Table 14.8: Input parameters for DATCOM method.

Parameter	Value	Parameter	Value
$\frac{c_f}{c}$	0.4	η_{in_e}	0.2
$\frac{c_b}{c_f}$	0.25	η_{out_e}	0.95
$\frac{t}{c}$	0.11	A_{ht}	8
$\frac{t_c}{2c}$	0.15	Λ_{ht}	0 deg

stability and is given in Equation 14.25. The stick position stability can then be calculated using Equation 14.26.

$$x_{n_{fix}} = \frac{C_{N_{h\alpha}}}{C_{N_\alpha}} \frac{S_h l_h}{S\bar{c}} \bar{c} + x_w \tag{14.25}$$

$$\frac{d\delta_e}{dV} = \frac{4mg}{\rho V^3 S} \frac{1}{C_{m_{\delta_e}}} \frac{x_{cg} - x_{n_{fix}}}{\bar{c}} \tag{14.26}$$

The neutral point stick free $x_{n_{free}}$ is linked to the stick force stability and is given in Equation 14.27. The stick force stability is calculated by Equation 14.28.

$$x_{n_{free}} = \frac{C_{m_{\delta_e}}}{C_{N_\alpha}} \frac{C_{h_\alpha}}{C_{h_\delta}} \bar{c} + x_{n_{fix}} \tag{14.27}$$

$$\left(\frac{dF_e}{dV}\right)_{F_e=0} = -2\frac{d\delta_e}{ds_e} S_e \bar{c}_e \frac{mg}{S} \frac{C_{h_\delta}}{C_{m_{\delta_e}}} \frac{x_{cg} - x_{n_{free}}}{\bar{c}} \frac{1}{V_{tr}} \tag{14.28}$$

The manoeuvre point stick fixed is related to the stick displacement per g and is given in Equation 14.29. The stick displacement per g is calculated using Equation 14.30.

$$x_{m_{fix}} = -\frac{C_{m_q}}{2\mu_c} \bar{c} + x_{n_{fix}} \tag{14.29}$$

$$\frac{d\delta_e}{dn} = \frac{-1}{C_{m_{\delta_e}}} \frac{mg}{\frac{1}{2}\rho V^2 S} \frac{x_{cg} - x_{m_{fix}}}{\bar{c}} \tag{14.30}$$

Finally the manoeuvre point stick free is related to the stick force per g and is given in Equation 14.31. The stick force per g is calculated by Equation 14.32.

$$x_{m_{free}} = -\frac{C_{m_{q_{free}}}}{2\mu_c} \bar{c} + x_{n_{free}} \tag{14.31}$$

$$\frac{dF_e}{dn} = \frac{d\delta_e}{ds_e} \frac{mg}{S} S_e \bar{c}_e \frac{C_{h_\delta}}{C_{m_{\delta_e}}} \frac{x_{cg} - x_{m_{free}}}{\bar{c}} \tag{14.32}$$

In Table 14.9 the calculated values for the handling quality measures together with their compliance with the above stated conditions are indicated. In Figure 14.7 the positions of the neutral and manoeuvre points are shown.

Table 14.9: Calculated handling quality measures and their compliance.

Handling quality measure	Value	Condition met?
$\frac{d\delta_e}{dV} > 0$	1.25e-4	Yes
$\left(\frac{dF_e}{dV}\right)_{F_e=0} > 0.041$	-0.0311	No
$\frac{d\delta_e}{dn} < 0$	-0.0096	Yes
$-2.31 kg < \frac{dF_e}{dn} < -1.37 kg$	-0.156	No

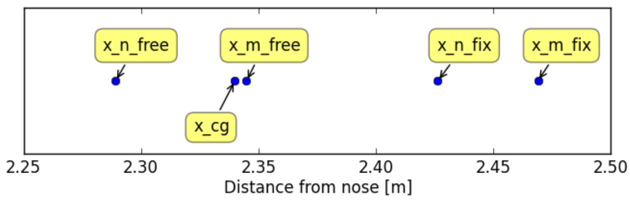

Figure 14.7: Relative position of neutral and manoeuvre points and cg.

As can be seen $\left(\frac{dF_e}{dV}\right)_{F_e=0}$ does not have the required positive sign. This is due to the c.g. lying behind the neutral point in stick free condition. Furthermore the stick force per g, $\frac{dF_e}{dn}$, is too low in absolute magnitude. Since the c.g. position is constrained by the stability requirement, to improve these handling qualities, bobweights or springs could be installed in the control system [106]. However since the sensitivity of the results due to the hinge moment coefficient estimates is high, wind tunnel tests are recommended in the detail design phase to improve estimates of those values and check the stick behaviour.

14.5 ACTUATORS

Control actuator selection depends on the stick forces and the constraints imposed by the aircraft packaging. To allow for precise and responsive steering of the aircraft through the pilot, it was decided to use a reversible flight control system. This system uses a direct mechanical connection from the control surfaces to the input controls the pilot can operate. Stick forces should thus be checked in the detailed design phase and should remain within constraints set by CS23. Aerodynamic balancing of the control surfaces might be necessary. In order to control the actuation system and thus the control surfaces, foot pedals and a control stick are utilised.

An important decision that has to be made on how to connect the control surfaces to the controllers. The established means are cables or rods. Since the aircraft operates under high g loads and has to perform fast, extreme maneuvers, rods have an advantage over cables which can have cable slack. They should provide a longer lifetime and offer more safety in operation. The rod system could be integrated inside the aircraft entirely, given the constraints imposed by fuselage geometry and packaging. For the ailerons and elevator rods are used. For the rudder a cable system will be used, due to the location of the rudders in the winglets and the many corners to make. In order to work like one big rudder, as was assumed in Section 14.3.3, the rudders both have to be deflected in the same direction and, if tests show that in fact the direction of the incoming velocities is equal, by the same angle.

14.6 EIGENMOTION ANALYSIS

To judge how the aircraft performs in flight, the eigenmotions as results of different inputs are considered. The aircraft is designed to be statically stable. For the dynamic analysis, the theories presented in [106] are used. By simplifying the equations of motion the eigenvalues corresponding to the four eigenmotions "Short Period Oscillation", "Phugoid", "Dutch Roll" and "Aperiodic Spiral Motion" can be determined. By writing the equations of motion in a matrix form and analysing the 4x4 state space matrix by simplifying the respective characteristic equations, the coefficients of the characteristic equations can be determined. These coefficients are shown in Table 14.10 and 14.11. The eigenvalues result from Equation 14.33. For this approach, several assumptions regarding the individual eigenmotions have to be made [106].

- ***Short Period Oscillation*** $V = constant$. This assumption is made since the motion is so rapid that no change in velocity is taken into account.
- ***Phugoid*** $\dot{q} = 0, \alpha = 0$. This motion is assumed to be so slow that no substantial changes in angle of attack and pitch rate occur.
- ***Dutch Roll*** $\psi = \frac{pb}{2V} = 0$. For the ease of calculation and since the rolling moment have to balance, these parameters are not considered. Thus, only the lateral force and the yawing moment related equations are considered further.
- ***Aperiodic Spiral*** *All accelerations in linear and angular direction are set to 0.* The motion is so slow that these accelerations are not considered since the change over time of a characteristic is not substantial.

For the response to be stable, the eigenvalues corresponding to a particular motion have to be negative. Furthermore, a symmetric and oscillatory response will only be present if the eigenvalues are complex numbers. In this case, damping to counteract the oscillation is required [106].

$$\lambda_{1,2} = \frac{-B \pm \sqrt{B^2 - 4AC}}{2A} \tag{14.33}$$

Table 14.10: Coefficients of the characteristic equations for the Short Period Oscillation.

Eigenmotion	Short Period Oscillation	Phugoid	Dutch Roll
A	$4\mu_c^2 K_Y^2$	$-4\mu_c^2$	$8\mu_b^2 K_Z^2$
B	$-2\mu_c(K_Y^2 C_{Z_\alpha} + C_{m_{\dot{\alpha}}} + C_{m_q})$	$2\mu_c C_{X_u}$	$-2\mu_b(C_{n_r} + 2K_Z^2 C_{Y_\beta})$
C	$C_{Z_\alpha} C_{m_q} - 2\mu_c C_{m_\alpha}$	$-C_{Z_u} C_{Z_0}$	$4\mu_b C_{n_\beta} + C_{Y_\beta} C_{n_r}$
$\lambda_{1,2}$	-0.01839, -0.11336	-3.62467 $\pm i$0.00289	-0.05495 $\pm$ i0.22387

The inputs used for the calculations are the same as shown in previous tables in this chapter. The analysis shows that the Short period oscillation is stable but has two real, negative eigenvalues. It therefore does not oscillate,

Table 14.11: Coefficients of the characteristic equations for the Aperiodic Spiral Motion.

Eigenmotion	Aperiodic Spiral Motion	Value
λ_{b3}	$\frac{2C_L(C_{l_\beta}C_{n_r}-C_{n_\beta}C_{l_r})}{C_{l_p}(C_{Y_\beta}C_{n_r}+4\mu_b C_{n_\beta})-C_{n_p}(C_{Y_\beta}C_{l_r}+4\mu_b C_{l_\beta})}$	0.00626

which is deemed more comfortable for the pilot. The motion can only become oscillatory if the discriminant D calculated from A, B and C in Table 14.10 is negative. Plotting the discriminant over a range of centre of gravity locations with the aerodynamic coefficients assumed in this design stage shows that D will not become negative in a range that is acceptable for the centre of gravity position. Only at far forward centres of gravity, oscillatory behaviour is found, as can be seen in Figure 14.8.

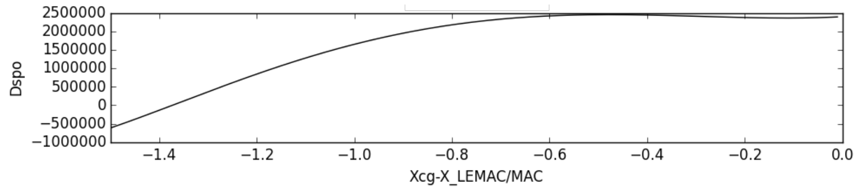

Figure 14.8: The discriminant for different centre of gravities for the short period oscillation.

The fact that the eigenvalues are negative shows that the motion will level out. The value closer to the origin is decisive for this behaviour, which is why a time to half amplitude can be calculated with Equation 14.34 using this eigenvalue. A smaller time to half amplitude indicates a faster response to control inputs. Due to this, it would be best to have a critically damped system, resulting in an aircraft with the same, negative eigenvalues. The discriminant in the formulas shown above is then zero. This would lead to the fastest possible response to an input.

$$T_{\frac{1}{2}} = \frac{ln(0.5)c}{V\lambda} \tag{14.34}$$

The eigenvalues for the Phugoid and the Dutch Roll are both complex with negative real parts, meaning that they are both stable and damped. As was to be expected, the Phugoid has a considerably longer period and a lower damping ratio, since it is a motion that lasts for longer time. The Aperiodic Spiral Motion has a positive eigenvalue. This means that E-SPARC is not stable in this motion. However, since it is an eigenvalue that is just positive and the motion takes long, this instability is considered not dangerous for the pilot and is accepted for the aircraft, since it gives enough time to react.

Further steps and recommendations

Even though the eigenmotions, apart from the aperiodic spiral, are stable, it is yet unknown what the aircraft response times are. For aerobatic racing, the pilots require fast responses to their control inputs. Thus, it is necessary to avoid an overdamped system. In next steps, wind tunnel tests have to be performed to find more precise estimates of the aerodynamic coefficients and build a control model.

14.7 VERIFICATION AND VALIDATION

During the stability and control analysis, tools were used for the aileron analysis, the elevator analysis and the rudder analysis, as well as for the stick behaviour analysis and the investigation of the eigenmotions. These have to be verified. Also, validation strategies for later stages of the design process are presented.

14.7.1 VERIFICATION

Aileron Analysis

Since only the DATCOM method is used for the final assumptions in the aileron analysis, the verification of the tool is performed with respect to this method. However, for verification, the intermediate results of both methods are taken into account to investigate on the behaviour of the tool. The two methods deliver different results for $C_{l_{\delta_e}}$. Thus, a different response is expected from the tool. This is in fact the case, as the responses for the roll rate differ by the same factor as the $C_{l_{\delta_e}}$ values, which can be seen in Figure 14.4. This was expected since the relation between the moment gradient and the roll rate is purely linear. The tool relies on many different parameters that have to be estimated from statistical data. Altering these values should change the outcome of the analysis. Several values were altered and the outcome was checked. The different approaches are shown in Table 14.12.

Table 14.12: Parameters changed to verify the roll model analysis tool.

Parameter	Changed from - to:	Behaviour of tool outcome	Performance as expected
η_{i_a}	0.95-0.99	roll rate increases	yes
η_{i_0}	0.3-0.2	roll rate increases	yes
C'_{l_δ}	0.5-0.6	roll rate increases	yes

Rudder Analysis

Firstly, it is investigated whether the deflection of the rudder goes in the right direction according to the set sign convention. Since the heading angle deviates positively from the sideslip angle β under a crosswind coming in from the right, a negative rudder deflection is required to allow for a controlled landing approach. This is in fact the case. Thereafter, both σ and δ_r are plugged in back into Equations 14.14 and 14.15 and it is found that they solve the equations correctly. Thereafter, it is investigated if the tool performs well under different conditions. When increasing the crosswind, the rudder deflection increases slightly as could be expected, since more force needs to be generated by the vertical tail and thus the rudder to stabilise the aircraft. It is also assumed that the rudder deflection should change its sign as soon as the centre of gravity lies in front of the aerodynamic centre of the fuselage, since the moment generated by the tail has to oppose the (now changed) moment introduced by the fuselage. This is in fact the case, However the deflection heavily depends on the aerodynamic characteristics assumed for the vertical tail. The more force the tail creates in the direction of the crosswind without the rudder deflection, the more extreme the rudder deflection has to be to trim the aircraft. While this was expected and verifies the correct working of the tool, it has to be tested with other means of analysis which exact parameters can be achieved by the tail under these conditions.

Stick behaviour

To verify the code written to calculate the measures for stick behaviour, a simple check can be performed. With the cg far forward, all the conditions for the measures should be met, since the cg is in front of the neutral and manoeuvre points. This is the case. If the cg is far backward, all the conditions should indicate to not be met, since the cg is behind the neutral and manoeuvre points. This is also the case. To further verify the code, one could insert the inputs from another aircraft, e.g. the Cessna Citation, and then check the values for the different handling quality measures with what is expected and how it is experienced in actual flight.

Eigenmotion Analysis

Since the eigenvalues corresponding to the separate eigenmotions are calculated using simplified formulas it can be investigated whether they match the eigenvalues calculated by a python script when using the same characteristics as inputs for a state matrix (A-Matrix). The script uses the numpy.linalg.eig(A-Matrix) function to analyse these eigenvalues. It was found that the eigenvalues hardly differ, as was expected following the theories presented in [106].

14.7.2 VALIDATION

Validation cannot take place yet since no real test data of the aircraft is available yet. The control surface analysis tools have to be validated as soon as real models of the aircraft exist and are tested under real-life conditions. Then it can be seen whether the predicted performance can be achieved and whether the tools calculate the correct parameters. In order to avoid having to build the entire aircraft only to test and alter single control surfaces, it can be started by building simple models and test them in wind tunnels. Predicting their behaviour and comparing the tools predictions to the observed state will yield a first impression whether the tools indicate the right trends. Only then they should be taken to the bigger and more complex models in order to fully verify them for the entire aircraft. Otherwise one might build a model and find out later that the tool can not even be validated for the most simple cases.

15 Data Handling and Communications

The aircraft has a large number of sensors, processing units and other data- and communications components. This chapter will provide an overview over the main data handling units in Section 15.1. The communication between these main data handling components and the surrounding components is discussed in Section 15.2.

15.1 Data Handling Units

This section discusses the data handling of the aircraft in terms of the required processing units. This overview is given in Figure 15.1. All the major components and a selection of the in- and outputs have been included in the diagram. The actual number of in- and outputs of the data handling is larger and should be determined during detailed design.

Table 15.1: Overview of abbreviations in the data flow diagram

Symbol	**Meaning**
BMS	Battery Management System
AHRS	Attitude and Heading Reference System
EFIS	Electronic Flight Instrument System
PFD	Primary Flight Display
MFD	Multi-Function Display
PVI	Peripheral Vision Indicator
AWG	Aural Warning Generator

For data handling a number of units are required, in particular for an electric powertrain where battery management and electric motor control are needed. The logic controller as part of the electronic flight instrument system will have to be programmed for the functioning, reliability, longevity and safety of the electronic circuit and components. Table 15.1 gives an overview of the main data units in the aircraft.

15.2 Communications

The main processing units communicate with each other using the CANbus protocol, which can also be seen in Figure 15.1. This is a standard data transferring protocol in a wide number of industries. On the left side of Figure 15.1 it can be seen that the sensors provide information to the battery management system (BMS), AHRS and air data processing unit. This information - along with GPS information - is shared over CANbuses with EFIS, the main control unit of the aircraft. The EFIS is programmed to make logical decisions based on the input information and gives feedback to the other processing units such as the BMS and Motor Controller.

The main function of the BMS is checking the state of the battery cells, modules and entire pack. Voltmeters, ammeters and temperature sensors are required. If the battery temperature is nearing the border of the maximum allowable operating value, several actions could be taken. The EFIS could increase the mass flow of the air cooling fans, reduce the current draw from the battery or possibly cut the circuit. The BMS is also of great importance for the cycle life by avoiding overcharging the batteries. The BMS furthermore makes sure that the SoC of the individual cells or modules is the same.

The motor controller has similar functions and checks the I, V and T as well. Furthermore, the motor controller includes a watchdog timer (WD Timer) for increased safety. The controller decides on the proper input voltage and amperage to control the rotating speed and torque. It also checks the phase-shift of the three phases which is adjusted accordingly. The motor controller as well as the electric motor is cooled by a water/glycol liquid so the mass flow of the cooling pumps can be adjusted accordingly through the logic processing inside EFIS. Again, the logic controller can decide to reduce or cut off the electric motor power if cooling is insufficient and the situation is hazardous.

The entire electrical system is attached to a (line) isolation monitor that measures the insulation resistance between the active conductors and earth. Once the resistance drops to a certain value, the system is not immediately cut off, but a priority warning should be sent to the logic controller. Cutting off the power completely while in operation at low altitudes would be disastrous for the pilot of the aircraft.

EFIS is attached to all the instrumentation, including the primary flight display (PFD), multi-function display (MFD), peripheral vision indicator (PVI), aural warning indicator (AWG) and storage. This should update the pilot about its attitude, G-loads, state of subsystems and warnings. This information is required during the RBAR as well as for post-race analysis of the flight.

Table 15.2: Parameters overview of Figure 15.1

I/O Parameter	**Meaning**	**Unit**	**Subscript**	**Meaning**
I	Current	[A]	EM	Electric Motor
V	Voltage	[V]	M	Battery Module
T	Temperature	[K]	P	Battery Pack
SoC	State of Charge	[%]	C	Battery Cell
SoH	State of Health	[%]	CON	Controller
V_{air}	Air speed	[m/s]	-	-
T_{air}	Ambient air temperature	[K]	-	-
h	Altitude	[m]	-	-
m_{flow}	Mass flow	[kg/s]	-	-
θ	Pitch angle	[°]	-	-
ϕ	Roll Angle	[°]	-	-
β	Slip Angle	[°]	-	-
V_{climb}	Climb rate	[m/s]	-	-
V_G	Ground Speed	[m/s]	-	-
WD Timer	Watchdog Timer	N/A	-	-
T_{con}	Controller Temperature	[K]	-	-
ϕ_{comp}	Phase difference	[rad]	-	-

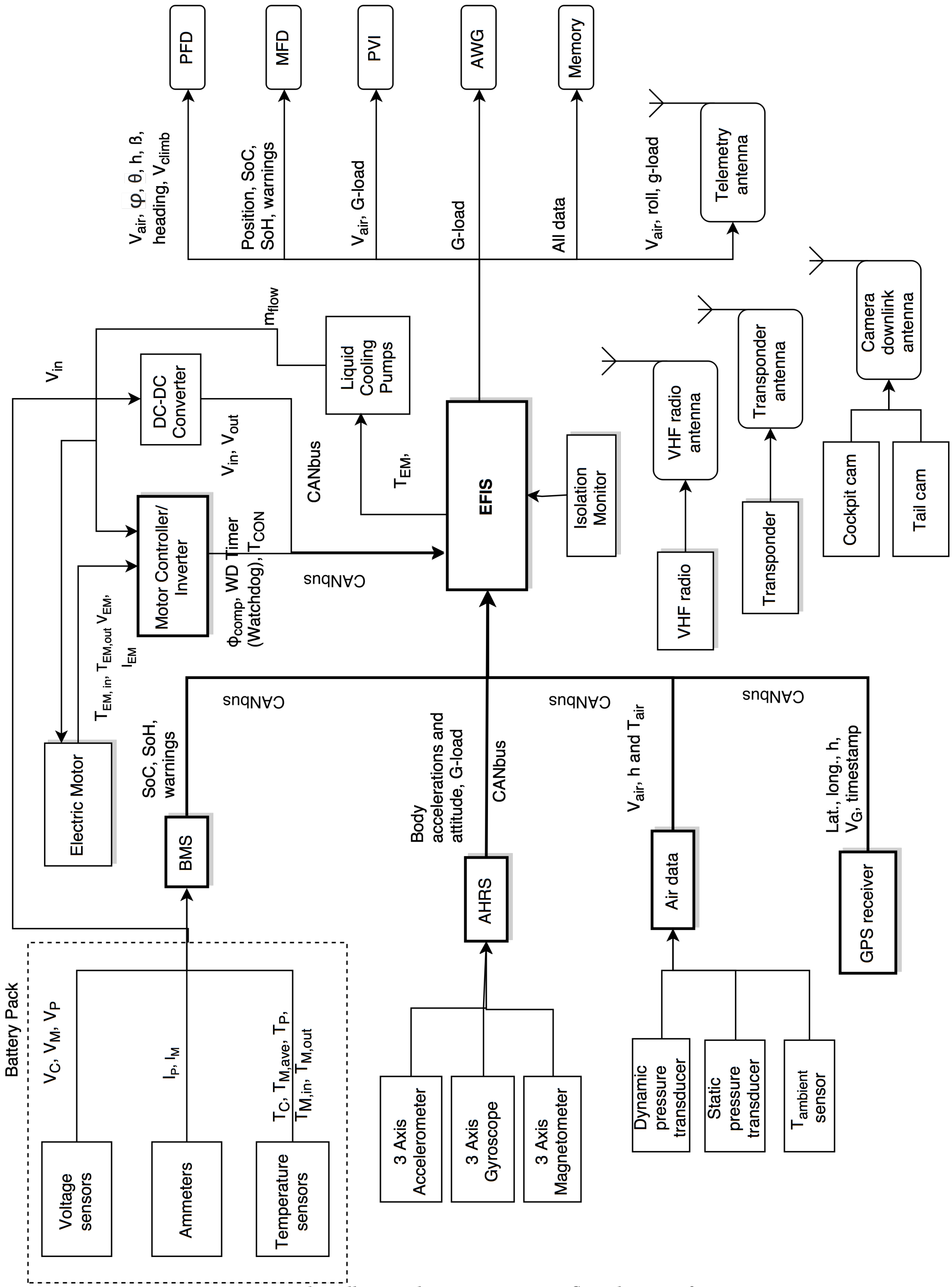

Figure 15.1: Data handling and communication flow diagram for E-SPARC

16 Reliability, Availability, Maintainability and Safety Analysis

For a successful design of E-SPARC not only design and production need to be considered, but also every aspect related to the use of the aircraft. This chapter takes a look at the aircraft reliability, availibility, maintainability of the system and individual parts and safety of the pilot and crew.

Reliability

A first version of the RAMS characteristics is presented, based on similarity with existing aircraft. For an aircraft optimized for racing a reliability of one race day would be sufficient. However cost and sustainability factors do not allow this. The required reliability of the major components for the aircraft in race configuration could be set to equal about 75 hours of flight or one race season [125]. In after life, components could be replaced by more durable ones to allow for a longer maintenance interval and lower operational costs.

The following redundancy philosophies are used. For electronic hardware such as the battery management systems (BMS) passive and active redundancy and automatic fault detection and isolation are used. The accumulator itself uses twelve individual battery modules that are connected in parallel. If one module fails it is shut off from the system and the engine can continue running at almost full power. This is done either directly by the fuse installed with every module or by the BMS. The battery management systems continuously monitors the modules and can shut them off if irregularities in temperature or current are detected. Single points of failure are avoided and diversity used as much as possible. For software N-version programming will reduce the chances of faults. Where possible structural components are designed according to the fail safe principle. Large composite parts that are difficult to repair and prone to fatigue and the landing gear are designed according to the safe life design principle.

Availability

The aircraft is available when it is ready to perform the race mission. Operational limitations are daytime and meteorological conditions. With the to be installed flight instruments, the aircraft is capable of flying in 'Visual Flight Rules' (VFR) [126]. During flight testing a maximum crosswind component will be determined wherein the aircraft is still able to land. The availability is reduced due to downtime before and between the races. Before the race, the aircraft needs to be assembled and certain maintenance activities need to be performed. The batteries need to be recharged or replaced. The batteries of the E-SPARC are installed in the front and back of the aircraft and not designed to be replaced after each race due to cost of the system. Recharging of the batteries will take a minimum of 20 minutes (Chapter 7). Downtime between races and tests therefore consists of charging the batteries, maintenance activities and eventually downloading the on board data. Unscheduled downtime due to hardware or software failure can occur as well. To increase availability, use of fault monitoring, redundancy, easily accessible parts and line replaceable units will be used.

Maintainability

Maintenance consists of scheduled and non-scheduled activities. For experimental aircraft, no maintenance regulations are stated. Maintenance intervals of certified aircraft are stated by the manufacturer according to CS-23 [109] or at least an annual inspection is required according to FAR23 [127]. Typically for RBAR aircraft the heavy check interval is 75 flight hours [125]. CS-23 requires the issuance of an aircraft maintenance manual with instructions for personnel, which could also be considered for this aircraft.

Because of the novel use of electric propulsion in this race aircraft, focus should be placed on maintenance activities associated with the electric motor(s) and batteries. Electric motors require less maintenance since they are composed of less parts compared to combustion engines. Furthermore they are much simpler and cheaper in operation [128]. Inspection activities for electric motors include, amongst others, bearing inspection and rotor/stator inspection [129]. The batteries will be accessible through the cockpit for maintenance and safety checks. Also for maintainability reasons it was decided against contra-rotating propellers. A single rotor propeller together for a direct transmission without gear box allows for a single shaft that reduces required maintenance activities. The safe life carbon fiber fuselage and wings are resistant to fatigue and corrosion, thereby decreasing the number of maintenance intervals for the primary structure. Regular inspection however, for failure modes related to composites such as micro cracks and delaminations are required.

Safety

Safety critical functions are functions intended to achieve or maintain a safe state [130]. Safety is the freedom from unacceptable risk of physical injury or of damage to the health of people, either directly, or indirectly as a result of damage to property or to the environment [131]. The following safety critical functions during regular aircraft operation are identified:

- Protect pilot from environment (heat, electric circuits, fire, CO poisoning).
- Protect ground crew from electric circuits.
- Prevent battery thermal runaway.

These functions are implemented in E-SPARC design using a number of safety measures. The safety situation for the pilot and crew is much different for an electric than for a conventional aircraft. An electric aircraft generates much less heat due to a more efficient power train. The danger from hot lubricant is also decreased due to the smaller number of rotating parts. The main heat sources such as the electric motor and the batteries are positioned away from the pilot, so that no direct contact is possible. Additionally a fire extinguisher is installed in the aircraft while poisoning from exhaust gases is no issue for an electric aircraft. All high voltage lines are properly insulated and the insulation protected against damage where the lines run through the cockpit or other accessible sections of the aircraft. The batteries are protected from thermal runaway by active cooling (Section 7.6.1) and temperature monitoring through the battery management system. A casing protects the modules from fire or structural damage.

17 Compliance and Sensitivity Analysis

In this chapter, the compliance matrix and the sensitivity analysis are presented in Section 17.2 and Section 17.1 respectively.

17.1 Sensitivity Analysis

A sensitivity analysis is undertaken to investigate how the overall design changes with deviations to the main parameters. Firstly the main parameters that have a large effect on the overall design had to be identified. After that the effects of those parameters are analysed. The outcome of the sensitivity analysis is shown in Figure 17.1. In the paragraphs below the major system parameters that were identified are briefly explained.

The flow diagrams start with the main system parameters which are numbered in the figure. The rectangles are the logical results or steps to be taken. A rhombus represents an OR-box from which a design choice can be made on how to deal with the specific case. The dashed box **A** is a part that comes back multiple times and is used to reduce space.

1. **Endurance not sufficient** If after the detailed design phase it becomes clear that the endurance requirement can not be met the aircraft should for example be designed with a lighter structure around the battery to still meet the requirement.
2. **Battery efficiency/energy density lower than estimated** During the design phases so far, estimations were made about the batteries that will be available in the future. If it turns out that these estimations were too optimistic the steps in the flow diagram have to be taken.
3. **Aircraft velocity lower than estimated** If the aircraft velocity is lower than estimated the performance of the aircraft in the races will be lower, which will lead to a less competitive design. If this occurs the steps can be followed as is shown in the diagram.
4. **L/D lower than estimated** If the L/D ratio changes it has an effect on the entire design and one of the design options shown in the flow diagram should be addressed. For example changing the aspect ratio to reduce the induced drag and the canard interference.
5. **Number of passengers changes** If it is at some point in the lifetime of the aircraft decided to convert the aircraft to a two-seater aircraft there will be an increase in payload weight. There are several ways to accommodate this as is shown in the flow diagram. One possibility is to descrease the battery size to account for an increase in fuselage size, however a lower endurance will be the consequence then.

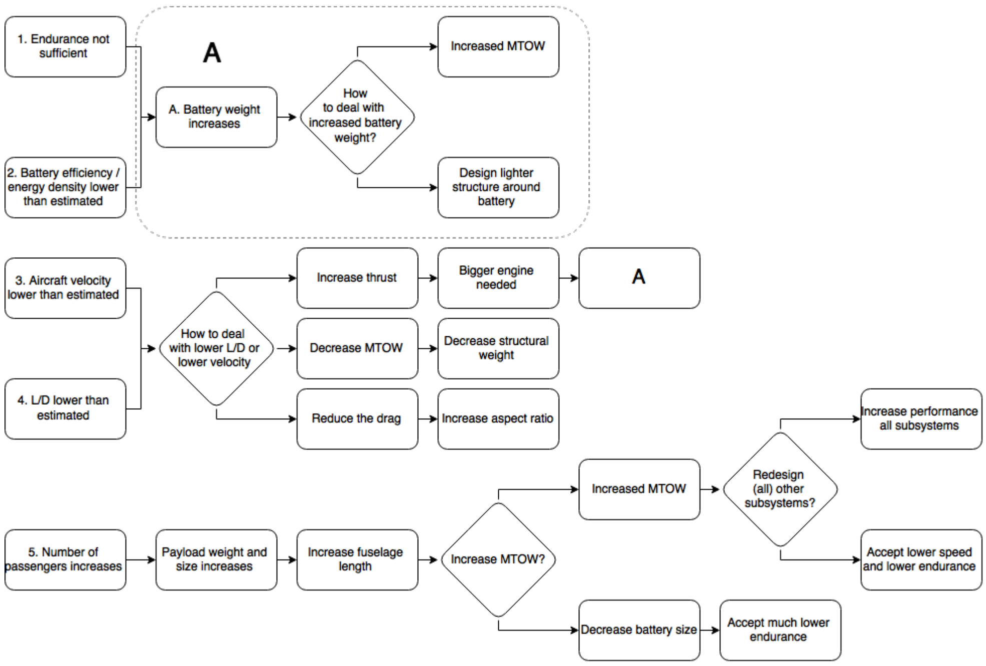

Figure 17.1: Sensitivity analysis for a change in major system paramters

17.2 Compliance Matrix

The compliance matrix in Table 17.1 and 17.2 presents the top level requirements and whether or not they are fulfilled. When the requirement is fulfilled, the compliance method is given. When the requirement is not fulfilled, the mitigation method is given, e.g. consider it in detailed design. A reference to the section handling the requirement is shown in the last column. Top level requirements were selected from the requirement database based on following criteria. Requirements with major influence on the conceptual and preliminary design of this specific aircraft with its electric powertrain are focused upon. Furthermore since the design will not be certified, as it is an experimental aircraft, only the main requirements from CS23 which can be followed for safety are included.

Table 17.1: Compliance matrix showing the top level requirements

Source	ID	Description	Compliance	Compliance or mitigation method	Section
Project guide	ESP-AF-FUS-001	The aircraft shall fit 1 pilot.	Y	Cockpit size sufficient.	6.1
Project guide	ESP-MIS-001	The aircraft shall be producible at the laboratories of Delft University of Technology.	N	Outsourcing of some components, assembly at laboratories is possible.	5.3
Project guide	ESP-MIS-002	The aircraft shall have a production cost of less than 300,000 Euros.	Y	Cost breakdown estimate performed [224.000 Euros].	6.4.3
Project guide	ESP-MIS-003	The aircraft shall have a development cost of less than 100,000 Euros.	Y	Cost breakdown estimate performed [92.000 Euros].	6.4.3
Project guide	ESP-MIS-004	The aircraft shall be able to perform its first flight in 2025.	Y	Battery technology readiness sufficient [2019].	7
Project guide	ESP-MIS-005	The aircraft shall be powered entirely electrically.	Y	Electric powertrain feasible.	7
Project guide	ESP-MIS-007	The aircraft shall allow for a sustainable disposal of all its parts at the end of its life.	Y/N	Only fuselage and battery disposal checked and met.	5.4
Project guide	ESP-MIS-008	The aircraft shall be able to withstand a maximum load factor of 12g.	Y	Incorporated in structural design.	8.2, 11
Project guide	ESP-MIS-010	The aircraft shall be able to climb at a minimum rate of 7 m/s.	Y	P/W and W/S ratio sufficient [15 m/s].	6.3.1
Project guide	ESP-MIS-011	The aircraft shall have a minimum cruise speed of 120km/h.	Y	$V_{cruise} = 160 km/h$	7
Project guide	ESP-MIS-012	The aircraft shall have a service ceiling of 5000 m.	Y	Performance checked [6000 m].	12.4
Project guide	ESP-PW-EST-006	The aircraft shall have an energy recovery system.	N	Not advantageous to have one on board.	7.9
Project guide	ESP-PW-EST-007	The aircraft shall be able to operate at full throttle for 3 minutes	Y	Battery capacity sufficient.	7.9
Project guide	ESP-PW-EST-008	The aircraft shall be able to operate 50% throttle for 30 minutes	Y	Battery capacity sufficient	7.5
E-SPARC Team	ESP-AF-FUS-002	The aircraft shall allow for access to parts and subsystems contained in preflight checks, race maintenance and rule checking directly or by removable access panel.	Y/N	More detailed CAD Model necessary.	6.1
E-SPARC Team	ESP-CP-ENV-003	The aircraft shall protect the pilot from the environment.	Y	Protection by canopy design, cockpit design.	6.1
E-SPARC Team	ESP-CP-ENV-005	The pilot and maintenance crew shall be protected from aircraft internal high voltages.	N	Check in detailed design phase.	-
E-SPARC Team	ESP-MIS-018	The aircraft shall be transportable to worldwide race locations.	Y	Detachable wings using spars and locking bolts	6.2
E-SPARC Team	ESP-MIS-020	The aircraft shall be able to perform 3 runs per day with a minimum ground interval between races of 20 minutes.	Y	Recharge time OK [20 min.]	7.7
RBAR regulations 2014	ESP-AF-LDG-001	The wheels and tyres shall be large enough to operate safely on unpaved runways.	Y	Wheel size sufficient.	10.2
RBAR regulations 2014	ESP-AF-WNG-001	The wing span of the aircraft shall not be more than 8.5m.	Y	Smaller wingspan [5.56 m].	8.1
RBAR regulations 2014	ESP-CP-ENV-002	The pilot shall be able to escape the aircraft in a maximum of 10 sec in emergency situations.	Y	Incorporated in canopy design and cockpit design.	6.1
RBAR regulations 2014	ESP-CP-ERG-001	The cockpit shall allow for the pilot to wear a helmet.	Y	Cockpit size sufficient.	6.1

Table 17.2: Compliance matrix showing the top level requirements

Source	ID	Description	Compliance	Compliance or mitigation method	Section
RBAR regulations 2014	ESP-CP-ERG-002	The cockpit shall allow for the pilot to wear an emergency parachute of thickness 5 cm.	Y	Cockpit size sufficient.	6.1
RBAR regulations 2014	ESP-CP-ERG-003	The cockpit shall allow for the pilot to wear a G-race suit.	Y	Cockpit size sufficient.	6.1
RBAR regulations 2014	ESP-CP-ERG-004	The seat recline shall be more than 30 degrees with respect to the vertical.	Y	Seat recline checked [40 degrees].	6.1
RBAR regulations 2014	ESP-MIS-013	The take off distance shall not be more than 500 m.	Y	P/W and W/S ratio sufficient [300 m].	6.3.1
RBAR regulations 2014	ESP-MIS-014	The landing distance shall not be more than 500 m.	Y	P/W and W/S ratio sufficient [500 m].	6.3.1
RBAR regulations 2014	ESP-MIS-016	The aircraft shall have a maximum stall speed of 61 kts.	Y	$V_{stall} = 29 m/s$	6.3.1
CS23	ESP-AF-ALL-002	There shall be no vibration or buffeting severe enough to result in structural damage.	N	Check in detailed design phase.	-
CS23	ESP-AF-ALL-003	At limit loads any deformation must not be permanent or interfere with safe operation, ultimate loads must not lead to failure for three seconds	Y/N	Designed for ultimate load, deformations checked in detailed design phase.	8.2, 11
CS23	ESP-CP-ERG-003	The cockpit shall be arranged with sufficiently extensive clear and undistorted view to enable the pilot to safely taxi, take-off, approach, land and perform any manoeuvres within the operating limitations of the aeroplane	Y	Canopy size and pilot position checked.	6.1
CS23	ESP-CT-ALL-001	The aircraft shall be longitudinally stable.	Y	CG location within stability limits [2.28-2.35 m].	9.1
CS23	ESP-CT-ALL-002	The aircraft shall be directionally stable.	Y	Vertical stabilizer size sufficient.	9.2
CS23	ESP-CT-ALL-003	The aircraft shall be laterally stable.	Y	Keel area sufficient.	9.3
CS23	ESP-CT-CSF-001	Control forces from pilot shall not exceed values stated in CS23.143.	N	Check in detailed design phase.	-
CS23	ESP-PERF-017	The short period oscillation shall be heavily damped, dutch roll damped, long-period oscillation not so unstable as to cause unacceptable increase in pilot workload.	Y	Eigenmotion analysis	14.6
CS23	ESP-PERF-018	The aircraft shall be able to recover from spinning	N	Airplane is not allowed to stall due to canard configuration, so it cannot enter spin.	-
CS23	ESP-PP-POW-004	The powertrain cooling provisions must maintain the temperatures of powertrain components within the limits established for those components.	Y	Cooling system sized sufficiently.	7.6
CS23	ESP-PP-POW-006	The motor must be isolated from the rest of the aeroplane by firewalls.	Y	Foreseen in CAD model.	6.1
CS23	ESP-PW-EST-002	Each electrical system must be protected from water and mechanical damage and must be designed so that the risk of electrical shock to crew, passengers and ground personnel is reduced to a minimum.	N	Check in detailed design.	-
CS23	ESP-PW-EST-003	For batteries safe cell temperatures must be maintained during charging and discharging.	Y	Cooling system sized sufficiently [60 degrees C].	7.6
CS23	ESP-PW-EST-004	No explosive or toxic gases emitted by any battery may accumulate in hazardous quantities within the aeroplane.	Y	Incorporated in battery choice.	7.5
CS23	ESP-PW-EST-005	No corrosive fluids or gases that may escape from the battery may damage surrounding structures or essential equipment.	Y	Incorporated in battery choice.	7.5

18 Conclusion and Recommendations

This report takes the reader through the design process of E-SPARC, a newly developed electric aerobatic racing aircraft, developed to make aerobatic racing innovative and sustainable in the future. It starts from conceptual design with first weight and performance estimations and describes the preliminary design phase, where the overall design as well as the subsystems are refined.

The focus of the project is set on designing a prototype of an aircraft to perform in aerobatic racing, more specifically in the Red Bull Air Races, by the year 2025, and to compete with or even outperform aircraft that are currently flying in this competition. A one-seater canard configuration is chosen as the design configuration because of its aerodynamic benefits, allowing for great maneuverability and a lightweight design, and its marketability as exciting and exotic new aircraft. Based on its novel use of technology in its electric propulsion system, market analyses predict a profitable future for eventual series production of the aircraft. A selling price of 350,000 Euros is aimed at for the eventual series production.

To be able to compete in the races, E-SPARC features a canard, generating positive lift together with the main wing, allowing for both more aerodynamic efficiency as well as for sharper turns under high G loads. Due to the resulting decreased size and inertia, sharp maneuvers can be performed even faster than what is achieved by aircraft used in aerobatic racing at this day. The selected subsystems allow for a efficient and cheap operation. They are distributed over the aircraft as such that it is stable and controllable in all flight conditions. For comfort of the pilot, he is positioned close to the centre of gravity of the aircraft. Aerodynamically, E-SPARC is designed in a way that the canard will always stall first, increasing the safety of the design in flight. The canard features a modified NACA-12311-62 airfoil, while the main wing is shaped using a NACA-9216-42 airfoil. The fuselage houses all subsystems used for powering the aircraft, as well as the pilot and the retractable nose landing gear for reduced drag. The aircraft is powered by 12 battery modules, delivering energy for over 30 minutes of flight at 50% throttle and a 3 minute race at full throttle. A single pusher propeller drives the aircraft forward.

E-SPARC is a small and light aircraft. The maximum take-off weight is only 414.95 kg. Its fuselage is only 4 meters long. The wings, with a wingspan of 5.562 metres and an area of 5.156 metre^2, extend in the rear of the fuselage without leading edge sweep and incorporate the ailerons. The wingtips are bend upwards, forming winglets that house the rudders. The canard, with a span of 3.02 metres and an area of 1.140 metres^2, is mounted in the front of the fuselage and holds the elevators. The control surfaces allow for fast maneuvering and performance on the track. A roll rate of 460 $°/second$ can be achieved.

Even though these parameters are the result of a preliminary design and may still change slightly over the remainder of the design process, they give a good indication of the final product and allow E-SPARC to compete in the Red Bull Air Races. Additionally, due to its novel design, it is expected that it will gain the interest of the broader public, possibly leading the way to a new type of aerobatic racing. This is also due to the sustainable design approach, making E-SPARC an exciting product. Using batteries and energy from renewable sources, as well as the high efficiency from the electric engine, adds a new aspect to aerobatic racing.

In further design steps the aircraft has to be further refined and optimised. More detailed aerodynamic analyses using established tools such as CFD analysis, and later wind tunnel tests are necessary to verify and validate the design and prove its readiness for the racing application. Also, more detailed connections between the subsystems and the fuselage or wings as well as the exact positioning and operation of controls have to be determined. Thereby it is crucially important to manage the weight distribution to maintain a stable and controllable aircraft since the range of possible centre of gravities of the entire configuration is limited. While these activities may still have an influence on certain design parameters it can be concluded that the E-SPARC design as presented in this report will prove the feasibility and marketability of an electrically propelled aerobatic racing aircraft.

BIBLIOGRAPHY

[1] Red Bull Air Race, *Red Bull Air Race Pays Tribute to Earth Day*, http://www.redbullusa.com/cs/Satellite/en_air/Article/Red-Bull-Air-Race-pays-tribute-to-Earth-Day-021242835814786, Last visited on 20/06/2015.

[2] FAA, *Use of Aicraft Issued Experimental Airworthiness Certificates in Flight Instruction for Compensation or Hire*, Tech. Rep. (FAA, 2011).

[3] Light Aircraft Association, *A Guide to LAA Aircraft Ownership*, Tech. Rep. (LAA, 2014).

[4] Ministère de l'écologie, du développement durable et de l'énergie, *Navigabilité des aéronefs*, http://www.developpement-durable.gouv.fr/-Navigabilite-des-aeronefs,1706-.html, Last visited on 11/05/2015.

[5] Red Bull Air Race, *Master Class Pilots*, http://www.redbullairrace.com/en_INT/pilots, Last visited on 23/04/2015.

[6] Extra Aircraft Information & Sales, *Extra 330SC Equipment and Options 2015*, http://www.extraaircraft.co.uk/, Last visited on 23/04/2015.

[7] MX Aircraft, *MXS Aircraft Options and Price list*, http://www.mxaircraft.com/mxs-pricelist.php, Last visited on 23/04/2015.

[8] MX Aircraft, *MX-2 Aircraft Options and Price list*, http://www.mxaircraft.com/mx2-pricelist.php, Last visited on 11/05/2015.

[9] Aircraft Compare, *Zivko Edge 540*, http://www.aircraftcompare.com/helicopter-airplane/Zivko-Edge-540/401, Last visited on 20/05/2015.

[10] Red Bull, *Red Bull Air Race Operations*, http://www.redbullusa.com/cs/Satellite/en_air/Article/Red-Bull-Air-Race-Rises-To-Logistics-Challenge-021242745716250, Last visited on 12/05/2015.

[11] Dr. ir. R. Vos, Ir. B.T.C. Zandbergen, *AE1201 Aerospace Design and Systems Engineering Elements I – Lecture 1: Introduction and organization in aircraft development* , Delft University of Technology.

[12] *Report of the World on Environment and Development: Our Common Future* (United Nations, Development and International Co-operation: Environment, 1987) UN Documents, Gathering a body of global agreements.

[13] Oxis Energy, *Oxis Energy - Li-S*, http://www.oxisenergy.com/technology, Last visited on 12/05/2015.

[14] B. Albrecht, *How Green is Lithium*, http://www.kitco.com/ind/Albrecht/2014-12-16-How-Green-is-Lithium.html, Last visited on 12/06/2015.

[15] Oak Ridge National Laboratory, *New all solid sulfur based battery outperforms lithium ion technology*, http://electricvehicle.ieee.org/battery-technologies/new-all-solid-sulfur-based-battery-outperforms-lithium-ion-technology/, Last visited on 12/06/2015.

[16] Zivko Aeronautics Inc., *Pilot's Operating Handbook and Flight Manual Edge 540-T*.

[17] YASA Motors, *YASA 750 Axial Flux Electric Motor*.

[18] A. Yazdanbakhsh, *A Critical Review of Research on Reuse of Mechanically Recycled FRP Production and End-of-Life Waste for Construction*, Tech. Rep. (City College of New York, Civil Engineering Department, June 2014).

[19] A. Hedlund-Astrom, *Model for end of life treatment of polymer composite Materials*, Tech. Rep. (KTH Royal Institute of Technology, Stockholm, 2005).

[20] Battery University, *How to Recycle Batteries*, http://batteryuniversity.com/learn/article/recycling_batteries, Last visited on 12/06/2015.

[21] A. Kumar, *The Lithium Battery Recycling Challenge*, http://www.waste-management-world.com/articles/print/volume-12/issue-4/features/the-lithium-battery-recycling-challenge.html, Last visited on 12/06/2015.

[22] R. Vos, *A/C Preliminary Sizing (T/W-W/S diagram)*, Delft University of Technology.

[23] European Aviation Safety Agency, *Certification Specifications for Normal, Utility, Aerobatic and Commuter Category Aeroplanes CS-23* (European Aviation Safety Agency, 2012).

[24] D. P. Raymer, *Aircraft Design: A Conceptual Approach* (American Institue of Aeronautics and Astronautics (AIAA) education series, 1989).

[25] Race Committee, *Red Bull Air Race World Championship Regulations Part E Technical Regulations* (Red Bull Air Race GmbH, 2010).

[26] Race Committee, *Red Bull Air Race World Championship Regulations Part A Sporting Regulations* (Red Bull Air Race GmbH, 2010).

[27] Siemens AG, *Siemens develops world-record electric motor for aircraft*, Press release: München, March 24 2015 .

[28] Prof. Z. S. Spakovszky, *Performance of Propellers*, http://web.mit.edu/16.unified/www/FALL/thermodynamics/notes/node86.html, Last visited on 11/05/2015.

[29] Siemens AG, *Siemens develops world-record electric motor for aircraft*, http://www.siemens.com/press/en/feature/2015/corporate/2015-03-electromotor.php?content[]=Corp, Last visited on 08/05/2015.

[30] Cub Crafters, *Specifications CC11-160 Carbon Cub SS*, http://www.cubcrafters.com/carboncubss/specs, Last visited on 13/06/2015.

[31] Quality Fly Aviation Academy, *Cessna 152*, http://www.qualityfly.com/page6/page10/page10.html, Last visited on 13/06/2015.

[32] E. Torenbeek, *Synthesis of Subsonic Airplane Design: An introduction to the preliminary design of subsonic general aviation and transport aircraft, with emphasis on layout, aerodynamic design, propulsion and performance* (Nijgh-Wolters-Noordhoff Universitaire Uitgevers B.V., 1976).
[33] NextCraft, *Berkut Long EZ info,* http://www.nextcraft.com/berkut01.html, Last visited on 13/06/2015.
[34] Velocity Aircraft, *Production Aircraft Specifications,* http://www.velocityaircraft.com/airplane-specifications.html, Last visited on 13/06/2015.
[35] IHS, *Jane's All the World's Aircraft,* https://janes.ihs.com/CustomPages/Janes/ReferenceHome.aspx via TU Delft Library, Last visited on 01/05/2015.
[36] Red Bull Air Race, *Red Bull Air Race Aircraft,* http://www.redbullairrace.com/en_US/article/planes, Last visited on 13/06/2015.
[37] Garmin, *Avionics and Flight Technology,* (2015).
[38] Aircraft Spruce & Specialty Co., *CHRISTEN 820 AEROBATIC SEAT BELT / HARNESS SYSTEM,* http://www.aircraftspruce.com/catalog/appages/christen820.php, Last visited on 13/06/2015.
[39] MH Aviation Oxygen Systems, *AL Series Cylinders,* http://www.mhoxygen.com/cylinders/aluminum, Last visited on 13/06/2015.
[40] Free Flight Enterprises Inc., *Preserve III - Pilot Emergency Parachutes,* http://www.freeflightent.com/pilot-emergency-parachutes.php, Last visited on 13/06/2015.
[41] J. Roskam, *Airplane Design Part III: Layout Design of Cockpit, Fuselage, Wing and Empennage: Cutaways and inboard profiles* (Roskam Aviation and Engineering Corporation, 1985).
[42] Hartzell Propeller Inc., *Application Guide* (2014).
[43] SmokeFly Switzerland, *Smoke Cartridges,* http://www.smokefly.ch/index.php?page=products.html&lang=en, Last visited on 13/06/2015.
[44] I. D. Steenhuizen, *Aerospace Design and Systems Engineering Elements II - Wing Design Part 2* (2013 publisher=Delft University of Technology).
[45] United Instruments Inc., *Maintenance Manuals from United Instruments,* http://www.unitedinst.com/Publications/, Last visited on 16/06/2015.
[46] United Instruments Inc., *Turn and Slip,* http://www.unitedinst.com/Products/TurnandSlip/.
[47] Sarasota Avionics International, *VSI (Vertical Speed),* http://sarasotaavionics.com/category/flight-instruments/vsi-(vertical-speed), Last visited on 16/06/2015.
[48] Bequiet, *Shadow Wings,* http://www.bequiet.com/en/casefans/264, Last visited on 16/06/2015.
[49] Tanis, *Battery Heat Element,* http://www.tanisaircraft.com/tb02643-22-115-42.html, Last visited on 16/06/2015.
[50] Nate Blank, Josh Wang, Daniel Holloway Campos, Gemma Hatton, Damien Gaignard, Damian Greavy, Gustavo Sánchez, *The Cranfield Formula Electric Series MSc Advanced Motorsport Engineering Group Design Project – Team 2,* https://www.cranfield.ac.uk/courses/masters/files/impulse-poster-group2.pdf, Last visited on 20/06/2015.
[51] Garmin, *G3x-Touch,* http://www.garmin.com/us/products/intheair/sport-aviation/g3x-touch/, Last visited on 16/06/2015.
[52] Sarasoto Avionics International, *GSU25 ADAHRS,* http://sarasotaavionics.com/avionics/gsu25, Last visited on 16/06/2015.
[53] M. M. Farag, *Materials and process selection for engineering design* (CRC Press, 2013).
[54] P. Johnson, *Retractable Gear,* http://www.canardaviation.com/PhillipJohnson/General/retractable_gear.htm, Last visited on 16/06/2015.
[55] AEVA, *Soapbox on regenerative braking,* http://forums.aeva.asn.au/forums/soapbox-on-regenerative-braking_topic824_page11.html, Last visited on 16/06/2015.
[56] Sarwant Singh, *Elon Musk's 500,000 Unit Battery Plant - Myth or Reality?* http://www.forbes.com/fdc/welcome_mjx.shtml, Last visited on 16/06/2015.
[57] Airmaster, *AP430 System Overview,* http://www.airmasterpropellers.com/products/productdescription/type/view/id/53/ap430-system-overview, Last visited on 16/06/2015.
[58] Aircraft Spruce, *Smoke System Kit Models SA2,* http://www.aircraft-spruce.com/catalog/appages/sa102-103.php, Last visited on 16/06/2015.
[59] Aircraft Spruce, *WC2 5-WIRE TEFLON® INSTALLATION CABLE,* http://www.aircraft-spruce.com/catalog/appages/sa102-103.php, Last visited on 16/06/2015.
[60] Aircraft Spruce, *A-740 RACHET CONTROL,* http://www.aircraftspruce.com/catalog/appages/a7401.php?clickkey=43487, Last visited on 16/06/2015.
[61] Aircraft Spruce, *ULTRALIGHTS BUCKET SEAT,* http://www.aircraftspruce.com/catalog/appages/bucketseat.php?clickkey=6739, Last visited on 16/06/2015.
[62] Aircraft Spruce, *INFINITY AEROSPACE MILITARY STICK GRIPS,* http://www.aircraftspruce.com/catalog/elpages/infinitygrips.php?clickkey=8992.
[63] Aircraft Spruce, *DELUXE HOMEBUILDERS RUDDER PEDALS,* http://www.aircraftspruce.com/catalog/lgpages/rudderpedalkit.php?clickkey=12349.
[64] Bell's Aviation, *Anti-G,* http://www.bellsaviation.com/mm5/merchant.mvc?Screen=CTGY&Store_Code=BA&Category_Code=Anti-GSuits.
[65] Gibson & Barnes, *HGU-68 Helmet Features,* http://www.gibson-barnes.com/assets/files/sme-product/293960/data-sheet.pdf.

[66] Bell's Aviation, *Oxygen Mask Parts,* http://www.bellsaviation.com/mm5/merchant.mvc?Screen=CTGY&Store_Code=BA&Category_Code=A-13, Last visited on 16/06/2015.

[67] Bell's Aviation, *Oxygen Equipment,* http://www.bellsaviation.com/mm5/merchant.mvc?Screen=PROD&Store_Code=BA&Product_Code=392&Category_Code=OE, Last visited on 16/06/2015.

[68] Pay Scale, *Automobile Mechanic Salary,* http://www.payscale.com/research/US/Job=Automobile_Mechanic/Hourly_Rate.

[69] Mark E. Gunnison, *What it Costs to Fly,* http://www.gnjpc.com/mark/flying/cost/index.php.

[70] www.loonwijzer.nl, *Salaris Check,* http://www.loonwijzer.nl/home/salaris/salarischeck, Last visited on 29/06/2015.

[71] CBS, *CBS: Arbeid kost in Nederland gemiddeld 33 euro per uur,* http://www.cbs.nl/nl-NL/menu/themas/arbeid-sociale-zekerheid/publicaties/artikelen/archief/2014/2014-4189-wm.htm, Last visited on 29/06/2015.

[72] Forum, *Anyone using CATIA V5 ?* http://www.boatdesign.net/forums/design-software/anyone-using-catia-v5-902.html, Last visited on 29/06/2015.

[73] www.mathworks.com, *Matlab License,* http://nl.mathworks.com/pricing-licensing/, Last visited on 29/06/2015.

[74] Forum, *Price of FEA software?* http://www.eng-tips.com/viewthread.cfm?qid=370796, Last visited on 29/06/2015.

[75] http://www.inventionstatistics.com/, *Invention Costs and Manufacturing Costs,* http://www.inventionstatistics.com/Invention_Costs.html, Last visited on 29/06/2015.

[76] Prof. E.G.Tulapurkara, *Flight dynamics-I Chapter IV,* https://www.coursehero.com/file/7066806/Module-4-Chapter-4-Engine-characteristics-2/, Last visited on 20/06/2015.

[77] I. GONZALEZ-MARTINO, B. FRANÇOIS, and B. RODRIGUEZ, *A physical insight into counter-rotating open rotor in-plane loads,* 21ème Congrès Français de Mécanique, 26 au 30 août 2013, Bordeaux, France (FR) (2013).

[78] J. Vanderover and K. Visser, *Analysis of a contra-rotating propeller driven transport aircraft,* AIAA Student Paper Competition (2006).

[79] Sevcon, *Sevcon Gen 4 Size 10 AC Motor Controller,* (2015).

[80] Oxis Energy, *Ultra Light Lithium Sulfur Pouch Cell,* (2014).

[81] Panasonic Industrial, *Panasonic Lithium-ion NCR18650B,* (2015).

[82] D. Andrea, *Battery management systems for large lithium-ion battery packs* (Artech House Boston, 2010).

[83] M. Muratori, *Thermal characterization of lithium-ion battery cell,* (2010).

[84] R. Slabospitsky, M. Khazhmuradov, V. Lukyanova, and S. Prokhorets, *Using the analytical calculation method for cooling systems,* Problems of Atomic Science and Technology , 303 (2013).

[85] A. Pesaran, A. Vlahinos, and S. Burch, *Thermal Performance of EV and HEV Battery Modules and Packs* (National Renewable Energy Laboratory, 1997).

[86] University of Waterloo, *Fluid Properties,* http://www.mhtl.uwaterloo.ca/old/onlinetools/airprop/airprop.html, Last visited on 20/05/2015.

[87] *E-SPARC DSE14 Mid Term Report*, Tech. Rep. (Delft University of Technology, 2015).

[88] M. Drela, *XFoil, Subsonic Airfoil Development System,* http://web.mit.edu/drela/Public/web/xfoil/, Last visited on 22/06/2015.

[89] T. Cebeci, *An Engineering Approach to the Calculation of Aerodynamic Flows* (Horizons Publishing, 1999).

[90] *United States Air Force Stability and Control DATCOM*, Tech. Rep. (McDonnell Douglas Corporation, 1975-1977).

[91] *Computer Program To Obtain Ordinates for NACA Airfoils* .

[92] Royal Aeronautical Society, *Program for calculation of maximum lift coefficient of plain aerofoils and wings at subsonic speeds,* https://www.esdu.com/cgi-bin/ps.pl?sess=delft_1150617094705lgr&t=doc&p=esdu_93015b, Last visited on 17/06/2015.

[93] A. Deperrois, *A comparison of performance measurements to XFLR5 results,* CEAT Toulouse.

[94] Ira H. Abbott, Albert E. Von Doenhoff, Louis S. Stivers, *REPORT No. 824 Summary of Airfoil Data*, Tech. Rep. (National Advisory Commitee for Aeronautics, 1945).

[95] W. Young, R. Roark, and R. Budynas, *Roark's formulas for stress and strain* (McGraw-Hill, 2002).

[96] Dr. ir. Gianfranco LaRocca, *AE3211-I Systems Engineering and Aerospace Design – Lecture 4: Requirement Analysis and Design principles for A/C stability & control (Part 1)* , Delft University of Technology.

[97] Dr. ir. Gianfranco LaRocca, *AE3211-I Systems Engineering and Aerospace Design – Lecture 5: Requirement Analysis and Design principles for A/C stability & control (Part 2)* , Delft University of Technology.

[98] J. Philips, *Approximate Neutral Point of a Subsonic Canard Aircraft*, Tech. Rep. (NASA, Ames Research Center).

[99] European Aviation Safety Agency, *Certification Specifications for Normal, Utility, Aerobatic and Commuter Category Aeroplanes CS-23* (European Aviation Safety Agency, 2010) paragraph 23.233.

[100] Mohammad Sadraey, *Aircraft Design: A System Engineering Approach* (Wiley Publications, 2012) chapter 12.

[101] TU Delft, *AE3-021 Aircraft Design: Design for stability and control (Part 2),* Delft University of Technology.

[102] E. Torenbeek, *Synthesis of Subsonic Airplane Design: An introduction to the preliminary design of subsonic general aviation and transport aircraft, with emphasis on layout, aerodynamic design, propulsion and performance* (Kluwer Academy, 1982).

[103] N. Kumar, N.S. Rao, *Estimation of stability and control derivatives of light canard research aircraft from flight data,* (2002).

[104] FAA, *Pilot's Handbook of Aeronautical Knowledge* (US Department of Transportation, 2008).

[105] *Lateral Stability (Rolling),* http://avstop.com/ac/flighttrainghandbook/lateralstability.html, Last visited on 21/06/2015.
[106] A. in t Veld, *Lecture Notes AE3202 Flight Dynamics* (Delft University of Technology, 2013).
[107] Goodyear, *Global Aviation Tirebook,* .
[108] *Grove aerospace landing gear systems inc.* http://www.groveaircraft.com/, Last visited on 22/06/2015.
[109] European Aviation Safety Agency, *Certification Specifications for Normal, Utility, Aerobatic and Commuter Category Aeroplanes CS-23* (European Aviation Safety Agency, 2012).
[110] E. D. M. Field, *Structural Analysis and Design of Airplanes* (Wexford College Press, 2005).
[111] T. H. G. Megson and T. Megson, *Aircraft Structures for Engineering Students* (Butterworth-Heinemann, 2013).
[112] Red Bull Air Race, *Video Track San Diego 2008,* http://www.redbullusa.com/cs/Satellite/en_air/Video/Track-San-Diego-2008-021238615471106, Last visited on 16/06/2015.
[113] Marc Naeije and Erwin Mooij, *Static Transformations, Reference Frames, AE3212-I - Aerospace Flight Dynamics and Simulation,* Delft University of Technology.
[114] Race Committee, *Red Bull Air Race World Championship Regulations Part B Race Track and Race Airport* (Red Bull Air Race GmbH, 2010).
[115] Red Bull Air Race, *TECH TALK - Pylon Changes for 2014,* http://www.redbullairrace.com/en_US/article/tech-talk-pylon-changes-2014, Last visited on 17/06/2015.
[116] C. Liem, *Trajectory optimization and conceptual aircraft design of an aerobatic aircraft*, Tech. Rep. (Delft University of Technology, 2009).
[117] Red Bull Air Race, *San Diego 2008 (USA),* http://www.redbullusa.com/cs/Satellite/en_air/Event/San-Diego-2008--USA--021238611594758, Last visited on 17/06/2015.
[118] Red Bull Air Race, *RACE PLANES: MXS, EDGE 540 & EXTRA 300 SR,* http://www.redbullusa.com/cs/Satellite/en_air/Video/Race-Planes--MXS,-Edge-540-Extra-300-SR-021238615472068, Last visited on 17/06/2015.
[119] Made, Jack E and Kurtz, Donald W, *A review of aerodynamic noise from propellers, rofors, and liff fans,* (1970).
[120] D. Muller, *Drag Force and Drag coefficient*, Tech. Rep. (Aircraft Performance Analysis, 2009).
[121] H. Kirchoff,C. Sutton, A. Kail, S. Fears, *Senior Design II Final Report: Red Bull Air Racer,* http://trace.tennessee.edu/cgi/viewcontent.cgi?article=2425&context=utk_chanhonoproj, Last visited on 20/05/2015.
[122] R. D. Finck, *USAF Stability and Control DATCOM*, Tech. Rep. (McDonnel Douglas Corporation, April 1978).
[123] M. Sadraey, *Aircraft Design: A Systems Engineering Approach* (Wiley Publications, 2012).
[124] *MIL-F-8785C Military Specification Flying Qualities Of Piloted Airplanes* (U.S. Military, 1980).
[125] A. D. Parker, *Racecars with wings: maintenance on the Red Bull circuit* (Aviation Today, 2009).
[126] FAA, *Section 91.155, 14 CFR Part 91, General Operating and Flight Rules* (2015).
[127] AOPA, *Aircraft ownership: aircraft inspection,* http://www.aopa.org/Pilot-Resources/Aircraft-Ownership/Aircraft-Inspections, Last visited on 19/05/2015.
[128] A. Ingram, *Electric Car Maintenance A Third Cheaper Than Combustion Vehicles?* (Green car reports, 2012).
[129] ECM, *Preventive maintenance of motors and controls,* http://ecmweb.com/content/preventive-maintenance-motors-and-controls, Last visited on 19/05/2015.
[130] IADC, *Definition of safety function,* http://www.iadclexicon.org/safety-function/, Last visited on 19/05/2015.
[131] International Electrotechnical Commission, *Definition of safety,* http://www.iec.ch/functionalsafety/explained/, Last visited on 19/05/2015.
[132] E. van der Zwan, *F.22 Pinguino/Sprint,* http://seqair.com/Frati/Designs/F22/F22.html, Last visited on 01/05/2015.
[133] D. York, *York Enterprises - Laser Z-300,* http://www.yorkaircraft.com/Z300.html, Last visited on 30/04/2015.
[134] R. Bayerl; M. Berkemeier; et al, *World Directory of Leisure Aviation* (WDLA, 2011).
[135] *T30 Katana,* http://www.pietroterzi.com/site/pro/t30katana.htm, Last visited on 30/04/2015.

A Reference Aircraft

Table A.1: Non-electric reference aircraft with their corresponding parameters

Category	Type	Engine type	EW [kg]	MTOW [kg]	W_{en} [kg]	$EW-W_{en}$ [kg]	P_{br} [kW]	$\frac{W}{P}$ $\left[\frac{N}{W}\right]$	$\frac{W}{S}$ $\left[\frac{N}{m^2}\right]$	b [m]	S [m^2]	V_{stall} $\left[\frac{m}{s}\right]$	$C_{L_{max}}$ [−]	A [−]	s_{TO} [m]	TOP $\left[\frac{Ns}{m^3}\right]$	Source
Aerobatic	Cap 10C	AEIO-360-B2F	540	780	125	415	134	0.057	705.3	8.08	10.85	27.5	1.52	6.0	395	26.5	[35]
Aerobatic	Extra EA-300L	AEIO-540-L1B5	672	820	204	468	224	0.036	751.4	8.00	10.70	28.3	1.53	6.0	248	17.7	[35]
Aerobatic	Extra EA-300S	AEIO-540-L1B5	585	820	204	381	224	0.036	820.1	7.50	9.81	30.6	1.43	5.7	248	20.6	[35]
Aerobatic	Aviat Pitts S-2C	AEIO-540-D4A5	524	771	175	349	194	0.043	641.0	6.10	11.80	28.8	1.26	3.2	366	22.0	[35]
Aerobatic	Zivko Edge 540	IO-540	531	703	216	316	254	0.032	757.3	7.42	9.10	26.4	1.78	6.1	90	13.5	[35]
Aerobatic	Nemesis NXT	TIO-540-NXT	726	1179	181	545	261	0.044	1778.	7.32	6.50	40.8	1.74	8.2	762	45.3	[35]
Aerobatic	XtremeAir XA-42	AEIO-580-B1A	610	850	204	406	235	0.032	741.6	7.50	11.25	27.5	1.60	5.0	400	14.8	[35]
Aerobatic	Slick 360	AEIO-360	465	625	127	338	161	0.032	659.2	7.31	8.60	28.9	1.39	6.2	351	15.0	[35]
Aerobatic	Slick 540	AEIO-540	550	716	204	346	221	0.032	814.2	7.31	8.60	30.6	1.43	6.2	351	18.3	[35]
Aerobatic	Sukhoi Su-31T	Vedeneyev M14P	750	1050	214	536	294	0.032	804.4	7.80	11.83	29.4	1.64	5.1	110	15.6	[35]
Kit	GlasAir III	IO-540-K1H5	737	1098	199	538	224	0.048	1413.6	7.11	7.60	35.0	1.89	6.7	275	35.8	[35]
Kit	Van's RV14	IO-390	562	862	140	422	157	0.058	778.9	8.23	11.70	23.3	2.17	5.8	161	20.9	[35]
Kit	Van's RV10	IO-540	726	1225	188	538	194	0.062	874.1	9.68	13.70	28.3	1.78	6.8	153	30.4	[35]
Kit	Van's RV7	IO-360	505	816	147	359	149	0.054	718.1	7.62	11.10	26.4	1.69	5.2	153	22.8	[35]
Aerobatic	Grob G 120A	AEIO-540-D4D5	1080	1440	175	905	194	0.075	1098.7	10.18	13.30	28.3	2.16	7.8	654	38.3	[35]
Aerobatic	General Avia F.22	O-320-D2A	582	850	127	455	119	0.035	770.7	8.50	10.82	36.0	0.97	6.7	400	27.8	[132]
Aerobatic	Yakovlev Yak-54	VOKBM M-14P	769	901	214	555	265	0.037	753.4	8.15	12.89	29.0	1.33	5.2	170	20.8	[35]
Aerobatic	Laser Z-300	IO-540	522	658	213	309	224	0.029	694.3	7.62	9.29	25.9	1.69	6.3	300	11.8	[133]
Aerobatic	Peña Joker	O-235	520	700	113	407	75	0.029	660.0	8.00	10.40	22.2	2.19	6.2	-	8.7	[134]
Aerobatic	Mü30 Schlacro	AEIO-540	748	1050	199	549	223	0.043	861.2	9.00	11.96	36.0	1.08	6.5	-	34.3	[35]
Aerobatic	Zlin Z-50	AEIO-540-D4B5	570	720	204	366	194	0.04	565.1	8.58	12.50	27.2	1.24	5.9	-	18.4	[35]
Aerobatic	MXS-R	IO-540-E	572	835	181	391	194	0.047	864.1	7.32	9.48	29.8	1.58	5.7	-	25.6	[35]
Aerobatic	Mylius MY-103/200	IO-360	620	950	136	484	149	0.063	891.8	8.65	10.45	31.4	1.48	7.2	-	37.8	[35]
Aerobatic	Extra EA-200	AEIO-360-A1E	562	700	137	426	149	0.046	657.5	7.50	10.44	30.6	1.15	5.4	-	26.3	[35]
Kit	Altitude Radial Rocket	VOKBM M-14P	748	1157	214	534	265	0.048	1351.2	7.77	8.40	38.1	1.52	7.2	-	42.2	[35]
Aerobatic	Yakovlev Yak-55M	VOKBM M-14P	645	840	214	431	265	0.035	643.8	8.10	12.80	30.6	1.13	5.1	-	19.8	[35]
Aerobatic	Dyn'Aero CR100	AEIO-360-B2F	550	760	125	425	134	0.056	701.4	8.50	10.65	-	-	6.8	351	-	[35]
Aerobatic	Corvus CA-41 540	TIO-540-U	545	685	263	282	257	0.029	746.7	7.40	9.00	26.4	1.75	6.1	-	-	[35]
Aerobatic	RUD RA-2	AEIO-540 [315hp]	612	855	204	408	235	0.036	-	7.32	-	28.3	-	-	351	-	[35]
Aerobatic	RUD RA-3	IO-360 [180hp]	499	816	136	363	134	0.06	-	7.32	-	25.8	-	-	351	-	[35]
Aerobatic	Terzi T30C Katana	IO-540 [300hp]	658	880	213	445	224	0.043	-	7.57	-	-	-	-	-	-	[135]
		Averages	622	875	180	442	201	0.044	839.9	7.89	10.55	29.6	1.56	6.1	316	24.3	

B Class II inputs

Table B.1: Inputs Class II weight estimation

Parameter	Input Value	Unit
W_{fw}	0.005	$[kg]$
A_w	6.0	$[-]$
$\Lambda_{w_{\frac{c}{4}}}$	-0.063	$[rad]$
q	4937	$[N/m^2]$
λ_w	0.45	$[-]$
t/c_{root}	0.15	$[-]$
N_{ult}	18	$[-]$
L/W	1.0	$[-]$
L/D	8.6	$[-]$
W/S	790	$[N/m^2]$
Λ_{vt}	0.349	$[rad]$
λ_{vt}	0.5	$[-]$
$\frac{H_c}{H_{vt}}$	0.0	$[-]$
S_{vt}	1.3	$[ft^2]$
Λ_c	0.0	$[rad]$
λ_c	1.0	$[-]$
A_c	10	$[-]$
t/c_c	0.18	$[-]$
LW_c	0.1	$[-]$
Wfw_c	0.005	$[kg]$

Parameter	Input Value	Unit
L_c	3.2	$[m]$
S_f	12.1	$[m^2]$
N_{land}	2.5	$[-]$
L_m	1.0	$[m]$
L_n	0.5	$[m]$
L	5.0	$[m]$
$W_{payload}$	94.75	$[kg]$
$W_{subsystems}$	40.44	$[kg]$
PW	0.043	$[kW/kg]$
p_{motor}	5.2	$[kW/kg]$
η_{prop}	0.85	$[-]$
η_{en}	0.95	$[-]$
η_{bat}	0.9	$[-]$
e_{bat}	1800	$[kJ/kg]$
v_{bat}	1980	$[kJ/L]$
t	1080	$[s]$

C Track Coordinates

Table C.1: The coordinates and altitude of the estimated trajectory used for the track simulation

Point	Latitude			Longitude			Altitude
	°	′	″	°	′	″	[m]
0	32	42	18.5	117	10	29.9	16
1	32	42	18.7	117	10	28.8	16
2	32	42	18.99	117	10	26.85	16
3	32	42	19.38	117	10	25.38	16
4	32	42	19.9	117	10	23.93	16
5	32	42	20.44	117	10	22.5	16
6	32	42	20.92	117	10	20.81	16
7	32	42	21.06	117	10	19.07	16
8	32	42	21.08	117	10	16.97	16
9	32	42	20.76	117	10	15.28	16
10	32	42	20.14	117	10	14.12	16
11	32	42	19.26	117	10	13.15	16
12	32	42	17.72	117	10	11.87	17
13	32	42	16.54	117	10	10.97	18
14	32	42	15.63	117	10	10.01	18
15	32	42	14.83	117	10	8.39	19
16	32	42	14.65	117	10	6.71	20
17	32	42	14.01	117	10	5.12	21
18	32	42	13.26	117	10	4.12	21
19	32	42	11.82	117	10	3.27	20
20	32	42	10.44	117	10	3.31	19
21	32	42	8.96	117	10	4.09	18
22	32	42	7.71	117	10	4.81	17
23	32	42	6.29	117	10	5.59	16
24	32	42	4.91	117	10	5.79	16
25	32	42	3.29	117	10	5.41	16
26	32	42	2.25	117	10	4.62	16
27	32	42	1.44	117	10	3.55	16
28	32	42	0.9	117	10	2.8	16
29	32	42	0.21	117	10	1.68	17
30	32	41	59.37	117	10	0.46	19
31	32	41	58.7	117	10	59.06	20
32	32	41	58.5	117	10	57.46	21
33	32	41	58.94	117	10	55	21
34	32	41	59.88	117	10	53.41	21
35	32	41	1.13	117	10	52.57	21
36	32	42	2.75	117	10	52.14	20
37	32	42	4.08	117	10	52.62	19
38	32	42	4.84	117	10	53.28	18
39	32	42	5.3	117	10	53.9	17
40	32	42	5.8	117	10	54.63	18
41	32	42	6.49	117	10	56.14	19
42	32	42	6.69	117	10	57.63	19
43	32	42	6.52	117	10	59.69	18
44	32	42	6.11	117	10	1.94	18
45	32	42	5.57	117	10	4.37	17
46	32	42	4.75	117	10	7.35	16
47	32	42	4.18	117	10	10.21	16
48	32	42	3.66	117	10	13.71	16
49	32	42	3.79	117	10	15.38	16
50	32	42	4.34	117	10	16.77	18
51	32	42	5.29	117	10	17.91	18
52	32	42	6.56	117	10	18.43	19
53	32	42	8.83	117	10	18.76	18
54	32	42	10.7	117	10	19.2	19
55	32	42	12.16	117	10	19.2	18
56	32	42	13.63	117	10	19.32	17
57	32	42	15.5	117	10	18.57	16
58	32	42	16.67	117	10	17.03	18
59	32	42	16.87	117	10	14.97	20
60	32	42	16.11	117	10	13.19	22
61	32	42	14.44	117	10	11.6	24
62	32	42	12.66	117	10	11.63	26
63	32	42	11.4	117	10	12.93	28
64	32	42	10.73	117	10	14.96	28
65	32	42	10.78	117	10	16.6	27
66	32	42	10.83	117	10	18.23	26
67	32	42	10.7	117	10	19.2	24
68	32	42	10.54	117	10	20.65	21
69	32	42	10.41	117	10	22.53	18
70	32	42	10.31	117	10	24.73	16
71	32	42	10.41	117	10	26.85	16
72	32	42	10.73	117	10	29.01	16
73	32	42	11.43	117	10	30.97	16
74	32	42	12.3	117	10	32.79	16
75	32	42	13.81	117	10	34.41	17
76	32	42	15.36	117	10	34.65	18
77	32	42	17.08	117	10	33.7	17
78	32	42	18.11	117	10	32.21	17
79	32	42	18.3	117	10	31.15	16

Table C.2: The coordinates of the verification trajectory used for the track simulation

Point	Latitude			Longitude			Altitude
	°	′	″	°	′	″	[m]
0	51	59	26.31	04	22	31.99	30
1	51	59	30.51	04	22	24.28	28
2	51	59	37.38	04	22	16.63	26
3	51	59	44.25	04	22	14.17	24
4	52	59	50.60	04	22	10.69	22
5	51	59	56.96	04	22	15.08	20
6	52	00	02.74	04	22	20.02	20
7	52	00	04.72	04	22	33.34	23
8	52	00	01.18	04	22	45.53	26
9	51	59	53.52	04	22	49.99	29
10	51	59	44.50	04	22	54.63	32
11	51	59	38.54	04	22	51.80	34
12	51	59	33.53	04	22	49.63	32
13	51	59	28.48	04	22	45.32	31

D AIRCRAFT PARAMETERS

Table D.1: Summary of E-SPARC's parameters

Parameter	Symbol	Value	Unit	Source
Wing				
Span	b	5.562	$[m]$	Table 6.7
Surface area	S	5.156	$[m^2]$	Table 6.7
Aspect ratio	A	6.0	$[-]$	Section 6.3.1
Taper ratio	λ	0.45	$[-]$	Section 8.1.2 [24]
Mean aerodynamic chord	MAC	0.984	$[m]$	Table 6.7
Thickness over chord ratio	t/c	0.16	$[-]$	Section 8.1.1
Sweep at quarter chord	$\Lambda_{LE_{0.25c}}$	-3.6	[°]	Section 8.1.2
Maximum lift coefficient	$C_{L_{max}}$	1.78	$[-]$	Table 8.10
Lift slope	C_{L_α}	4.710	[1/°]	Table 8.10
Airfoil	-	NACA 9216-42	-	Section 8.1.1
Canard				
Span	b_c	3.02	$[m]$	Table 6.7
Surface area	S_c	1.14	$[m^2]$	Table 9.3
Aspect ratio	A_c	8.0	$[-]$	Section 8.1.2
Taper ratio	λ_c	1	$[-]$	Section 8.1.2
Chord	c_c	0.377	$[-]$	Table 6.7
Thickness over chord ratio	$(t/c)_c$	0.11	$[-]$	Section 8.1.1
Sweep leading edge	Λ_{LE_c}	0	[°]	Section 8.1.2
Maximum lift coefficient	$C_{L_{max c}}$	2.0	$[-]$	Section 8.1.1
Lift slope	$C_{L_{\alpha c}}$	4.83	[1/°]	Section 8.1.1
Airfoil	-	NACA 12311-62	-	Section 8.1.1
Winglet				
Surface area (both winglets)	S_{vt}	0.30	$[m^2]$	Table 9.3
Root chord	$c_{r_{vt}}$	0.575	$[m]$	Section 9.2.3
Longitudinal moment arm	l_{vt}	0.31	$[m]$	Section 9.2.3
Control Surfaces				
Aileron surface area	S_a	0.45	$[m^2]$	Table 14.1
Maximum aileron deflection	δ_a	$-20/+20$	[°]	Table 14.2
Elevator surface area	S_e	0.45	$[m^2]$	Table 14.1
Maximum elevator deflection	δ_e	$[-30,-25]/[15,25]$	[°]	Table 14.2
Rudder surface area	S_r	0.51	$[m^2]$	Table 14.1
Maximum rudder deflection	δ_r	$[-30,-25]/[25,30]$	[°]	Table 14.2
Fuselage				
Length	l_f	4.0	$[m]$	Chapter 11
Maximum radius	r_f	0.5	$[m]$	Chapter 11
Landing Gear				
Length	$H_{mg,static}$	0.72	$[m]$	Section 10.2
Tire width	wmg	10.160	$[m]$	Section 10.2 [107]
Tire diameter	dmg	33.655	$[m]$	Section 10.2 [107]
Propulsion				
Motor available from power	$P_{m,out}$	136.4	$[kW]$	Table 7.6
Propeller type	-	Single open 3bladed	-	Section 7.2
Propeller diameter	D_{prop}	1.62	$[m]$	Section 7.2
Power output	P_r	115.5	$[kW]$	Table 7.6
Power				
Energy stored	E	50.37	$[kWh]$	Section 7.5
Battery type	-	Li-S		Section 7.5
Performance				
Maximum (level) speed	V_{max}	101.6	$[m/s]$	Section 12.2
Maximum stall speed	V_{stall}	29.3	$[m/s]$	Table 6.3
Maximum rate of climb	RC_{max}	15.3	$[m/s]$	Table 6.3
Maximum roll rate	p	460	[°/s]	Section 14.3.1